2012

Enhancement of MgB2 superconductor by magnetic nanoparticle doping

Mislav Mustapic
University of Wollongong, mislav@uow.edu.au

Recommended Citation

Mustapic, Mislav, Enhancement of MgB2 superconductor by magnetic nanoparticle doping, Doctor of Philosophy thesis, Institute for Superconducting and Electronic Materials, University of Wollongong, 2012. http://ro.uow.edu.au/theses/3822

Institute for Superconducting and Electronic Materials

Enhancement of MgB_2 Superconductor by Magnetic Nanoparticle Doping

Mislav Mustapić

This thesis is presented as part of the requirements for the
Award of the Degree of Doctor of Philosophy
of the
University of Wollongong

November 2012

UNIVERSITY OF
WOLLONGONG

Declaration

I, Mislav Mustapić, declare that this thesis, submitted in partial fulfilment of the requirements for the award of Doctor of Philosophy, in the Institute for Superconducting & Electronic Materials (ISEM), Faculty of Engineering, University of Wollongong, Australia, is wholly my own work unless otherwise referenced or acknowledged. This document has not been submitted for a qualification at any other academic institution.

Mislav Mustapić
November, 2012

Acknowledgements

I would like to express my deep gratitude to my supervisors, Assoc. Prof. J. Horvat, Prof. S. X. Dou, and Prof. E. Babić for their continuous academic guidance, encouragement, and all kinds of support during my PhD study.

My special thanks go to Dr. G. Peleckis and Dr. Md. Shariar Hossain for all help and support during my PhD study at ISEM.

I am pleased to thank Prof. K. Zadro, Dr. Z. Skoko, Dr. D. Pajić, Dr. N. Novosel, and Mr. S. Galić for all their help and advice in my joint work at the University of Zagreb. Also I am very grateful to the Unity through Knowledge Fund (UKF) organisation for providing my stipend during my work at the University of Zagreb.

I thank Dr. T. Silver for her kind help in correcting the English in this thesis.

I would like to thank all my colleagues at ISEM, Sujeewa, Ashkan, Igor, Victor, Thomas, Babar, Nanda, Alfred, Steven, and Dr. Xun for the friendly atmosphere and their help in my research work.

At this special moment, I have to remember all my friends in Croatia, who make me smile and keep me cheerful all the time with stories and jokes, Hrvoje, Zrinka, Bartul, Štef, Brzi, Bora, Vule, Pera, Bodež, Jurić, Oršolić, Čoki, Lipi, and Brki.

Finally, my success up to this point would not have occurred without the endless support of my family, primarily my parents Vinko and Ana, and their unconditional help and encouragement in all my decisions during my lifetime.

Abstract

Magnesium diboride superconductor is easy and cheap to produce, and it can be operated at temperatures that can be maintained by inexpensive cryocoolers, requiring only electrical power input. In order to make it competitive with classical superconductors, its performance in high magnetic field needs to be improved. This is done by improvement of vortex pinning through including non-superconducting nano-defects. Theoretical work shows that magnetic nanoparticles could give better vortex pinning than the non-magnetic ones. Existing experimental reports on this topic are patchy and inconclusive. This work presents a systematic study on the preparation of various magnetic nanoparticles, their incorporation into MgB_2, and mechanisms for improvement of current carrying capabilities for the most successful nanoparticles.

A number of different nanoparticles were prepared and tried: carbon coated Co, carbon coated Fe, carbon coated Ni, $CuFe_2O_4$, Fe_2B, Co_2B, NiCoB, Fe_3O_4, CoB, SiO_2 coated Fe_2B, Co_2B, and commercial Eu_2O_3 and Dy_2O_3. Most of them resulted in marginal improvement of MgB_2, or even in degradation of its properties. The most successful results were obtained with NiCoB nanoparticles 5 nm in size. They are the focus of this project.

The best NiCoB nanoparticles were prepared by the wet method of chemical reduction of metallic salts, which yielded nanoparticles small enough to be successful pinning centres in MgB_2.The success of this method is due to the medium level alkaline environment with surfactants which supported their growth. The nanoparticles were clearly superparamagnetic. Optimization of the preparation procedure for nano-NiCoB doped MgB_2 gave the best performance for 2.5 wt% NiCoB doping, the use of amorphous 500 nm-size boron with micron-sized Mg, and heat treatment at 850°C for 30 minutes.

Detailed analysis of the improvement of critical current density, J_c, by this doping revealed that the connectivity between superconducting crystals and the vortex pinning were both

improved as a result of this procedure. The connectivity improved due to refinement of crystals and, at the same time, due to removal of MgO from the crystals due to the reaction between Mg and the dopant nanoparticles.

The vortex pinning improved only at low temperatures. High temperature heat-treatment was required to obtain the vortex pinning. A reaction between the NiCoB nanoparticles and Mg led to formation of Mg_2Ni and Co_2Mg nanoparticles that were incorporated into the MgB_2 matrix, where they acted as pinning centres. Competition of NiCoB for Mg with MgO was the most likely cause of the decrease in MgO content in the samples, leading to better connectivity. These new nanoparticles did not have a spontaneous magnetic moment.

No effects of magnetic pinning were observed in this project, although a large number of different magnetic nanoparticles were used as dopants. Therefore, this project casts doubt on the effectiveness of magnetic nanoparticles as a means of improvement of vortex pinning in MgB_2 through the interaction of magnetic vortices with the magnetic moment of nanoparticles.

TABLE OF CONTENTS

LIST OF TABLES

LIST OF FIGURES

1: INTRODUCTION

1.1 Brief history of superconductivity

The phenomenon of superconductivity started with the initial discovery by Heike Kamerlingh Onnes in 1911 of zero resistance in the element mercury. When he cooled it to the temperature of liquid helium, 4.2 Kelvin, its resistance suddenly disappeared[1].

Onnes realized that superconductivity represents a new physical state of matter. The temperature of transition to the superconducting state is called the critical temperature, T_c. Kamerlingh Onnes received the Nobel Prize in 1913 for his discovery of superconductivity and for research in this field.

Walther Meissner and his graduate student Robert Ochsenfeld discovered in 1933 that a superconducting material will expel magnetic field from its volume upon cooling through the superconducting transition in a constant field[2].

This is due to the appearance of superconducting screening currents in a thin surface layer of superconductor. These currents produce magnetization of the same magnitude as the external field, but in the opposite direction. In this way, the net magnetic field is zero inside the superconductor, except for a thin surface layer: $B = \mu_0 (H-M) = 0$.

In 1935, the brothers Fritz and Heinz London showed that the Meissner effect was a consequence of the minimization of the electromagnetic free energy carried by the superconducting current. The London brothers applied the well-known theory of electromagnetism based on what are known as Maxwell's equations to the case of a superconductor. They established that the magnetic field B(x) at a point at a distance *x* from the surface of the superconductor is:

$$B(x) = B(0)\exp(-x/\lambda_L) \qquad (1.1)$$

where λ_L is the London penetration depth and B(0) is the magnetic field at the surface. The London penetration depth is a parameter in the so-called London equations that were derived to explain magnetic field penetration into superconductor.

In 1950 two Russian physicists, Ginzburg and Landau**,** derived the London equations based on the free energy of the system and expanded them with a new parameter Ψ whose square is proportional to the density of superelectrons. The Ginzburg-Landau (GL) theory provided the same expression for the penetration depth as the London model and also an expression for the second characteristic length parameter, ξ, called the coherence length, and the ratio $\kappa = \lambda/\xi$ which is known as the Ginzburg–Landau parameter. The Ginzburg-Landau theory provides a good description of many of the properties of both classical and high-temperature superconductors. The Ginzburg-Landau theory is also a phenomenological theory, however, and does not explain the microscopic mechanism of superconductivity.[3]

Alexei A. Abrikosov showed that the Ginzburg-Landau theory predicts the division of superconductors into two categories, now referred to as Type I and Type II superconductors. In type II superconductors there are two fields, the lower critical field, H_{c1}, and the upper critical field, H_{c2}. In the mixed state, between H_{c1} and H_{c2}, the external field penetrates the superconductor in the form of vortices, which form a proper hexagonal lattice.[4, 5]

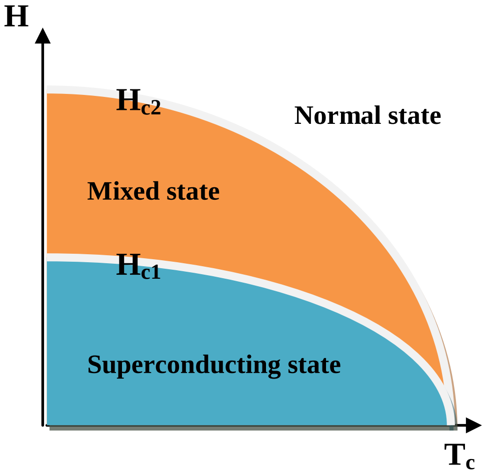

Figure 1.1: Magnetic phase diagram of a Type II superconductor.

In 1950 the theorist Herbert Fröhlich concluded that vibrating atoms of a material must play an important role in causing it to superconduct. Fröhlich proposed that an electron-phonon interaction between the electrons carrying the supercurrent and the vibrating lattice bring about superconductivity. In the same year, Fröhlich's prediction was confirmed using different isotopes of the element mercury. It was observed that the transition temperature decreased as the mercury atoms became heavier.[6]

The first microscopic understanding of superconductivity was advanced in 1957 by three American physicists, John Bardeen, Leon Cooper, and John Schrieffer. The fundamental conceptual element of the Bardeen Cooper Schrieffer (BCS) theory is the formation of electron pairs, the so-called Cooper pairs, by interaction between electrons close to the Fermi level. Cooper pairs interacting through the exchange of phonons (an electron-lattice interaction) condense into a boson-like state. The Cooper pair's interaction region has the size of the coherence length ξ. The Fermi level in the superconducting state produces an energy gap, E_g, which represents the binding energy of the Cooper pairs: $E_g = 2\Delta(0) = 3.52\ k_B T_c$, where $\Delta(0)$ is the energy gap between the ground state and the quasi-particle state that exists for superconducting materials.[7]

In 1962 Brian D. Josephson, a graduate student at Cambridge University, predicted that electrical current would flow between 2 superconducting materials − even when they are separated by a non-superconductor or insulator. This phenomenon is broadly used in applications of superconductors, such as the superconducting quantum interference device (SQUID).[8]

In 1986, Bednorz and Mueller discovered superconductivity in a lanthanum-based cuprate perovskite material with transition temperature of 35 K (Nobel Prize in Physics, 1987)[9]. Ching-Wu Chu, shortly after this discovery, replaced the lanthanum atom with yttrium and made $YBa_2Cu_3O_{7-x}$ (YBCO).[10]

The thus-obtained new compound had a critical temperature of 92 K. That was the first reported high-temperature superconductor (HTS), a compound which superconducts above the boiling point of liquid nitrogen (77 K). In this new class of layered superconductors, the properties are dominated by CuO_2 planes. Overall, research on these complex compounds was boosted, and year by year, new T_c records were launched.

Material	**T_c (K)**	**Year**
$Ba_xLa_{5-x}Cu_5O_9$	30-35	1986
$(La_{0.9}Ba_{0.1})_2Cu_4O_{4-x}$ (at 1 GPa pressure)	52	1986
$YBa_2Cu_3O_{7-x}$	95	1987
$Bi_2Sr_2Ca_2Cu_3O_{10}$	110	1988
$Tl_2Ba_2Sr_2Ca_2Cu_3O_{10}$	125	1988
$Tl_2Ba_2Sr_2Ca_2Cu_3O_{10}$ (at 7 GPa pressure)	131	1993
$HgBa_2Sr_2Ca_2Cu_3O_{8+x}$	133	1993
$HgBa_2Sr_2Ca_2Cu_3O_{10}$ (at 30 GPa pressure)	147	1994

Table 1.1: Critical temperatures of some of the cuprate superconductors, together with the year they were discovered.

The discovery of superconductivity in MgB_2 by Prof. J. Akimitsu has spurred significant research boom as well, thanks to the many good qualities of this relatively simple compound.[11]

MgB_2 superconducts below 39 K and is neither a low- nor a high-temperature superconductor. It is relatively easy to produce, however, is cheap, and its superconductivity can be maintained by inexpensive cryocoolers at 20 K.

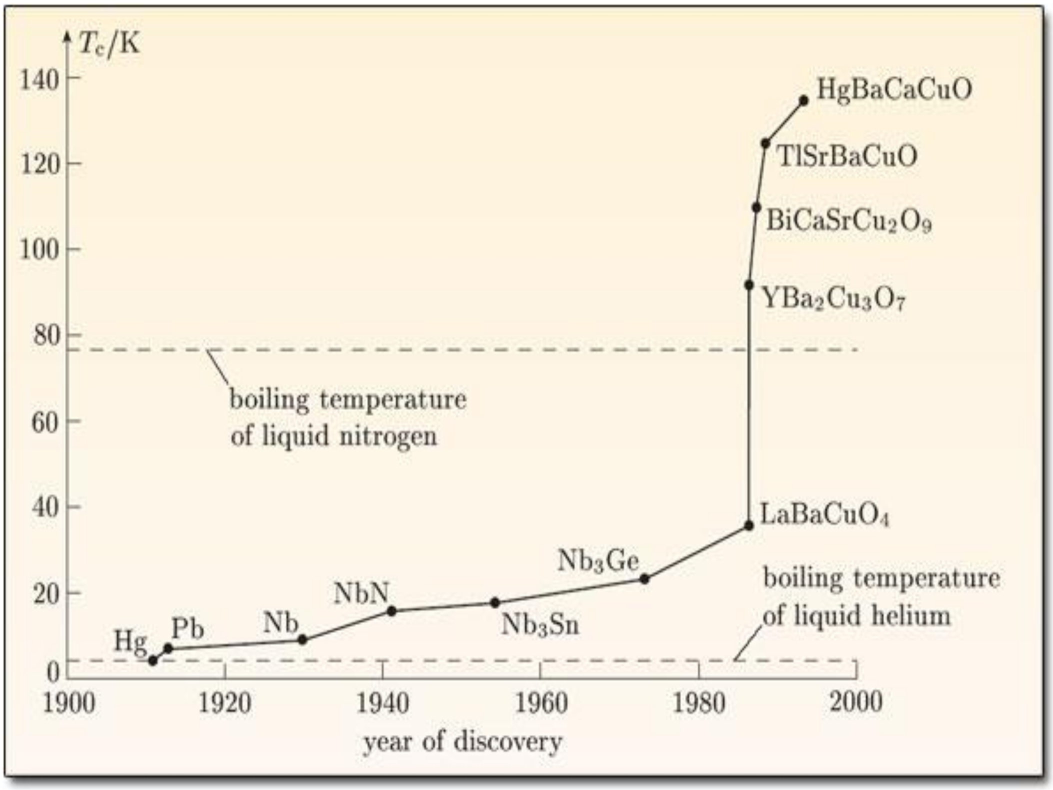

Figure 1.2: Timeline of discovery for different groups of superconductors, together with their critical temperatures. Adopted from [12]

1.2 Magnesium diboride

1.2.1 Introduction

The intermetallic compound magnesium diboride was first synthesized and described in 1954 in USA[13]. 50 years after its first synthesis, however, Jun Akimitsu's group first discovered that it was superconducting in 2001[11]. Good superconductivity properties, such as low anisotropy, large coherence length, high critical current densities, and good weak-link tolerance, make this superconductor easily adaptable for practical use. Its T_c of more than double that for similar binary compounds and its generally useful properties, such as cheap starting materials and suitability for a simple fabrication process, spurred an enormous research effort worldwide. Besides its great advantages over similar Nb-based superconductors in terms of its T_c (NbTi, T_c = 9 K; $NbSn_3$, T_c = 18 K), MgB_2 also has a weakness in regard to its superconducting current carrying capability in magnetic field. This capability is described by the maximum current density that produces electric field of 1 µV/cm, which is for practical purpose defined as the critical current density, J_c. J_c of pure MgB_2 decreases rapidly with magnetic field.

Possibilities for practical applications prompted intense research, mainly to improve the properties of the critical current density in magnetic field. MgB_2 has been made in different forms, such as thin films, bulk, wires, tapes, and single crystals, and enhanced via various chemical and mechanical routes. Much of the research is based on nanoparticle doping of the MgB_2 matrix.

Doping with different types of nanoparticles from organic nanocarbon to inorganic silica carbide has given significant enhancement to the superconducting properties of MgB_2.

Production and characterization of various suitable nanoparticles requires an interdisciplinary approach to this effort. Nanotechnology offers great opportunities for applications and has even become an autonomous discipline of science, which is becoming involved in all parts of life and industry. This chapter will first describe the general theoretical and practical aspects of magnesium diboride, followed by basic preparation principles and properties of magnetic nanoparticles.

1.2.2 Crystal structure of MgB_2

The intermetallic compound MgB_2 has the simple hexagonal structure of AlB2 (space group P6/mmm), as shown in Fig. 1.2.3(a). The alternating layered structure contains graphite-type layers separated by hexagonal close-packed-like magnesium layers. The atoms in MgB_2 are held together by covalent B-B and ionic B-Mg bonding. The magnesium atoms donate electrons to the boron planes. The basic lattice parameters are $a = b = 3.086$ Å (defined by the in plane Mg-Mg distance) and $c = 3.524$ Å (defined by the distance between the Mg- and B-layers). MgB_2 shows anisotropic behaviour in its electromagnetic properties due to the different distance between in-plane B-B atoms and the considerably longer distance between boron planes.[14, 15, 16]

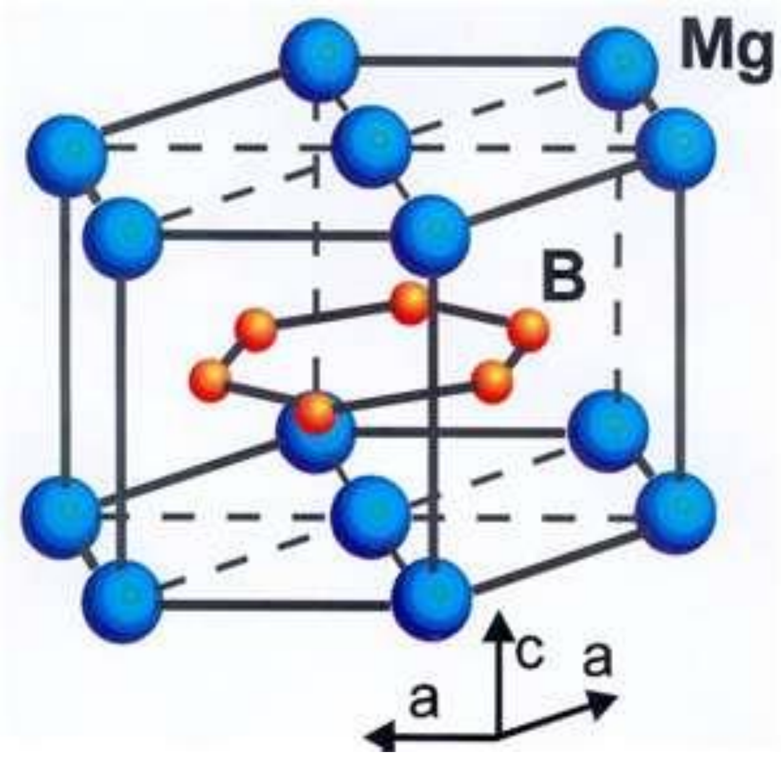

Figure 1.2.3(a): Layered structure of MgB_2. Adopted from [14].

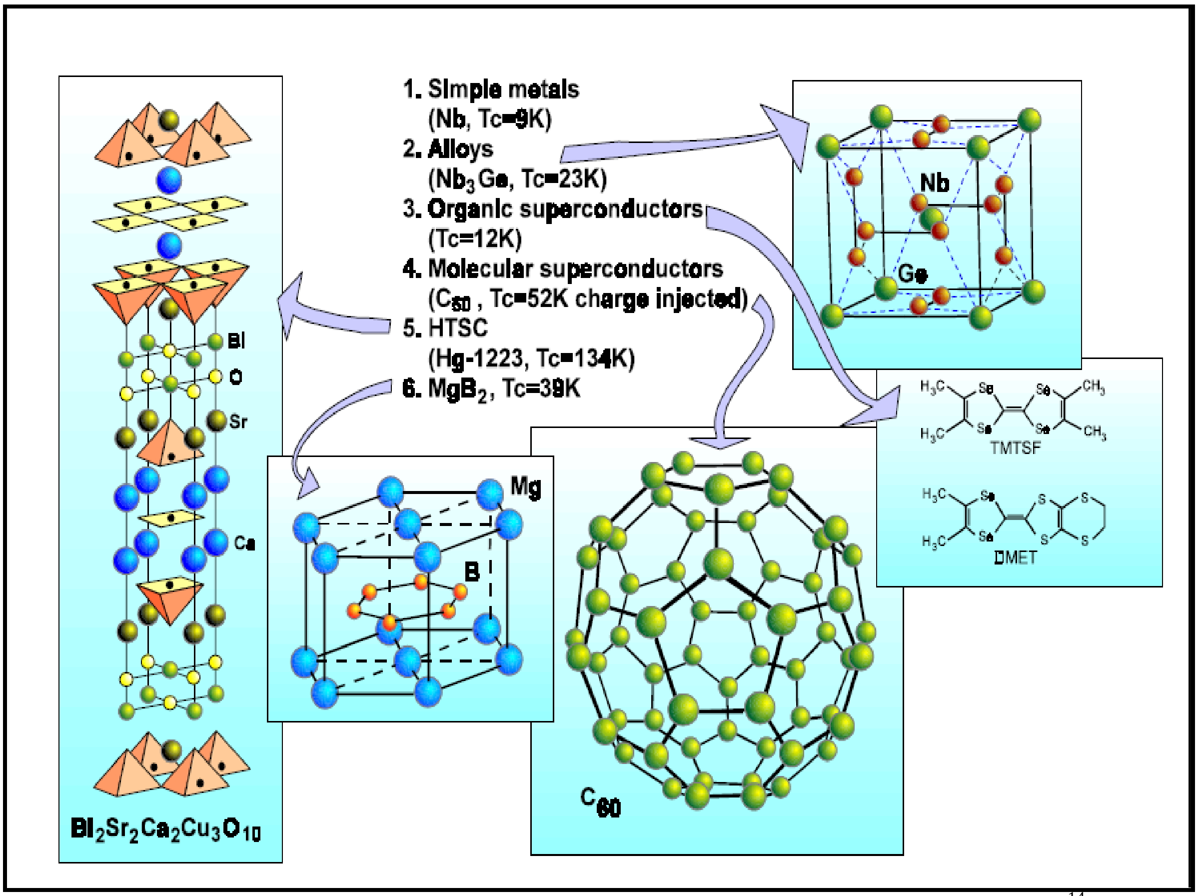

Figure 1.2.3(b): Comparison of MgB_2 with other types of superconductors. Adopted from [14].

1.2.3 Superconducting energy gap

MgB_2 is a phonon-mediated BCS superconductor, with superconductivity originating in the B planes[17]. The superconducting mechanism is mainly interpreted in terms of BCS-type phonon mediated pairing, where electrons form Cooper pairs via the electron-phonon interaction. Elements with low mass result in higher frequency phonon modes, which may lead to enhanced transition temperatures[18]. Normally in a superconductor below T_c, only one temperature-dependent superconducting energy gap, $\Delta(T)$, exists. The energy gap represents the energy needed to break apart the basic carriers of superconductivity, the Cooper pairs.

According to BCS theory, the size of the energy gap in the superconductor is expressed by the equation $E_g = 2*\Delta(0) = 2*1.76\ k_B T_c$. When putting T_c = 39 K into this expression, one obtains the energy gap as $\Delta(0) = 5.9$ meV.

Experimental confirmation arrived shortly afterwards, when Karapetrov[19] found by using scanning tunnelling spectroscopy that the energy gap was ~ 5 meV.

Further studies have confirmed that MgB_2 has two different superconducting gaps of about $\Delta(0) = 6.8$ meV for the σ sheet, and $\Delta(0) = 1.8$ meV for the π sheet.[17, 19, 20, 21, 22, 23, 24, 25]

Neighbouring boron atoms in the plane create σ bonds by overlapping their sp^2 orbitals (2D). The remaining p-bound orbitals (3D) are formed between adjacent planes and create the π bands. As shown in Figure 1.2.4(a), the golden hexagonal network is associated with the σ bands, whereas the six green lobes above and below the boron plane are associated with the π bands.

The Fermi surface represents the highest occupied electron energy states at zero Kelvin. One π-band is electron-type (shown as a blue tubular network along the LHL-line in Fig. 1.2.4(b), and the other one is hole-type (blue tubular, MKM-line in Fig. 1.2.4(b). The other two are σ bands assembled from the covalent $p_{x,y}$ orbitals (yellow and red cylinders centered around the ΓAΓ line).

The charge distribution is not symmetric in the boron plane and causes strong coupling of the σ-band state, which defines the in-plane vibrations and production of E_{2g} phonons. These phonons interact with charge carriers, creating Cooper pairs. Cooper pair formation also occurs in the π-band producing electron pair formation, but these pairs are coupled much more weakly.[26, 27]

The unexpectedly high T_c of MgB_2 is related to the hole-phonon coupling between the in-plane boron phonons in E_{2g} mode and holes in the σ-band.[17]

MgB_2 has holes in the bonding σ-bands, which contribute 42 per cent to the density of states. The total interaction strength, $\lambda = 0.87$, is dominated by the coupling of the σ-holes to the bond-stretching optical phonons, with wavenumbers in a narrow range around 590 cm^{-1}.[28] Like the holes, these phonons are quasi two-dimensional and have wave-vectors close to ΓA, where their symmetry is E. The π-electrons contribute merely 0.25 to λ.[28] This strong coupling between a few zone centre holes and optical phonons is what drives the high-temperature superconductivity in MgB_2. The coupling constant is given by the Hopfield

$$\lambda = \frac{ND^2}{M\omega^2}$$

(1.2.2)

where $\boldsymbol{N}$ is the density of states (DOS) per spin at the Fermi level of the σ holes, ω is the phonon frequency, M is the atomic mass, and D^2 is the square of the electron–phonon matrix element averaged over the Fermi surface. The optical phonons are softened by the interaction with the holes and that significantly enhances λ and $T_c \sim \omega \exp(-1/\lambda)$.[29]

Both gaps decrease with rising temperature and finally become zero at critical temperature T_c, (Fig 1.2.5). The two gap superconductivity of MgB_2 has been confirmed by several experimental techniques, such as tunneling spectroscopy[30-33] and specific heat[34,35], as well as from the magnetic[36] and optical properties[37,38]. Even though the two-gap superconductivity was predicted theoretically much earlier, MgB_2 is the first superconductor where it can be studied experimentally.[39]

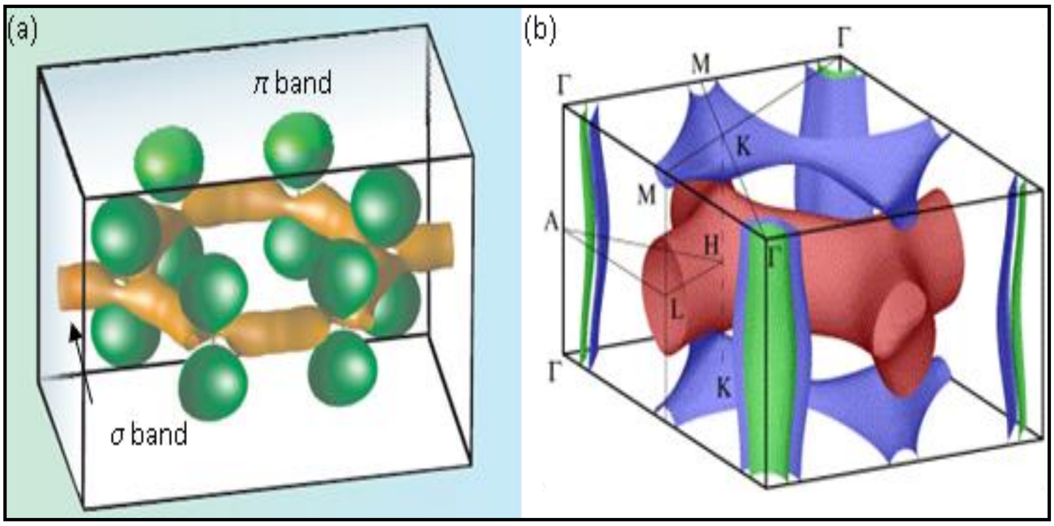

Fig 1.2.4: Electronic structure of MgB_2: (a) the 2D network of σ bands and 3D network of *π* bands[40]; (b) Fermi surface of MgB_2. The vertical sections of cylinders at the corners are associated with the σ bands; the 3D network of tunnels and caves in the center of the zone is associated with π bands[40]. There are cylindrical Fermi surfaces around the *Γ*-*A*-*M* line (x, y, z axes). Adopted from [40].

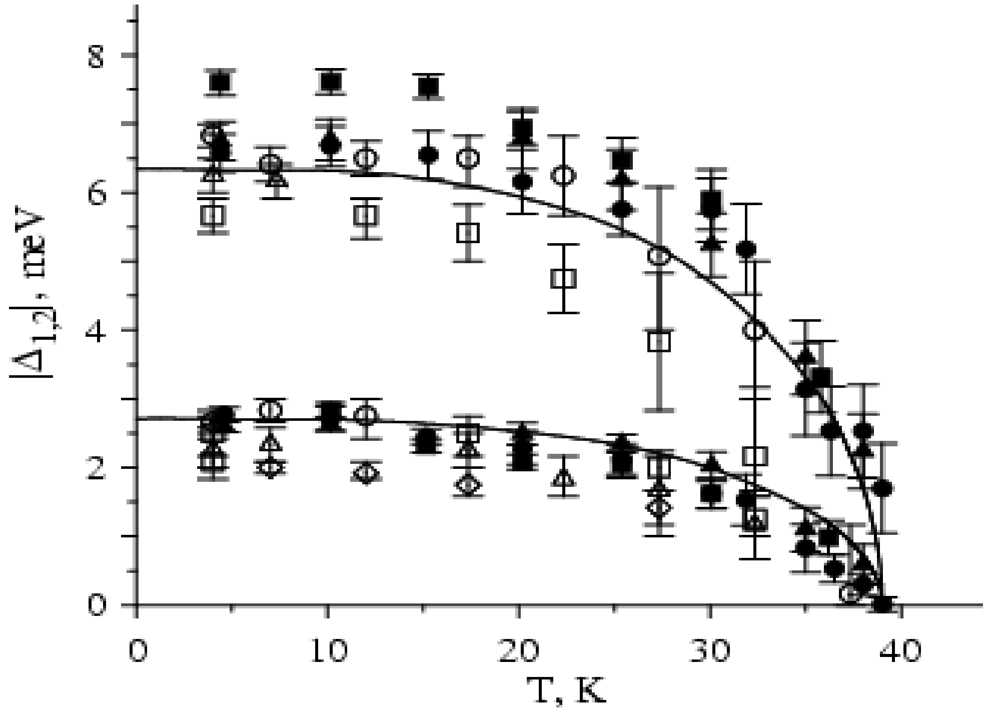

Figure 1.2.5: MgB_2 superconductivity gaps vs. temperature. Solid lines: theory. Filled symbols: the experimental data of [30]; open symbols: the experimental data of [31]. Adopted from [30,31].

1.2.4 Hall effect

The Hall effect represents displacement of current carriers towards the edges of the sample in a direction perpendicular to both the applied magnetic field and to the current. This charge gathering towards the sample edges creates an internal electric field. The Hall effect is observed through measurements of the voltage drop between the two edges of the sample, in the direction perpendicular to the current flow and the field. The Hall coefficient is defined as $R_H = -1/(en)$ for electron conductivity, where e is the electron charge and n the concentration of electrons. On the other hand, it is $R_H = +1/(ep)$ for hole conductivity, where p is the concentration of holes.

According to Kang et al., the Hall coefficient R_H is positive[41,42]. Charge carriers in MgB_2 are holes with a density at 300 K of between 1.7 - 2.8 × 10^{23} holes/cm^3, about two orders of magnitude higher than the charge carrier density for Nb_3Sn[43] and two orders of magnitude higher than for YBCO.[44]Anisotropy in the normal state Hall Effect was observed in MgB_2 single crystal by Eltsev et al.[45]

They found positive carriers (holes) from the in-plane Hall coefficient (H parallel to the *c*-axis) in agreement with previous experiments. The out-of-plane Hall coefficient (with H parallel to the *ab*-plane) is negative, however, indicating negative carriers (electrons), as shown in Fig 1.2.6.

The anisotropy in the Hall coefficient can be explained by the Fermi surface of MgB_2. As explained before, the Fermi surface is composed of four bands, two hole-like σ-bands in the form of two-dimensional (2D) cylindrical Fermi surfaces and two hole-like and electron-like 3D π-bands. For the in-plane case (H parallel to *c*); the hole-like carriers dominate the behaviour of R_H, resulting in positive values of R_H. On the other hand, when H is parallel to the *ab*-plane (out-of-plane), the σ-bands become less important, and the electron-like carriers dominate the R_H.[41,42]

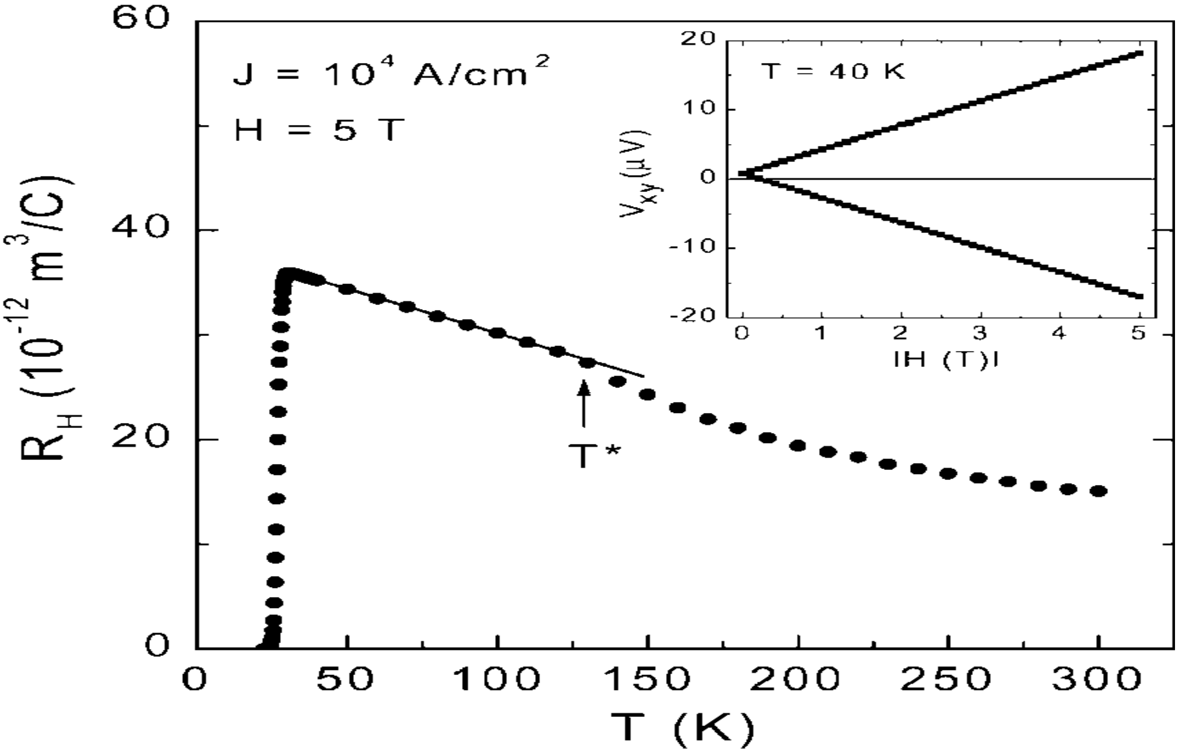

Figure 1.2.6: R_H versus temperature of MgB_2 thin films at 5 T. Distinct temperature dependences of the R_H are evident below and above130 K. The data were measured by reversing the magnetic field from −5 T to 5 T at a fixed temperature, as shown in the inset. Adopted from[41,42].

1.2.5 Total isotope effect

Theoretical physicist Herbert Fröhlich concluded that vibrating atoms in a crystal lattice must play a crucial role in creating the superconductive state. Fröhlich proposed that an electron-phonon interaction between electrons carrying the supercurrent and the vibrating lattice brings about superconductivity. An isotope effect on a superconductor transition temperature was confirmed for the first time with isotopes of elemental mercury. Change in the critical temperature T_c is correlated with isotope mass (atomic) M of a particular atom in the lattice according to the formula:

$$T_c \propto M^{-\alpha} \tag{1.2.3}$$

MgB_2 is a special system with two elements which both have different isotope masses that can change T_c. For superconductive compounds such as MgB_2 the total isotope effect coefficient α is the sum of the separate coefficient of Mg and B and has a value of $\alpha_T = \alpha_B + \alpha_{Mg} = 0.28$. The large value of the partial boron isotope exponent, α_B, of 0.26 shows that phonons associated with the B vibration play a main role in MgB_2 superconductivity[18]. On the other hand, the magnesium isotope effect, α_{Mg}, is very small, 0.02.[46]

Within BCS theory, which successfully describes the properties of such superconductors, one has:

$$k_B T_c = 1.13\, \hbar\omega_D\, e^{(1/VN(E_F))} \tag{1.2.4}$$

where $\hbar\omega_D$ is the energy of the phonon (where ω_D is the Debye frequency), $N(E_F)$ is the density of states at the Fermi level, and V is the electron-phonon coupling constant. The low mass elements result in higher Debye frequency of phonons and therefore, increase the transition temperature. That relationship can be explained with the simple harmonic oscillator equation,

$$T_c \propto \omega_D \approx (k/M)^{1/2} \tag{1.2.5}$$

where M is the mass of the vibrating atom and k the elastic coefficient. This gives $\alpha = 0.5$ in straight BCS theory. The dissimilarity between the value of the total isotope effect $\alpha_T = \alpha_B + \alpha_{Mg} \approx 0.28$ in MgB_2 and the 0.5 BCS-value may be associated to the high T_c of this material and electron-electron interaction.[14]

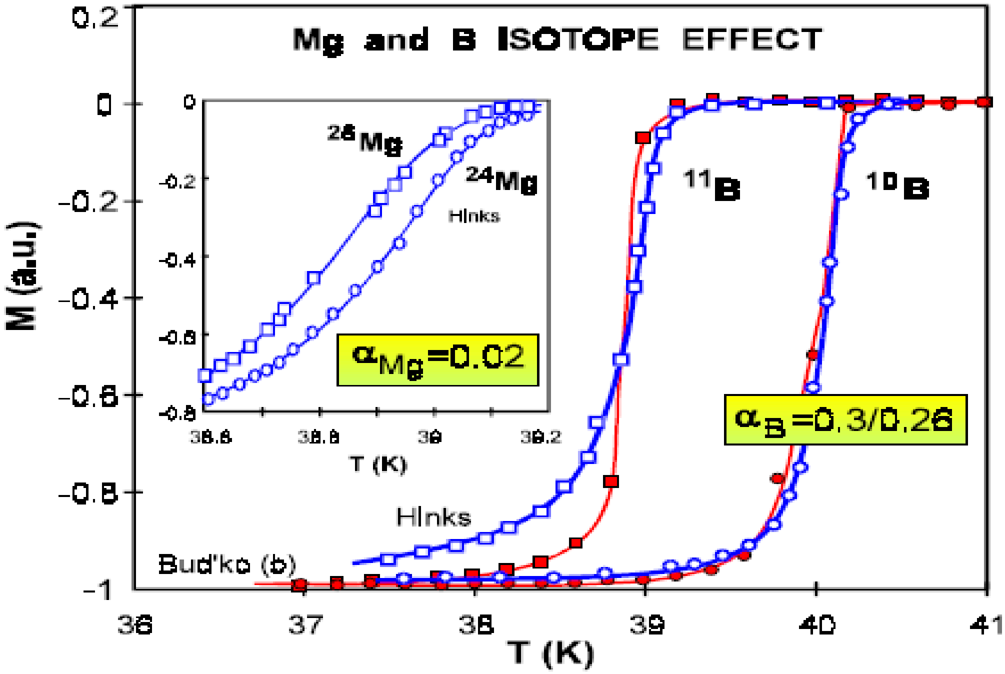

Figure 1.2.7: Boron isotope effect. Inset shows Mg isotope effect. Adopted from [14].

The large difference (Fig. 1.2.7) between the values of the partial boron isotope exponent, α_B, of 0.26(^{10}B) [18] and 0.3(^{11}B) indicates that phonons related to the B vibration play a substantial role in MgB_2 superconductivity.

1.2.6 Anisotropy

As MgB_2 is a layered structure, different electromagnetic properties of MgB_2 depend on the direction of measurement. The anisotropy is crucial for the basic description and understanding of this material, as well as for practical applications, especially given the strong influence on current carrying capacity by external magnetic field.

The values of the anisotropy ratio of the upper critical field, $\gamma = H_{c2}^{//ab} / H_{c2}^{//c}$, vary considerably. Figure 1.2.8 shows that values of γ obtained by several group range from 1.2 to 7.

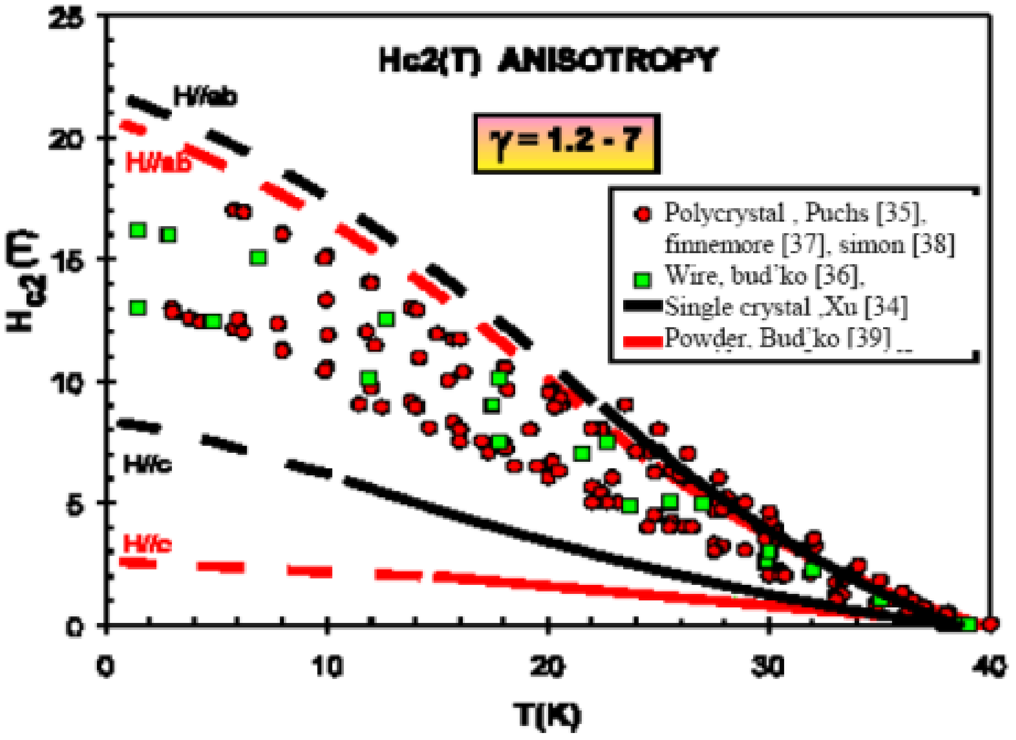

Fig 1.2.8: Upper critical field anisotropy versus temperature for MgB_2 single crystals, wire, and powders. Adopted from [14].

Measurements of anisotropy in H_{c2} were performed on different types of MgB_2 samples, including single crystals, bulks, thin films, and powders. For bulk samples, the anisotropy ratio $\gamma = H_{c2}^{//ab} / H_{c2}^{//c}$ is reported to be between 1.1 and 1.7 [47,48]; for *c*-axis oriented thin films, it is between 1.2 and 2.[49,50]

A slightly smaller anisotropy ratio was determined for tapes, around 1.3 for H_{c2} parallel to and orthogonal to the surface of the tape.[51,52] The large values of γ were obtained for powders, ranging from 5 to 9.[53,54] The critical field has anisotropy due to the anisotropic crystal structure of MgB_2.

Due to its simple crystal structure, MgB_2 has much smaller anisotropy than HTS superconductors such as Bi-2223, having $\gamma \approx 50\text{-}80$.[55] Reducing the anisotropy can be crucial for improving the critical current density and upper critical field. This is very important for polycrystalline materials where the grains are oriented at diverse angles to the applied field.

1.2.7 Grain connectivity and absence of weak links

Compared with HTS superconductors[56,57], MgB_2 shows an absence of weak links, as confirmed by magnetic and transport measurements (Fig. 1.2.9). Transport measurements in high magnetic fields of dense bulk samples yield very similar J_c values to the magnetic measurements[58]. This confirms that the grain boundaries are highly transparent to current flow, and the flux motion will determine J_c dependence on field and temperature. This good characteristic of MgB_2 gives big opportunities in practical application for use in wires or tapes with no degradation of J_c, compared to cuprate high temperature superconductors.

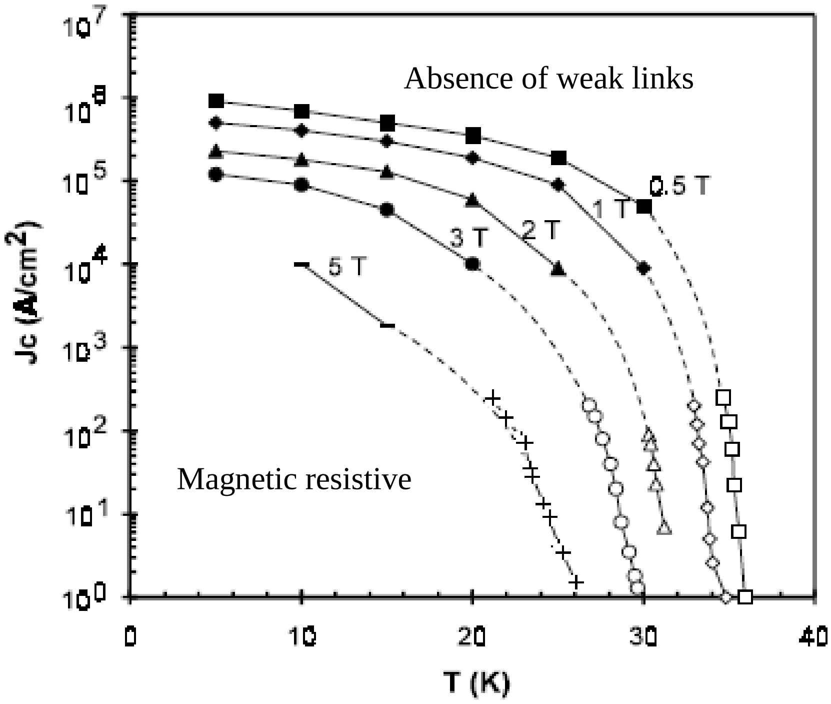

Figure 1.2.9: Critical current density dependence in magnetic field.[14,58] Adopted from [14].

1.2.8 Critical temperature

Compared with other borides and other binary compounds such as Nb_3Sn, MgB_2 has a significantly higher critical temperature, T_c = 39 K. The critical temperature of a superconductor is affected by many factors, such as material synthesis conditions, crystal structure, crystal defects, strains[59,60], chemical composition, purity of the sample (chemical doping), external pressure[61,62], irradiation with energetic ions[63,64], the presence of a magnetic field, etc. Every change in the standard lattice parameters finally results in decreasing the $T_{c.}$ Some parameters change the T_c more than others. Low crystallinity always reduces the transition temperature of MgB_2.

Lower crystallinity is usually connected with lower sintering temperature. The doping of MgB_2 compound with electrons, which contributes to an increase in the chemical potential, decreases the upper critical field H_{c2} and the value of T_c in comparison with the case of pure MgB_2. This behavior is especially observed in the case of doping with C and Al. Doping with holes does not affect the superconducting transition temperature and the upper critical field H_{c2}. Doping MgB_2 significantly changes the temperature dependence of the anisotropy coefficient.[65-71]

Hole doping by substitution of Li for Mg also decreases T_c[71]. Li et al.[69] have reported alkali metal substitution effects on the structure and superconductivity of $Mg_{1-x}A_xB_2$ (A = Li and Na) compounds.[71] T_c is affected adversely. Eisterer et al.[72] have identified four mechanisms that can potentially reduce the T_c: reduction of the density of states (DOS), reduction of the σ-gap anisotropy, hardening of the E_{2g} phonons, and intraband scattering.

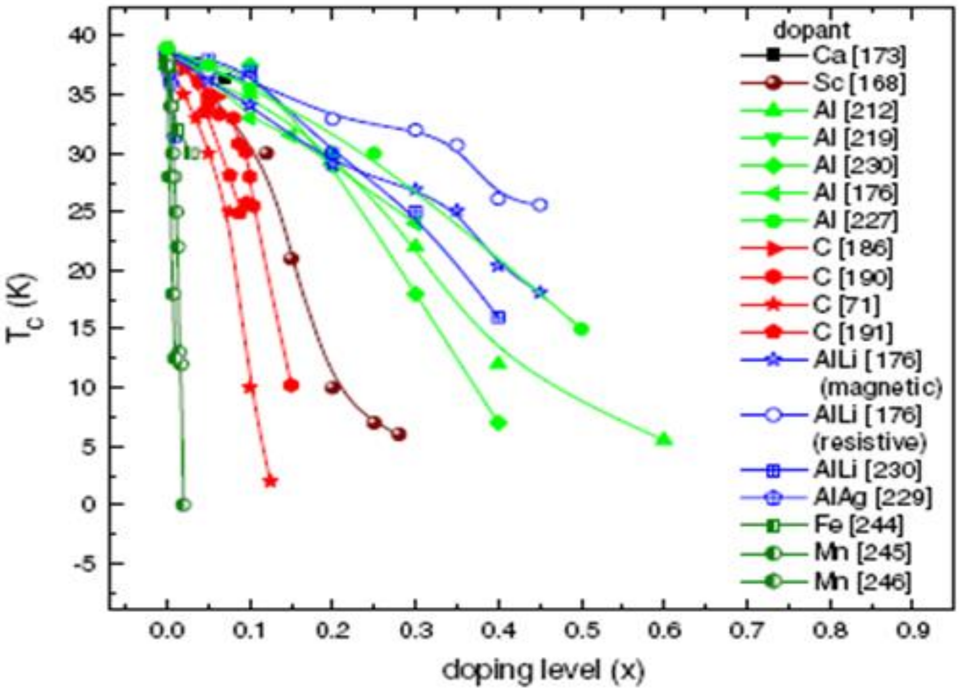

Figure 1.2.10: Variation of T_c of MgB_2 with doping level for various dopants. Adopted from [73].

1.2.9 Critical current density

Critical current is one of the most important characteristics of superconductors for technical application. When a current flows through a type-II superconductor, it will drive magnetic vortices into motion. Due to the local change of magnetic flux around the moving vortices, some of the screening current around each moving vortex is pushed into its normal core. This current pushed into the normal core of the moving vortex is subject to electrical resistance, resulting in a voltage drop along the superconductor. Because of this, vortices have to be pinned down, to prevent their motion and avoid the creation of voltage.[74]

Thermal excitations promote depinning of vortices, however, together with the Lorentz-like force acting on the vortices due to the current flow. Because of this, voltage will gradually increase with current at finite temperatures. This makes it difficult to define the "critical current", which would signify the maximum current at which the superconductor just starts developing the voltage. The practical definition of critical current for type-II superconductors is the current that produces a voltage drop in the superconductor of 1 μV over a 1 cm length of the superconductor.

One more important parameter derived from critical current (I_c) is the critical current density (J_c). J_c is defined as critical current per cross-sectional area (A) of the superconductor i.e. $J_c = I_c/A$. Critical current is a structure-dependent characteristic due to its dependence on the vortex pinning (i.e. structural imperfections), cross-sectional area, and geometry of the samples.

Even in zero magnetic field and without taking into account vortex motion, the current density produces a magnetic field at the surface of the sample that quenches the superconducting state and is called the depairing current density.[75]

$$J_{dp} = \Phi_o 3\sqrt{3}\, \xi\, \mu_0 \lambda^2 \tag{1.2.6}$$

where μ_0 is the magnetic permeability of vacuum, $\mu_0 = 4\pi * 10^{-7}$ Tm/A, while λ is the penetration depth and ξ the coherent length, two critical parameters of every superconductor, which will be explained in a later section. The depairing current would be the critical current in the absence of magnetic vortices. The vortex motion, however, regularly results in large enough voltage at currents smaller than the depairing current. Therefore, vortex pinning is the main parameter that defines the practical critical current.

The highest critical current density value for MgB_2 has been achieved in MgB_2 thin films around 4×10^{11} A/m^2 at low temperature and self field (external magnetic field 0 T)[76,77]. This promises a huge potential for further improvement of J_c for MgB_2 wires[78,79]. Compared with the critical current in Nb_3Sn films[80] and Nb-Ti[81], the critical current density of the best MgB_2

films is higher, but it decreases more rapidly with external magnetic fields. Most of the research on J_c worldwide has been on bulk and wire samples (Figs. 1.2.11-1.2.13). The J_c value is normally below 10^{10} A/m^2 at low temperature and zero magnetic field. In the presence of external magnetic field, J_c is strongly decreased, as is clearly shown in Figs. 1.2.11 and 1.2.12.

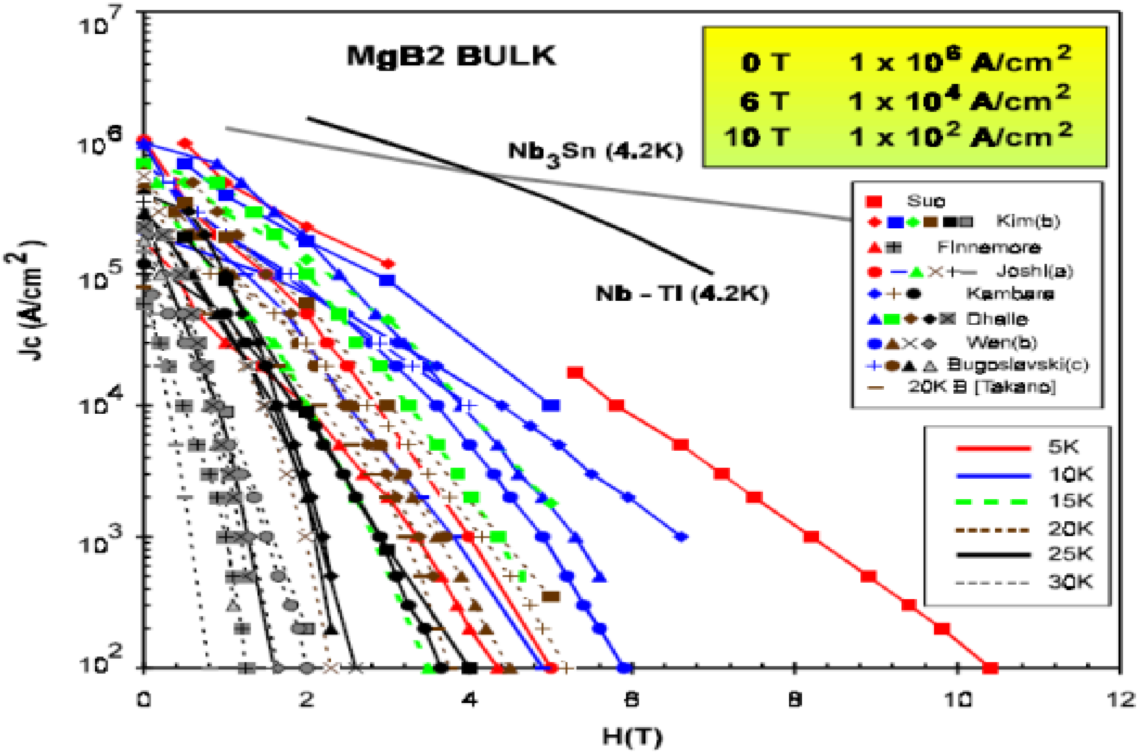

Figure 1.2.11: Critical current density versus magnetic field for MgB_2 bulk samples. The data for Nb-Ti and Nb_3Sn at 4.2 K are shown for comparison. Adopted from [14].

An interesting effect on J_c is observed with iron-clad sheaths. The iron shields the core from external fields, although the shielding becomes less effective for fields parallel to the tape plane.

Even when an external field is not applied, the transport current generates a self-field in the wire. As a ferromagnetic material, the Fe sheath will draw the flux lines into the sheath and finally reduce the effects of self-field of I_c.

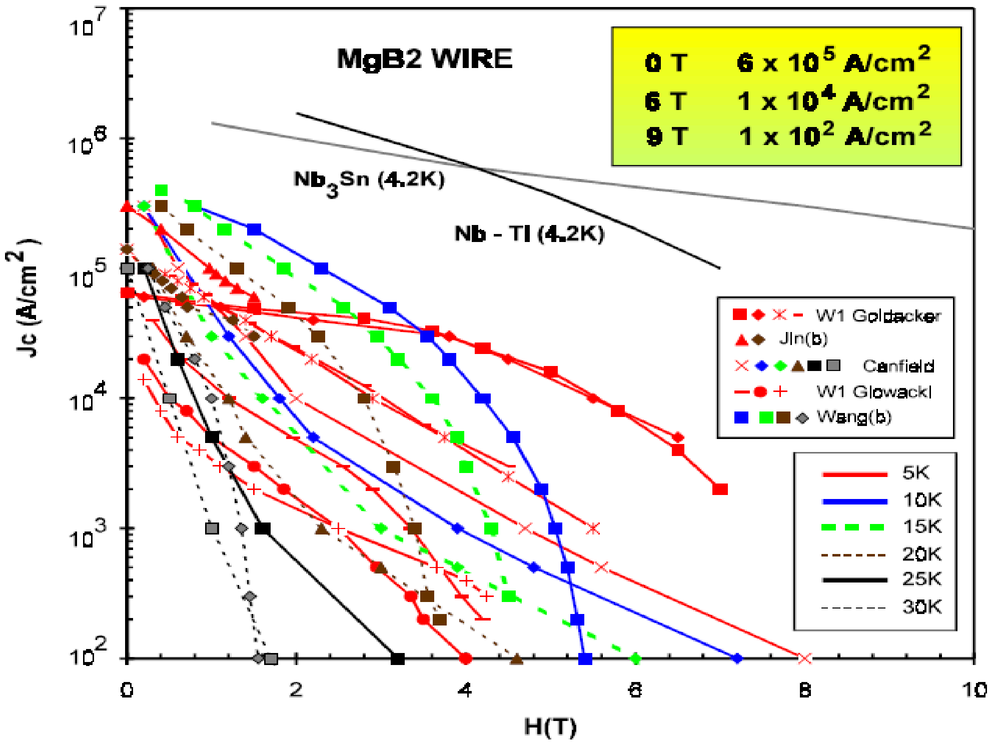

Fig. 1.2.12: Critical current density versus magnetic field MgB_2 for wire. Adopted from [14].

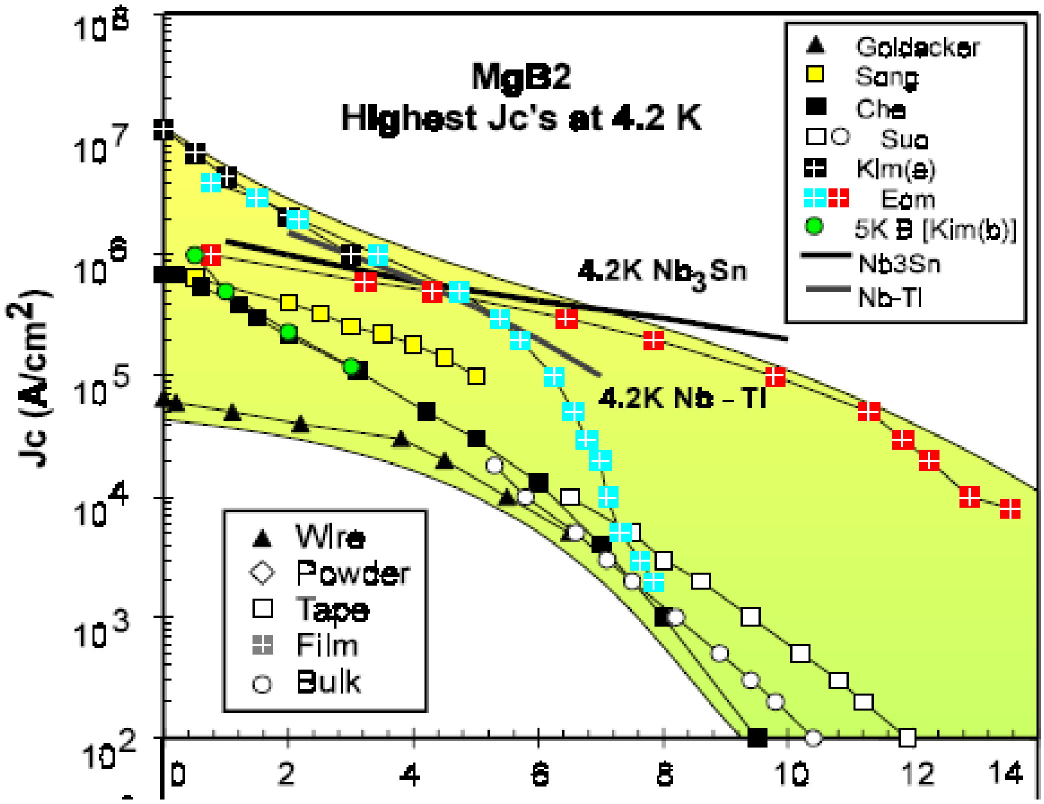

Fig. 1.2.13: Highest critical current densities versus magnetic field for MgB_2 at 4.2K, for bulk, film, tape, powder, and wire. Adopted from [14].

New data of critical current density results are given by [82,83].

1.2.10 Characteristic fields

As a type II superconductor, MgB_2 has two different critical fields to measure, the lower (H_{c1}) and the upper (H_{c2}) critical fields. The critical field anisotropy, γ, can be determined as $\gamma H_{c1} = H_{c1}^{//ab} / H_{c1}^{\perp ab}$ for the lower critical field and $\gamma H_{c2} = H_{c2}^{//ab} / H_{c2}^{\perp ab}$ for upper critical field.

There is also the irreversibility field, H_{irr}, which represents the highest field at which there is a measurable superconducting current density.

1.2.10.1 Upper critical field

The upper critical field has essential role for practical application of superconductors, representing the upper limit to which the useable range of the superconductors can be extended by improvement of vortex pinning. A wide range of H_{c2} values has been reported for different samples, from bulk to thin films[84-87,53]. Due to the anisotropy of MgB_2, two different values for H_{c2} are obtained, even for the same samples.

H_{c2} also strongly depends on the geometry of samples and has a wide range of values. So, for single crystal, there have been reported values of the upper critical fields of about $\mu_0 H_{c2}^{\parallel ab}(0) \approx 18$ T and $\mu_0 H_{c2}^{\perp ab}(0) \approx 3.5$ T [86,87]. For pure MgB_2 wire, the most important application of MgB_2, the obtained value of H_{c2} is around 9 T at 20 K.[86] This is a very usable value in a cryocooler closed system.

The upper critical field for bulk samples is slightly higher than for wire, and almost 20 T has been achieved at 4 K.[89,90] The highest values of the upper critical field are achieved for films. Thin films with higher transition temperature around 39 K have a value of H_{c2} of 32 T.

Decrease of transition temperature in thin films has been observed due to higher concentrations of impurities, mostly MgO. At the same time, record high values of H_{c2}, of around 40 T have been reported, as shown in Figs. 1.2.14 and 1.2.15.[85]

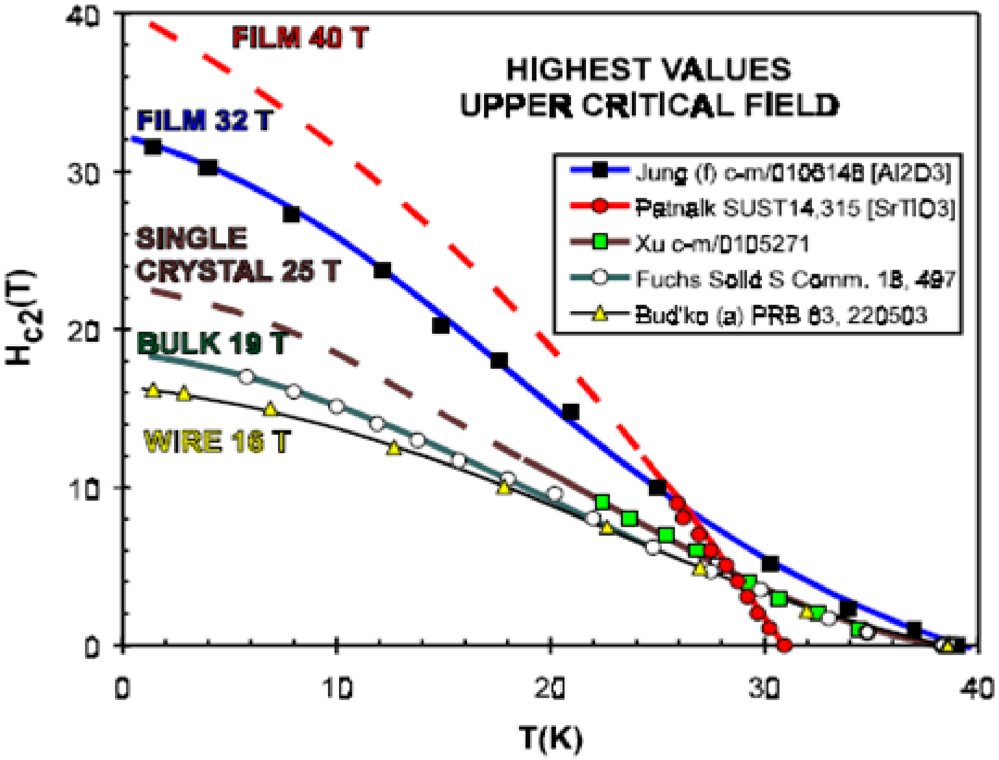

Figure 1.2.14: Highest values of H_{c2}(T) for MgB_2 in different geometries (bulk, single crystals, wires, and films). Adopted from [14].

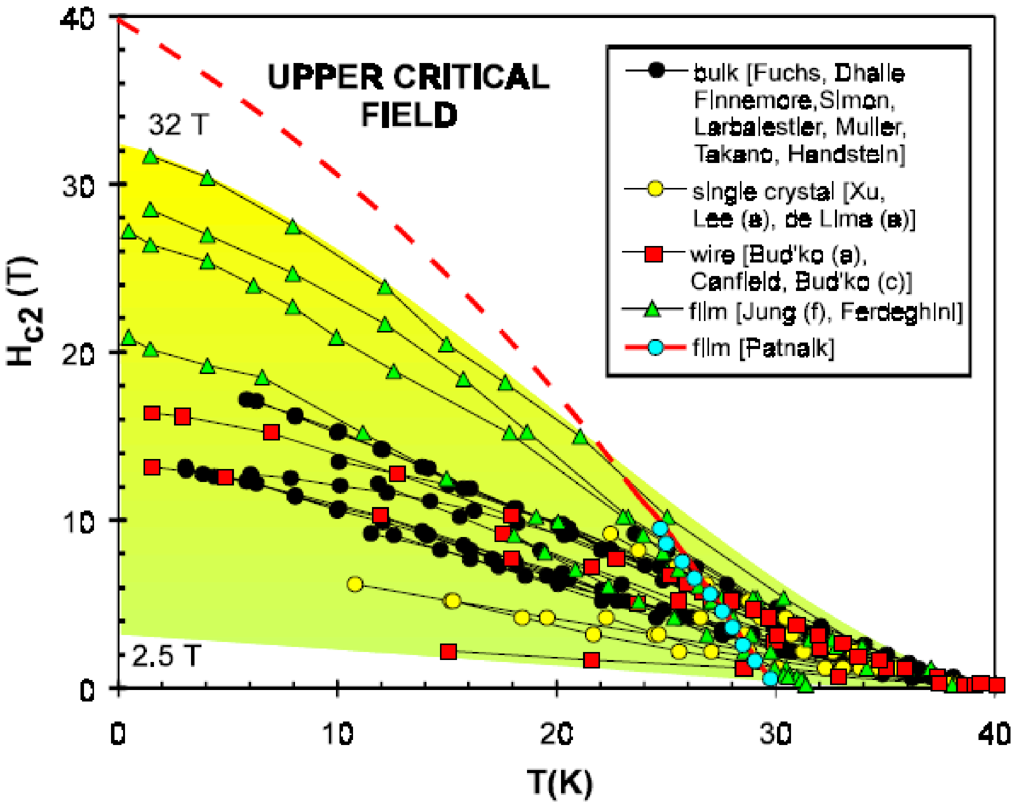

Figure 1.2.15: Upper critical field H_{c2} versus temperature T for MgB_2 in different configurations: bulk, single crystals, wires, and films. Adopted from [14].

1.2.10.2 Lower critical field

Reported values of the lower critical field $\mu_0 H_{c1}$ range between 150 mT and 480 mT. Recent measurements on a high purity single crystal sample, however, showed the new results for the lower critical field, $\mu_0 H_{c1}^{\parallel ab}$ (5 K) ≈ 120 mT and $\mu_0 H_{c1}^{\perp ab}$ (5 K) ≈ 250 mT, as can be seen in Figure 1.2.16.[87, 89, 90, 92, 93]

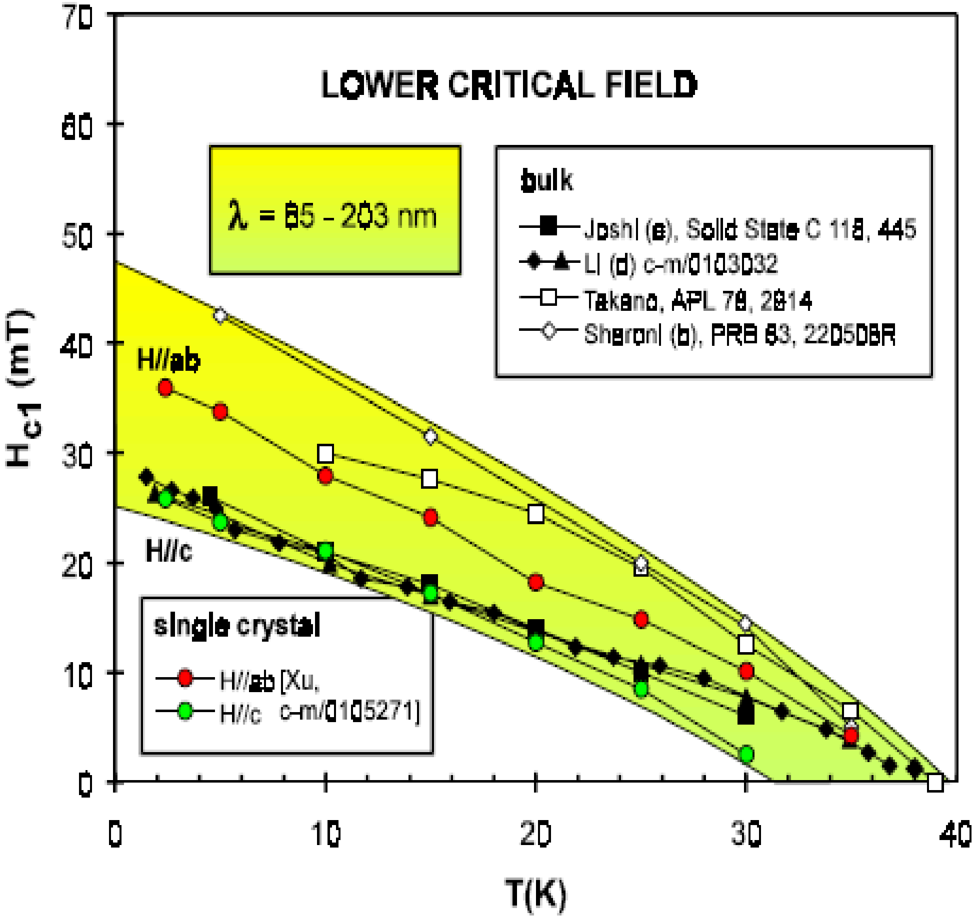

Fig. 1.2.16: Lower critical field versus temperature for MgB_2.[14] The reference names and numbers are shown in the legend according to[14]. Adopted from [14].

1.2.10.3 Irreversibility field (H_{irr})

There are several definitions of the irreversibility field. The first is that this is the field at which the bulk current density goes to zero: $J_c \rightarrow 0$ when $H > H_{irr}$

H_{irr} can also be described as a depinning field at which magnetic vortices start moving across the superconductor and destroying the zero resistance state. H_{irr} is a field above which the magnetization curve becomes reversible.

Knowledge of the irreversibility field is important in potential applications, as a parameter which determines the upper limit of the magnetic field in practical applications. Many research groups have reported enhancement of the irreversibility line with different methods, which were associated with high values of J_c. Kumakura et al.[94] investigated the use of nanoparticles, SiO_2 and SiC by an in-situ process, and reported significant improvement of J_c and H_{irr}. Strong improvement of H_{irr} was reported by Dou et al.[95,97] for SiC nanoparticle doped MgB_2, This was explained by reaction of nano-SiC with Mg, which released fresh C into the sample and by simultaneous doping of MgB_2 with this C, as well as by inclusion of nanoparticles that resulted in this reaction in the MgB_2 matrix[96]. The size of defects obtained in this process was comparable to the coherence length, ξ, of MgB_2. Yamamoto et al.[95] reported that H_{irr} can be enhanced by degradation of crystallinity due to a low temperature solid-solid reaction.

Flükiger et al.[52] reported enhancement of H_{irr} and J_c by intensive ball milling of the powders used for preparing MgB_2 samples. Generally, the irreversibility field is extrapolated to zero temperature range between 6 and 12 T for MgB_2 bulk, films, wires, tapes, and powders, as illustrated in Fig. 1.2.17[14] Despite big progress in increasing H_{irr}, there is still is a big gap between a H_{c2} of 29 T and the current values of H_{irr} in the range of 6-12 T at 4.2 K.

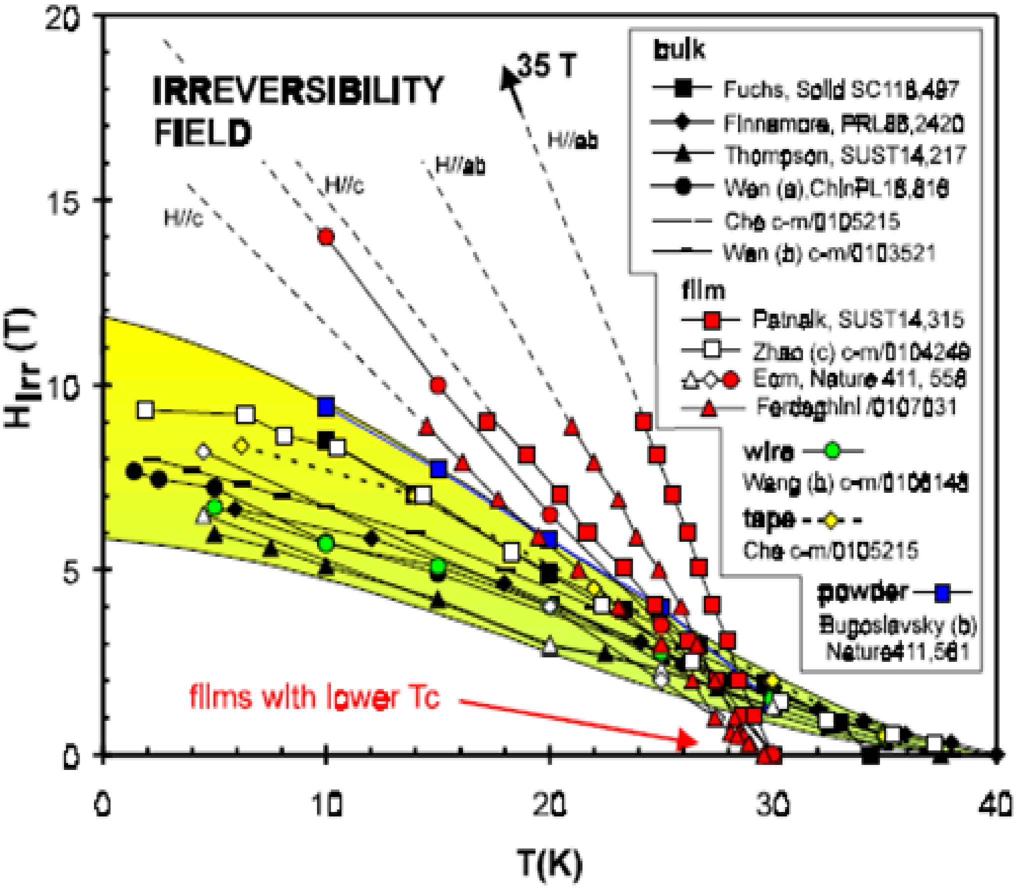

Fig. 1.2.17: Irreversibility field versus temperature for different geometries of MgB_2 (bulk, film, wire, and powder). Adopted from [14].

1.2.11 Penetration depth and coherence length

Very important fundamental length scales of superconductivity were introduced by the Ginzburg-Landau theory (GLT),[3]: the penetration depth, λ, and the coherence length, ξ.

The penetration depth describes the depth to which an external magnetic field can penetrate into type-I superconductor. It is given by the formula:

$$\lambda = (M / 4\mu_0 e^2 \psi_0^2)^{1/2} \tag{1.2.7}$$

where ψ_0 is the equilibrium value of the order parameter in the absence of an electromagnetic field. μ_0 is the magnetic permeability of free space, M is mass of the charge carriers and e is the elementary charge. The penetration depth has a minimal value at 0 K, and becomes extremely large close to the transition temperature. Approaching T_c, λ shows an asymptotic behavior.

$\lambda\ (T \rightarrow T_c) \propto (1-t)^{-1/2}$ (1.2.8)

where t = T/T$_c$. Recent measurements in a high purity single crystal sample show the penetration depth to be λ_{ab} (0) ≈ 22±2 nm and λ_c (0) ≈ 100±10 nm.[98,99]

The coherence length sets the length scale on which the superconducting order parameter shows no significant change. In BCS theory, the coherence length gives the approximate spatial dimension (size) of the Cooper pair. The coherence length**,** ξ, also represent the radius of the cores of magnetic vortices in type-II superconductors. Formulation of coherence length by GLT:

$$\xi = \sqrt{\frac{\hbar^2}{2m|\alpha|}} = \frac{2\hbar v_f}{\pi E_g} \qquad (1.2.9)$$

where α is a phenomenological parameter[7], m is the effective mass, v_f is the Fermi velocity, and E_g is the energy gap.

Different values of $\xi_{ab}(0)$ = (10 ± 0.2) nm and ξ_c (0) = (5 ± 0.2) nm were recently reported for single crystal, which are relatively higher than other values in the literature.[14,83]

1.2.12 Fabrication/preparation of MgB_2 superconductor

Various sample preparation methods for bulk samples and wires have been used, for example: *in-situ*, e*x-situ*, mechanical alloying, hot and cold isostatic pressing, powder-in-tube methods for wires and tapes, the liquid infiltration method, etc. The most important experimental techniques for preparing wires and bulk samples are *in-situ*, *ex-situ*, and the liquid infiltration method. For the *in-situ* method, Mg and boron (B) powders are mixed and either packed or pressed into a metallic tube, or a pellet is formed by pressing the powders in a die. This is followed by heat treatment[100-102]. The heat treatment is usually done at 650 –

900°C under oxygen (O) protective conditions. Doped particles can be added by mixing them with boron and Mg before the heat treatment. In the *ex-situ* processing method, already formed MgB_2 powder is packed into metal tubes or pressed into pellets and thermally processed[102-106]. With the *ex-situ* technique, better density and homogeneity of the MgB_2 core is obtained, which is reflected in high values of J_c. On the other hand, doping with impurities is not effective, as compared to *in-situ* processing. *Ex-situ* samples can develop large cracks in the core during the mechanical processing, which directly causes weakening of links between grains and finally results in low J_c.

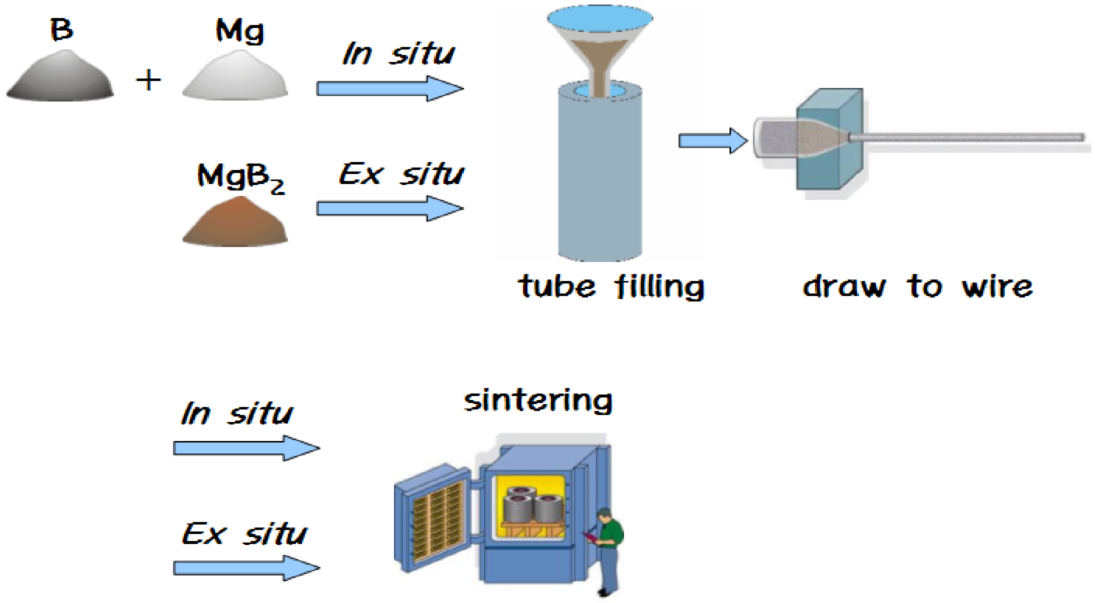

Figure 1.2.18: The powder-in-tube (PIT) process for the *in situ* and *ex situ* methods. Adopted from [106].

In the infiltration method, a pure Mg rod 2 mm in diameter is placed at the centre of a Fe tube, and the space between the Mg and the Fe tube is filled with B powder or a powder mixture of boron and dopant material. The composite is cold worked into 1.2 mm diameter wire and finally heat treated at temperatures above the melting point of Mg (~650 °C). During the heat treatment, liquid Mg infiltrates into the B layer and reacts with B to form MgB_2.

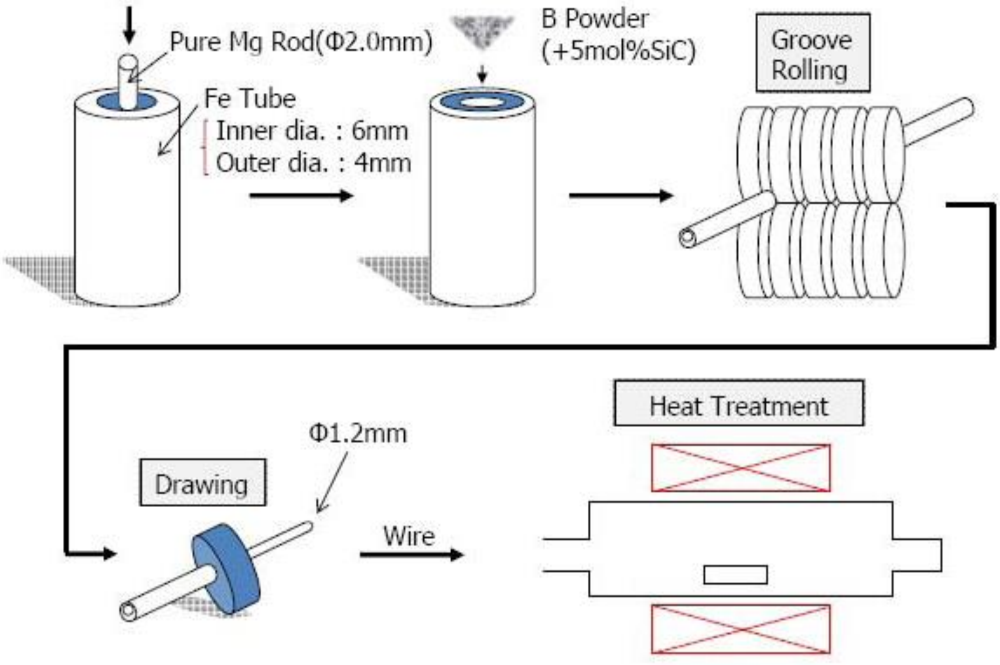

Figure 1.2.19: Schematic illustration of the MgB_2/Fe composite wire fabrication process by the internal Mg diffusion method. Adopted from [107].

1.2.13 Influence of precursor powders on superconductivity of MgB_2

1.2.13.1 Mg precursor powder

Magnesium is a silvery-white, lightweight metal. Mg is very reactive in its elementary state; on exposure to water, it undergoes an exothermal reaction with release of hydrogen. Magnesium tarnishes slightly in air, forming a thin layer of MgO, which protects it from further oxidation. Mg is much applied in various industrial sectors, where it appears in the form of ribbon, powder, rods, foil, sheets, chips, and granules.

The quality of the starting Mg powder, in such aspects as purity and particle size, plays an important role in determining the superconducting properties of MgB_2. Replacement of commercial Mg powder with nanosize Mg powder can improve the performance of MgB_2.[108,109]

Nanosize Mg has a larger surface area and is more effective in enhancing the reaction between magnesium and boron. In a complete reaction between Mg and B, grain connectivity is much better, and hence, the J_c is improved. Yamada et al. confirmed that using nanosize magnesium powder has a strong influence on improving J_c results, mostly due to enhancing the reaction between boron and magnesium, and improving grain connectivity. On the other hand, the nanosize Mg powders are considerably more expensive than commercial Mg powder. [108,109]

Because of the high cost of nano-Mg, some groups have prepared an ultra-fine Mg and B powder mixture by ball milling, which also effectively improved the grain connections and enhanced the J_c values.

The Ma's group prepared MgB_2 with micron-size (10 μm) spherical magnesium powder and achieved enhancement of J_c. Uniform and spherical Mg particles react better with boron powders and also improve connectivity between grains.[110,111]

Mg is highly volatile and can easily be lost during the preparation of samples. As a result, prepared MgB_2 samples usually show Mg deficiency. Generally deficiency of Mg degrades the critical temperature and introduces strain into the crystalline lattice of MgB_2 according to a report by X. Z. Liao[112]. Jiang et al. reported improvement of high-field J_c for MgB_2/Fe wire prepared with Mg deficiency.[113]

Some groups have explored the influence of non-stoichiometric MgB_2 samples on J_c results, especially to prevent the problem of Mg deficiency and remove microcracks. An excess of Mg powder in the starting powder assists oxygen incorporation into the MgB_2 lattice, improves connectivity, and considerably improves J_c and the upper critical field. Susner et al.

researched the effects of doping and excess Mg. The best result below 20 K was obtained for samples with excess of Mg + SiC doping.[114]

Kumakura's group has studied the effects of Mg on the J_c. They reported twice as large a J_c by using MgH_2 as the Mg source.[115]

The MgH_2 + B mixture was effective in obtaining a high density of the core layer. During the heat treatment, the reaction occurs as follows: $MgH_2 + 2B \rightarrow MgB_2 + \uparrow H_2$

Using MgH_2 as a starting precursor avoids oxidation of boron and magnesium, and enhances the reaction rate between magnesium and boron. The starting Mg powder is likely to be contaminated with oxygen in Mg + B processing, which causes a decrease in the reactivity of Mg with boron.

1.2.13.2 Boron precursor powder

Boron is a metalloid, chemical element with properties that are in between those of metals and non-metals. Boron exists naturally as 19.9% ^{10}B isotope and 80.1% ^{11}B isotope. Chemically, only boron compounds appear in the Earth's crust. High purity boron is very difficult to obtain. Brown amorphous boron contains boron atoms randomly bonded to each other without long-range order. Crystalline boron is a very hard black material with a high melting point, 2076 °C. Boron is similar to carbon in its capability to form stable covalently bonded molecular networks. At room temperature, boron is a poor electrical conductor, but it is a good conductor at high temperatures.

Boron was isolated for the first time by Sir Humphrey Dave[116] and by Joseph Louis Gay-Lussac[117], independently of each other. Henri Moissan prepared pure boron in 1895 by reduction of B_2O_3 with magnesium[118]. High-purity crystalline boron may be prepared by the vapor phase reduction of boron trichloride or tribromide with hydrogen on electrically heated filaments. Pure amorphous boron can be obtained in a technically demanding process from the decomposition of diborane.[119-122]

Impure, mostly amorphous, boron, a brownish-black powder, is usually obtained by heating boron trioxide with magnesium powder.[118]

C. K. Chen[123] studied the influence of the nature of the boron precursor on the superconducting properties of MgB_2. The study compared crystalline and amorphous boron.

Crystalline boron contains large particles tens of microns in size, whereas the amorphous powders have particle sizes of ~0.5 μm. The reactivity of the amorphous powders is much greater than that of the crystalline powders, and the reduced particle size further enhances the reaction rate.

Boron powder	Source	Form	Purity (%)
B-C98	Alfa Aesar	Crystalline	98
B-C99	FluoroChem	Crystalline	99
B-A9597	Fluka	Amorphous	95-97
B-A9999	Alfa Aesar	Amorphous	99.99

Table 1.2.1: Source, form, and purity of the different boron powders with their particle size distribution. Adopted from [123].

MgB_2 samples made from amorphous boron present better J_c, even one order of magnitude higher than for MgB_2 made with crystalline boron (Fig. 1.2.21). SEM images of MgB_2 made from various boron precursors confirmed a large difference in grain size (Fig. 1.2.20). Grains of crystalline samples were around a few hundred nm in size compared to those made from amorphous boron with grain sizes of 100 nm or less.

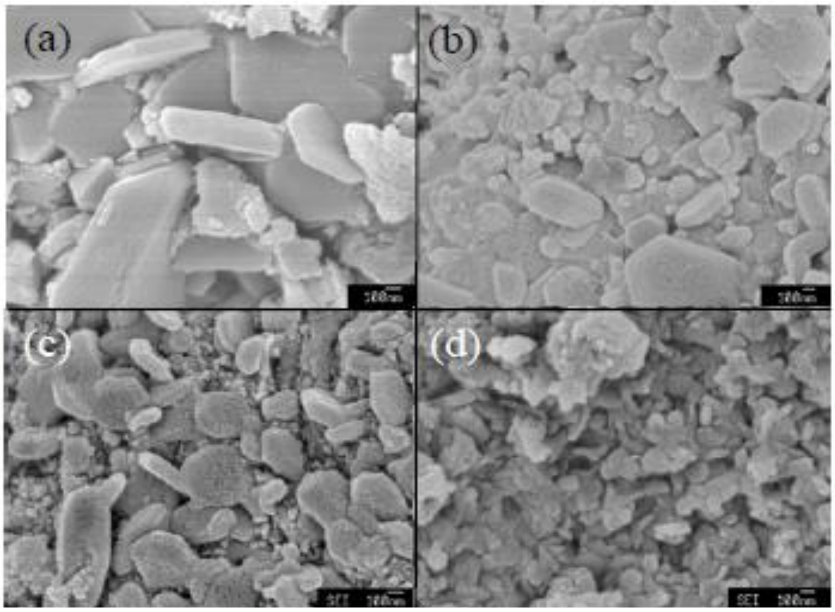

Figure 1.2.20: SEM images of samples a) C98. b) C99. c) A9597. d) A9999. Adopted from [123].

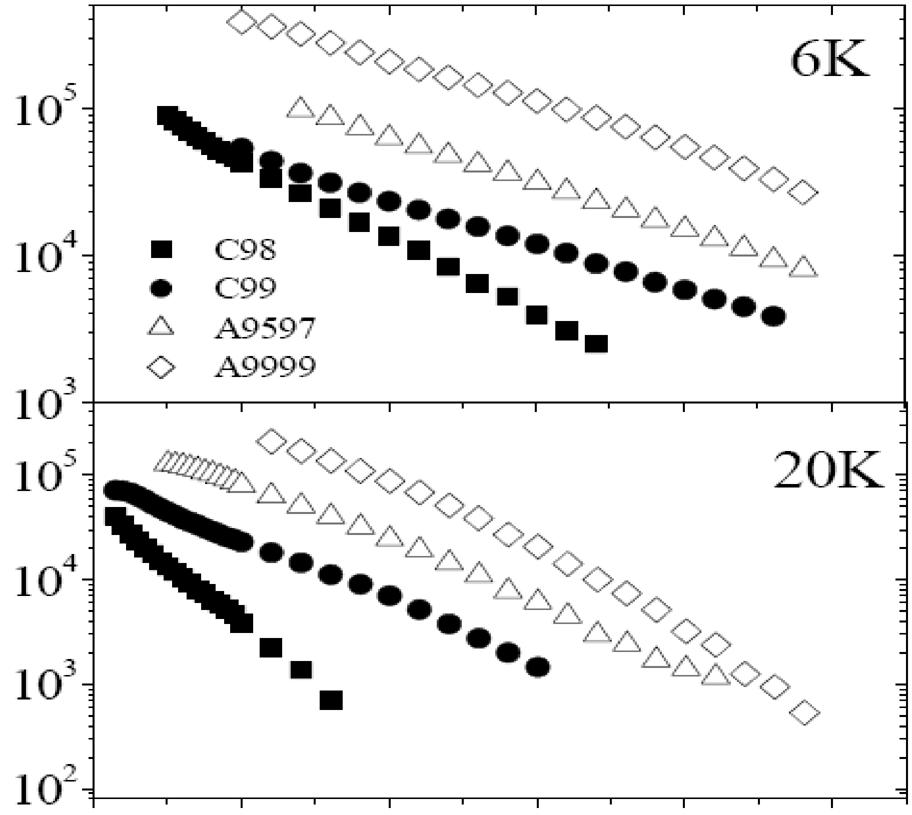

Applied field (T)

Figure 1.2.21: Magnetic critical current density versus applied magnetic field at 6 K and 20 K. Adopted from [123].

This is explained as due to MgB_2 containing far fewer Mg(B)–O phases when made with amorphous boron as a precursor, despite the fact that the amorphous B contains more B_2O_3.[123,124]

Recently, the availability of 99% amorphous boron became severely limited due to military applications of this boron and limited resources.

One of the most important tasks in developing high quality MgB_2 is finding a new method for the synthesis of pure amorphous boron or enhancement of one of the lower quality borons available on the market. The reactivity of 96% B powder can be improved by using ball-mill processing, leading to enhanced magnetic critical current density, J_c, compared to the original 96% B powder. The MgB_2 made using low grade 96% B powder could be particularly useful for industrial applications because of its low material cost.[125]

1.2.13.3 Chemical doping

One of the most important and broadest subjects of MgB_2 research is related to the doping of MgB_2 with different kinds of materials. The need for doping arises because of poor flux pinning and low J_c, H_{c2}, and H_{irr} values of pristine MgB_2. Various materials show different results, from remarkable enhancement of critical current density (J_c) with carbon source doping or SiC[126-132] to significant degradation of MgB_2 properties, as with iron doping.[133,134]

There are several aims for chemical doping into MgB_2. Element substitution for Mg or B can change the electronic state, lattice parameters, and crystallinity. Furthermore, impurity particles with small grain size comparable to the coherence length can be effective pinning centres. Finally, chemical doping can support grain growth and improve the links between MgB_2 grains. Many elements and compounds have been tried as dopants in MgB_2, which can be divided into several groups according to similar properties.

Light elements such as Li[135,136], Al[137] , Zn[140], and Na[135] all showed small enhancement of J_c in low field. Al substitution for Mg causes strong degradation in T_c. Also, Al donates electrons into the interplane region. Doping with Al results in degradation of all critical parameters, according to the research of Xiang et al. and Toulemonde et al.[138,139]

Only doping with elementary Zn has resulted in a slight increase in or nearly the same T_c. Theoretical band structure calculations predicted increased T_c in MgB_2 for Li or Na as dopants.

Light atomic elements theoretically result in higher Debye frequency ($\omega_D = (3N/4\pi V)^{1/3} v_S$, where is v_S speed of sound, and N/V the number density of the crystal) and therefore in higher T_c. Improvement of T_c with such doping, however, has not been observed, probably due to unsuccessful substitution of these elements into MgB_2 crystal.

Improvement of the high field $J_c(B)$ performance of MgB_2 has been observed for the silicides $ZrSi_2$ [141], WSi_2 [142], $MgSi_2$ [142,143], SiO_2 [144-146], and elementary Si [147]. Ma and co-workers have researched the effects of $ZrSi_2$ and WSi_2 doping. Fe-sheathed MgB_2 tapes were prepared through *in-situ* PIT.[141,142]

The explanation can be found in the reactions between Si and silicides with Mg, where products of the reaction, as well as dopant particles, themselves act as pinning centres.

Nano-SiC-doped MgB_2 achieved the highest J_c in field at 20 K ever reported for MgB_2 wires and bulks. For 10 wt% SiC-doped MgB_2 bulk samples, $H_{irr} \approx 8$ T and $J_c \approx 10^5 Acm^{-2}$ under 3 T at 20 K.[148]

An interesting study of doping MgB_2 with nano-SiC and sintering under applied magnetic field yielded improvement of J_c.[149]

A significant enhancement of all superconductive performance in MgB_2 has been achieved through chemical doping with carbon (C) containing composites or compounds, such as nano-C, B_4C, carbon nanotubes (CNT), hydrocarbons, carbohydrates, and the already mentioned SiC. Atoms of carbon enter into the MgB_2 structure, partially substituting onto boron sites, and change the crystal and electron configurations. Besides J_c, H_{c2} and H_{irr} are considerably improved due to the increased impurity scattering in the two-band MgB_2. Even doping with carbon leads to decreases in the T_c value, however.[150-153,154-157]

Nano-carbon doping generally results in C substitution onto the boron sublattice ($MgB_{2-x}C_x$) and provides a great impact on the carrier density and impurity scattering.

An enhancement of J_c by nano-C doping was also observed by Ma et al. for MgB_2 tapes.

Carbon nanotubes (CNTs) have unusual electrical and thermal properties[158-160] and hence are a good dopant, especially in terms of the mechanical and thermal properties of MgB_2 wires. Kovač et al. also showed that uniform distribution of CNTs is an important factor for effective carbon substitution.[162]

W. X. Li et al. reported CNT doped MgB_2 samples sintered in 5 T magnetic field.[163]

Effects of doping with a number of nano-C sources, such as graphite, diamond and carbide compounds, on the flux pinning and critical current density of MgB_2 have been studied, and all such doping presented improvement of J_c at higher field. [164-168]

Doping with silver was reported by Sun et al. in 2002[169]. It was found that Ag reacted with MgB_2 at high temperature (950°C for 2 h) to form the binary compounds $Mg_{0.5}Ag_{0.5}$ and MgB_4.

Doping with rare earths also results in good performance of J_c in high field. As a good example, doping with Y_2O_3 causes inclusions of YB_4, which are responsible for a considerable improvement of J_c(B) and H_{irr} at low temperature (4.2K).[170]

Small amounts of Dy_2O_3 doped into MgB_2 significantly increase pinning, creating DyB_4 and MgO incorporated within MgB_2 grains[171]. Improvement of J_c in low fields was reported for this doping. Doping with Ho_2O_3 is quite different from the doping effects of Y_2O_3 and Dy_2O_3. Impurities, mostly HoB_4 nanoparticles from 5 to 10 nm in size, serve as pinning centres. They keep T_c and H_{c2} largely unchanged, but improve both H_{irr} and J_c[172]. Therefore, Ho_2O_3 doping improves high-field J_c. When elementary La is doped into MgB_2, it undergoes a reaction with B and forms LaB_6 nanoparticle inclusions. In fact, LaB_6 impurity phase within the bulk MgB_2 is believed to be responsible for the enhancement of J_c.[173-174]

Metal dopants, such as Ti [175,176], Zr [177,178], W [179], Pb [180], Cu [181,182], and Cd [183], mostly have a limited effect on J_c(H) at 4.2 K, often decreasing J_c. The only consistently observed benefit of this type of doping is to improve grain connectivity, with limited improvement of vortex pinning, if any.

Magnetic elements, such as Fe [131,132], Ni [184], Co [185], and Mn [186], mostly resulted in degradation of J_c(B). Prozorov et al., however, produced magnetic Fe_2O_3 nanoparticles embedded in the MgB_2 bulk by the sonication technique.[187]

They reported strong vortex pinning improvement, which they claimed to be due to magnetic interaction between the vortices and the magnetic nanoparticles. The main reason for the decreasing superconductive performance of MgB_2 was claimed to be breaking of Cooper pairs by spin flipping due to magnetic interaction.

Theory shows, however, that the interaction of magnetic vortices with localized magnetic moments of magnetic inclusions in MgB_2 should improve vortex pinning. These inclusions, however, should not cause significant breaking of Cooper pairs. The challenge of this thesis is to find appropriate dopants and procedures for their inclusion in MgB_2, so that these conditions are met.

Many research groups have tried doping with different metal oxide compounds. Doping with Al_2O_3 led to a decrease in critical-current density and irreversibility field with increasing Al_2O_3 level. The opposite result has been observed for Co_2O_3 doping, where J_c increased until maximal doping level at 4% wt. After that, J_c considerably decreased.

Small enhancements of J_c and H_{irr} have been observed for ZrO_2 [188] and TiO_2 [189] doping.

Doping with boride compounds, such as a ZrB_2 [190], TiB_2 [191], and WB [192], gave rise to improvement of J_c and H_{irr}. The improved grain connection and decreased MgB_2 grain size were generally responsible for the enhancement of J_c.

1.2.14 Vortex pinning

As mentioned above, superconductors are classified by the way they behave in an external magnetic field, B_{app}. For type-I superconductors, the external magnetic field is excluded from inside the superconductor up to the critical field H_c, at which the external field breaks down Cooper pairs and fully penetrates the superconductor. Type-II superconductors are more complex and possess two critical fields. Up to the first critical field H_{c1}, the type-II superconductor has the same behaviour as a type-I superconductor. Between H_{c1} and H_{c2}, the type-II superconductor is in mixed state, with regions of non-superconducting (i.e., normal) material embedded in a perfectly superconducting matrix.

Here, the field penetrates the superconductor in the form of thin filaments called magnetic vortices[4]. The magnetic flux in each vortex is quantized, with the quantum of flux Φ_o having a value equal to the ratio of Planck's constant h to the charge of two electrons, e**:** $\Phi_o = h/2e = 2.067910^{-15}$ Tm^2.

The vortex consists of a core and a layer of superconducting screening currents around the core. The core is in the non-superconducting state. The diameter of the core is equal to the coherence length, ξ. The superconductor screens itself from the magnetic field inside the cure by producing persistent supercurrents around the core. The value of the supercurrents decreases approximately exponentially with the distance from the vortex centre, with characteristic length scale equal to the London penetration depth, λ.[193]

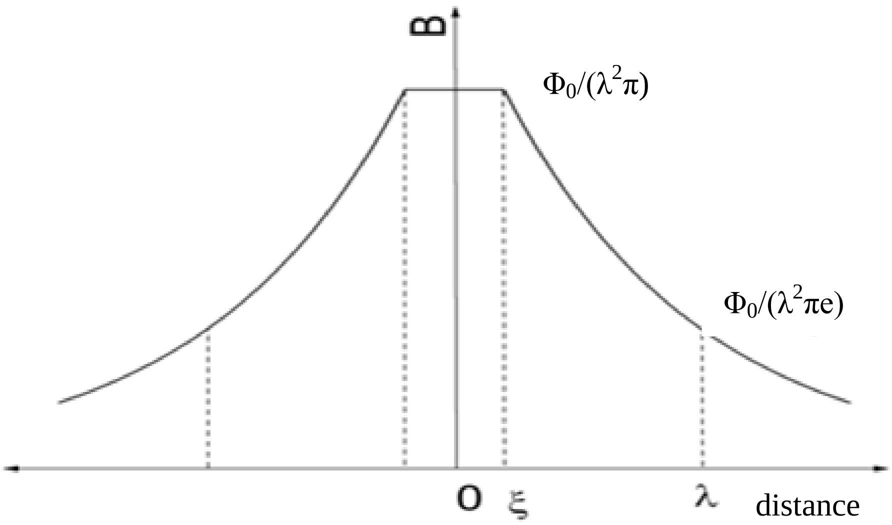

Figure 1.2.22: B is constant inside the non-superconducting core with radius equal to the coherence length ξ. It decreases approximately exponentially with distance outside the core, with the decay length equal to London penetration depth λ. Adopted from [193].

On increasing the external magnetic field, the number of vortices becomes larger, and they start to spread into the volume of the superconducting sample. Each vortex carries a magnetic flux quantum, and it behaves like a small magnet. Because all vortices are aligned in the same direction, there is a repulsive force between them.

Due to this repulsive force, vortices maximise the distance between each other by forming a proper hexagonal lattice, which is called an Abrikosov lattice.[193]

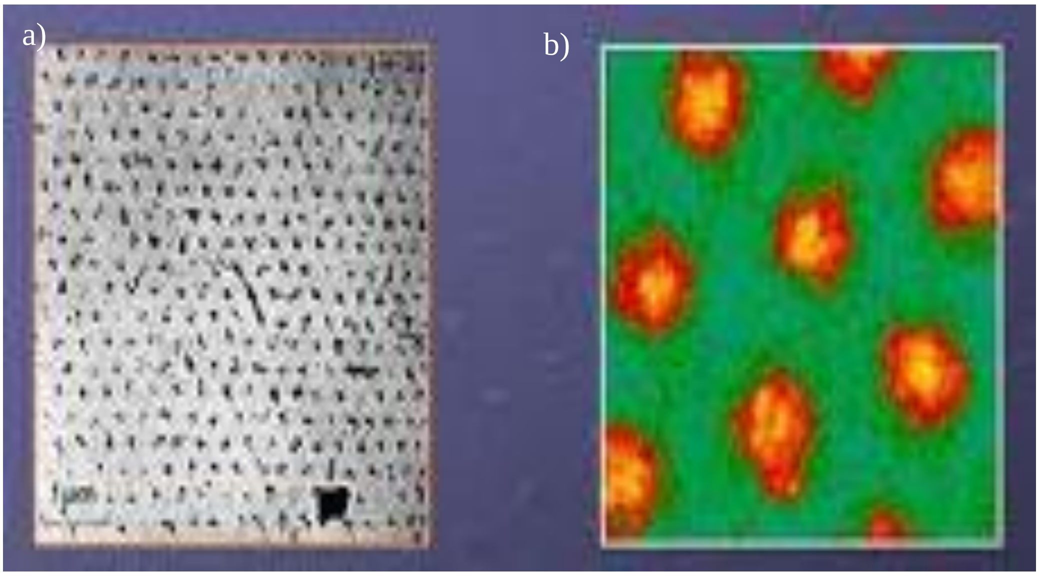

Figure 1.2.23 Abrikosov lattice, a two-dimensional hexagonal lattice of vortex cores: (a) First image of Abrikosov lattice, 1967[5]. (b) Vortices in MgB_2 taken by scanning tunnel microscopy, 2002. Adopted from [194].

If a current I is sent through a type-II superconductor in a direction perpendicular to an applied field, then each vortex experiences a force due to the current, which resembles the Lorentz force. The average Lorentz force, F_L, per unit volume of the crystal is: $F_L = J \times B$, where J and B are the spatially averaged transport current density and magnetic field inside the crystal, respectively. Because of this, vortices will move through the crystal. Vortex movement in a superconductor is undesirable, because it is associated with energy dissipation and the occurrence of voltage. Namely, some of the screening currents around the vortex are pushed into the normally-conducting vortex core dues to the local change in the magnetic flux around the vortices as they move. The charge carriers travelling through the normal vortex core are subject to scattering in crystal imperfections, thus leading to the energy loss.[74]

Crystal defects, however, microstructural features such as grain boundaries, voids, point defects, strains, twin planes, inhomogeneities, and second phases can be energetically favourable sites for magnetic vortices. Such sites are called pinning centres. On applying a large magnetic field or transport current, the Lorentz force easily overcomes the pinning forces, however, so vortices are set into motion again.

Additionally, if the thermodynamical temperature is raised high enough, vortices are set into motion as well, following the thermal energy equation: $E_{th} = k_B T$**;** where $k_B = 1.38 \times 10^{-23}$ J K^{-1} is the Boltzmann constant.

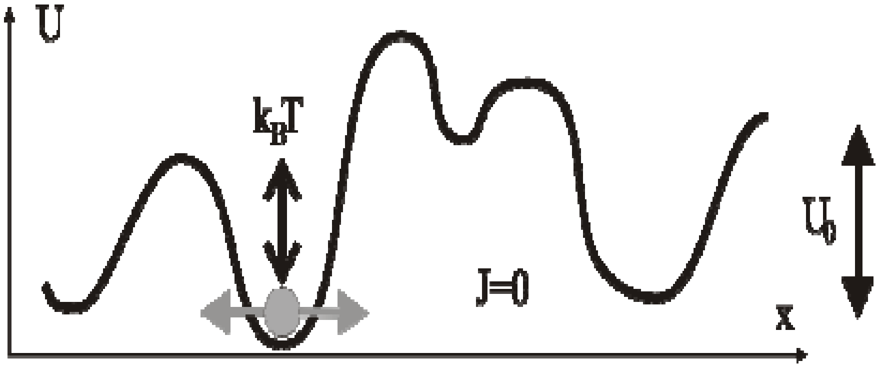

Figure 1.2.24: Schematic representation of the potential wells for magnetic vortices along a superconductor sample with no current flowing, $J = 0$. Adopted from [8].

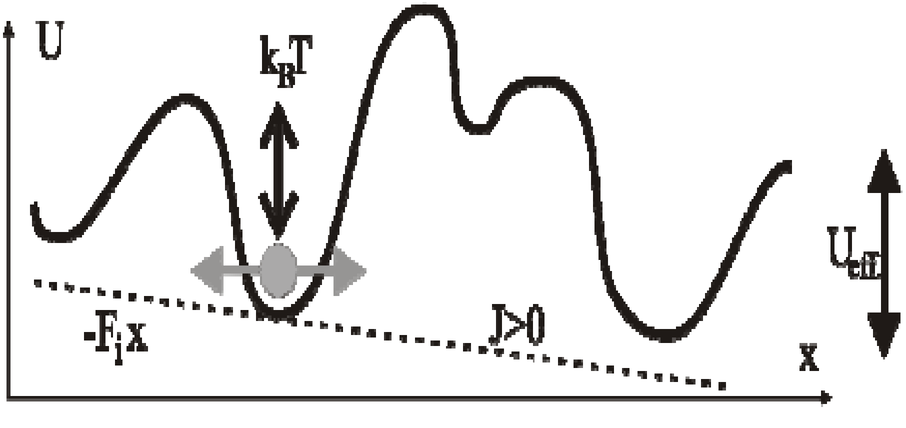

Figure 1.2.25: Schematic diagram of the impact of the Lorenz force as an addition to the potential energy in the case when the current is flowing. Adopted from [8].

Further it is important to say that significant energy dissipation does not begin at the upper critical field H_{c2} but at the irreversibility field H_{irr}, ($H_{c2} > H_{irr}$).

The field and temperature at which vortices are just starting to be released in significant numbers from the pinning centres are called the irreversibility field ($\mathrm{H_{irr}}$) and irreversibility temperature (T_{irr}), respectively. Values of H_{irr}, T_{irr}, and the critical current density (J_c) are defined by the vortex pinning. The irreversibility line in the (H, T) diagram therefore determines the limit for the technological applications of superconductors.

1.2.14.1 Elementary mechanisms of vortex pinning

The cores of vortices are in the non-superconducting state and their volume is in a state with a higher energy than the superconducting matrix. The energy of the core per unit length is [195]:

$$E_{core} = \frac{H_c^2}{2\mu_0}\pi\xi^2 \quad , \tag{1.2.10}$$

where

$$H_c = \Phi_0 /(2\pi\xi\lambda\sqrt{2}) \tag{1.2.11}$$

The core is surrounded by circulating super-currents. The magnetic energy associated with the currents per unit length of the vortex was estimated as [195]:

$$E_{mag} \approx \frac{H_c^2}{2\mu_0} 4\pi\xi^2 \ln\kappa \tag{1.2.12}$$

where $\kappa = \lambda/\xi$ is the Ginzburg-Landau parameter.

The total energy of the superconducting system is lower than in the normal state, which means that superconducting state is thermodynamically more stable.

On the other hand, the non-superconductive parts act as defects, and the vortices are on a higher energy level. Defects, inclusions, and other non-superconductive parts are energetically favourable sites for magnetic vortices, where they will be pinned down. After the vortices are pinned on a defect in the crystal structure there is no more electrical resistance or increasing thermodynamic temperature of the system. If too large a magnetic field or transport current is applied, the Lorentz force on the vortices will exceed the pinning force of the pinning centres.

There are three fundamental types of interaction between the vortices and the pinning centres: vortex core pinning, magnetic energy pinning, and elastic pinning. They are mediated by a decrease in the net vortex core energy (Eq. 1.2.10) or vortex magnetic energy (Eq. 1.2.12), and change in the elastic constant of the superconductor around the vortex, respectively. The vortex core energy pinning is by far the strongest one in most cases.[193,195] The elementary pinning force in the superconductor can be expressed by:

$$f_p = \left(-\frac{\partial U}{\partial x}\right)_{\max} \tag{1.2.13}$$

This expression shows that the pinning force depends on the depth of the pinning potential well and its spatial distribution. Because each vortex is typically pinned by a large number of pinning centres, the net pinning force has to be summarized over all elementary pinning forces: $F_P = \Sigma f_P$.

In the case of MgB_2 at lower temperature, smaller defects are involved in pinning nanoparticles, for example, while at higher temperature, the main contribution to the pinning force comes from larger defects on the order of the grain size and the connectivity between grains. Pinning at low temperature is more connected with the δl pinning mechanism, i.e., pinning associated with charge-carrier mean free path fluctuation. On the other hand at high temperature, close to the critical temperature, there is more evidence for δT_C pinning, which is associated with spatial fluctuations of the transition temperature.[196]

1.2.14.2 Core pinning

Pinning via *core interaction* occurs to minimise the core energy of the vortices when they encounter pinning centres.[195,197]

As the vortices move through the superconducting crystal with its defects, they will encounter places in the crystal with suppressed superconductivity. A vortex has a normal core, whose energy is higher than the energy of the superconducting state. When a vortex occupies a volume in the crystal where superconductivity is also suppressed, the net energy of the system consisting of the vortex and the volume with suppressed superconductivity is lower.

Because of this, vortices will be pinned at such volumes with suppressed superconductivity, which act as pinning centres. Typically, the volumes with supressed superconductivity are defects in crystals, impurities, or inclusions. The volume of suppressed superconductivity acts as a potential well for the vortex.

The pinning force of a pinning centre depends on the gradient of the energy variation within the pinning centre. In the Ginzburg-Landau theory, the pinning force is calculated through the equation of free energy, and for some certain value of size, an impurity has a maximal pinning force; $r_{n,max} \approx 1.8\ \xi$ If the pinning centre is much larger than that, it will be a weak pinning centre.[3]

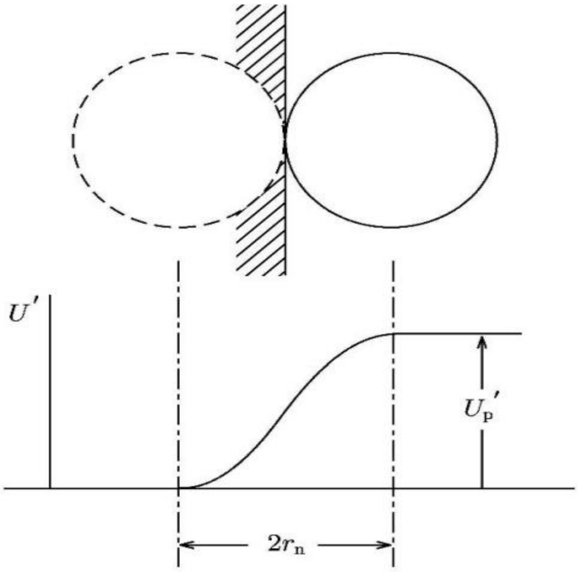

Figure 1.2.26: Schematic diagram of the pinning potential well of an impurity (U_p') as a function of the impurity radius. The pinning force of a pinning centre depends on the gradient of the energy variation within the pinning centre. Adopted from [193].

This is because the energy of the vortex will change very gradually as it passes the pinning centre. On the other hand, if it is much smaller than ξ, it cannot contribute substantially to lowering the energy of the system, and the energy gradient is again small, even though the variation occurs on much smaller scale. Therefore, the most effective pinning centres are of the size of $\sim\xi$. For MgB_2 superconductor, the ideal pinning centres will be macrostructural features with size of $2\xi \approx 10$ nm.

1.2.14.3 Pinning through minimization of magnetic energy of currents circulating around the vortex

When a vortex approaches a defect in the crystal, its circulating current and associated magnetic field are re-distributed because of the inhomogeneities around the defect. This is reflected in a change in the magnetic energy of the vortex (Eq. 1.2.11). Numerous reports have shown that this interaction can result in vortex pinning.[198,199,200]

1.2.14.4 Interaction through variation of elastic energy

Superconductivity is connected with small changes of volume ($\Delta V/V \approx 10^{-7}$) and elastic constants ($\Delta K/K \approx 10^{-4}$) of the crystal lattice.[195] Because of this, the non-superconducting cores of magnetic vortices will have different crystal lattice parameters and elastic constants. Consequently, they will behave like inclusions in the superconducting matrix, producing a permanent elastic stress field around the vortices. This field will interact with crystal imperfections, which can result in pinning of the vortices.[201, 202, 203]

1.2.14.5 Pinning through magnetic interaction between vortices and magnetic inclusions

In addition to the general mechanisms of vortex pinning, described in section 2.5.1, additional pinning is possible in a special case where magnetic atoms or particles are included in a superconductor.

According to Prozorov et al., magnetic nanoparticles and magnetic vortices interact via screening current around the magnetic particle and the magnetic flux quantum of the magnetic vortex.[187] The corresponding screening supercurrent induced by a magnetic sphere incorporated into the superconductor has only one component ($0, j_\varphi(\rho, \theta), 0$).

The supercurrent flowing around the magnetic sphere is given by:[187]

$$j_\varphi = \frac{1/\sqrt{\mu_0\varepsilon_0}\, mR}{1+3(\lambda/R)+3(\lambda/R)^2}\,\frac{(1+\frac{\rho}{\lambda})}{\rho^2}\exp\left(-\frac{\rho-R}{\lambda}\right)\sin\theta \qquad (1.2.14.)$$

The pinning force connected with magnetic interaction between the vortex and the spherical magnetic nanoparticle (Fig. 1.2.28) can be obtained using:

$$\vec{F} = \frac{1}{\sqrt{\varepsilon_0\mu_0}}\int \vec{j}\times\vec{\Phi}_O\, d\vec{l} \qquad (1.2.15)$$

where dl is a flux line element, $\mu_0 = 4\pi\times10^{-7}$ Hm^{-1} is the magnetic permeability, $\varepsilon_0 = 8.854187817\times10^{-12}$ Fm^{-1} is the vacuum permittivity, $j(\rho, \theta)$ is the supercurrent density (Eq. 1.2.14) at the location of the vortex core, and Φ_0 is the flux quantum.

According to the Prozorov analysis, the magnetic pinning force shows that for $\rho - R > \lambda$ the magnetic pinning force dependence on ρ is approximately $f_{mag} \propto \exp[(-(\rho - R)/\lambda]$.

Therefore, the magnetic pinning force has a much larger range of ~λ, compared to the core pinning force, which acts at distances of ξ. The resulting force is attractive (repulsive), and maximal when the particle's magnetization and the magnetic field of a vortex are collinear. In the case of magnetic pinning, the vortex experiences an additional force due to magnetic interaction of the vortex (carrying a magnetic flux quantum) and the magnetic particle. The magnitude of the force which is trying to align the vortex along the magnetic moment of the magnetic sphere is specified by [187]

$$K = 2m\phi_0 R\sin(\alpha)\frac{\exp(R/\lambda)}{1+3(\lambda/R)+3(\lambda/R)^2}P(\frac{\rho}{\lambda}) \ , \tag{1.2.16}$$

where

$$P(\frac{\rho}{\lambda}) = \int_{\rho/\lambda}^{\infty} (1+x)x^{-2}\sqrt{x^2-(\rho/\lambda)^2}\exp(-x)dx \tag{1.2.17}$$

where ρ is the distance between the magnetic particles and the vortex, m is the magnetisation of the particles, R the radius of the particles, α is the angle of misalignment (between the magnetic particles and the vortex line), and the value of magnetic pinning force is scaled by the factor $\cos(\alpha)$. For angles $\pi/2 < \alpha < \pi$, the magnetic pinning force becomes repulsive. From Eq. 1.2.16, it can be concluded that the force increases with increasing particle size and moment.

In comparison with short-range core pinning force, this magnetic pinning force is of long-range (Fig. 1.2.28.). This force acts on the length-scale of London penetration depth unlike the core pinning which is effective at distance of the order of the coherence length.

The force can be attractive or repulsive, depending on the relative orientation of magnetisation and magnetic flux. For a uniform distribution of magnetic nanoparticles in a superconductor, even a repulsive force can improve the net pinning[187], if there is strong interaction between the vortices themselves. Since all ferromagnetic nanoparticles also contribute to the elementary core pinning, one can talk about dual pinning.[187] In the bulk of a superconductor, nanoparticles usually are randomly distributed, and even repulsive forces can contribute to some enhancement of pinning force.[187]

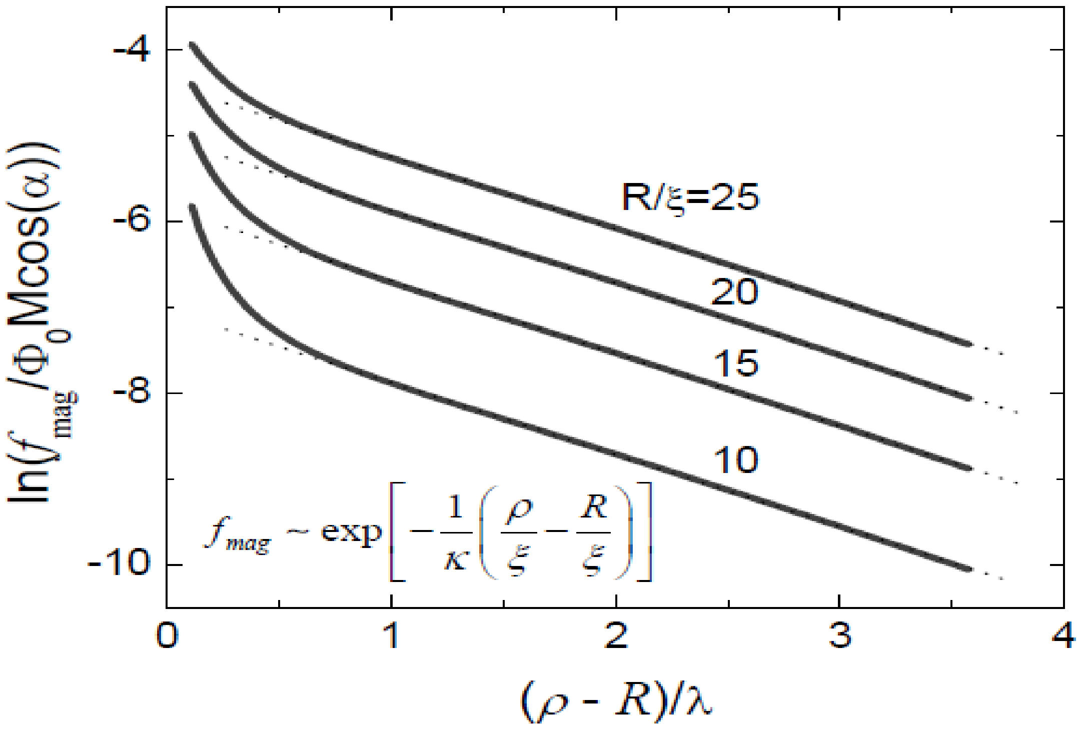

Fig. 1.2.27: Magnetic pinning force (f_{mag}) as a function of the distance between a vortex and a magnetic sphere calculated for spheres of different size. Adopted from [187].

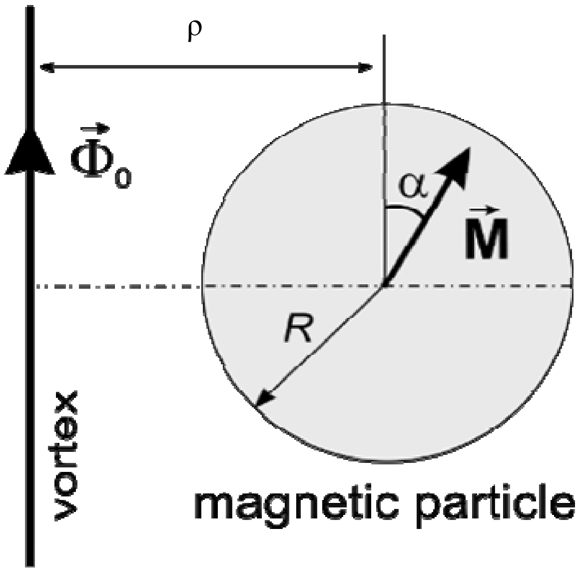

Figure 1.2.28: Magnetic nanoparticle and magnetic vortex, as considered in the model of vortex interaction with magnetic inclusion into a superconductor. Adopted from [187].

Milosevic's group from Antwerp University theoretically and experimentally studied the influence of magnetic pinning in thin films[204]. A small ferromagnetic (FM) particle in a type-II superconductor may be considered as a point-like magnetic dipole (MD).

The magnetic field of the MD was supposed to be weak and not be able to drastically change the structure of the superconducting state in the sample. Even a magnetic point dipole with magnetization *m*, placed outside a type-II superconducting (SC) film can interact with a single vortex in the SC.

According to Figure 1.2.30, observing two particular cases for the position of the magnetic particle and vortex in a thin film superconductor, the interaction energy can be presented by Equations (1.2.18, 1.2.19):[204]

$$F_{mv} = \frac{mL\phi_0^2}{2\pi\lambda} U_{\perp}(\rho_v) \quad , \tag{1.2.18}$$

for magnetic particles out of plane, and

$$F_{mv} = \frac{mL\phi_0^2}{2\pi\lambda} U_{II}(\rho_v, \varphi) \tag{1.2.19}$$

for magnetic particles in the plane of a superconductive thin film, where Φ_0 is the flux quantum of a vortex with vorticity L positioned at $\rho_v = \rho$, m is the magnetization of the dipole, and $U_\perp$, $U_\parallel$ are the distance between particles and vortices in thin film calculated with respect to the cylindrical coordinates.

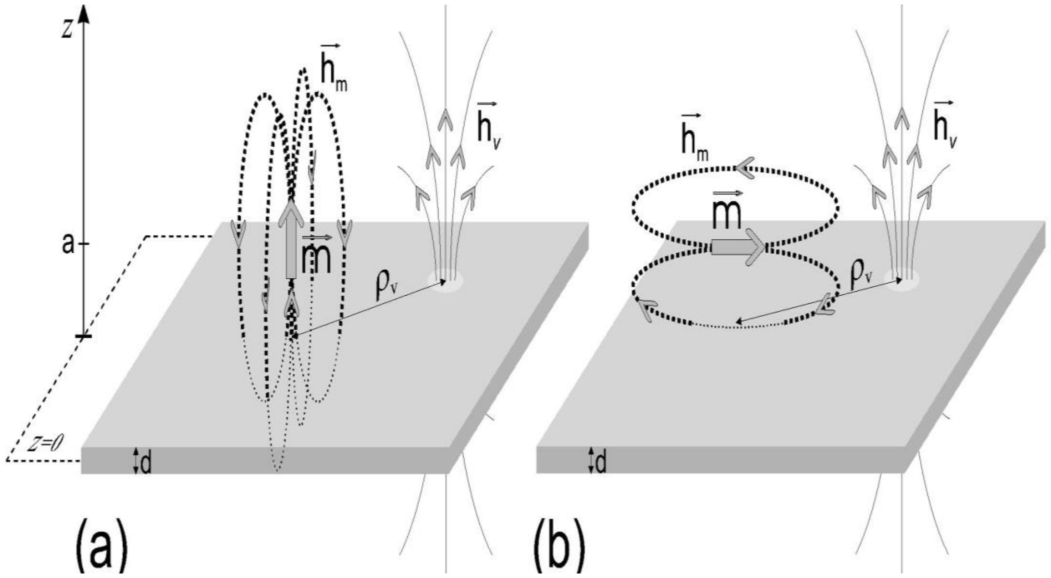

Figure 1.2.29: Schematic diagram of the systems under investigation with a) out-of-plane and b) in-plane directed magnetic dipole above a superconducting film interacting with a vortex. Adopted from [204].

The interaction energy in this system consists of two parts: 1) the interaction between the Meissner currents generated in the SC (j_m) by the FM particle and the vortex and 2) the interaction between the vortex magnetic field and the FM particle. Current is induced in the superconductor by a magnetic dipole with moment ***m*.**

Finally, Milosevic’s group presents results that an out-of-plane magnetized dipole attracts a vortex if aligned parallel to it, and to the contrary, for antiparallel alignment the vortex is repelled. For in-plane magnetization, the dipole-vortex interaction shows a double-natured behavior, so that the vortex is attracted to the negative pole of the MD and repelled on the other side.[204]

1.2.15 REFERENCES

1 H.K. Onnes, Comm. Phys. Lab. Univ. Liden, 122b, pp.124 - 128., 1911.

2 W. Meissner and R. Ochsenfeld, Naturwissenschaften, 21; p.787, 1933.

3 V.L. Ginzburg, and L.D. Landau, Zh. Eksp. Teor. Fiz., 20: p.1064, 1950.

4 A.A. Abrikosov, Sov. Phys. JETP, 5: p. 1174, 1957.

5 U. Essmann and H. Trauble, Physics Letters, 24A, 526, 1967.

6 H. Frohlich, Theory of the superconducting state. I. The ground state at the absolute zero of temperature, Physical Review, 79(5): p. 845-856, 1950.

7 J. Bardeen, L.N. Cooper, and J.R. Schrieffer, Theory of superconductivity, Physical Review, 108(5): p.1175-1204, 1957.

8 B.D. Josephson, Possibile new effects in superconductive tunnelling. Phys. Lett.,1: p.251-253, 1962.

9 J.G. Bendorz, K.A. Muller, Zeitschrift fur Physik B Condensed matter, 64, 189. 1986.

10 M.K. Wu, J.R. Ashburn, C.J.Torng, P.H. Hor, R.L. Meng, L. Gao, D.J. Huang, Y.Q.Wang, C.W. Chu, Physical Review Letters, 58, 908, 1987.

11 J. Nagamatsu, N. Nakagawa, T. Muranaka, Y. Zenitani, J. Akimitsu, Superconductivity at 39 K in magnesium diboride. Nature, 410, 63-64**,** 2001.

12 www.doitpoms.ac.uk/tlplib/superconductivity

13 M. Jones, and R. Marsh, The preparation and structure of magnesium diboride, MgB_2. Journal of American Chemical Society, 76: p.1434, 1954.

14 C. Buzea, T. Yamashita, Superconductor Science and Technology, 14, R115-R 146, 2001.

15 J. Kortus, I.I. Mazin, K.D. Belashchenko, V.P. Antropov, L.L. Boyer, Physical Review Letters, 86, 4656-4659, 2001.

16 H.J. Choi, D. Roundy, H. Sun, M.L. Cohen, S.G. Louie, Nature, 418, 758-760, 2002.

17 M. Eisterer, Superconductor Science and Technology, 20 R47, 2007

18 S. L. Bud'ko, G. Lapertot, C. Petrovic, C. E. Cunningham, N. Anderson and P. C. Canfield, Boron isotope effect in superconducting MgB_2, Phys. Rev. Lett. 86, 1877, 2001.

19 G. Karapetrov, M. Iavarone, W.K. Kwok, G.W. Crabtree, D.G. Hinks, Physical Review Letters, 86 4374, 2001.

20 F. Giubileo, D. Roditchev, W. Sacks, R. Lamy, D.X. Thanh, J. Klein, S. Miraglia, D. Fruchart, J. Marcus, P. Monod, Physical Review Letters, 87, 177008, 2001.

21 P. Szabó, P. Samuely, J. Kacmarcik, J. Klein, J. Marcus, D. Fruchart, S. Miraglia, C. Marcenat, A.G.M. Jansen., Physical Review Letters, 87, 137005, 2001.

22 C. Wälti, E. Felder, C. Degen, G. Wigger, R. Monnier, B. Delley, H.R. Ott, Physical Review B, 64, 172515, 2001.

23 A. Sharoni, I. Felner, O. Millo, Physical Review B 63, 220508, 2001.

24 H. Schmidt, J.F. Zasadzinski, K.E. Gray, D.G. Hinks, Physical Review B, 63, 220504, 2001.

25 F. Bouquet, Y. Wang, R. A. Fisher, D. G. Hinks, J. D. Jorgensen, A. Junod, N.E. Phillips, EPL (Europhysics Letters), 56, 856, 2001.

26 T. Dahm, N. Schopohl, Physical Review Letters, 91, 017001, 2003.

27 K.P. Bohnen, R. Heid, and B. Renker, Physical Review Letters, 86, 25, 2001.

28 Y. Kong, O.V. Dolgov, O. Jepsen, O.K. Andersen, Phys. Rev. B. 64, p.020501, 2001.

29 B.Lilia et al., Three-Dimensional MgB_2-Type Superconductivity in Hole-Doped Diamond. Physical Review Letters, 93**,** 237002, 2004.

30 Y. Bugoslavsky, Y. Miyoshi, G.K. Perkins, A.V. Berenov, Z. Lockman, J.L MacManus-Driscoll, L.F. Cohen, A.D. Caplin, H. Y. Zhai, M.P. Paranthaman, H.M. Christen, and M. Blamire, Supercond. Sci. Technol. 15, 526, 2002.

31 F. Giubileo, D. Roditchev, W. Sacks, R. Lamy, D. X. Thanh, J. Klein, S. Miraglia, D. Fruchart, and J. Marcus Phys. Rev. Lett. 87, 177008, 2001.

32 R. S. Gonnelli, D. Daghero, G. A. Ummarino,V. A. Stepanov, J. Jun, S. M. Kazakov, and J. Karpinski, Phys. Rev. Lett. 89, 247004, 2002.

33 M. Iavarone, G. Karapetrov, A. E. Koshelev, W. K. Kwok, G. W. Crabtree, and D. G. Hinks, W. N. Kang, Eun-Mi Choi, Hyun Jung Kim, Hyeong-Jin Kim, and S. I. Lee, Phys. Rev. Lett. 89, 187002, 2002.

34 F. Bouquet, R. A. Fisher, N.E. Philips, D. G. Hinks, and J. D. Jorgensen, Phys. Rev. Lett. 87, 047001, 2001.

35 F. Bouquet, Y. Wang, I. Sheikin, T. Plackowski, A. Junod, S. Lee, and S. Tajima, Phys. Rev. Lett. 89, 257001, 2002.

36 F. Manzano, A. Carrington, N.E. Hussey, S. Lee, A. Yamamoto, and S. Tajima, Phys. Rev. Lett. 88, 047002, 2002.

37 X. K. Chen, M.J. Konstantinovic, J.C. Irwin, D.D.Lawrie, and J.P. franck, Phys. Rev. Lett. 87, 157002, 2001.

38 S. Tsuda, T. Yokoya, T. Kiss, Y. Takano, K. Tongano, H. Kito, H.Ihara, and S. Shin, Phys. Rev. Lett. 87, 177006, 2001.

39 A. Bussmann-Holder and A. Bianconi, Phys. Rev. 67**,** 132509, 2003.

40 H. J. Choi, D. Roundy, H. Sun, M.L. Cohen, S.G. Louie, Nature, 418, 758-760, 2002.

41 W. N. Kang, C. U. Jung, K. H. P. Kim, M.-S. Park, S. Y. Lee, H.-J. Kim, E.-M. Choi, K. H. Kim, M.-S. Kim, and S.-I. Lee, Appl. Phys. Lett. 79, 982, 2001.

42 W. N. Kang, Hyeong-Jin Kim, Eun-Mi Choi, Heon Jung Kim, Kijoon H. P. Kim, H. S. Lee, Sung-Ik Lee, Phys. Rev., 65, 134508, 2002.

43 C. Nlscher, and G. Saemann-Ischenko, Physical Review B, 32(3): p. 1519, 1985.

44 Harris, J.M., Y.F. Yan, and N.P. Ong, Phys. Rev. B, 46(21): p. 14293-14296, 1992.

45 Y. Eltsev et al., Anisotropic resistivity and Hall effect in MgB_2 single crystals. Physical Review B, 6618(18): p.504-504, 2002.

46 D. G. Hinks, H. Claus and J. D. Jorgensen, The complex nature of superconductivity in MgB_2 as revealed by the reduced total isotope effect, Nature 411, 457, 2001.

47 C. U. Jung, M. S. Park, W. N. Kang, M. S. Kim, S. Y. Lee., and S.I. Lee, Physica **C,** 353, 162, 2001.

48 M. Xu, H. Kitazawa, Y. Takano, J. Ye, Nishida K., H. Abe, A. Matsushita, and G. Kido, 2001, Single crystal MgB_2 with anisotropic superconducting properties, condmat/0105271

49 M. H. Jung, M. Jaime, A. H. Lacerda, G. S. Boebinger, W. N Kang, H. J. Kim, E. M. Choi, and S. I.Lee, Chem. Phys. Lett. 343, 447, 2001.

50 S. Patnaik, L.D. Cooley, A. Gurevich, A.A. Polyanskii, J. Jiang, Y. CaiX, A.A. Squitieri, M. T. Naus, M.K. Lee, J.H. Choi, L . Belenky, S.D. Bu, J. Letteri, X. Song, D.G. Schlom, S.E. Babcock, C.B. Eom, E.E. Hellstrom, and D. Larbalestier, Supercond. Sci. Technol., 14 315, 2001.

51 R. Flükiger, P. Lezza, C. Beneduce, N. Musolino, H. L. Suo, Superconductor Science and Technology, 16(20): p. 264-270, 2003.

52 R. Flükiger, H.L. Suo, N. Musolino, et al., Superconducting properties of MgB_2 tapes and wires. Physica C, 385(1-2): p. 286-305, 2003.

53 S. L. Bud'ko, V. G. Kogan, and P. C. Canfield, Determination of superconducting anisotropy from magnetization data on random powders as applied to $LuNi_2B_2C$, YNi_2B_2C and MgB_2, cond-mat/0106577, Phys. Rev. B, 2001.

54 F. Simon, A. Janossy, T. Feher, F. Muranyi, S. Garaj, L. Forro, C. Petrovic, S. L. Bud'ko, G. Lapertot, V. G. Kogan and Canfield P. C., Phys. Rev. Lett. 87 047002, 2001.

55 D. Larbalestier, A. Gurevich, D. M. Feldman, and A. Polyanskii, Nature 414, 368, 2001.

56 J.W. Ekin, A.I. Braginski, A.J. Panson, M.A. Janoco, D.W. Capone, N.J. Zaluzec, B. Flanndermeyer, O.F. de Lima, M. Hong, J. Kwo, and S.H. Liou, Journal of Applied Physics, 62, 4821-4828, 1987.

57 J. Mannhart, P. Chaudhari, D. Dimos, C.C. Tsuei, T.R. McGuire, Physical Review Letters, 61(21): p. 2476-2479, 1998.

58 K. H. P. Kim, W. N. Kang, M. S. Kim, C. U. Jung, H. J. Kim, E. M. Choi, M. S. Park and S. I. Lee, Origin of the high DC transport critical current density for the MgB_2 superconductor, cond-mat/0103176, 2001.

59 T. Takenobu, T. Ito, D. Hieu Chi, K. Prassides, Y. Iwasa, Physical Review B, 64, 134513. 2001.

60 S. Lee, T. Masui, A. Yamamoto, H. Uchiyama, S. Tajima, Physica C: Superconductivity, 397, 7-13., 2003.

61 T. Schneider,and D. Di Castro, Physical Review B, 72, 054501, 2005.

62 S. Deemyad, T. Tomita, J.J. Hamlin, B.R. Beckett, J.S. Schilling, D.G. Hinks, J.D. Jorgensen, S. Lee, S. Tajima, Physica C: Superconductivity, 385, 105-116, 2003.

63 C. Tarantini, H.U. Aebersold, V. Braccini, G. Celentano, C. Ferdeghini, V. Ferrando, U. Gambardella, F. Gatti, E. Lehmann, P. Manfrinetti, Marr, eacute, D., A. Palenzona, I. Pallecchi, I. Sheikin, A.S. Siri, M. Putti, Physical Review B, 73, 134518, 2006.

64 M. Putti, V. Braccini, C. Ferdeghini, F. Gatti, G. Grasso, P. Manfrinetti, D. Marre, A. Palenzona, I. Pallecchi, C. Tarantini, I. Sheikin, H.U. Aebersold, E. Lehmann, Applied Physics Letters, 86, 112503-112503, 2005.

65 J. S. Ahn and E. J. Choi, Carbon substitution effect in MgB_2, cond-mat/0103169, 2001.

66 M. J. Mehl, D. A. Papaconstantopoulos and D. J. Singh, Effects of C, Cu and Be substitutions in superconducting MgB_2, cond-mat/0104548, Phys. Rev., 2001.

67 S. Y. Zhang, J. Zhang, T. Y. Zhao, C. B. Rong, B. G. Shen and Z. H. Cheng, Structure and superconductivity of $Mg(B_{1-x}C_x)_2$ compounds, condmat/ 0103203, 2001.

68 A. Bianconi, D. Di Castro, S. Agrestini, G. Campi, N.L. Saini, A. Saccone, S. De Negri and M. Giovannini, A Superconductor Made by a Metal Heterostructure at the Atomic Limit Tuned at the "Shape Resonance": MgB_2, cond-mat/0103211, 2001.

69 J. Q. Li, L. Li, F. M. Liu, C. Dong, J. Y. Xiang and Z. X. Zhao, Superconductivity and Aluminum Ordering in $Mg_{1-x}Al_xB_2$, cond-mat/0104320, 2001.

70 S. M. Kazakov, M. Angst and J. Karpinski, Substitution effect of Zn and Cu in MgB_2 on T_c and structure, cond-mat/0103350, 2001.

71 M. R. Cimberle, M. Novak, P. Manfrinetti and A. Palenzona, Magnetic characterization of sintered MgB_2 samples: effect of the substitution or doping with Li, Al and Si, cond-mat/0105212, 2001.

72 M. Eisterer, Supercond. Sci. technol. 20, R47, 2007.

73 K. Vinod, N. Varghese and U. Syamaprasad, Supercond. Sci. technol. 20 R31-R45, 2007.

74 J. Bardeen and M. J. Stephen, Phys. Rev. 140, A1197, 1965.

75 E. J. Nicol and J. P. Carbotte, Phys. Rev B 72, 014520, 2005.

76 C. B. Eom, M.K. Lee, J.H. Choi, L. Belenky, X. Song, L.D. Cooley, M.T. Naus, S. Patnaik, J. Jiang, M. Rikel, A. Polyanskii, A. Gurevich, X.Y. Cai, S.D. Bu, S.E. Babcock, E.E. Hellstrom, D.C. Larbalestier, N. Rogado, K.A. Regan, M.A. Hayward, T. He, J.S. Slusky, K. Inumaru, M.K. Haas and R.J. Cava, Nature 411 558, 2001.

77 T. H. Johansen, M. Baziljevich, D.V Shantsev, P.E. Goa, Y.M Galperin, W.N Kang, H.J Kim, E.M Choi, M.S Kim, S.I Lee, Complex flux dynamics in MgB_2 films, cond-mat/0104113, 2001.

78 P. C. Canfield, D. K. Finnemore, S. L. Bud'ko, J. E. Ostenson, G. Lapertot, C. E. Cunningham and C. Petrovic, Superconductivity in dense MgB_2 wires, Phys. Rev. Lett. 86 2423, 2001.

79 B. A. Glowacki, M. Majoros, M. Vickers, J. E. Evvets, Y. Shi, I. McDougall, Superconductivity of powder-in-tube MgB_2 wires, Supercond. Sci. Technol. 14 193, 2001.

80 Y. B. Kim and M. J. Stephen, Flux flow and irreversible effects, in Superconductivity, Vol. 2, Ed. Parks R. D. (Marcel Dekker, New York) pp. 1107-1165, 1969.

81 R. W. Heussner, J. D. Marquardt, P. J. Lee, and D. C. Larbalestier, Increased critical current density in Nb-Ti wires having Nb artificial pinning centers, Appl. Phys. Lett. 70 17. 1997.

82 W. Pachla, P. Kováč, I. Hušek, T. Melišek, M. Müler, V. Štrbík, A. Mazur, A. Presz., Superconductor Science and Technology, 18 (2005) 552.

83 M. Eisterer, Magnetic properties and critical currents of MgB_2, Supercond. Sci. Technol. 20 R47 (2007)

84 A. Handstein, D. Hinz, G. Fuchs, K.H Muller, K. Nenkov, O. Gutfleisch, V.N Narozhnyi and L. Schultz, Fully dense MgB_2 superconductor textured by hot deformation, cond-mat/0103408, 2001.

85 S. Patnaik, L.D. Cooley, A. Gurevich, A.A. Polyanskii, J. Jiang, X.Y Cai, A.A Squitieri, M.T Naus, M.K Lee, J.H Choi, Belenky L., S.D. Bu, J. Letteri, X. Song, D.G. Schlom, S.E Babcock, C.B. Eom, E.E. Hellstrom, Supercond. Sci. Technol. 14 315, 2001.

86 C. U. Jung, M.S Park, W.N Kang, M.S Kim, S.Y Lee and S. Lee, Temperature- and magnetic-field-dependences ofnormal state resistivity of MgB_2 prepared at high temperature and high pressure condition, Physica C**,** 353. 162, 2001.

87 M. Xu, H. Kitazawa, Y. Takano, J. Ye, K. Nishida, H. Abe, A. Matsushita and A.Kido, Single crystal MgB_2 with anisotropic superconducting properties, condmat/0105271, 2001.

88 S. L. Bud'ko, C. Petrovic, G. Lapertot, C.E Cunningham, P.C Canfield, Jung M-H and A.H Lacerda, Magnetoresistivity and H_{c2}(T) in MgB_2, Phys. Rev. 63, 220503, 2001

89 Y. Takano, H. Takeya, H. Fujii, H. Kumakura, T. Hatano, K. Togano, H. Kito and H. Ihara, Superconducting Properties of MgB_2 Bulk Materials Prepared by High Pressure Sintering, Appl. Phys. Lett. 78 2914, 2001.

90 G. Fuchs, K.H Muller, A. Handstein, K. Nenkov, V.N Narozhnyi, D. Eckert, M. Wolf and L. Schultz, Upper critical field and irreversibility line in superconducting MgB_2, Solid State Comm. 118 497, 2001.

91 S. L. Li, H. H. Wen, Z. W. Zhao, Y. M. Ni, Z. A. Ren, G. C. Che, H. P. Yang, Z. Y. Liu and Z. X.Zhao, Lower Critical Field at Odds with A S-Wave Superconductivity in The New Superconductor MgB_2, Phys. Rev., 64 094522, 2001.

92 A. G. Joshi, C. G. S. Pillai, P. Raj and S. K.Malik, Magnetization studies on superconducting MgB_2 – lower and upper critical fields and critical current density, Solid State Commun. 118 445, 2001.

93 A. Sharoni, I. Felner and O. Millo, Tunneling spectroscopy measurement of the superconducting properties of MgB_2, Phys. Rev. 63 220508R, 2001.

94 H. Kumakura, H. Kitaguchi, A. Matsumoto, and H. Hatakeyama, Appl. Phys. Lett. 84, 3669, 2004.

95 S. X. Dou, S. Soltanian, J. Horvat, X. L. Wang, S. H. Zhou, M. Ionescu, H. K. Liu, P. Munroe, and M. Tomsic, Appl. Phys. Lett. 81, 3419, 2002.

96 S. X. Dou, W. K. Yeoh, J. Horvat, and M. Ionescu, Appl. Phys. Lett. 83 4996, 2003.

97 A. Yamamoto, J. Shimoyama, S. Ueda, Y. Katsura, I. Iwayama, S. Horii, and K. Kishio, Appl. Phys. Lett. 86 212502-1-212502-3, 2005.

98 X. H. Chen, Y.Y Xue, R.L Meng, and C.W Chu, Penetration Depth and Anisotropy in MgB_2, condmat/ 0103029, to appear in Phys. Rev.**,** 2001.

99 F. Manzano and A. Carrington, Exponential Temperature Dependence of Penetration Depth in MgB_2, cond-mat/0106166, 2001.

100 Q. Feng, C. Chen, J. Xu, L. Kong, X. Chen, Y. Wang, Y. Zhang, and Z. Gao, Physica C, 411 41-46, 2004.

101 T. Nakane, H. Takeya, H. Fujii, and H. Kumakura, Supercond. Sci. Technol. 18, 521-525 2005.

102 J. H. Kim, W. K. Yeoh, M.J. Qin, X. Xu, and S. X. Dou, J. Appl. Phys. 100 013908, 2006.

103 H. L. Suo, C. Beneduce, M. Dhallé, N. Musolino, J. Y. Genoud, and R. Flükiger, Appl. Phys. Lett. 79 3116-3118, 2001.

104 H. Kumakura, A. Matsumoto, H. Fujii, and K. Togano, Appl. Phys. Lett. 79, 2435-2437, 2001.

105 G. Grasso, A. Malagoli, C. Ferdeghini, S. Roncallo, V. Braccini, A. S. Siri, and M. R. Cimberle, Appl. Phys. Lett. 79 230-232, 2001.

106 A. Serquis, L. Civale, D. L. Hammon, J. Y. Coulter, X. Z. Liao, Y. T. Zhu, T. G. Holesinger, D. E. Peterson, and F. M. Mueller (unpublished)

107 J. M. Hur, K Togano, A. Matsumoto, H. Kumakura, H. Wada and K. Kimura, Fabrication of high performance MgB_2 wires by an internal Mg diffusion process. Supercond. Sci. Technol. 21, 032001, 2008.

108 H. Yamada, M. Hirakawa, H. Kumakura, A. Matsumoto, and H. Kitaguchi, Appl. Phys. Lett. 84 1728, 2004.

109 H. Yamada, M. Hirakawa, H. Kumakura, A. Matsumoto, and H. Kitaguchi, IEEE Trans. Appl. Supercond. 15 3337, 2005.

110 C. Fischer, C. Rodig, W. Hassler, O. Perner, J. Eckert, K. Nenkov, G. Fuchs, H. Wendrock, B. Holzapfel, and L. Schultz, Appl. Phys. Lett. 83 1803, 2003.

111 H. Fang, S. Padmanabhan, Y. X. Zhou, and K. Salama , Appl. Phys. Lett. 82 4113, 2003.

112 X. Z. Liao, A. Serquis, Y. T. Zhu, J. Y. Huang, L. Civale, D. E. Peterson, F. M. Mueller, and H. F. Xu, J. Appl. Phys. 93 6208, (2003).

113 C. H. Jiang, T. Nakane, and H. Kumakura, Supercond. Sci. Technol. 18 902, 2005.

114 M.A. Susner, M.D. Sumption, M. Bhatia, X. Peng, M.J. Tomsic, *M.A.* Rindfleisch, and E.W. Collings, Physica C 456, 180-187, 2007.

115 H. Fujii, K. Togano, and H. Kumakura, Supercond. Sci. Technol. 15 1571, 2002.

116 H. Davy, Electro-Chemical Researches, on the Decomposition of the Earths; With Observations on the Metals Obtained from the Alkaline Earths, and on the Amalgam Procured from Ammonia (Read June 30, 1808), Phil. Trans. R. Soc. Lond., vol. 98, pp. 333–370, 1808.

117 J.L. Gay-Lussac, and L. J. Thenard, Sur la Décomposition et la Recomposition de l’Acide Boracique, Ann. Chim. Phys., vol. 68, pp. 169–174, 1808.

118 H. Moissan, Etude du Bore Amorphe, Ann. Chim. Phys., vol. 6, pp. 296–320, 1895.

119 F. Weintraub, Trans. Am. Electrochem. Sot., 16 165, 1909.

120 F. Weintraub, Ind. Eng. Chem., 3, 300; 5, 106, 1913.

121 L. Hackspill, A. Stieber and R. Hocart, Compt. rend., 193, 776, 1931.

122 L. Ya, D. I. Markovsky, D. Lvova, and J. D. Kondrachev, Proc. Conf. on Boron; its Chemistvy and its Compounds, GHI, Moscow, p. 36., 1958.

123 S. K. Chen, K. A. Yates, M. G. Blamire, and J. L. MacManus-Driscoll, Supercond. Sci. Technol. 18 1473, 2005.

124 W. X. Li, Y. Li, M.Y. Zhu, R. H. Chen, S. X. Dou, M. J. Qin, X. Xu and P. Yao, Physica C 460-462, 602-603, 2007.

125 X. Xu, J. H. Kim, M. S. A. Hossain, J. S. Park, Y. Zhao, S. X. Dou, W. K. Yeoh, M. Rindfleisch, and M. Tomsic, J. of Appl. Phys. 103, 023912, 2008.

126 S. X. Dou, O. Shcherbakova, W.K. Yeoh, J.H. Kim, S. Soltanian, X.L. Wang, C. Senatore, R. Flukiger, M. Dhalle, O. Husnjak, and E. Babic, Mechanism of enhancement of electromagnetic properties of MgB_2 by nano-SiC doping, *cond-mat*/0701391, 2007.

127 S. X. Dou, S. Soltanian, J. Horvat, X. L. Wang, S. H. Zhou, M. Ionescu, H. K. Liu, P. Munroe, and M. Tomsic, Appl. Phys. Lett. 81 3419-3421, 2002.

128 S. X. Dou, V. Braccini, S. Soltanian, R. Klie, Y. Zhu, S. Li, X. L. Wang, and D. Larbalestier, J. Appl. Phys. 96 7549, 2004.

129 S. H. Zhou, A.V. Pan, S.X. Dou, and D. Wexler, Adv. Mater. **19** 13, 2007.

130 Z. S. Gao, Y. W. Ma, X. P. Zhang, D. L. Wang, Z. G. Yu, K. Watanabe, H. Yang, and H. H. Wen, Supercond. Sci. Technol. 20 485-489, 2007.

131 M. S. A. Hossain, J. H. Kim, X. L. Wang, X. Xu, G. Peleckis, and S X Dou, Supercond. Sci. Technol. 20 112-116, 2007.

132 B. H. Jun, and C. J. Kim, Supercond. Sci. Technol. 20 980–985, 2007.

133 M. M. A.Sekkina, and K. M. Elsabawy, Fluoride doping and Boron particle size effect on $MgB_{2-x}F_x$ superconductor, Solid State Communications 123, 1-6, 2002.

134 S. X. Dou, S. Soltanian, Y. Zhao, E. Getin, Z. Chen, O. Shcherbakova and J. Horvat, Supercond. Sci. Technol. 18**,** 710–715, 2005.

135 S.Y. Li, Y. M. Xiong, W. Q. Mo, R. Fan, C. H. Wang, X. G. Luo, Z. Sun, H. T. Zhang, L. Li, L. Z. Cao, X. H. Chen, Physica C, 363(4): p.219-223, 2001.

136 Y.G. Zhao, X.P. Zhang, P.T. Qiao, H.T. Zhang, S.L. Jia, B.S. Cao, M.H. Zhu, Z.H. Han, X.L. Wang, B.L. Gu, Physica C, 361(2): p.91-94, 2001.

137 O. de la Pena, A. Aguayo, and R. de Coss, Phys. Rev. B 66, 012511, 2002.

138 J. Y. Xiang, D. N. Zheng , J. Q. Li, S. L. Li, H. H. Wen, and Z. X.Zhao, Physica C 386, 611, 2003.

139 P. Toulemonde, N. Musolino, and R. Flükiger, Supercond. Sci.Technol. 16, 231, 2003.

140 E. Martinez, L. A. Angurel, R. Navarro, A. Millan, C. Rillo, and M. Artigas, IEEE Trans. Appl. Supercond. 13, 3210, 2003.

141 Y. Ma, H. Kumakura, A. Matsumoto and K. Togano, Appl. Phys. Lett. 83 1181, 2003.

142 Y. Ma, H. Kumakura, A. Matsumoto, H. Takeya, and K. Togano, Physica C 408–410 138, 2004.

143 C. H. Jiang, T. Nakane, and H. Kumakura, Supercond. Sci. Technol. 18 902, 2005.

144 Matsumoto, H. Kumakura, H. Kitaguchi, and H. Hatakeyama, Supercond. Sci. Technol. 16 926, 2003.

145 X. F. Rui, Y. Zhao, Y. Y. Xu, L. Zhang, X. F. Sun, Y. Z. Wang, and H. Zhang, Supercond. Sci. Technol. 17 689, 2004.

146 P. Perner, W. Häßler, J. Eckert, C. Fischer, C. Mickel, G. Fuchs, B. Holzapfel, and L. Schultz, Physica C 432, 15, 2005.

147 X. L. Wang, S. H. Zhou, M. J. Qin, P. R. Munroe, S. Soltanian, H. K. Liu, and S. X. Dou, Physica C 385 461-465, 2003.

148 S. Soltanian, X. L. Wang, J. Horvat, S. X. Dou, M. D. Sumption, M. Bhatia, E. W. Collings, P. Munroe, M. Tomsic, Superconductor Science & Technology, 18(5): 658-666, 2005.

149 W. X. Li, Y. Li, R. H. Chen, M. Y. Zhu, H. M. Jin, R. Zeng, L. Lu, Y. Zhang, and S. X. Dou, T_c enhancement for nano-SiC doped MgB_2 superconductors sintered in 5T pulsed magnetic field, Int. J. Mod. Phys. B, 3482, 2005.

150 E. W. Collings, E. Lee, M. D. Sumption, M. Tomsic, X. L. Wang, S. Soltanian, and S. X. Dou, Physica C 386, 555, 2003.

151 M. Bhatia, M. D. Sumption, M. Tomsic, and E. W. Collings, Physica C 15, 153, 2004.

152 P. Kovač, I. Hušek, V. Skakalova, J. Meyer, E. Dobrocka, M. Hirscher, and S. Roth, Supercond. Sci. Technol. 20, 105, 2007.

153 M. D. Sumption, M. Bhatia, F. Buta, S. Bohnenstiehl, M. Tomsic, M. Rindfleisch, J. Yue, J. Phillips, S. Kawabata, and E. W. Collings, Supercond. Sci. Technol. 18, 961, 2005.

154 H. L. Xu, Y. Feng, Y. Zhao, G. Yan, M. H. Pu, H. X. Lu, R. Zhang,and Z. Xu, Physica C 449, 53, 2006.

155 S.-F. Wang, S.-Y. Dai, Y.-L. Zhou, Y.-B. Zhu, Z.-H. Chen, H.-B. Lu, and G.-Z. Yang, J. Supercond.: Incorporat. Novel Mag. 17, 397, 2004.

156 S. M. Kazakov, M. Angst, J. Karpinski, I. M. Fita, and R. Puzniak, Solid State Commun. 119, 1, 2001.

157 Y. P. Sun, W. H. Song, J. M. Dai, B. Zhao, J. J. Du, H. H. Wen, and Z. H. Zhao, Cond-mat/0103101, 2001.

158 R. H. Baughman, A. A. Zakhidov, and W. A. de Heer, Science 297, 787, 2002.

159 B. Q. Wei, R. Vajtai, and P. M. Ajayan, Appl. Phys. Lett. 79, 1172, 2001.

160 P. Kim, L. Shi, A. Majumdar, and P. L. McEuen, Phys. Rev. Lett. 87, 215502, 2001.

161 M. M. J. Treacy, T. W. Ebbesen, and J. M. Gibson, Nature, 381, 678, 1996.

162 P. Kovač, I. Hušek, V. Skakalova, J. Meyer, E. Dobrocka,M. Hirscher, and S. Roth, Supercond. Sci. Technol. 20, 105, 2007.

163 W. X. Li, Y. Li, R. H. Chen, R. Zeng, L. Lu, Y. Zhang, M. Tomsic, M. Rindfleisch, and S. X. Dou, Increased superconductivity for CNT Doped MgB_2 Sintered in 5T Pulsed Magnetic Field, IEEE Trans. Appl. Supercond., 19(3), 2752-2755, 2009.

164 H. L. Xu, Y. Feng, Z. Xu, G. Yan, L. Z. Cao, and X. G. Li, Chin.Phys. Lett. 21, 2511, 2004.

165 S. Ueda, J. Shimoyama, A. Yamamoto, S. Horii, and K. Kishio, Supercond. Sci. Technol. 17, 26, 2004.

166 E. Ban, R. Sakaguchi, Y. Matsuoka, T. Goto, K. Watanabe, and G. Nishijima, Physica C 1249, 426, 2005.

167 A. Yamamoto, J. Shimoyama, S. Ueda, S. Horii, and K. Kishio, Physica C 445–448, 801, 2006.

168 V.P.S. Awana, A. Vajpayee, M. Mudgel, V. Ganesan, A.M. Awasthi, G.L. Bhalla and H. Kishan, Eur. Phys. J. B 62, 281–294 (2008)

169 T. Sun, X. P. Zhang, Y. G. Zhao, R. Shen, K. Wang, L. W. Zhang, B. S. Cao, Y. H. Xiong, P. J. Li, and H. H. Wen, Physica C 382, 367, 2002.

170 J. Wang, Y. Bugoslavsky, A. Berenov, et al., Applied Physics Letters, 81(11): p. 2026-2028, 2002.

171 S. K. Chen, M. Wei, and J. L. MacManus-Driscoll, Appl. Phys. Lett. 88, 192512 (2006).

172 C. Cheng and Y. Zhao, Appl. Phys. Lett. 89, 252501, 2006.

173 Y. Kimishima, M. Uehara, T. Kuramoto, S. Takano, and S. Takami, Physica C 412–414, 402, 2004.

174 C. Shekhar, R. Giri, R. S. Tiwari, D. S. Rana, S. K. Malik, and O. N. Srivastava, Supercond. Sci. Technol. 18, 1210, 2005.

175 S. H. Zhou, H. K. Liu, J. Horvat, and S. X. Dou, J. Low Temp. Phys. **131** 687, 2003.

176 S. Haigh, P. Kováč, T. A. Prikhna, Y. M. Savchuk, M. R. Kilburn, C. Salter, J.Hutchison, and C. Grovenor, Supercond. Sci. Technol.18, 1190, 2005.

177 P. Kováč, I. Husek, T. Melisek, C. R. M. Grovenor, S. Haigh, and H. Jones, Supercond. Sci. Technol. 17 1225, 2004.

178 G. Yan, Y. Feng, Y. F. Lu, L. Zhou, W. X. Jing, and H. H. Wen, Physica C 445–448 466, 2006.

179 H. Fujii, K. Togano, and H. Kumakura, Supercond. Sci. Technol. 16, 432, 2003.

180 D. W. Gu, Y. M. Cai, J. K. F. Yau, Y. G. Cui, T. Wu, G. K. Yuan, L. J. Shen, and X. Jin, Physica C, 386 643-647, 2003.

181 A. Tampieri, G. Celotti, S. Sprio, D. Rinaldi, G. Barucca, and R. Caciuffo, Solid State Commun. 121, 497, 2002.

182 W. J. Feng, T. D. Xia, T. Z. Liu, W. J. Zhao, and Z. Q. Wei, Physica C 425, 144, 2005.

183 S.-F. Wang, S.-Y. Dai, Y.-L. Zhou, Y.-B. Zhu, Z.-H. Chen, H.-B. Lu, and G.-Z. Yang, J. Supercond.: Incorporat. Novel Mag. 17, 397, 2004.

184 Y. Moritomo, and S. Xu, Effects of transition metal doping in MgB2 superconductor, cond-matt/0104568, 2001.

185 E. J. Kuzmann, Z. Homonnay, Z. Klencsar, M. Kuhberger, A. Vertes, and G. Gritzner, Supercond. Sci. & Technol. 15(11) 1479-1485, 2002.

186 S. Xu, Y. Moritomo, K. Kato, and A. Nakamura, J.of the Phys.Soc.of Japan 70 (7) 1889-1891, 2001.

187 A. Snezhko, T. Prozorov and R. Prozorov, Phys. Rev. B 71, 024527, 2005.

188 S. K. Chen, B. A. Glowacki, J. L. MacManus-Driscoll, M. E. Vickers, and M. Majoros, Supercond. Sci. Technol. 17, 243, 2004.

189 Y. Zhao, D. X. Huang, Y. Feng, C. H. Cheng, T. Machi, N. Koshizuka, and M. Murakami, Appl. Phys. Lett. 80, 1640, 2002.

190 Y. Ma, H. Kumakura, A. Matsumoto, H. Hatakeyama, and K. Togano, Supercond. Sci. Technol. 16, 852, 2003.

191 H. L. Xu, Y. Feng, Z. Xu, G. Yan, C. S. Li, E. Mossang, and A. Sulpice, *Physica C* 443, 5, 2006.

192 H. Fujii, K. Togano, and H. Kumakura, Supercond. Sci. Technol. 16, 432 (2003).

193 W. K. Yeoh, J. Horvat, S. X. Dou, Encyclopedia of Nanoscience and Nanotechnology, Volume X: Pages (1–16), 2009.

194 M. R. Eskildsen, M. Kugler, S. Tanaka, J. Jun, S.M. Kazakov, J. Karpinski, Ø.Fischer, Phys. Rev. Lett.. 89, 187003, 2002.

195 S. Sengupta and D. Shi, in “High Temperature Superconducting Materials Science and Engineering: New Concepts and Technology” (D. Shi, Ed.), 131, Elmsford, NY: Pergamon, 1995.

196 S.R. Ghorbani, X. Wang, S.X. Dou, S. Lee, M. Hossain, Flux-pinning mechanism in silicone-oil doped MgB_2, Physical Review B, 78(18), pp. 184502-1-184502-5, 2008.

197 L. D. Cooley and A. M. Grishin, Phys. Rev. Lett. 74, 2788, 1995.

198 G. S. Mktrchyan and V. V. Shmidt, Soviet Phys. JETP 34, 195, 1972.

199 W. E. Timms and D. G. Walmsley, Phys. Stat. Sol. B 71, 741, 1975.

200 A. Buzdin and D. Feinberg, Physica C 256, 303, 1996.

201 R. L. Fleischer, Phys. Rev. Lett. 3, 111, 1962.

202 W. W. Webb, Phys. Rev. Lett. 11, 191, 1963.

203 L. E. Toth and I. P. Pratt, Appl. Phys. Lett. 4, 75, 1964.

204 M. V. Milošević, S. V. Yampolskii and F. M. Peeters, Phys. Rev. B 66, 174519, 2002.

Chapter 1.3: Nanoparticles

1.3.1 Introduction

Renaissance pottery and stained glass windows often featured a distinct gold or copper coloured metallic glitter. This so-called lustre is caused by a metallic film or particles, which are applied to the transparent surface of a glaze or incorporated in the glass matrix of the windows. These lustres were created by artisans, who added metal salts and oxides with vinegar to the clay surface, which was then heated to a high temperature.

Michael Faraday provided the first scientific description of nanoparticles, nanosize gold, and theirs optical properties in his classical paper from 1857.

The first scientific observations and measurements of the size of nanoparticles were made by Richard Adolf Zsigmondy in the early twentieth century. His research on characterization of nanomaterials was published in a book, *Colloids and Ultramicroscope*, in 1914. A major contribution to understanding the properties and phenomena of nanoscale particles was made by physicist Richard Feynman, who pointed to the quantum phenomena that dominate the nanoscale.

The possibility of controlling the size and properties of materials on this scale commercially was first exploited by innovators from Silicon Valley. Gordon Moore (Moore's Law) predicted reduction of the size of transistors from 1 centimetre to 50 nm (i.e., the size of clusters of approximately 180 atoms of silicon). The first such a transistor was manufactured in 2007.

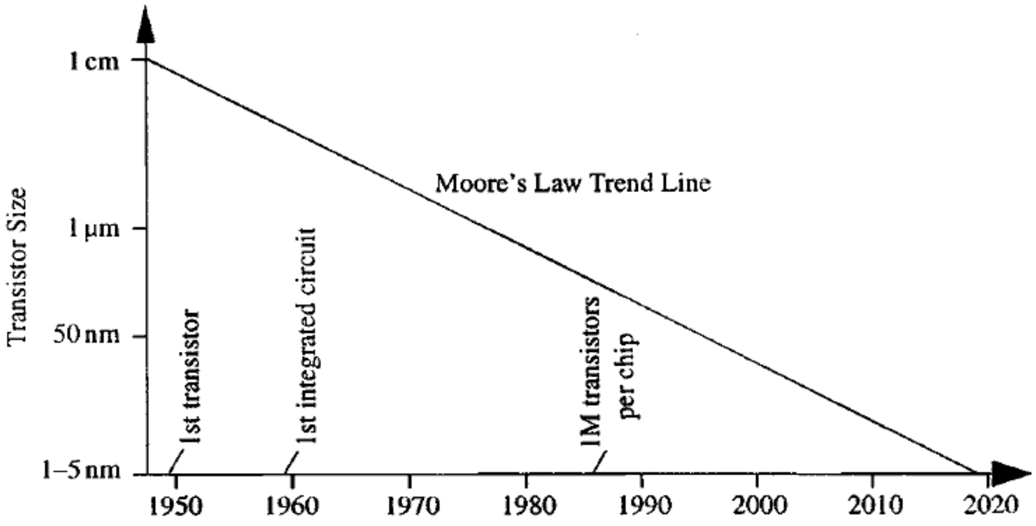

Figure 1.3.1: "Moore's Law" plot of transistor size versus year. Adopted from [1].

Since the initial proposal of Feynman [2], much progress has been made in the understanding of physics on the nanoscale. Based on these advances, an increasing number of technological applications, from magnetic read heads to automotive sensors, are now reaching the commercial market.

Nanoparticles are already deeply involved in all segments of human life and work. The important roles that nanoparticles have in medical applications are primarily in the diagnosis and treatment of various malignant diseases. The reason for such a large and successful application is the size of nanoparticles, which is very close to those of biological cells and structures. The integration of medicine, molecular biology, and nanotechnology acts to improve old techniques and create completely new techniques of treatment and diagnosis of disease, particularly in diagnostic devices, chemotherapy, drug delivery with nanoparticles, and analytical methods.

Implementation of nanoparticles and nanotechnology in the energy sector is very important, and is associated with the most efficient energy conversion and storage, thus saving energy and promoting better utilization of energy resources. One direct example that we have is in light-emitting diode (LED) and quantum caged atom (QCA) household lamps. Solar cells are becoming increasingly important renewable energy sources, but their efficiency is still only 15-20%.

Utilization can be improved by applying nanolayers of semiconductors and conductors in the production of solar cells. Great progress has been made in the production of batteries, where the nanoparticles and their large surface areas provide a multiple increase in capacity.

As the main parts of computer chips, transistors are in the nanometer size range of about 50 nm. New semiconductors are based on spintronics, where the electrical resistance of the material depends on the spin orientation of electrons in an external magnetic field (magnetoresistance). Quantum computers would utilize the laws of quantum physics and would be largely built on nanotechnology.

Applications in industry are widespread. So, nanotechnology has a strong influence on all facets of the transportation industry from bicycles and cars to airplanes and space shuttles. Nanoparticles and nanorods are incorporated in parts of various vehicles, giving them strength, elasticity, and other types of good performance. Production of steel and other special alloys with nanoparticles has opened up new possibilities in the construction industry, especially in the construction of skyscrapers and high-rise buildings.

1.3.2 Geometrical considerations

Nanoscience commonly refers to physical phenomena in ultra-small structures which have one or more dimensions below 100 nm. To give some idea of the scale, one nanometer is approximately a length equivalent to around 32 hydrogen atoms, the smallest atom in the periodic table or slightly more than two caesium atoms, the biggest one, aligned in a line.

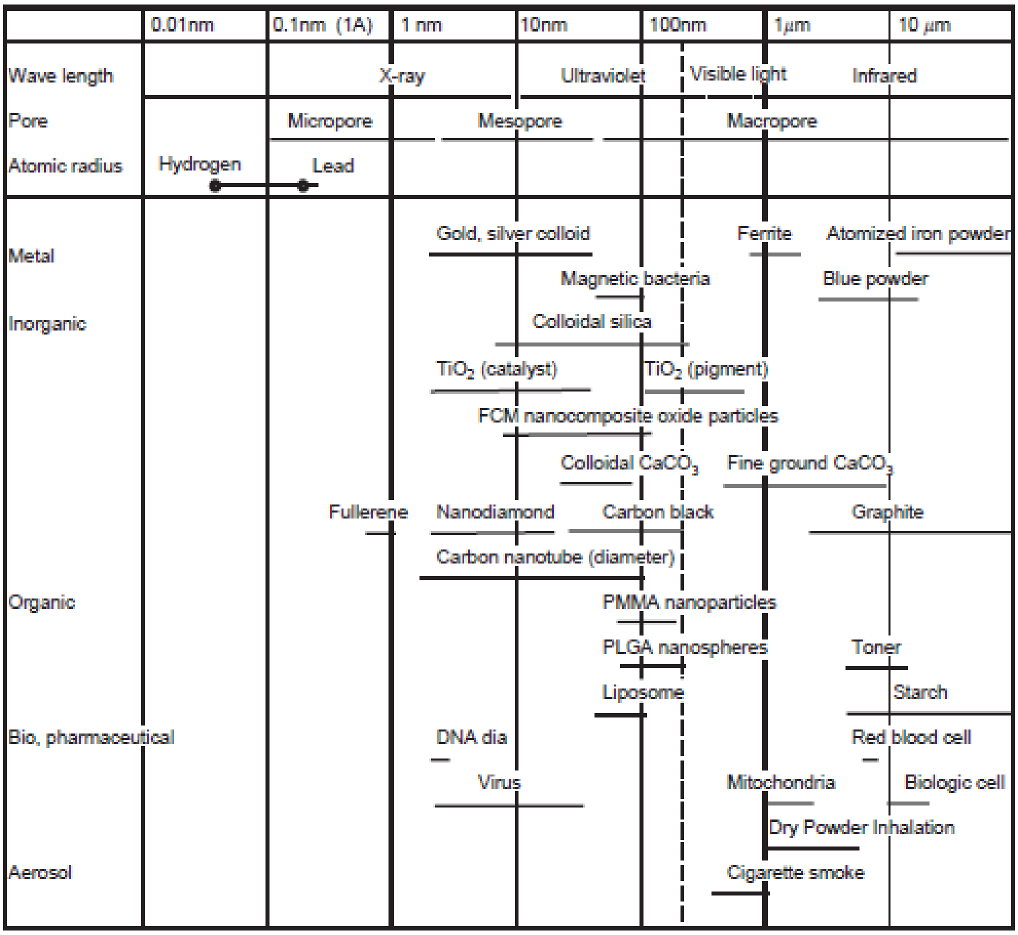

Figure 1.3.2: Examples of nanoparticles and related phenomena. Adopted from [3].

Actually, nanostructure is a bridge between the macroscopic world with classical laws of physics, and atoms and small molecules in the realm of quantum physics. Materials on the nanometer scale usually exhibit physical properties distinctively different to those found in the bulk size of the same material.

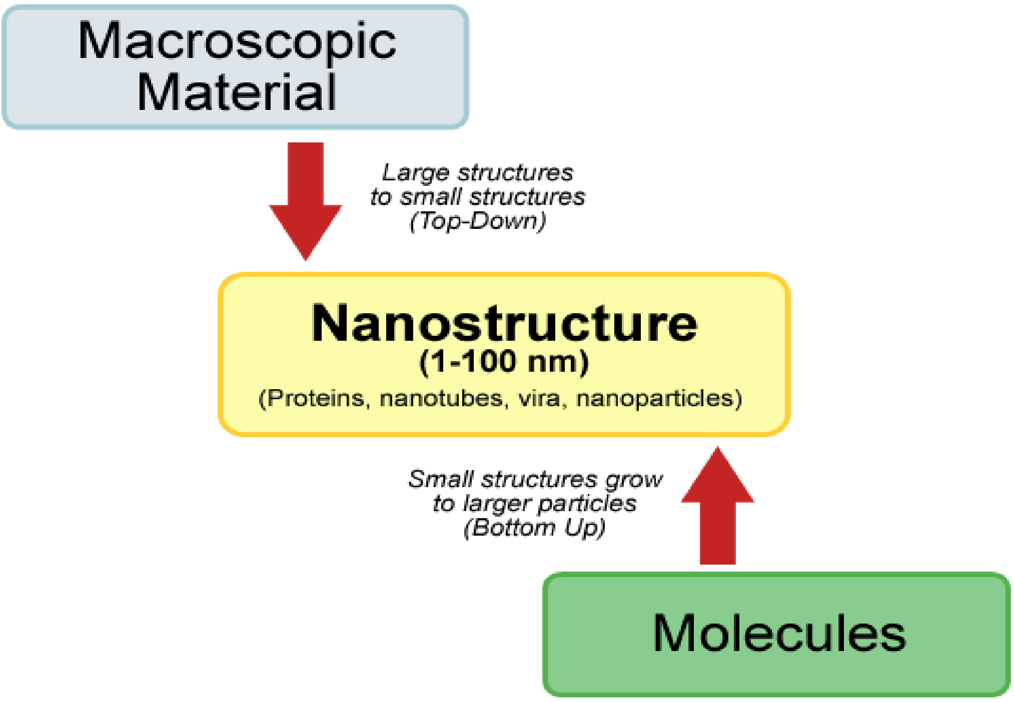

Figure 1.3.3: Schematic representation of the position of nanostructures in nature, as a bridge between the world of atoms and the macro world. Adopted from [4].

The reason for significant changes in the physicochemical properties lies in the fact that quantum mechanical principles play an important role. The surface-to-volume ration of the particles increases dramatically when the size of particles drops to the nanometer scale. For spherical particles, the surface to volume ratio is:

$$\frac{S}{V} = \frac{3}{r}, \qquad (1.3.1)$$

where *r* is the radius of the particle.

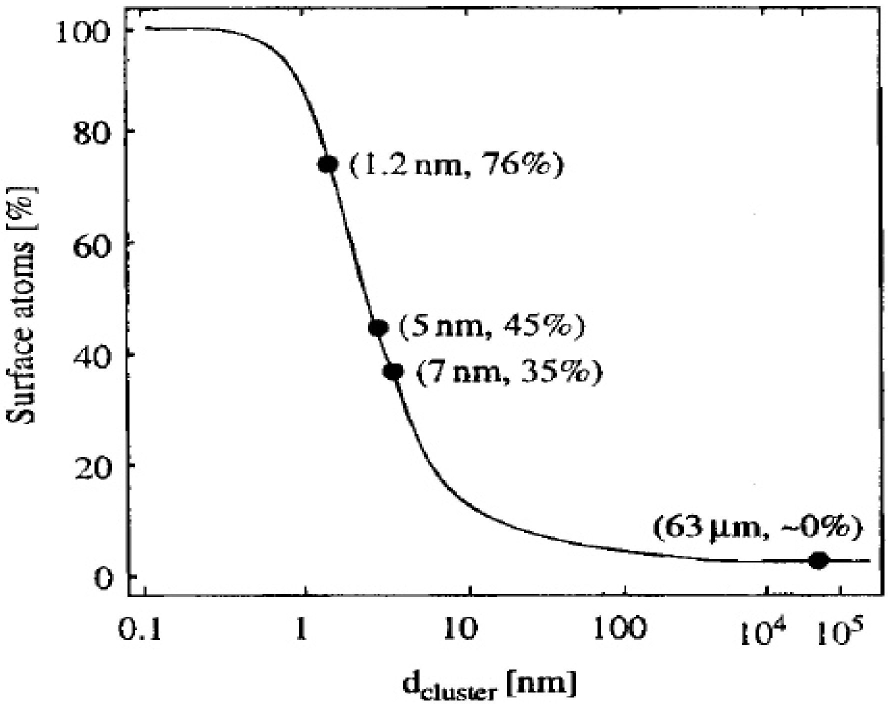

Figure 1.3.4: The percentage of surface atoms changes with the nanoparticle diameter. Adopted from [5].

Enlarging the contact surface increases the boundary between phases, which leads to unique features of nanoparticles in terms of their morphological/structural, thermal, electromagnetic, optical and mechanical properties. In a case of nanoparticles, the bond length between the surface atoms and interior atoms becomes considerably smaller and the lattice constants show an appreciable reduction[6]. The surface atoms possess additional energy, γ, described as a surface free energy or surface tension. Surface energy, is the energy needed to create a new surface area.

$$\gamma = \left(\frac{\Delta G}{\Delta A}\right)_{n_i,T} \qquad (1.3.2)$$

where *A* is the surface area and *G* the free energy. On the other hand, an approximation of the surface energy can be given by Equation 1.3.3:

$$\gamma = \frac{1}{2} N_b\, \varepsilon\, p_a \qquad (1.3.3)$$

where γ is the surface energy, N_b is the number of broken bonds between atoms, ε is the bond energy and p_a is the surface atomic density.[7]

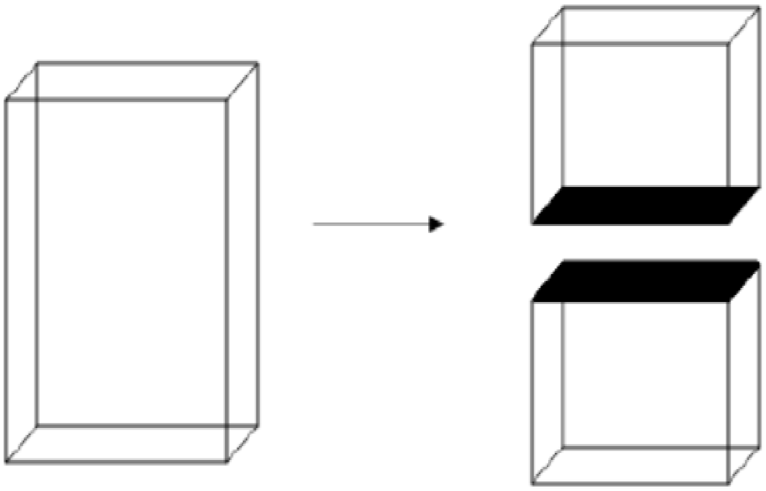

Figure 1.3.5: Schematic showing how two new surfaces are created when a block is divided into two pieces. Adopted from [7].

For example, a solid material, a cubic shape with an edge length of 1 cm, has less than 5% surface atoms. With an edge length of 10 nm percentage of surface atoms is around 10%. Eventually, when the edge length equals 1 nm we can say that all atoms are surface atoms. The thickness of the layer subject to the surface effects is more than one atomic layer. On reducing the particle size and increasing the surface energy of particles, particles become thermodynamically unstable or metastable, and thus they are more difficult to synthesize than particles of macroscopic size.[8]

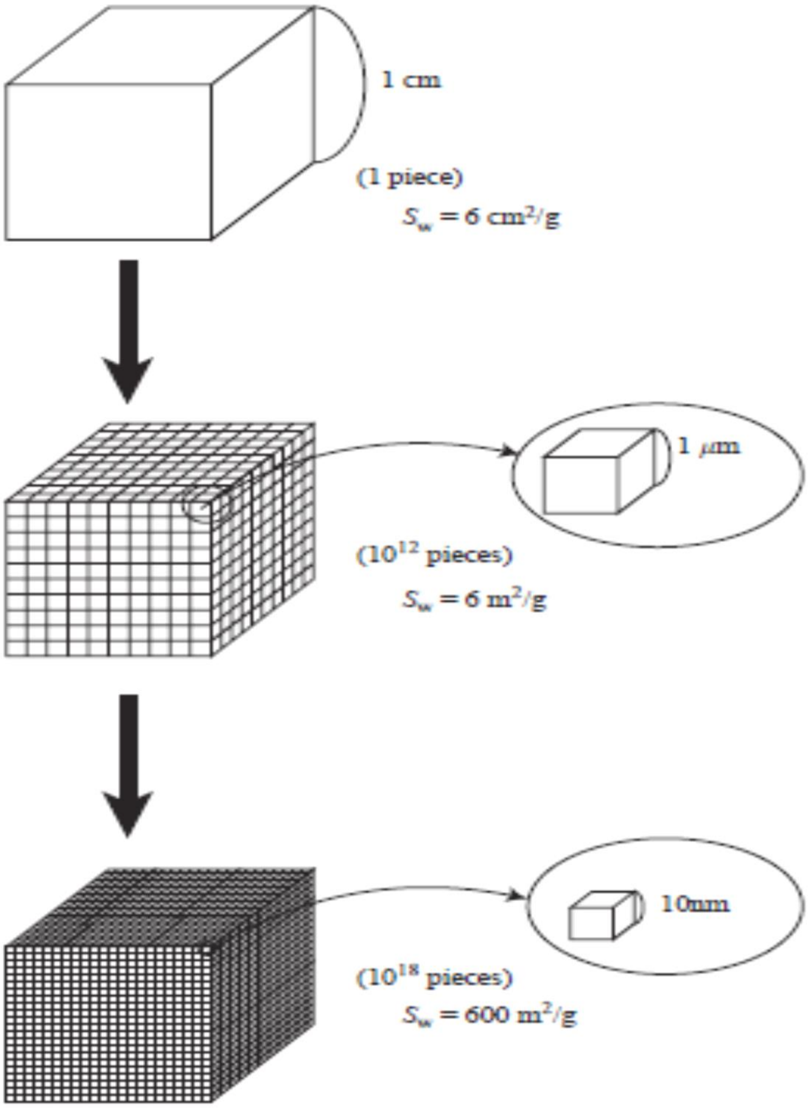

Figure 1.3.6: Change of specific surface area (S_W) by dividing a solid cube assuming a density of 1 g/cm^3. Adopted from [3].

1.3.3 Forces between nanoparticles

According to the DLVO theory (named after the authors Derjaguin, Landau, Verwey, and Overbeek), the total interaction between two electrostatically stabilized nanoparticles is the sum of the Van der Waals attraction and the electrostatic repulsion[9]. These two opposite forces can be presented as a function of distance from the surface of both nanoparticles. A maximum of potential energy among the nanoparticles is located at a little distance from the surface, where the forces are in equilibrium. The maximum is also called the repulsive barrier and is a possible cause of agglomeration, depending on the amount of barrier.

$$\Phi = \Phi_A + \Phi_R, \qquad (1.3.4)$$

where Φ is the total energy, Φ_A the van der Waals attractive energy, and Φ_R the electrostatic repulsive energy.

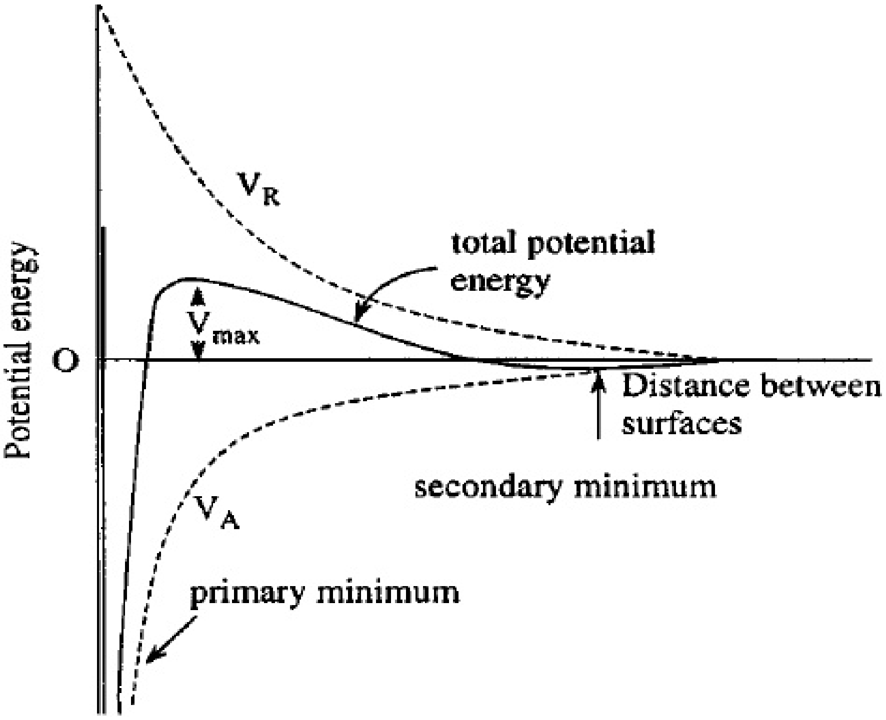

Figure 1.3.7: Schematic of DLVO potential: V_A = attractive van der Waals potential, V_R = repulsive electrostatic potential. Adopted from [10].

Figure 1.3.7 shows the combination of two opposite potentials (attractive van der Waals and repulsive electrostatic) as a function of distance between the surfaces of two particles. Very close to the surface is a deep minimum caused by van der Waals attraction. The potential maximum is placed a little further from the particle surface where the electric repulsion potential begins to dominate. The secondary minimum only appears when the concentration of ions is very high. In situations when secondary minimum is established, particles (ions) tend to be associated with each other and make clusters, a phenomenon which is known as flocculation.[10]

1.3.4 Properties of nanoparticles and size effect

Bulk macroscopic materials mostly have constant physical properties, regardless of their size or shape, but at the nanoscale, size-dependent properties are often observed, and these effects are utilized for a broad range of applications. In many different aspects, such as electromagnetic, mechanical, and optical properties, the properties of nanoparticles show difference from common bulk properties of the same materials and demonstrate the so-called "size-effect". One of the most observed phenomena is a decrease in the melting temperature with decreasing size of particles. The explanation for this phenomenon is the smaller number of atoms in the middle of crystal, which are surrounded by same number of atoms than from all sides compared with the surface atoms.

This means that there are less bonds for the surface atoms than there are for those deeper in the crystal. Consequently, for melting nanostructures, less energy is required for breaking bonds between atoms. As a salient example melting points of bulk gold and "nano-gold" can be mentioned, which have a considerable difference in their melting temperature.[11]

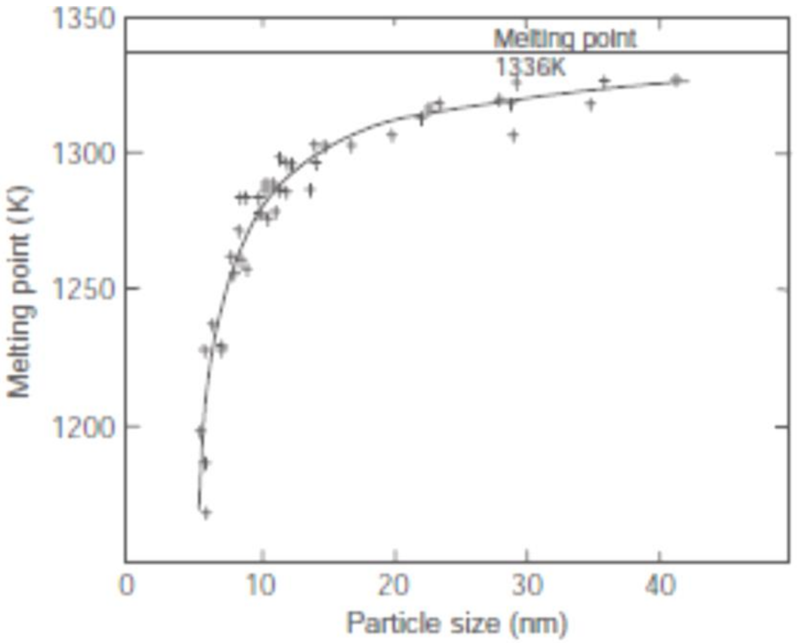

Figure 1.3.8 Relationship between melting point of gold and its particle size. Adopted from [11].

Optical properties of particles dramatically change on the nanometer scale. Nanoparticles absorb light with a specific wavelength, which is known as the plasmon absorption, due to the plasma oscillation of the electrons, causing absorption of photons with certain energies (i.e. colours).

This results in transmitted light with different colour depending on particle size and the nanoparticle material used[12,13]. Nanosize gold in a solution, for example, appears deep red to black.

The term “electromagnetic property” covers a broad range, and magnetic properties of nanostructures, in particular, will be discussed in a later section. For instance, the dielectric constant of $PbTiO_3$ tends to increase as the particles become smaller than about 20 nm. On the other hand the Curie point of $PbTiO_3$ is drastically reduced with decreasing particle size below 20 nm, as can be seen in Figure 1.3.9.[14]

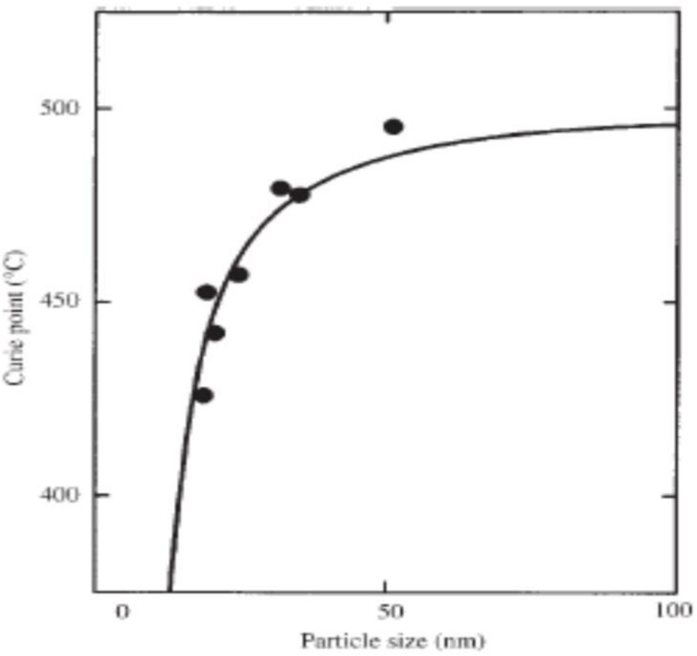

Figure 1.3.9: Change in the Curie point of $PbTiO_3$ with its particle size. Adopted from [14].

Manipulation of the mechanical properties of nanoparticles can find very wide use. With crystalline size of less than several hundred nanometers, unique super-plastic performance can be obtained[15]. Special carbon nanotubes may be extended several times beyond their original size[16]. Furthermore, it is observed that the hardness of t crystalline materials generally increases with the decreasing crystalline size. Mechanical strength of the materials considerably increases by adding nano-clay to the structure of a metal alloy or ceramic composite.[15, 16, 17]

1.3.5 Synthesis of Nanoparticles

Many technologies have been explored to fabricate nanostructures and nanomaterials. Depending on the type and purpose of nanoparticles, different synthesis technique can be used. The main techniques are mechanical attrition, pyrolysis, laser modelling of nanoparticles, wet techniques, or the sol-gel method.

Mechanical attrition (high energy ball milling): This technique, which is already a commercial technology, has been considered dirty because of contamination problems from the ball-milling process.

However, new materials such as tungsten carbide and the use of inert atmosphere have reduced impurities to acceptable levels for many industrial applications. Besides for tungsten-carbide, materials commonly used to make the mills are zinc oxide, silica-nitride, various ceramics, and hard chrome steel. This method is quite rough and not very reliable for getting the small size nanoparticles in a narrow distribution. On the other hand, the benefits are simplicity, low price of the equipment, and obtaining large quantities of fine powders for industrial application as special cements.[18]

Pyrolysis includes a wide number of methods that use high temperatures for the synthesis of nanoparticles. Samples are thermally processed, decomposed at high temperature into nanoparticles, and finally condensed in a separate chamber. This method for preparation of nanoparticles requires complex equipment and is usually used for obtaining "ultra-fine" nanoparticles with a narrow size distribution.[19]

Erosion by an electric arc is similar method to pyrolysis and one more technique for the production of "ultra-fine nanoparticles". Starting materials are placed between two electrodes that are connected to a high voltage source. Nanoparticles are formed by switching the electric spark that evaporates the material, and then the obtained nanoparticles are condensed on the cold walls of the apparatus. The size distribution of obtained nanoparticles is very narrow, and this method is very successful for producing nanoparticles from inert and stabile materials such as quartz, silicon, and various carbide compounds.[20]

Induction plasma technology consists of a conductive metallic piece inside a coil with a high frequency alternating current, which induces an alternating magnetic field[21]. An alternating magnetic field inside the coil produce current in the closed loop and heats it to the red-hot state, which evaporates the precursor.

In the synthesis process, the material is first heated up to evaporation in the induction plasma, and the vapours are subsequently subjected to a very rapid quenching in the quench/reaction zone. The quench gas can be inert gases such as Ar and N_2, or reactive gases as CH_4 and NH_3, depending on the type of nanopowders required. The induction plasma method has many advantages such as high purity, high flexibility, easy scaling up, and easy operation and process control.

Laser ablation is highly sophisticated method that requires specialized equipment and is used to obtain the smallest nanoparticles. This method is based on the exposure of the precursor to pulses of laser radiation. The material is finely processed under the influence of high energy radiation and collected in a specially provided chamber. In this method, it is possible to obtain a wide range of nanoparticles in a relatively simple way by changing the parameters of the laser beam.[22, 23]

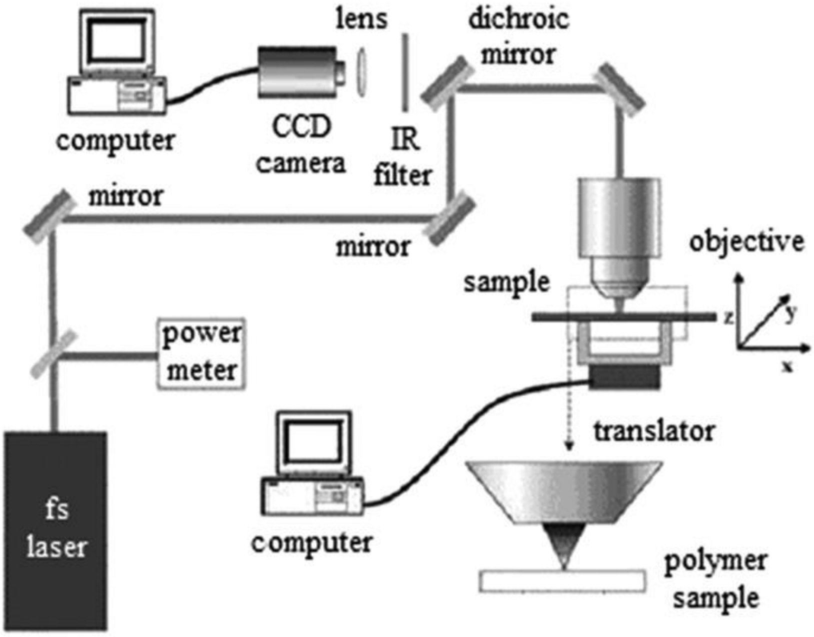

Figure 1.3.10: Schematic of laser ablation machine. Adapted from [23].

The sol-gel method is the most widespread and by far the simplest method, in which the nanoparticles are organized in different solutions or gels. This method has a large number of controlling mechanisms relating to the size and structure of nanoparticles. The controlling mechanisms are different solvents, concentrations of reactants, pH of solutions, temperature, reaction time, surfactants, etc. It is also possible to encapsulate nanoparticles with various protective layers, which leads to new properties of materials such as a higher melting point, higher thermal stability, reduced flammability, and toxicity reduction.[24, 25]

The sol-gel method has several basic subtypes. A nano-emulsion is a dispersion of two immiscible liquids, where the nano-droplets of either or both liquids are stabilized by surfactant molecules. Nanoparticles are formed in micro-droplets surrounded by monolayers of surfactant molecules. Nano-droplets have diameters that are typically in the range of 1–50 nm. [26]

Hydrothermal synthesis is a wet technique in which the reaction occurs under hydrothermal conditions. Usually, the starting materials are dissolved in solvent, sealed in a Teflon-lined stainless-steel autoclave, and heated for some time at a certain temperature. Under conditions of high pressure and temperature, nanoparticles can be obtained nanoparticles with complex structures and properties.

Thermal decomposition is a similar method for the synthesis of nanoparticles. Different types of nanoparticles can be synthesized through the thermal decomposition of organometallic compounds in high-boiling-point organic solvents containing stabilizing agents.[27,28]

The reaction temperature and reaction time are crucial for the precise control of size and morphology.Co-precipitation is method where different combinations of starting precursors precipitate the final nanoparticles. The obtained nanoparticles strongly depend on the type of salts used (e.g., chlorides, sulphates, nitrates), the ionic ratio, the reaction temperature, the pH value, and the ionic strength of the medium.[29, 30]

1.3.6 Magnetic properties of nanoparticles

Magnetic properties of nanoparticles are important for this project, and they are discussed in a separate section. Magnetic order occurs because the magnetic moments of neighbouring atoms couple by the interatomic exchange interaction.

The magnetic moments of atoms exist because of the filling of incomplete energy shells: the 3*d* shell for transition metals (Fe, Ni, Co) and the 4*f* shell for lanthanides. Because electrons in *d*- and *f*-states are close to each other, there is a strong Coulomb interaction between these electrons. Therefore, a large Coulomb energy increase is obtained due to electron-electron interaction. This energy can be minimized if electrons take up different *d*- or *f*-states. For example, a pair of electron can occupy the p_x and p_y states, instead both occupying the p_x state. When they are in the p_x and p_y states, they are further away from each other, and the repulsive Coulomb interaction is much lower. In order to ensure occupancy of different states by electrons, the spins of all unpaired d- and f- electrons are all aligned in the same directions. With such a spin alignment, no two electrons can occupy the same state due to the Pauli principle of exclusion. Therefore, minimization of repulsive Coulomb interaction between unpaired *d*- and *f*- electrons results in their spins being aligned in the same direction, which gives non-zero spin to the atoms.

When atoms with net magnetic moment form crystals, there will be an interaction between them that will align the atomic spins. This interaction has the same origin as the interaction between electrons in the atom: Coulomb interaction between unpaired electrons and the Pauli principle of exclusion.

A simple equation describing this interaction for a two-electron spin Hamiltonian system arises from Heisenberg exchange theory: $H_{ex} = -2J_{ex} S_1{*}S_2$, where J_{ex} is the exchange integral, arising from overlap of the wave functions of atomic electrons with spins S_1 and S_2.

Magnetic ordering is a complex phenomenon involving competing energies over different length scales.

For an example in the main magnetic characterization group, ferromagnetic and antiferromagnetic spin alignment is determined by the symmetry of the orbital wave function, resulting in a positive or negative sign of the exchange integral. Free electrons in metals can also couple via the exchange interaction. Net magnetic moment for free electrons is dependent on the exchange energy, the shift of the density of states for energy sub-bands with spins up and spins down, and the position of the Fermi level in these sub-bands. This approach can be generalized for a large number of ions by the same equation:

$$H_{ex} = -\sum 2J_{ex,ij}\, S_i{*}S_j \qquad (1.3.5)$$

where S_1 and S_2 are the spins of electrons 1 and 2, and J_{ex} is the exchange integral between wave functions of these two electrons.

Ferromagnetic alignment is obtained for $J_{ex} > 0$. In this case, H_{ex} has a minimum for $S_i * S_j > 0$, in other words when the spins are aligned in the same direction. Spontaneous ferromagnetic ordering is formulated by the Stoner criterion: $J_{ex} * Z(E_F) > 1$, which requires either a large exchange integral, J_{ex}, or a high Fermi density of states $Z(E_F)$ for ferromagnetism to be stable.

The consequence of the spin alignment due to the exchange interaction is that the material has a spontaneous magnetization giving a net magnetic moment per unit volume.

Transition metals present the peculiarity of having a high density of states at the Fermi level due to the 3*d* electron band.

As a result, the increase in kinetic energy is small compared to the exchange interaction, which has the net effect of reducing the total energy of the system and stabilizing ferromagnetism.

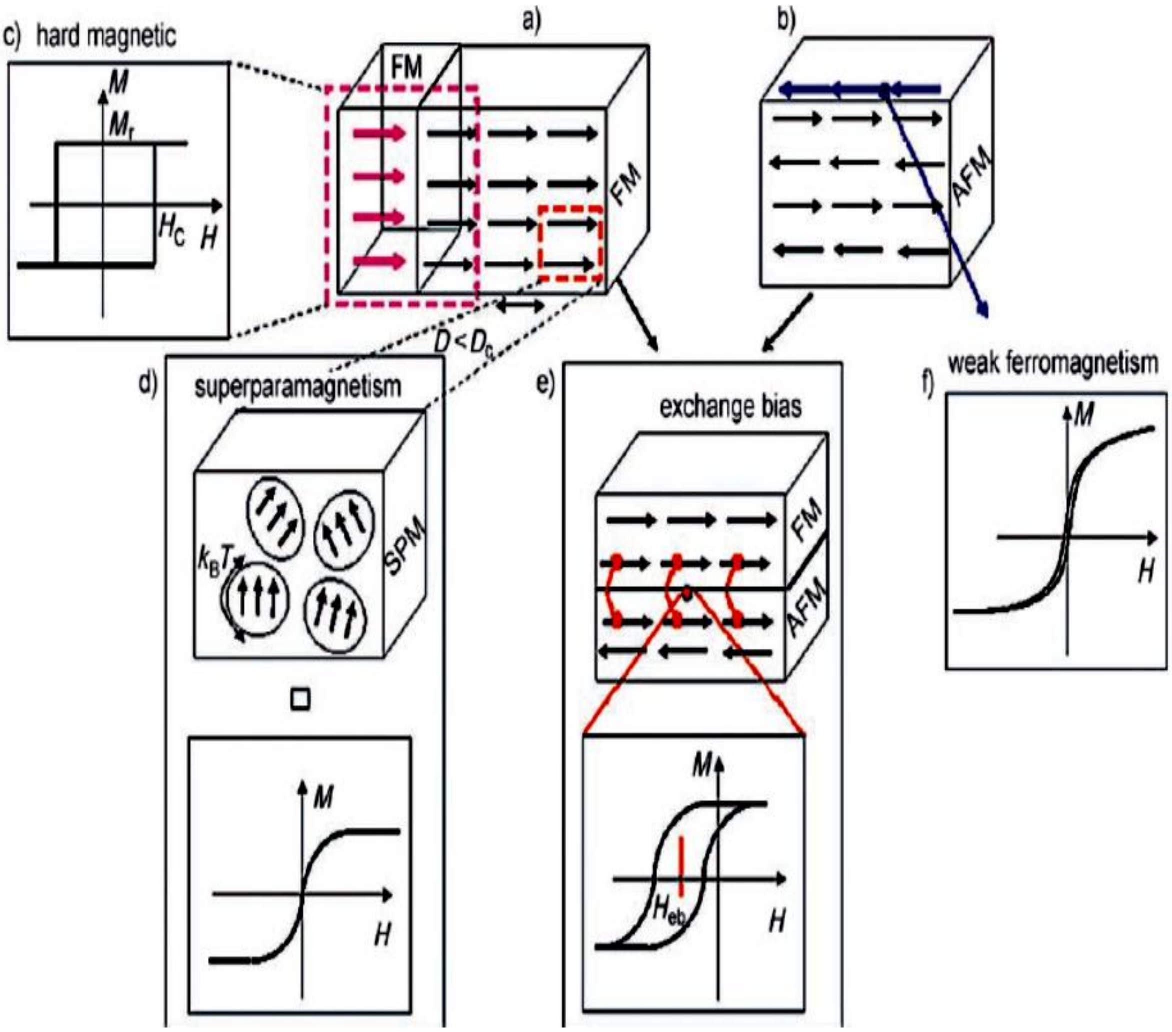

Figure 1.3.11: The different magnetic effects occurring in magnetic nanoparticles. Adopted from [31].

Figure 1.3.11 shows different magnetic effects and behaviour. The spin arrangement in (a) is that of a ferromagnet (FM) and in (b) an antiferromagnet (AFM). A combination of different ferromagnetic phases can produce permanent magnets, which are materials with high remanent magnetization (M_r) and high coercivity (H_C) (c), or superparamagnetic particles with giant magnetic moments, which are not interacting, and which can fluctuate when the thermal energy, k_BT, is larger than the anisotropy energy (d). The interaction (exchange coupling; linked red dots) at the interface between a ferromagnet and an antiferromagnet produces the exchange bias effect (e). Pure antiferromagnetic nanoparticles could exhibit superparamagnetic relaxation as well (f).[31]

1.3.6.1 Superparamagnetic behaviour

Macroscopic bulk size magnetic materials are assembled as multi-domains structures, where regions of uniform magnetization are separated by domain walls. Domains are magnetized in mutually different directions. The magnetic domains occur as a mechanism of minimization of the magnetic stray fields around a ferromagnetic sample. As the sample is broken down into magnetic domains, the volume occupied by stray fields is minimized because the magnetic flux is enclosed between neighbouring domains instead being spread all around the sample to reach the opposite magnetic pole.

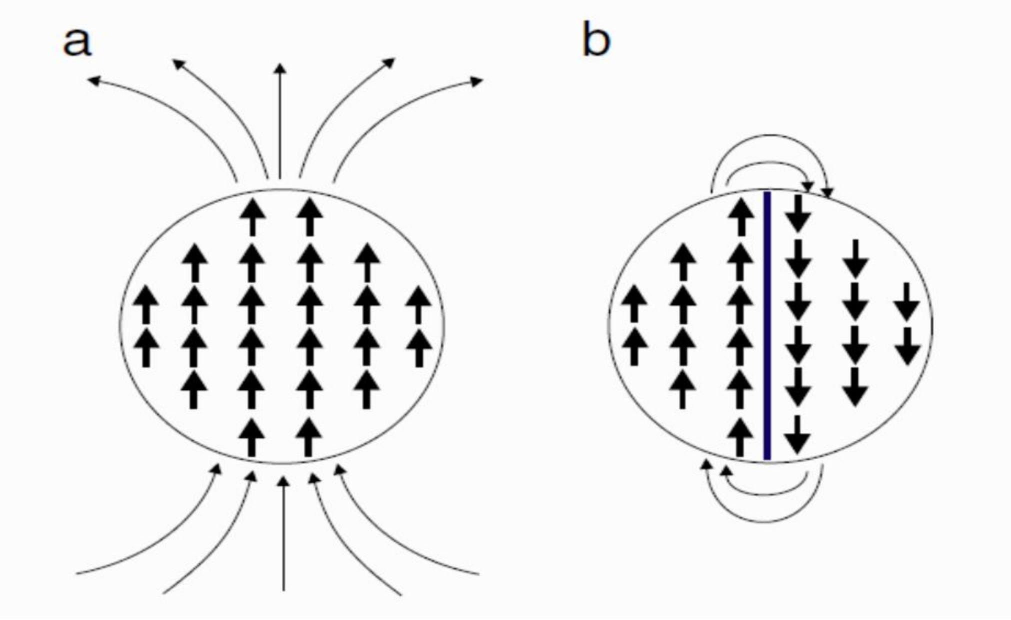

Figure 1.3.12 only one domain (single-domain state) and large stray fields, and (b) a system with two domains separated by a 180° domain wall and thus reduced stray fields. Adopted from [32].

This mechanism favours creation of as large a number of magnetic domains as possible. Each of the domains, however, is separated by a domain wall, a volume in which the direction of magnetization (i.e. electron spins) changes from one domain to the other. Because spins are not aligned perfectly with each other any more, the exchange energy increases in the domain wall. In addition to the exchange energy, the magnetic anisotropy energy increases in the domain wall, as well. The magnetic anisotropy occurs because of coupling of the spins to the orbital momentum of electrons. Because the direction of the vector of orbital momentum is defined by the crystal structure, the spins will also be oriented along well defined directions in the crystal.

The directions of spins for which the anisotropy energy is the lowest are called the easy axes of magnetization. Therefore, reorienting the spins in the domain walls also results in an increase in the anisotropy energy. While magnetic anisotropy favours domain walls that are as thin as possible, the exchange energy favours domain walls that are as thick as possible.

Consequently, an equilibrium thickness is obtained, for which the sum of the exchange and anisotropy energies is minimized. A domain wall, however, is always associated with an increase in energy. Because of that, the number of the magnetic domains is defined as the equilibrium between the decrease of the energy of magnetic stray fields around the sample and the increase of the domain wall energy.

This relationship becomes more complicated when the particle size is reduced. Particles can be decreased in size to a critical volume, below which creation of a domain wall costs more energy than to support the external (stray) field of the single-domain particle.

For a spherical particle, the critical diameter D_C, below which the particle exists in a single-domain state can be calculate by following formula:[32, 33]

$$R_C = 36\sqrt{AK}\ /\ \mu_O M_S^2 \qquad (1.3.6)$$

Where A is the exchange constant, K is the anisotropy constant, μ_O is the vacuum permeability, and M_S is the saturation magnetization. A single-domain particle has all the spins aligned in the same direction, except for the surface layer, where misalignments are possible due to surface atoms not having the same number of neighbours as the atoms deeper in.

Single-domain small particles are energetically more favourable and become more stable with smaller particle size. The magnetic anisotropy energy of a single-domain particle can be expressed by the equation

$$E(\theta) = K\,V \sin^2\theta \qquad (1.3.7)$$

where V is the particle volume, K the anisotropy constant of the material , and θ is the angle between the magnetization and the easy axis of magnetisation. The product $K\,V$ is called the anisotropy energy, and it represents the energy barrier between two energetically equivalent easy directions of magnetization. For uniaxial anisotropy, these directions correspond to $\theta = 0°$ or 180°, both having zero anisotropy energy.

By applying a magnetic field along the easy axis of magnetization, however, one direction becomes energetically more favourable than the other. Potential energy becomes less in the applied field direction and can be expressed by extension of the previous equation:

$$E(\theta) = KV\sin^2\theta - \mu_0 H \cos(\Phi - \theta) \qquad (1.3.8)$$

where θ is the angle between magnetic moment and anisotropy axis and Φ the angle between the applied field and the anisotropy axis.

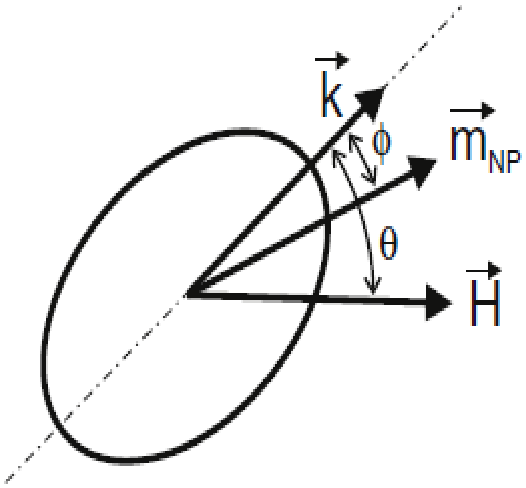

Figure 1.3.13: Schematic drawing supporting the argument on the effect of magnetic field on the anisotropy energy of a nanoparticle. Adopted from [32].

With decreasing particle size, the energy of anisotropy $K V$ decreases, too, and the thermal energy k_BT can easily switch the magnetization direction. In the case of $k_BT > K V$, the system behaves like a paramagnet, by analogy with paramagnets where single atom spins fluctuate due to thermal excitations.

Superparamagnetic particles have a very large magnetic moment (super) inside each particle, and in comparison with paramagnetic materials, the magnetic moment of the nanoparticle fluctuates as a whole. Because of the large moment of the nanoparticle, a system of nanoparticles whose magnetic moments can randomly fluctuate between the equilibrium directions by thermal excitations is called a superparamagnetic system.

The thermally exited fluctuations of the superspin directions or the relaxation time of the moment of a superparamagnetic particle has a characteristic relaxation time, $\tau = (f2\pi)^{-1}$

The relaxation time of the moment of a particle, τ, is given by the Néel-Brown expression [34, 35, 36], following the Arrhenius type of activation law:

$$\tau = \tau_0 \exp\left(\frac{KV}{k_BT}\right) \tag{1.3.9}$$

where k_B is the Boltzmann constant, and the pre-factor $\tau_0 \approx 10^{-9}$ s. The fluctuation of the particle magnetic moment is strongly controlled by the temperature. At high temperatures, the magnetic moments will rapidly fluctuate. The opposite situation occurs at low temperatures, where magnetic moments appear to remain in the blocked (frozen-in) state. The characteristic temperature separating these two regimes is called the blocking temperature, T_B.

The blocking temperature depends on the volume of the particles, the effective anisotropy constant, the applied external magnetic field, and the experimental measuring time, τ_{exp}. T_B can be calculated with the same formula as for the relaxation time,

$$\tau_{exp} = \tau(T_B) = \tau_0 \exp\left(\frac{KV}{k_B T_B}\right) \rightarrow T_B = KV / k_B \ln(\tau_{exp}/\tau_0) \qquad (1.3.10)$$

For example, the difference in relaxation time between 300 K and 5 K can be around 27 orders of magnitude ($\tau \approx 10^{-9}$ s at 300 K, and 10^{18} s at 5K). To summarize, for $T < T_B$ the superspins will appear blocked or frozen, while for $T > T_B$ they will be freely fluctuating due to thermal excitations, similar to a paramagnetic system.

Most nanoparticles will interact with each other through their magnetic moments. Some of them will exhibit a strong interparticle interaction, while for others this interaction is negligible.Different magnetic interactions between nanoparticles strongly affect superparamagnetic relaxation characteristics.

The superparamagnetic phenomena can be classified into four different groups depending on behaviour of the relaxation time, τ: [35]

(1) Superparamagnetism (SPM)

$$\tau = \tau_0 \exp\left(\frac{KV}{k_B T}\right) \qquad (1.3.11)$$

(2) Glass-like freezing

$$\tau = \tau_0 \exp \left(\frac{\Delta E}{k_B(T - T_o)}\right) \tag{1.3.12}$$

(3) Superspin glass (SSG)

$$\tau = \tau_0 \left(\frac{T - T_g}{T_g}\right)^{-zv} \tag{1.3.13}$$

(4) Superferromagnetism (SFM)

$$\tau = \tau_0 \left(\frac{T - T_c}{T_c}\right)^{-zv} \tag{1.3.14}$$

The first case (Eq. 1.3.11) is characterized by the independent, individual behaviour of the single particles.

With increasing interaction between particles, their behaviour becomes more collective in glass-like freezing of the superspins (Eq. 1.3.12). The Néel-Brown law is modified by adding a “glass temperature”, T_0, in a starting formula, and ΔE is modified by an effective contribution of the interparticle interactions.[35, 37]

For even stronger interactions in correlation with closer distances between particles, their behaviour can be described as a superspin glass (Eq. 1.3.13), which occurs below the transition temperature, T_g. In the formula for the super spin glass, the relaxation time has two critical exponents, z and υ, where υ is the critical exponent of the correlation length, $\zeta \approx ([T\text{-}T_g]/T_g)^{-\upsilon}$, and the exponent z relates the relaxation time to the correlation length via $\tau \approx \zeta^z$.[38, 39, 40, 41, 42, 43]

In the last case, when the interaction is so strong that dipolar interactions of nanoparticles arrange themselves in a spatially ordered system, the system is then termed a superferromagnet (Eq. 1.3.14).

1.3.6.2 Surface Effects

As mentioned before, with decreasing particle size, a large percentage of all the atoms in a nanoparticle are surface atoms. Surface and phase boundary effects become very important, and different physical conditions occur from atoms in bulk or large crystals. The surface spins make an important contribution to the magnetization.

This local breaking of the symmetry can change the band structure, lattice parameters, and coordination of atoms. For example, some such effects are surface anisotropy and core–surface exchange anisotropy.

1.3.6.3 ZFC & FC curves

The experimental value of blocking temperature T_B can be obtained by DC magnetometry measurements, in which a zero-field-cooled and field-cooled procedure is employed.

Briefly, in zero field cooling (ZFC) mode, the sample is cooled from room temperature to the minimum temperature without applied magnetic field, and then a field is applied, and the temperature is gradually increased as the sample properties are measured.

In the field cooling process (FC), a magnetic field is applied during the cooling to the same minimum temperature, and sample properties are measured upon warming up.As the temperature gradually increases, the thermal energy excites magnetic moments, occasionally providing enough energy to align their direction with the external field direction.

The numbers of unblocked moments aligned in the field direction reach the maximum value at T_B. Above the blocking temperature, the thermal energy is strong enough to randomize themagnetic moments, leading to a decrease in magnetization.

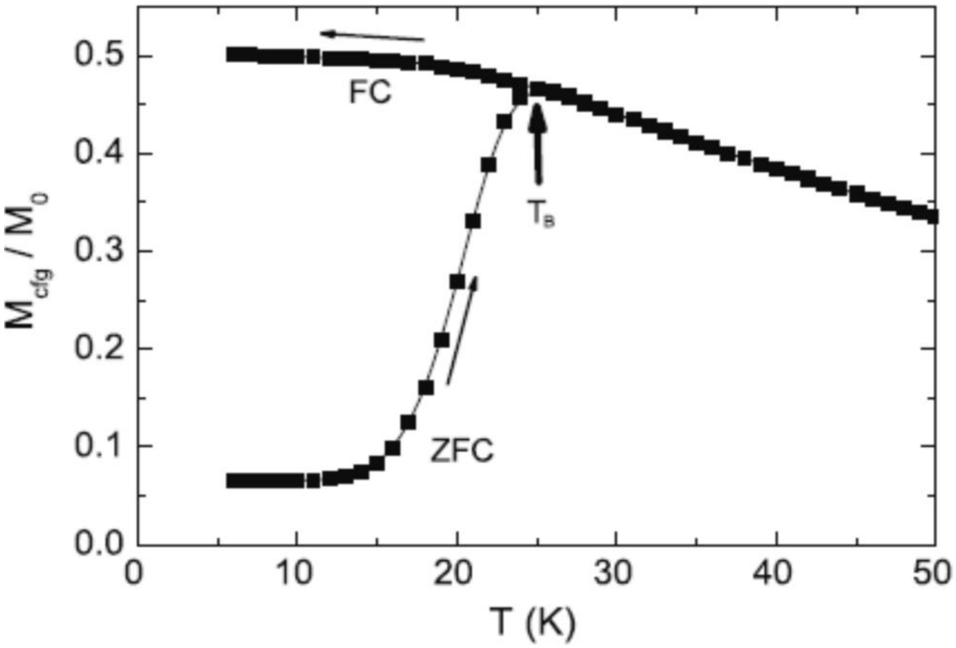

Figure 1.3.14: Magnetization curve after zero-field cooling, M_{ZFC} (T), and after field cooling, M_{FC} (T). Adopted from [32].

Figure 1.3.14 shows zero-field cooled (ZFC) and field cooled (FC) magnetization versus temperature curves for nanoparticles.

The blocking temperature is defined as temperature of maximum magnetization for the ZFC curve. The ZFC and FC curves often do not overlap above T_B, because there is still a significant interaction between the unblocked nanoparticles, even at elevated temperatures.

1.3.7 REFERNCES

1 G. E. Moore, Electronics, Volume 38, Number 8, April 19, 1965

2 R. P. Feynman, Engineering and Science magazine, vol. XXIII, no. 5, February 1960

3 M. Hosokawa, K. Nogi, M. Naito, T. Yokoyama, Nanoparticles Technology Handbook, Elsevier, p. 6, 2007.

4 Encyclopaedia Britannica, Britannica.com (2005b) Nanotechnology

5 C. Nützenadal, A. Züttel, D. Chartouni, G. Schmid, and L. Schlapbach, Eur. Phys. J.D8, 245, 2000.

6 A.W. Adamson and A.P. Gast, Physical Chemistry of Surfaces, 6th edition, John Wiely & Sons, New York, 1997.

7 G. Cao, Nanostructures and nanomaterials, Imperial collage press, p. 17, 2004.

8 A.N. Goldstein, C.M. Echer and A.P. Alivisatsos, Science 256, 1425, 1992.

9 P.C. Hiemenz, Principles of Colloids and Surface Chemistry, Marcel Dekker, New York, 1977

10 G.D. Parfitt, in Dispersion of Powders in Liquids with Special References to Pigments, Applied Science, London, 1981

11 M.J. Stowell, T.J. Law and J. Smart: Proc. Roy. Soc.London A, 318, 231–241, 1970.

12 Y. Kurokawa, Y. Hosoya: Surface, 34 (2) 100–106, 1996.

13 K. Kobayashi: J. Soc. Powder Technol., Jpn, 41, 473–478, 2004.

14 K. Ishikawa, K. Yoshikawa and N. Okada: Phys. Rev. B, 37, 5852–5855, 1988.

15 K. Niihara: J. Ceram. Soc. Jpn, 99 (10), 974–982, 1991.

16 T. Sekino: Mater. Integr., 13 (11) 50–54, 2000.

17 F. Wakai, Y. Kodama, S. Sakaguchi, N. Murayama, K. Izaki and K. Niihara: Nature, 344, 6265, 421–423, 1990.

18 A.W. Weeber, H. Bakker, Amorphization by ball milling, Physica B: Condensed Matter Volume 153, Issues 1–3, October 1988, Pages 93–135

19 S. P. Pramod Versatility of chemical spray pyrolysis technique, Materials Chemistry and Physics Volume 59, Issue 3, 15 June 1999, Pages 185–198

20 T. Leblanc, R. Andlauer and J-P. Chabrerie, Plasma Sources Sci. Technol. 10, 10-16,2001.

21 G. Jiayin, G. Jiayin, F. Xiaobao, R. Dolbec, X. Siwen, J. Jurewicz and M. Boulos, Plasma Sci. Technol. 12 188, 2010.

22 T. Guo, P. Nikolaev, D. Rinzler, D.T. Tomanek, D.T.Colbert, "Self-Assembly of Tubular Fullerenes". J. Phys. Chem. 99 (27): 10694–7., 1995

23 R. Suriano, A. Kuzntsov, S.M. Eaton, R. Kiyan, G. Cerullo, R. Osellame, B.N. Chichkov, M. Levi, S. Turri, Applied Surface Science 257, 6243-6250, 2011.

24 K. P. Lopes, L. S. Cavalcante, A. Z. Simoes, R. F. Goncalves, M. T. Escote, J. A. Varela, E. Longo, E. R. Leite, Journal of Sol-Gel Science and Technology, Vol. 45,151-155, 2008.

25 C. Barbe, J. Bartlet, L. Kong, K. Finnie, H. Q. Lin, M. Larkin, S. Calleja, A. Bush, G. Calleja, Silica Particles for Drug Delivers, Adv. Mater. 16, No.20, 2004.

26 N. Zhao et al. Key Engineering Materials Vols. 288-289, pp 179-182, 200527

27 H. Yan, X. Xie, K. Liu, H. Cao, X. Zhang, Y. Luo, Facile preparation of Co_3O_4 nanoparticles via thermal decomposition of $Co(NO_3)_2$, Volume 221, Pages 199–202, 2012.

28 S. Navaladian, B. Viswanathan, R. Viswanath, T. Varadarajan, Thermal decomposition as route for silver nanoparticles, Nanoscale Research Letters, 2:44-48, 2006.

29 P. D. Patnaik, Analytical Chemistry Handbook, 2nd ed. McGraw-Hill, 2004.

30 A. M. Davarpanah, A.A. Mirzae, M. Sargazi and M. Feizi, Journal of Physics: Conference Series 126, 2008.

31 F. Schüth, A.-H. Lu, and E. L. Salabas, Magnetic Nanoparticles: Synthesis, Protection, Functionalization, and Application, Angew. Chem. Int. Ed., 46, 1222 – 1244, 2007

32 O. Petracic, Superparamagnetic nanoparticle ensembles, Superlattices and Microstructures 47,569-578, 2010

33 S. Blundell, Magnetism in Condensed Matter, Oxford University Press, 2001.

34 L. Néel, Ann. Geophys. 5, 99, 1949.

35 J. L. Dormann, D. Fiorani, E. Tronc, Adv. Chem. Phys. 98, 283. 1997.

36 X. Batlle, A. Labarta, J. Phys. D 35, R15, 2002

37 J.A. Mydosh, Spin Glasses: An Experimental Introduction, CRC Press, 1993.

38 J.J. Binney, N.J. Dowrick, A.J. Fisher, M.E.J. Newman, Theory of Critical Phenomena, An Introduction to the Renormalization Group, Oxford University Press, 1992.

39 O. Petracic, W. Kleemann, Ch. Binek, G.N. Kakazei, Yu.G. Pogorelov, J.B. Sousa, S. Cardoso, P.P. Freitas, Phase Trans. 75, 2002.

40 S. Sahoo, O. Petracic, Ch. Binek, W. Kleemann, J.B. Sousa, S. Cardoso, P.P. Freitas, Phys. Rev. B 65 134406., 2002.

41 O. Petracic, S. Sahoo, Ch. Binek, W. Kleemann, J.B. Sousa, S. Cardoso, P.P. Freitas, Phase Trans. 76, 367. 2003.

42 S. Sahoo, O. Petracic, W. Kleemann, P. Nordblad, S. Cardoso, P.P. Freitas, Phys. Rev. B 67, 214422. 2003.

43 S. Sahoo, O. Petracic, W. Kleemann, S. Stappert, G. Dumpich, P. Nordblad, S. Cardoso, P.P. Freitas, Appl. Phys. Lett. 82, 4116, 2003

Chapter 2: Experimental Techniques

2.1 Chemical Laboratory Work

The equipment for producing nanoparticles required an enclosed system protected from air (oxygen). The entire system was assembled in a fume cupboard for protection from reactive and dangerous gases such as hydrogen and other dangerous goods.

Handling the chemical equipment and chemicals required the greatest caution and a strong chemical background. The system was assembled from a three-neck flask, an additional funnel, a Liebig condenser, and drying tubes and junctions.

During the experiment, the whole system was under inert argon atmosphere. Stirring equipment with a heater is shown below the three-neck flask in Fig. 2.1 for regulation of the stirring speed and the temperature of the solution.

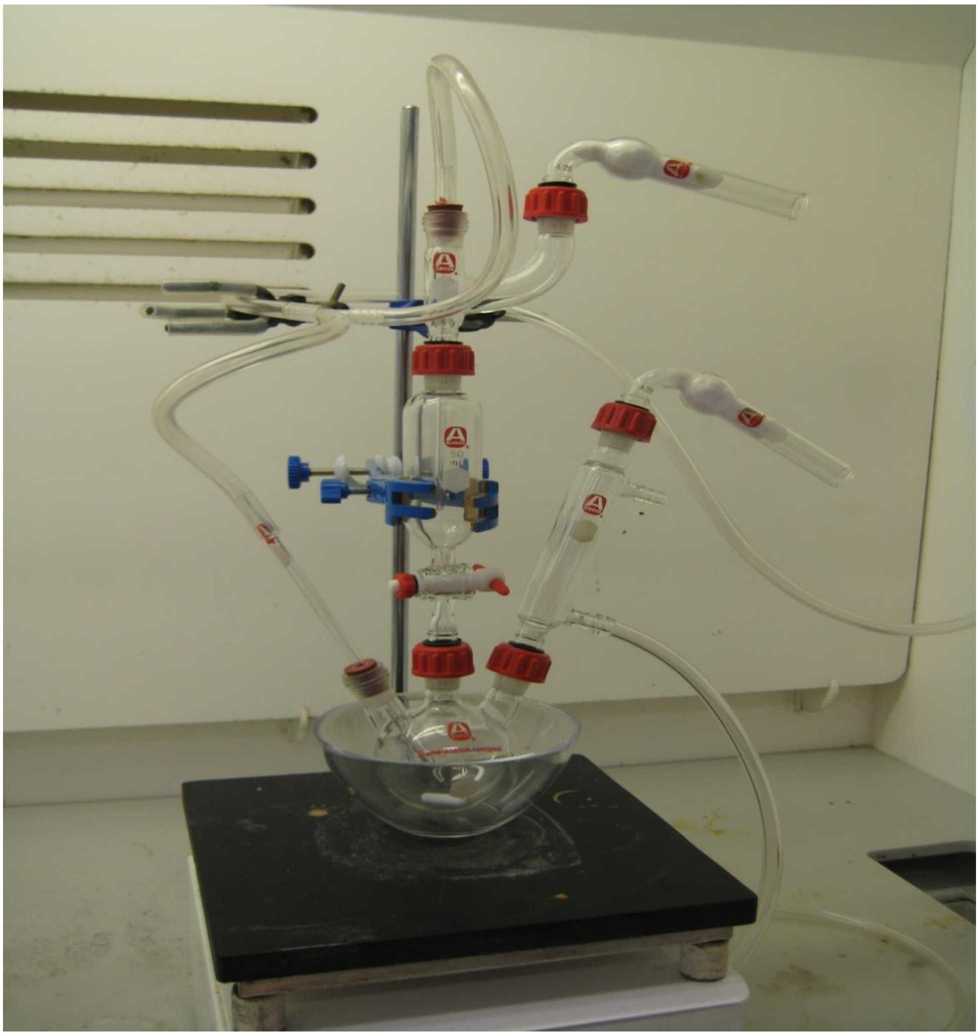

Figure 2.1: Air sensitive chemical equipment for producing nanoparticles.

2.2 Planetary Ball-Milling

Planetary ball mills are simple tools that are used for preparing fine powders from larger size starting samples. In the planetary mill, the grinding bowls rotate on their own axis while simultaneously rotating through an arc around the central axis. The grinding bowls and material are thus subjected to centrifugal forces, which constantly change in direction and intensity, resulting in efficient, fast grinding processes.

By grinding and crushing, the samples are effectively comminuted. The geometries and speed ratios allow optimum movement of the grinding balls. The grinding balls rotate against the inside wall of the bowl, until under specific conditions, they break away from it. The maximum speed of ball mills is approximately 1100 rpm. Powders obtained from the ball mill usually have large size distribution. Ball mills can be operated in a glove box under protected atmosphere, as shown in Figure 2.2.

Figure 2.2: Ball mill in protective glove bag.

2.3 Preparation of Bulk and Wire MgB_2 Samples and Nanoparticles

The samples discussed later are pure and doped MgB_2 bulks and wire samples, which were prepared from Mg and B via in situ reaction. Because of variation in the annealing process, details will be provided in each of the following Chapters 3-5.4. The nanoparticles were prepared by a wet chemical technique, and all detailed descriptions are provided in section 3.

2.4 X-ray Diffraction (XRD)

X-ray diffraction (XRD) was used to study the phase formation, and the obtained patterns were evaluated to investigate the phases, microstrains, lattice parameters, and grain sizes of the samples. X-ray diffraction was performed in the step-scanning mode θ - 2θ by using a Philips PW1730 diffractometer with a Cu-Kα radiation source (λ = 1.5418 Å).

Typically, diffraction data was collected from 10° – 105° in a step width of 1° and counting time per minute. The incident x-rays are reflected by the crystal plane at angle θ with respect to the incident ray. Consequently, a reflected ray is generated at an angle 2θ from the incident beam. In the θ - 2*θ* configuration, the X-ray tube is fixed, and the sample is moved by θ while the collector is moved by 2*θ* simultaneously, as shown in Figure 2.3 below.

Diffraction will occur whenever Bragg's Law is satisfied:

$$n\lambda = 2d \sin\theta \qquad (2.1)$$

where, n is an integer, λ=wavelength, d = lattice spacing, θ = angle.

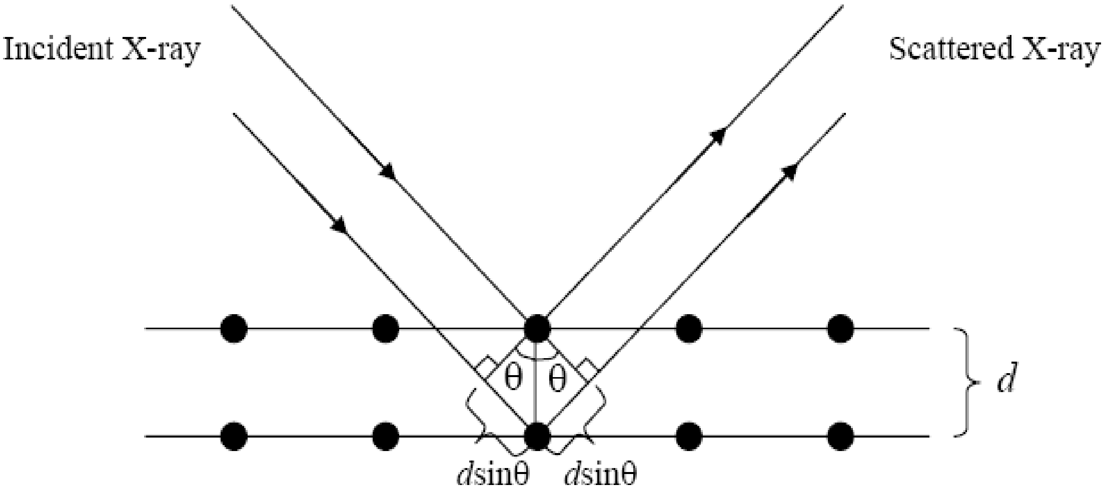

Figure 2.3: X-ray diffraction in θ - 2θ configuration taken from reference. Adopted from [1].

XRD patterns were used to calculate the lattice parameters of samples using the Rietveld refinement method and Full Prof as additional software. Phase analysis was conducted with TRACES™ software.

2.5 Differential Thermal Analysis (DTA)

Differential thermal analysis (DTA) is defined formally as a technique for recording the difference in temperature between a substance and a reference material against either time or temperature as the two specimens are subjected to identical temperature regimes in an environment heated or cooled at a controlled rate.

Fluctuations in the sample which lead to the absorption (endothermic) or release (exothermic) of heat can be detected relative to the inert reference. A schematic diagram is shown in Figure 2.4. From DTA, the martial decomposition with temperature and time can be computed. The crucibles used were alumina, and the sample mass was in the range of 50 mg. The system has a temperature ramp rate range of 0.1 to 50°C/min. Argon gas was used for all the results presented, with a constant flow rate of 50 ml/min. The maximum operating temperature is 1200°C.

The baseline of the DTA curve should then exhibit discontinuities at the transition or reaction temperatures, as shown in Figure 2.5, and the slope of the curve at any point will depend on the microstructure at that temperature.

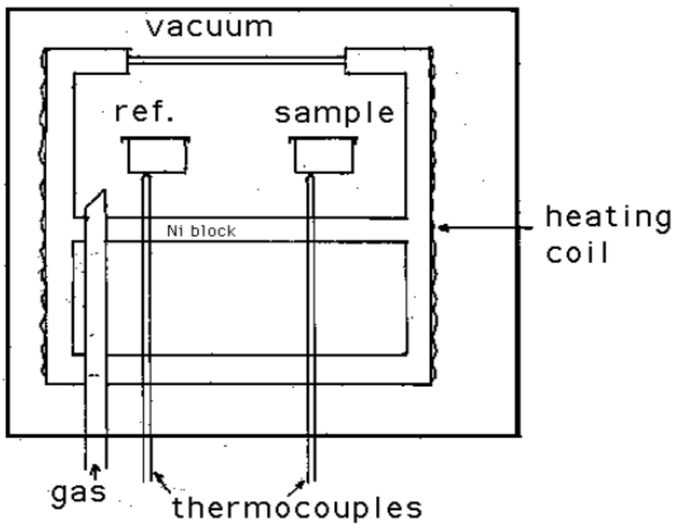

Figure 2.4: Schematic illustration of a DTA cell. Adopted from [2].

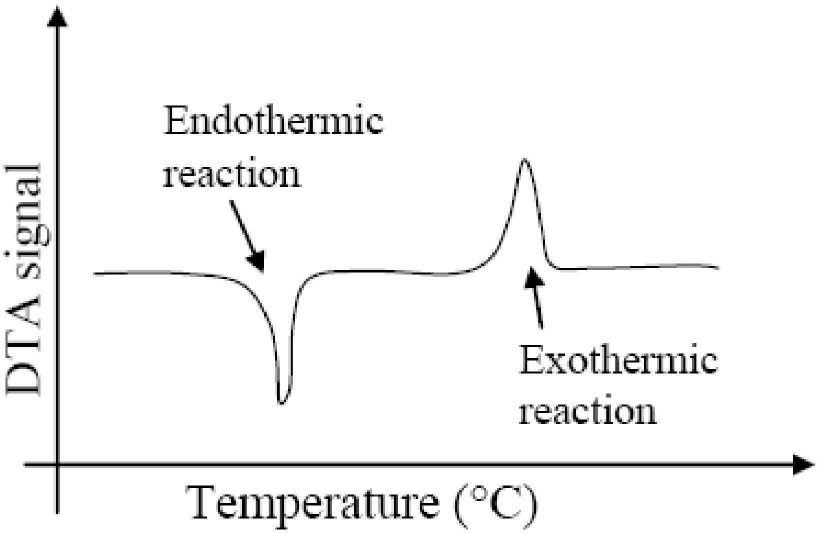

Figure 2.5: A typical DTA result for a sample with endothermic and exothermic reactions. Adopted from [2].

2.6 Scanning electron microscopy (SEM), Energy dispersive X-ray spectrometry (EDS)

In this work, two kinds of facilities were used: a JOEL 2011 analytical electron microscope with JOEL EDS system at the University of Wollongong, Australia and a Phillips CM 200 Field Emission Gun Transmission Electron Microscope at the University of New South Wales, Australia. The scanning electron microscope (SEM) was used to investigate the microstructure, morphology, and chemical compositions of the samples. The SEM uses a focused beam of high-energy electrons to generate a variety of signals at the surface of solid specimens. The SEM unit is also capable of analysis, qualitatively determining chemical compositions (using energy dispersive X-ray (EDX) analysis).

2.7 Measurements of T_c, J_c, H_{c2}, H_{irr}

Electromagnetic properties such as the critical temperature (T_c), the critical current density (J_c), and the critical fields (H_{c2} and H_{irr}) of the superconducting material were measured using a Quantum Design physical properties measurement system (PPMS).

The transport critical current, I_c, measurements were conducted by the standard four-point probe method with the criterion of 1μV/cm. J_c was obtained by dividing I_c by the cross section of the MgB_2 core.

2.7.1 Critical temperature (T_c)

T_c of superconducting materials can be determined by using a) the resistance measurement, or b) the magnetic AC susceptibility measurement. Both of these measurements were carried out on a Quantum Design PPMS.

The resistance measurement requires the sample to be contacted with four leads. The two outer leads are for current and the two inner leads are for voltage, which also can determine the resistivity of MgB_2 samples from room temperature to superconducting temperature by using this method, with sensitivity up to 1μΩ.

In the second method, T_c is defined as the onset of diamagnetism by measuring the real part of the ac susceptibility, with a sensitivity of up to 10^{-8} emu.

2.7.2 Critical current density (J_c)

The critical current density (J_c) can be determined by a) the transport method (J_{ct}) or b) the DC magnetization method (J_{cm}).

The critical current, I_c, was measured by a conventional four point-probe resistive method at 4.2 K in magnetic field below 18 T. Current leads and voltage taps were directly connected to the sheath materials of the wire.

The maximum current of the power supply was 300 A, and a nano-voltmeter was used to detect the signal of the sample. A magnetic field was applied parallel to the wire. The criterion of I_c definition was 1 μV/cm. The transport critical current density, J_{ct}, was calculated by dividing I_c by the cross-sectional area of the MgB_2 core.

DC magnetization was measured by using the Quantum Design PPMS. The sample is moved in a constant magnetic field, and the waveform signal from the sample is detected by the detection coil. Magnetic hysteresis loops were collected over a temperature range of 5 to 30 K in a time-varying magnetic field with sweep rate 50 Oe/s and from 0 to 10 T. J_c can be calculated from the measured magnetic hysteresis loop based on the Bean Model[3,4], as shown below.

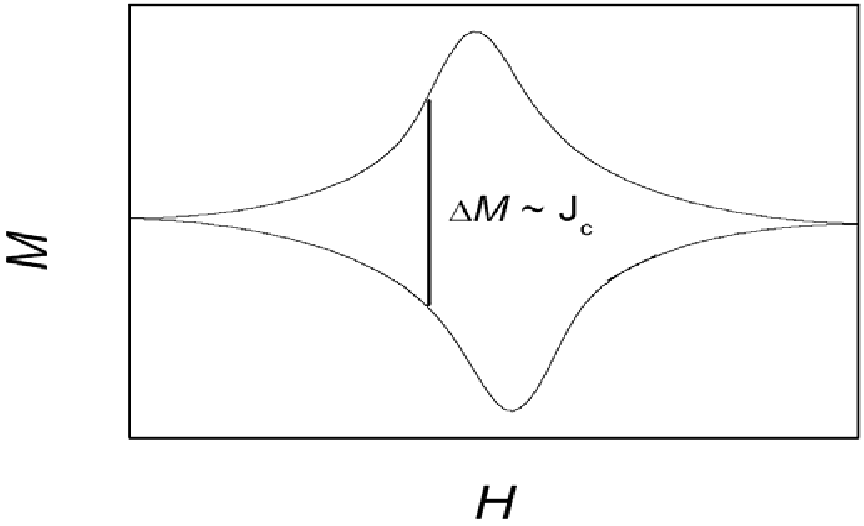

Figure 2.6: Schematic diagram of magnetic hysteresis loop of a superconductor showing the width of the magnetic hysteresis loop ΔM. Adopted from [3].

$J_{cm}=20\,\Delta M/[a(1-a/3b)]$

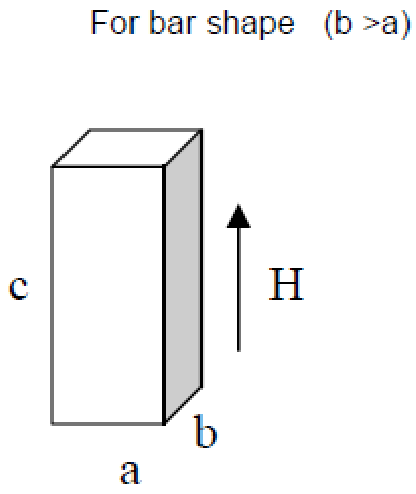

Figure 2.7: Rectangular shaped bulk sample with field direction. Adopted from [3,4].

With bar samples, a, b and c are the dimensions of sample in cm. J_{cm} and ΔM, the width of the hysteresis loop are in A/cm^2 and in emu/cm^3, respectively. Bar shaped samples (3 x 2 x 1 mm^3) and wire shaped samples (c = 200 mm, a = 0.8-0.9 mm) were cut from each pellet or peeled out from the wire for magnetic measurements. The low field J_{cm} below 10 K could not be measured due to flux jumping.

The upper critical field (H_{c2}) and the irreversibility field (H_{irr}) were determined using a resistivity versus temperature plot, which was collected in the Quantum Design PPMS up to 13 T. The H_{c2} and H_{irr} were obtained by measuring the temperature at which the normal state resistivity of the sample dropped by 90% and 10%, respectively.

2.8 REFERENCES

1 B. D. Cullity, and S. R. Stock, Elements of X-Ray Diffraction 3rd. ed. 187, 2001.

2 H. K. D. H. Bhadeshia, Steels: Microstructure and Properties 2nd ed Lightning Source Inc., 1971.

3 C. P. Bean, Magnetization of High-Field Superconductors, Rev. Mod. Phys. 36, 31, 1962.

4 J. Horvat, W. K. Yeoh, J. H. Kim, and S. X. Dou, Supercond. Sci. Technol. 21 065003, 2008.

CHAPTER 3: SYNTHESIS OF NANOPARTICLES

3.1 Introduction

Magnetic nanoparticles have received considerable attention as they pose the intriguing questions about the behaviour of matter on such a small scale and because they reveal processes that are not observable in the macroscopic world. They are the subject of intense research in many disciplines, such as material science, biomedicine, biotechnology, etc.

Magnetism in nanoparticles is strongly affected by the large surface-to-volume ratio of the nanoparticles. More striking is the possibility of observing quantum tunnelling of magnetization, as an additional process of the nanoparticles flipping their magnetic moment besides the classical thermal activation.[1]

The composition of the particles affects their basic magnetic properties and allows the tuning of interactions that control magnetic ordering. Numerous different synthesis techniques give a broad variety of particle structures with more or less narrow particle size distributions.

Synthesis routes will be described for the production of Fe_2B nanoparticles, both uncoated and coated in SiO_2, as well as coated FeCoB nanoparticles ($Fe_xCo_{2-x}B$). Furthermore, the synthesis of new nanoparticles will be described: NiCoB and NiCoB coated with SiO_2.

This work was a part of a broader project jointly conducted by the superconductivity groups at ISEM (University of Wollongong) and the Department of Physics (University of Zagreb). The PhD candidate was enrolled as an off-shore PhD student at the University of Wollongong, when conducting his research at the University of Zagreb. This took about half of his PhD candidature. His main tasks at the University of Zagreb were development of ways to grow magnetic nanoparticles suitable for doping into MgB_2, as well as finding the best ways for making MgB_2 wires doped with these nanoparticles. Physical characterization of the samples made in Zagreb was performed by collaborators in Zagreb: Nikolina Novosel and Stipe Galić.

In the second half of his candidature at the University of Wollongong, the candidate expanded his work to preparation procedures for the most promising magnetic nanoparticles, namely, NiCoB: finding the best methods for growing MgB_2 bulk samples doped with NiCoB and studying the effects of doping with these nanoparticles on MgB_2 properties, as well as explaining the mechanisms of improvement of the critical current density (J_c) by these nanoparticles. Additional work was done on silver nanoparticles and silver coated with graphene oxide.

The work described in this thesis draws mainly on the results obtained at the University of Wollongong (Chapters 3.5, 3.6, 5.1, 5.2, 5.3, 5.4). The work at the University of Zagreb, however, provided essential background, on the basis of which, the work at Wollongong was conducted. Because of this, an overview of the nanoparticles and the MgB_2 samples that the candidate prepared is given in Chapters 3 and 4, together with the properties of MgB_2 wires doped with these nanoparticles. Due reference is given to any work done by collaborators in Zagreb.

3.2 Nanoparticle characterization procedures

Nanostructure was studied using scanning electron microscope (SEM) imaging conducted with a JEOL JSM7500FA microscope, a cold field emission gun SEM (FEGSEM).

The obtained samples were examined at room temperature by X-ray powder diffraction (XRD) using an automatic Philips diffractometer, model PW1820 (Cu-Kα radiation, graphite monochromator, proportional counter), in Bragg-Brentano geometry. The diffraction intensities were measured in the angular range $10° \leq 2\theta \leq 70°$. The step size was set to 0.02° 2θ with measuring time of 2 s per step. Magnetization measurements on nanoparticles were performed using a commercial Quantum Design MPMS5 magnetometer equipped with superconducting quantum interferometer device (SQUID) technology. Magnetic hysteresis loops, M(H), were measured in the field range ±5 T at the temperatures of 5 and 290 K. The temperature dependence of magnetization $M(T)$ for the temperature range of 5−300 K was studied in different applied magnetic fields H was measured in two modes: zero field cooling (ZFC curves) and field cooling (FC curves), with the same field as that used for measurement. Both the ZFC and the FC data were measured upon warming the sample.

Assuming that the obtained particles are single domain, the Stoner-Wohlfarth model[3,4] enables us to calculate the anisotropy energy density $K = MH/2h$ from hysteresis loops, where for M, M_{5T} is used at 5 K, which is close to the saturation magnetization. According to the Stoner-Wohlfarth calculations $h = 0.5$ should be used for samples of randomly oriented magnetic spheroids if $H = H_c$ is taken. The values for K obtained in this way are presented in Table 3.1.

3.3 Fe_2B, Fe_2B/SiO_2, and FeCoB nanoparticles

3.3.1 Synthesis of Fe_2B, Fe_2B/SiO_2, and FeCoB

Amorphous nanoparticles of Fe-2B and Fe-Co-B were obtained by reduction of aqueous solutions of metallic salts of $FeSO_4$ and $CoCl_2$ with $NaBH_4$ solution. The experiments were performed with different reactants based on the procedure known to be efficient for amorphous particle production: 0.1 M solution of $FeSO_4$ or $CoCl_2$, 1.0 M solution of $NaBH_4$ or KBH_4, quantity ratio of $FeSO_4$ to $NaBH_4 \geq 0.6$ (1:1 used here), and reaction temperature $\leq$ 279 K.[4]

Fe-2B particles coated with SiO_2 were prepared using1.0 M $NaBH_4$ solution, which was added rapidly with stirring to the solution of 0.1 M $FeSO_4$. The volume ratio of the main reactants was 1:1 (70 ml of each was used). After adding $NaBH_4$, 70 ml of 96% ethanol was added immediately, which contained 1.5 ml tetraethoxysilane (TEOS) and 2 ml 0.4 M NH_4OH. To produce the particles without SiO_2 coating, the ethanol solution of TEOS was omitted. To prepare the particles of Fe-Co-B coated with SiO_2 the same quantities of 0.1 M solution of $CoCl_2$ and 0.1 M solution of $FeSO_4$ were added to the 1.0 M solution of $NaBH_4$ so that the quantity ratio of $CoCl_2$ and $FeSO_4$ to NaBH4 was ≥ 0.6.

The syntheses were performed in a closed system with argon atmosphere, and the solutions were bubbled with argon for one hour prior to the synthesis and one hour after the mixing of the solutions. A black powder was collected and washed with distilled water to remove residual ions, and then it was rinsed with acetone to remove water and finally dried in vacuum. Several syntheses, differing in the duration of the reaction, the contents and concentrations of the components, and the reaction temperatures, were performed.

The expected chemical reaction to form the core of the Fe_2B particles is based on reduction of metal ions by sodium borohydride, according to the following chemical equation:

$$4FeSO_4 + 8NaBH_4 + 18H_2O \rightarrow 2Fe_2B + 6B(OH)_3 + 25H_2 + 4Na_2SO_4 \qquad (3.1)$$

In the presence of oxygen during the reaction process the oxidation of Fe_2B into elementary α-Fe is possible:

$$4Fe_2B + 3O_2 \rightarrow 8Fe + 2B_2O_3 \qquad (3.2)$$

$$4FeSO_4 + 8NaBH_4 + 18H_2O + CoCl_2 \rightarrow FeCoB + 25H_2 + 4Na_2SO_4 + 2NaCl \qquad (3.3)$$

3.3.2 XRD analysis

X-ray diffraction (XRD) patterns of the samples are shown in Fig. 3.1. In the pattern of the Fe_2B+SiO_2 sample (middle curve, red trace), two broad maxima centred at $2\theta \approx 28°$ and $2\theta \approx 45°$ were observed; their broadness indicates the amorphous state. The position of the broad maximum centred at $2\theta \approx 45°$ corresponds to the strongest diffraction line of the (211) plane of crystalline Fe_2B, whereas the broad maximum around 28° probably arises from amorphous silica. Several rather sharp maxima were also detected, belonging to a crystalline SiO_2 (probably cristobalite) phase, present in traces.

These maxima are most likely associated with precipitated (ellipsoidal) pure SiO_2 particles and not with shells of magnetic particles. The blue trace in Figure 3.1 (lower curve) shows the XRD pattern of SiO_2 coated $Fe_XCo_{2-X}B$ particles. The alloy was in the amorphous state, which is clearly indicated by two broad maxima centred at $2\theta \approx 28°$ and $\approx 45°$. No crystalline peaks were present in this pattern.

The upper (green) trace in Figure 3.1 shows the XRD pattern of the nominally pure Fe_2B sample. This sample was crystalline, consisting of three phases, namely elemental Fe, Fe_2B, and FeB (JCPDS data card nos. 87-0721, 75-1062, 76-0092). The FeB phase was present in traces, whereas the Fe and Fe_2B phases were dominant.

Diffraction lines of the elemental Fe were rather broad, indicating small crystallite size (below 10 nm). At $2\theta \approx 45°$ there was an overlap of two diffraction lines, from the (110) plane of Fe ($2\theta = 44.7°$) and the (211) plane of Fe_2B ($2\theta = 45.1°$). The former line (the base of the common maximum peak) was broader than the latter (the upper part of the common maximum peak).

Taking also into account the width of the (200) plane of Fe at $2\theta \approx 65.0°$, one could conclude that the Fe_2B crystallites were bigger than the Fe ones. The presence of α-Fe in the SiO_2 coated Fe_2B particle was also detected in [5].

According to the XRD results, our coated particles are fully amorphous, whereas those in [5] (having thinner SiO_2 shells) showed the presence of nanosize crystalline domains, possibly coexisting with the amorphous phase.

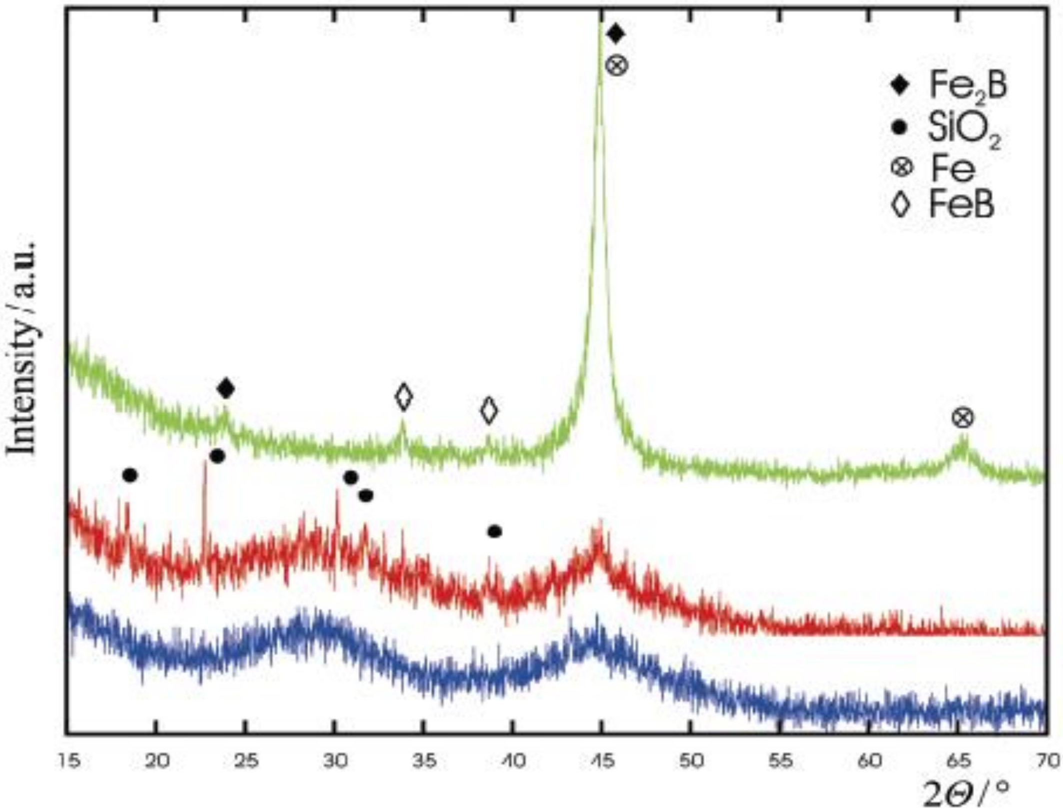

Figure 3.1: X-ray diffraction patterns of Fe_2B (green, upper), Fe_2B/SiO_2 (red, middle), and $Fe_XCo_{2-X}B/SiO_2$ (blue, bottom) particles. Adopted from [6].

3.3.3 SEM analysis

Typical scanning electron microscope (SEM) images for all three samples are presented in Figures 3.2 and 3.3. For uncoated particles, the grouping is chain-like, which is characteristic of magnetically interacting particles.

The uncoated nanoparticles have an average size of 80 nm and a broad size distribution, which ranges from 20 to 160 nm. Obviously, the strong magnetic attraction, depending on the amount of iron in Fe_2B, was crucial for the agglomeration into larger clusters. The coated particles, however, are grouped in piles or stacks, indicating possibly weak non-directional surface interactions. From a morphological point of view, the coated nanoparticles of Fe_2B/SiO_2 consist of large silicate spheres in which smaller particles of Fe_2B are trapped. The statistical processing was performed by measuring the grain sizes, putting the sizes into categories, and fitting the data by normal distribution functions. The histograms of particle sizes and the corresponding fit for the uncoated and SiO_2 coated Fe_2B particles are shown in Figure 3.4. The distributions for both types of particles are quite broad, with mean particle diameters of about 84 nm and 177 nm for uncoated and coated particles, respectively.

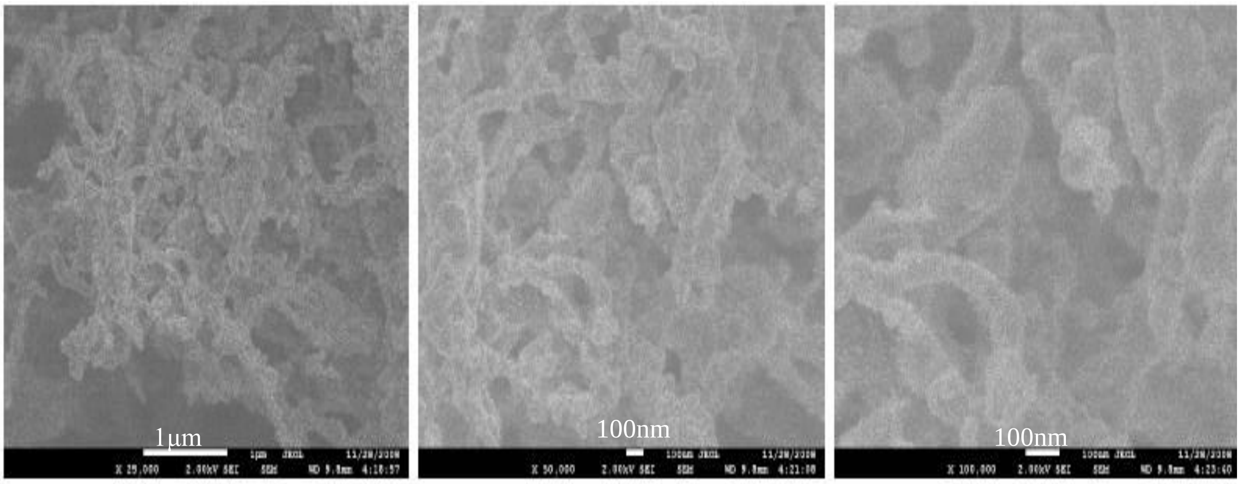

Figure 3.2: SEM images of Fe_2B particles. Adopted from [6].

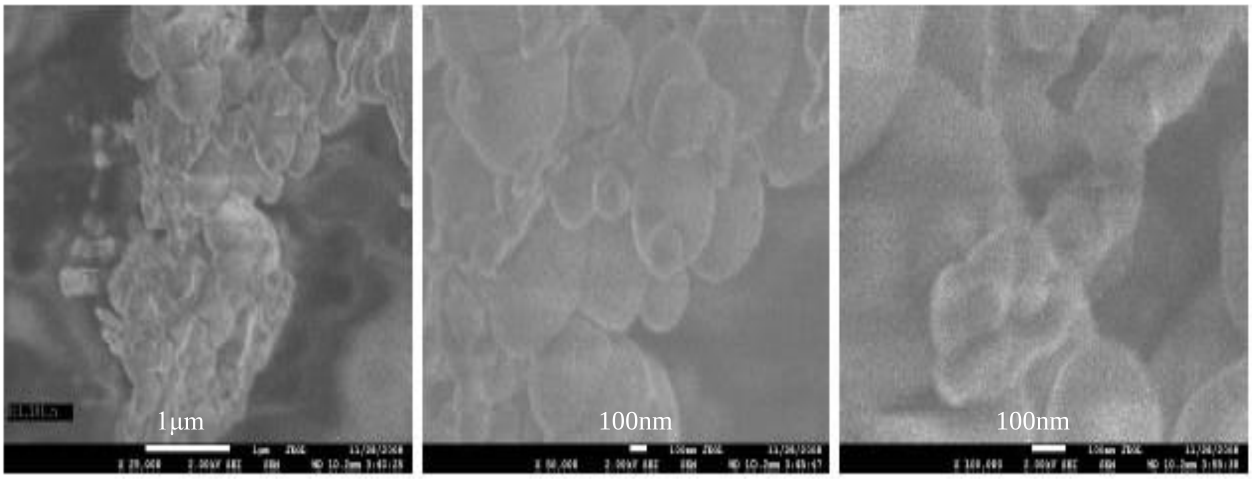

Figure 3.3: SEM images of Fe_2B/SiO_2 particles. Adopted from [6].

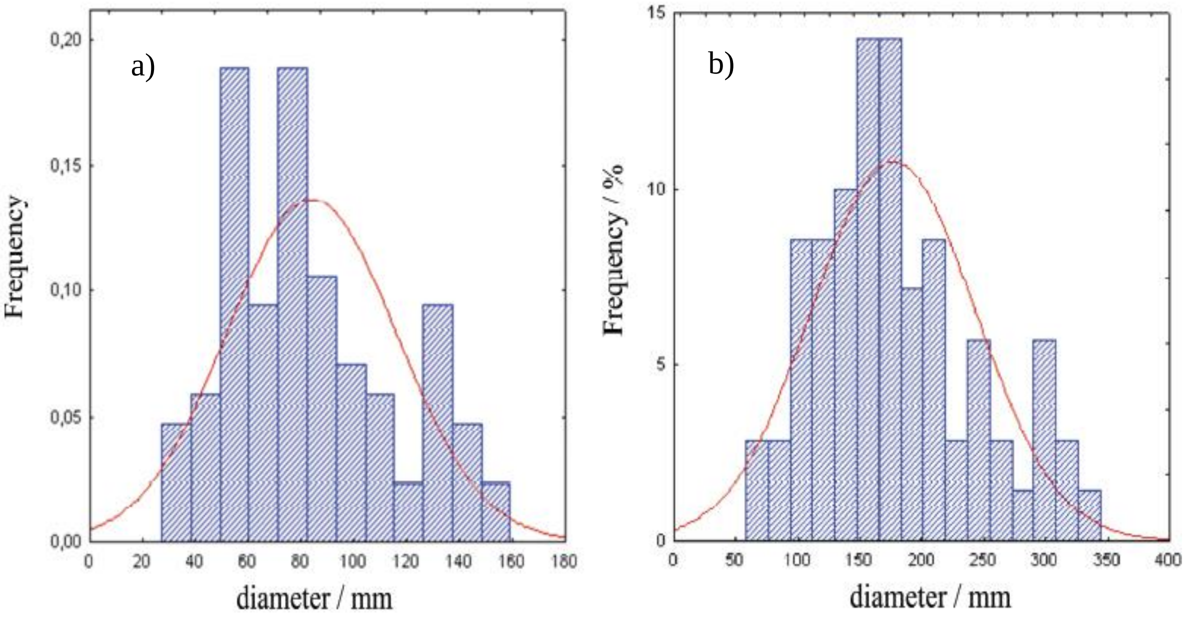

Figure 3.4: Size distributions of (a) Fe_2B and (b) Fe_2B/SiO_2 nanoparticles. Adopted from [6].

3.3.4 Magnetic properties

Magnetic hysteresis loops for the three samples are presented in Figure 3.5. High field magnetization behaviour shows that saturation was still not reached, so the magnetization at 5 T was used for comparison with other published data. The curved shape of the hysteresis loops also indicates a blocked superparamagnetic ensemble of particles, similar to the ones reported for $CuFe_2O_4$ nanoparticles and Al-doped Ni-ferrite.[7,8]

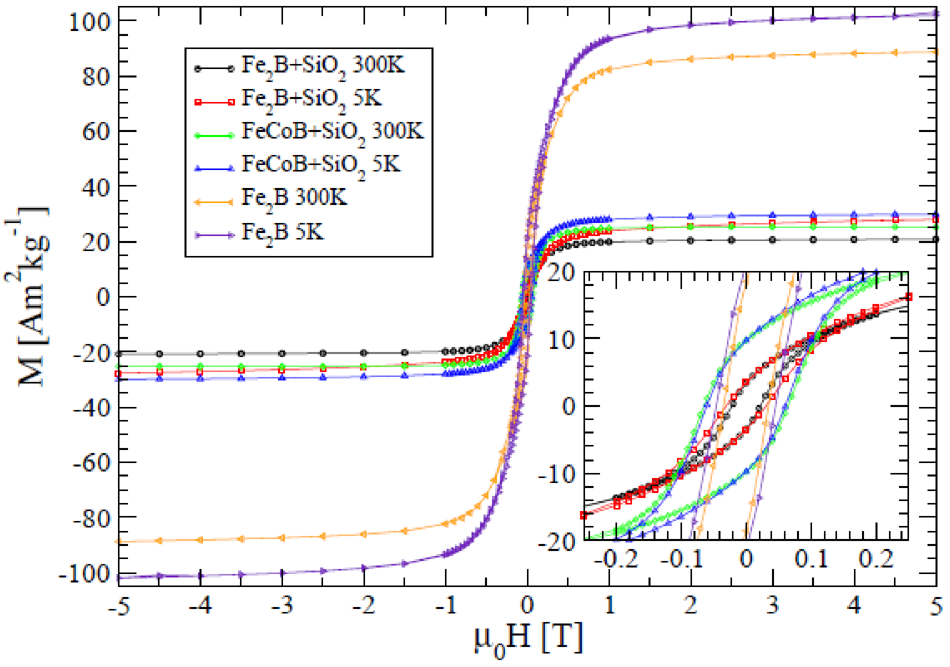

Figure 3.5: Magnetic hysteresis loops for all three samples at 300 K and 5 K. The inset shows an enlargement of the low-field region. Adopted from [6].

Coercive fields are bigger at 5 K than at 290 K, which is characteristic of magnetic materials in nanoparticle form. Also, the observed decrease in M_{5T} from 5 to 300 K is in accordance with the reported behaviour of magnetization for magnetic nanoparticles.[9,10,11] The higher coercive field for pure Fe_2B nanoparticles could originate from larger particle size, as higher field is needed to reorient their magnetic moment over the higher barrier ($U = K{\cdot}V$). The lower coercive field (H_c) of the SiO_2 coated Fe_2B particles compared to the bare Fe_2B

particles (Table 3.1.) is consistent with the observed higher amorphicity of the coated particles and the smaller magnetic cores of the particles.

More striking is the high saturation magnetization, M_S, in our samples. For uncoated Fe_2B particles M_{5T} was reported to be 102 Am^2kg^{-1} at 5 K[6]. Higher M_S in the uncoated Fe_2B sample is probably due to the presence of iron nanoparticles, whose saturation magnetization in the nanocrystalline phase is known to be 210 A m^2kg^{-1}.[12] It follows from these values that the mass content of the Fe_2B and Fe particles is 83 % and 17 %, respectively.

For the coated Fe_2B particles the lower saturation magnetization than in [5] (56.6 Am^2kg^{-1} at room temperature and 1 T) reflects the thicker SiO_2 shell in our sample. From the ratio of the magnetization at 5 T (Figure 3.5.) for uncoated and coated Fe_2B powder (Figure 3.5) we deduce that the mass ratio between SiO_2 and $Fe_2B \approx 3$.

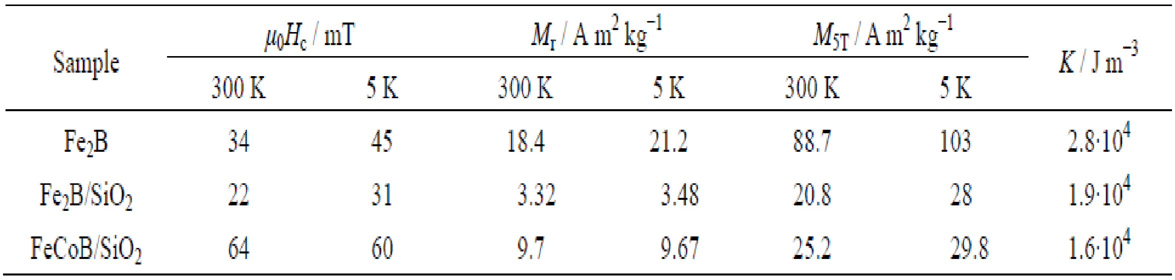

Sample	$\mu_0 H_c$ / mT		M_r / A m^2 kg^{-1}		M_{5T} / A m^2 kg^{-1}		K / J m^{-3}
	300 K	5 K	300 K	5 K	300 K	5 K	
Fe_2B	34	45	18.4	21.2	88.7	103	$2.8 \cdot 10^4$
Fe_2B/SiO_2	22	31	3.32	3.48	20.8	28	$1.9 \cdot 10^4$
$FeCoB/SiO_2$	64	60	9.7	9.67	25.2	29.8	$1.6 \cdot 10^4$

Table 3.1: Magnetic hysteresis parameters (coercive field H_C, remanent magnetization M_r, and magnetization at 5 T M_{5T}), and anisotropy energy density K. Adopted from [6].

The temperature dependence of magnetization for all the samples, measured upon warming the sample up in magnetic field of 0.01 T after cooling in zero field (ZFC) and after cooling in field (FC) is shown in Figure 3.6. The splitting between the ZFC and the FC curves is a sign of magnetic moment blocking in the system.

The measured ZFC curves are very broad, and they do not have the characteristic shape with a single localized maximum that would point to isolated or weakly interacting particles with a narrow size distribution.

This broad size distribution may include a ferromagnetic component associated with the bigger particles, added to the superparamagnetic behaviour of the smaller particles. The maxima in the ZFC curves represent the temperatures at which the largest number of nanoparticles is thermally unblocked.

A large difference between the temperature at the maximum and the splitting temperature between the ZFC and FC curves for the Fe_2B particles in the figure points to a broad distribution of barrier heights. Therefore, broad maxima in ZFC curves reflect a wide particle size distribution, as well as the interactions between the particles.[9,10,13] Taking the blocking temperature (T_B) as the temperature where the splitting between the ZFC and the FC curves appears, measured in a relatively small applied field of 10 mT, that is, between 260 K and 300 K for our samples, which leads to the effective barrier heights U_{eff} from 6500 to 7500 K.[8,13,14]

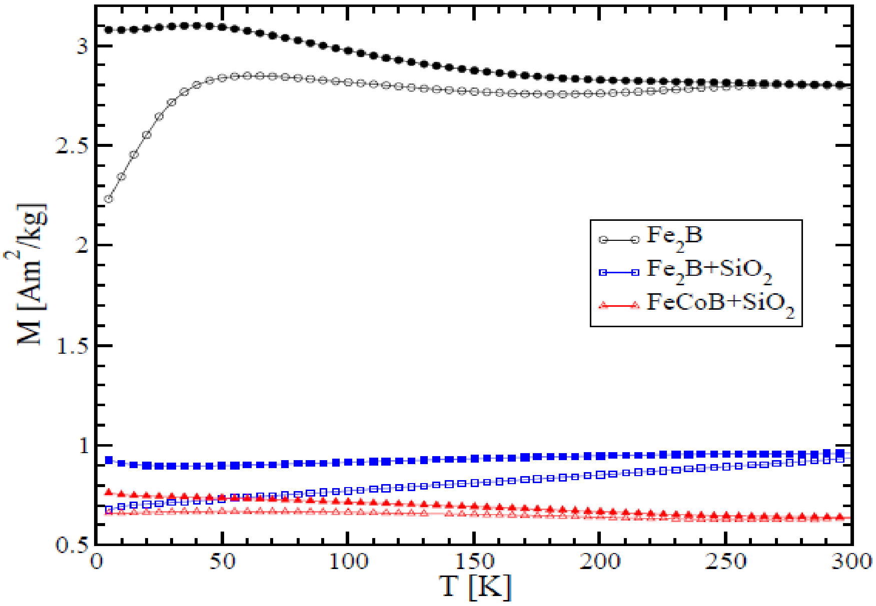

Figure 3.6: ZFC (hollow symbols) and FC (full symbols) curves for Fe_2B, Fe_2B/SiO_2 and $FeCOB/SiO_2$. Adopted from [6].

3.4 NiCoB nanoparticles Prepared by Chemical Reduction in Ethanol

3.4.1 Introduction

This procedure was the candidate’s first effort to prepare NiCoB nanoparticles, performed at University of Zagreb. It provided relatively coarse nanoparticles that by themselves were not likely to result in increased vortex pinning.

These procedures provided a good starting point, however, for further improvements in NiCoB nanoparticles, as described in section 3.5.

In order to produce nanoparticles suitable for specific applications or for fundamental scientific research into the physical properties of such particles, special attention was given to the synthetic routes for the preparation of magnetic nanoparticles and the possibility of tuning their magnetic properties by changing the synthesis parameters.

Many factors (such as chemical composition, anisotropy, size and shape of the particle, etc.), which could be controlled through chemical synthesis, determine the magnetic properties of the particles. Structural and chemical disorder in amorphous materials leads to magnetic properties that are different from magnetic properties of their crystalline counterparts.

3.4.2 Synthesis and characterization

Amorphous NiCoB alloy nanoparticles were prepared by chemical reduction of ethanol solutions of $NiNO_3 \cdot 6H_20$ and $CoCl_2$ using an aqueous solution of KBH_4 as the reducing agent. NiCoB/SiO_2 coated nanoparticles were prepared by the same method with the addition of tetraethyl orthosilicate (TEOS). Both reactions were carried out at a temperature of 273K (ice bath) in inert argon atmosphere.

The reaction temperature was 273 K. A black powder was formed instantly, and it was extracted from the solution by vacuum filtration. The black powder was washed with distilled water to remove residual ions and then rinsed with acetone to remove water. The powder was dried for three hours in argon atmosphere. For preparation of Ni-Co-B particles coated in SiO_2 we added 50 ml ethanol which contained 0.1 ml TEOS immediately after adding KBH_4.[15]

3.4.2.1 XRD analysis

According to the X-ray powder diffraction patterns (Figure 3.7) both samples were amorphous (so no sharp diffraction peaks could be resolved). According to the XRD patterns presented in Figure 3.7, prepared uncoated and coated NiCoB particles were in a fully amorphous state, as indicated by a broad amorphous maximum.

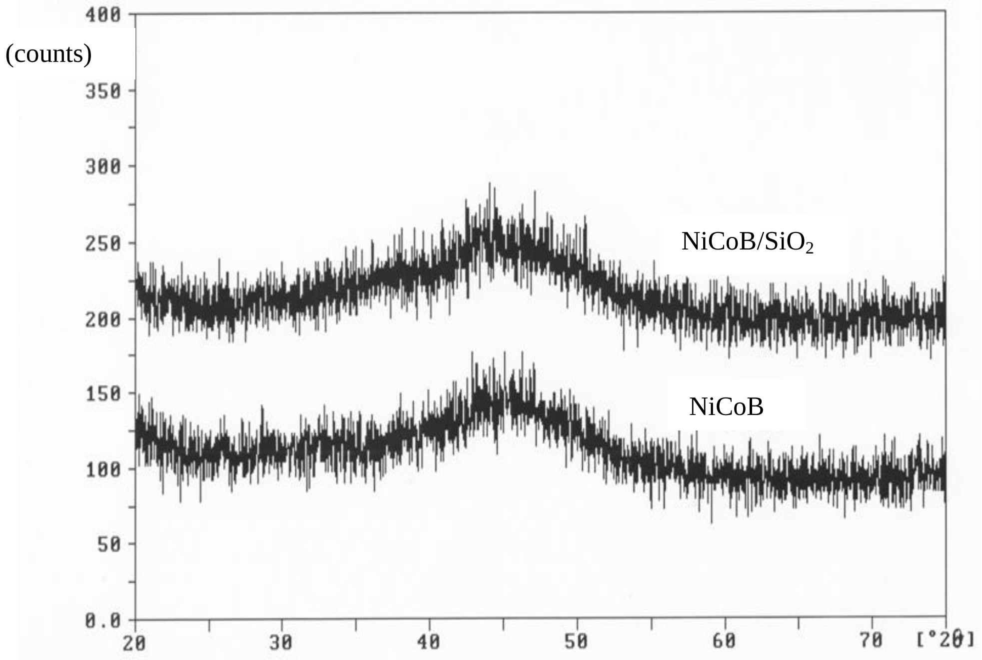

Figure 3.7: XRD patterns of NiCoB and $NiCoB/SiO_2$. Adopted from [15].

3.4.2.2 SEM analysis

Field emission SEM (FE-SEM) micrographs of uncoated NiCoB and coated NiCoB samples show that the samples are composed of fine spherical nanoparticles of similar size, which tend to form irregular agglomerates in both cases. A SEM image of NiCoB is presented in Figure 3.8 with the size distribution in Figure 3.9. A SEM image of silica coated NiCoB is shown in Figure 3.10, and its size distribution is presented in Figure 3.11. The distributions were fitted by normal distribution functions.

The FE-SEM observations that were carried out showed nearly uniaxial nanoparticles. The particles are sufficiently small to show superparamagnetic behaviour below room temperature, yet large enough to make the influence of surface atoms on their magnetic and other properties less important.[16]

Furthermore, their size is close to the critical parameters of MgB_2 superconductor, the coherence length and the London penetration depth. The size for coated NiCoB nanoparticles is around 19 nm and for uncoated, 17 nm. One can see that the average size of the coated NiCoB particles is slightly larger than for the uncoated NiCoB particles, which is due to the thin SiO_2 coating (which is due to the addition of a small concentration of TEOS at the beginning of the synthesis reaction), as can be seen in table 3.2.[15]

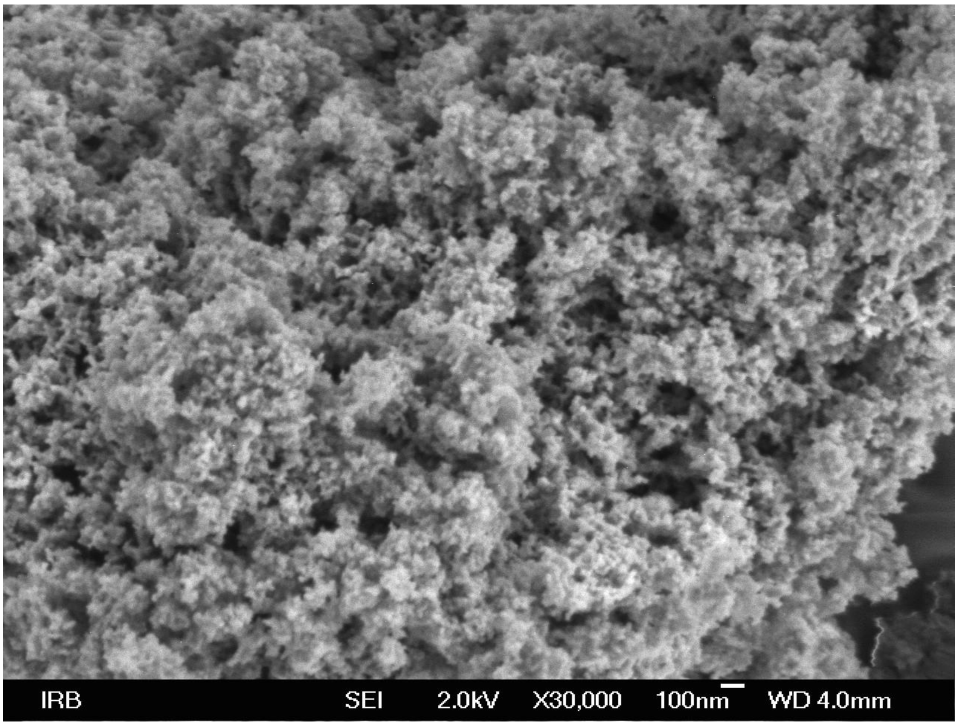

Figure 3.8: SEM image of NiCoB. Adopted from [15].

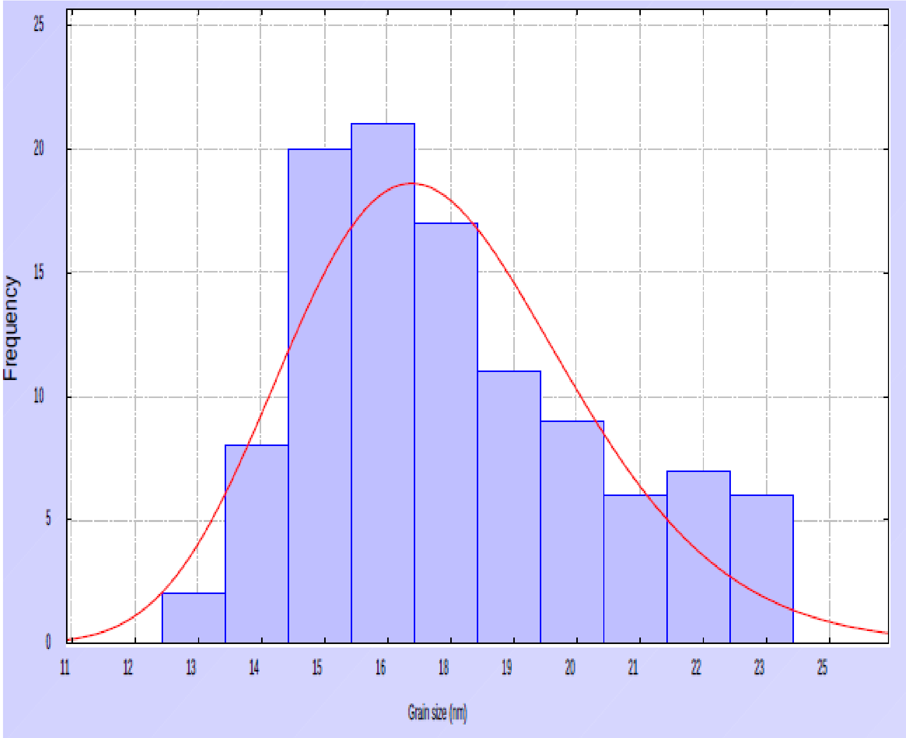

Figure 3.9: Size distribution of NiCoB particles. Adopted from [15].

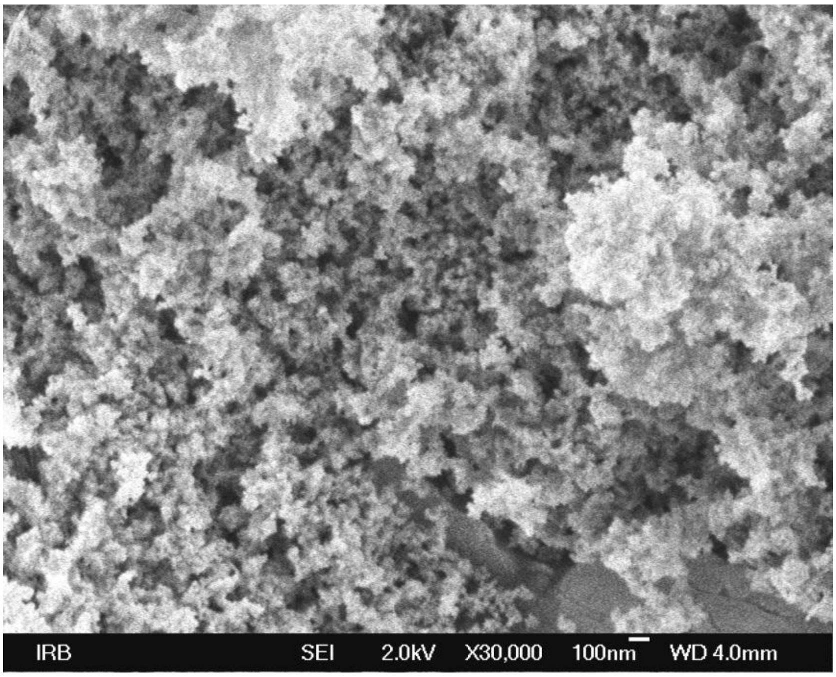

Figure 3.10: SEM image of NiCoB coated with SiO_2. Adopted from [15].

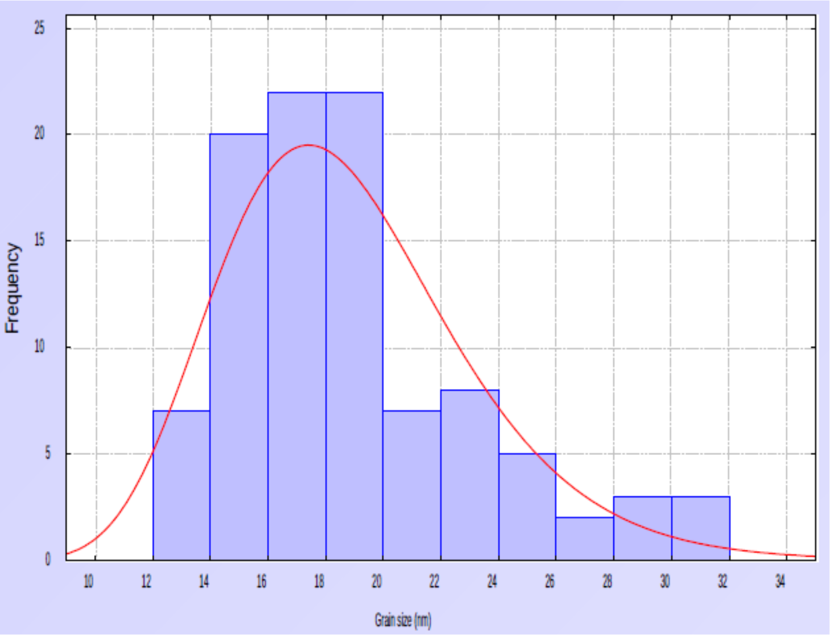

Figure 3.11: Size distribution of NiCoB/SiO_2 particles. Adopted from [15].

Sample	Number of analysed particles	Particle diameter [nm]
NiCoB	107	17±3
NiCoB/SiO_2	99	19±4

Table 3.2: Parameters of particles size for as-prepared uncoated and coated NiCoB. Adopted from [15].

The EDS data for the NiCoB nanoparticles is shown in Figure 3.12. The relative atomic percentages of main fractions Co, and Ni are almost equal to 13.15 at% and 14.63 at%, respectively. Percentage of boron exceeds the percentage of transition metals and is around 26.61 at%. Oxygen is present in the considerable amount of around 40.58 at%, which is unexpectedly high.

The reason could be that the oxygen is attached on the nanoparticle surfaces, and the content is very high due to the large surface area of the nanoparticles. The mapping results in Figure 3.13 shows the uniform spread of the transition elements Ni and Co throughout the whole sample, while boron is more agglomerated in the central part of the image.[15]

The same ratio of elements is found for the silica coated NiCoB nanoparticles as for the uncoated sample.

The only differences observed are that there is a small amount of silicon (1.89 at%) and a much smaller amount of oxygen (32.4 at%). This result shows the large similarity between the two samples. The mapping results for coated NiCoB are presented in Figure 3.15 with the same uniform spread of the transition metals Ni and Co.[15]

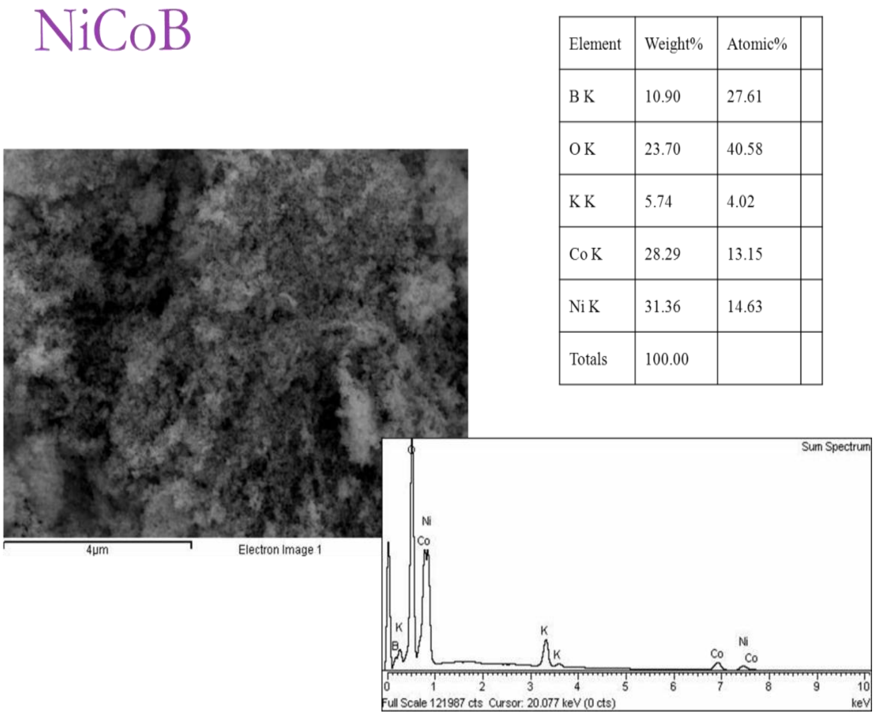

Element	Weight%	Atomic%	
B K	10.90	27.61	
O K	23.70	40.58	
K K	5.74	4.02	
Co K	28.29	13.15	
Ni K	31.36	14.63	
Totals	100.00		

Figure 3.12: EDS results for NiCoB. Adopted from [15].

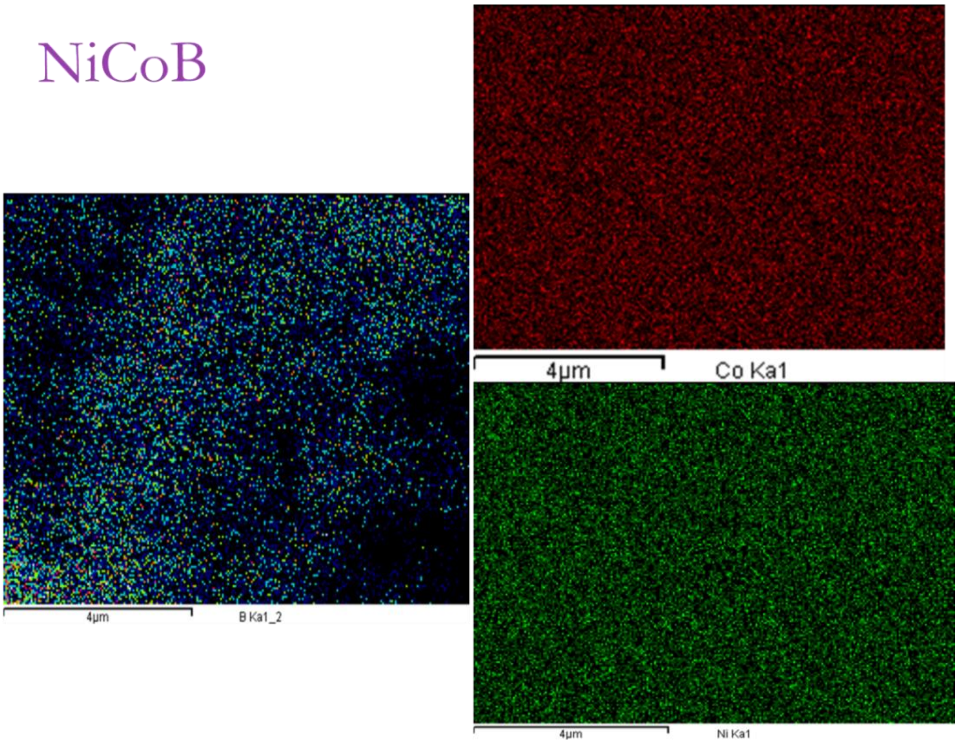

Figure 3.13: Element maps of NiCoB sample. Adopted from [15].

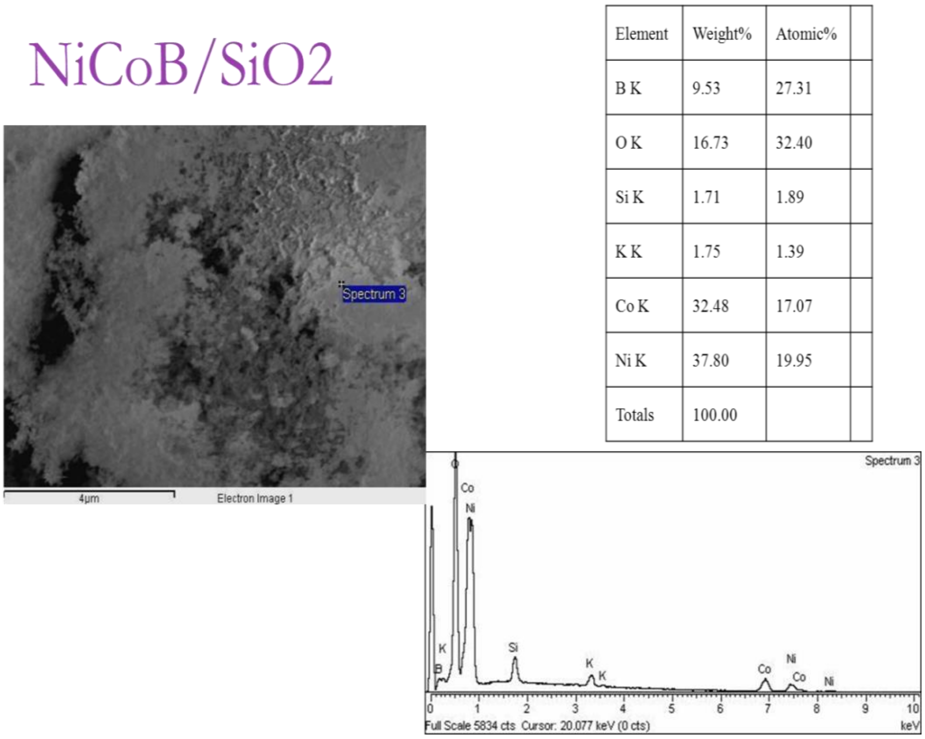

Element	Weight%	Atomic%	
B K	9.53	27.31	
O K	16.73	32.40	
Si K	1.71	1.89	
K K	1.75	1.39	
Co K	32.48	17.07	
Ni K	37.80	19.95	
Totals	100.00		

Figure 3.14: EDS results for $NiCoB/SiO_2$. Adopted from [15].

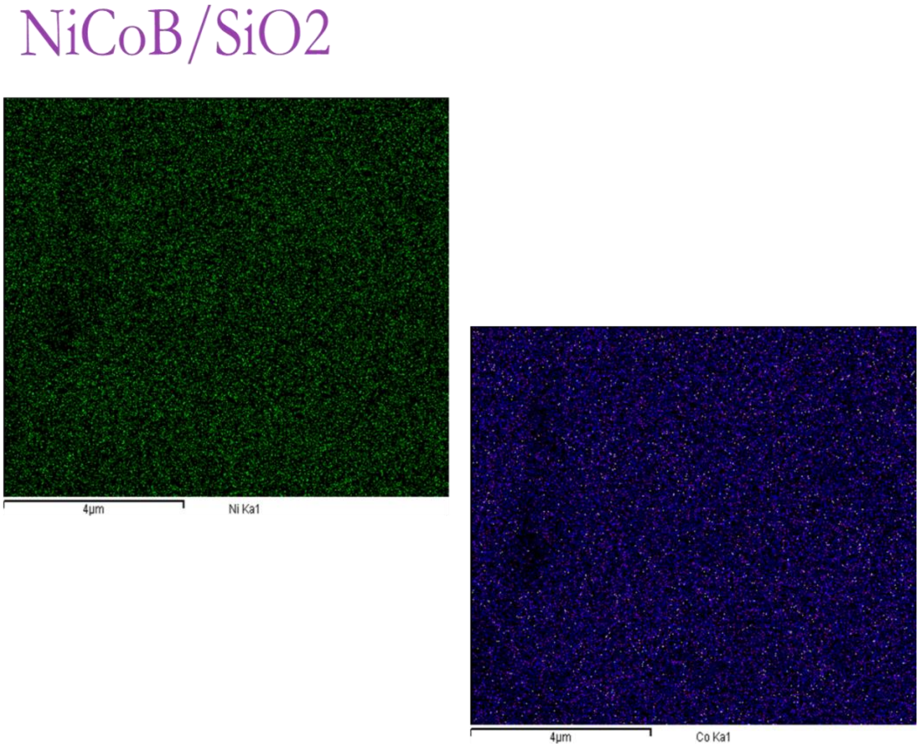

Figure 3.15: Element maps of NiCoB/SiO$_2$ sample. (These images were obtained with the help of Dr. Mira Ristić, IRB.). Adopted from [15].

3.4.2.3 Magnetic properties of NiCoB and NiCoB/SiO$_2$ nanoparticles

For both systems and all measuring fields, a distinct maximum of the ZFC curve and splitting of the ZFC and FC curves are observed, as shown in Figures 3.16 and 3.17. Two characteristic temperatures can be observed for all measured M(T) curves: temperature T_{max} at which maximum of the ZFC curve appears and temperature T_{irr} at which FC branch of the magnetization curve departs from ZFC branch.

It can be observed that T_{max} is lower than T_{irr} for all measurements. The difference between these temperatures, as well as the somewhat broad maximum on the ZFC curve, is connected to the particle size distribution and possibly to the weak magnetic interaction between aggregated particles [13]. Splitting between the ZFC and FC curves is a consequence of the magnetic moment blocking in the studied systems of nanoparticles, which causes slow relaxation of magnetization of the system.

It should be noted that even at the lowest field, T_{max} is below 150 K, and thus, both types of particles are mostly superparamagnetic at room temperature which should decrease the tendency towards agglomeration of particles within the powder.

The average size and size distribution of the particles were studied in this system by comparing the values and field dependences of T_{max} for the uncoated and coated NiCoB particles. For single domain particles with uniaxial anisotropy in the absence of applied field, the energy barrier is $U = KV$, where K is the magnetic anisotropy energy density and V is the volume of the particle.

The uncoated NiCoB particles are smaller than for the coated particles, leading to a smaller energy barrier and consequently lower T_{max}. Another important factor is magnetic interaction between particles. Interactions between particles lead to an increase in the effective energy barrier and therefore to a higher blocking temperature.

Therefore, magnetic interaction between uncoated NiCoB particles also causes an increase in T_{max} and contributes to the observed difference between T_{max} (μ_0H) curves for uncoated and coated NiCoB particles.

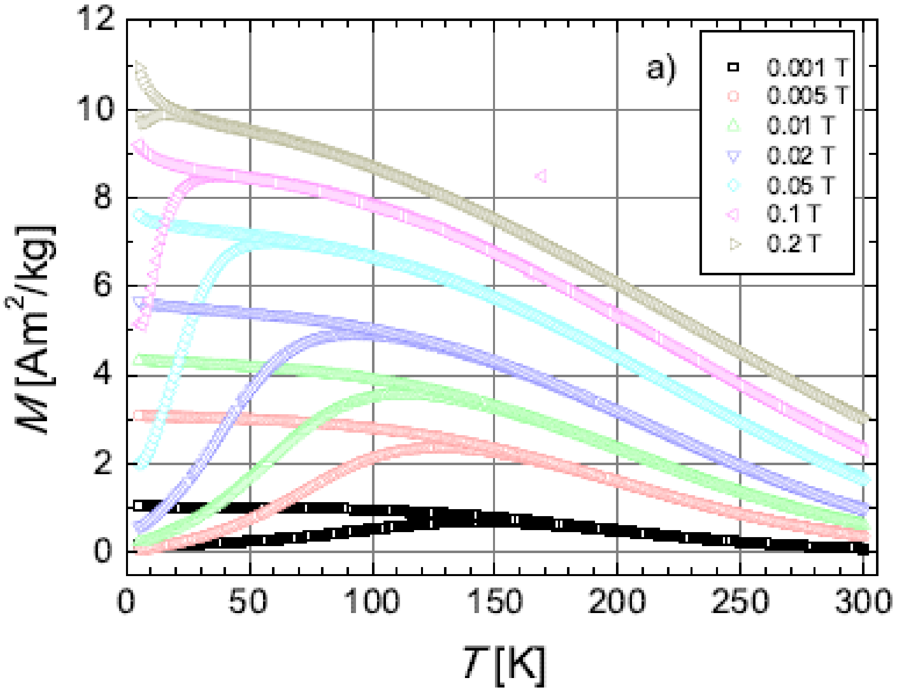

Figure 3.16: ZFC and FC magnetization curves for uncoated NiCoB particles measured in different applied magnetic fields. Adopted from [15].

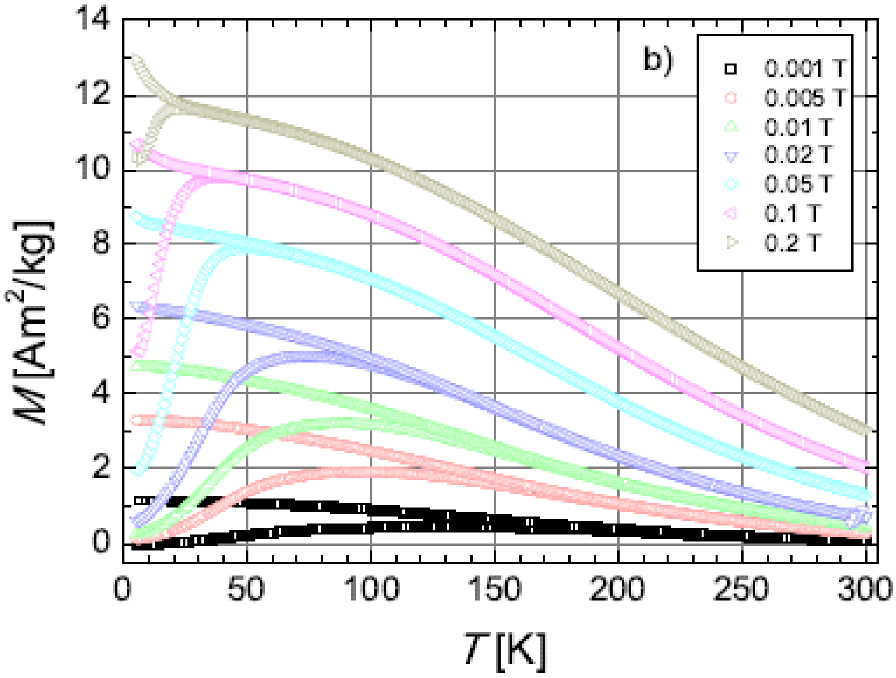

Figure 3.17: ZFC and FC magnetization curves of coated NiCoB particles measured in different applied magnetic fields. Adopted from [15].

M(H) curves measured at different temperatures for uncoated and coated NiCoB particles are shown in Figures 3.18 and 3.19. The hysteresis loops as well as the absence of saturation at high field (5 T) point to the superparamagnetic behaviour of the studied systems. The irreversible M(H*)* curves were obtained at low temperatures (5 to 60 K). In this case the hysteresis loops are a consequence of the slow relaxation of the magnetization of the system of nanoparticles. At high temperatures (≤ 100 K), M(H) curves are reversible.

The lower values of magnetization for the uncoated NiCoB particles compared to the coated ones may also be due to the dipolar interactions between NiCoB particles without any SiO_2 coating. The distribution of particle sizes and the magnetic interaction between particles produce a distribution of energy barriers within the system, which makes the magnetic behaviour of such a system very complex.

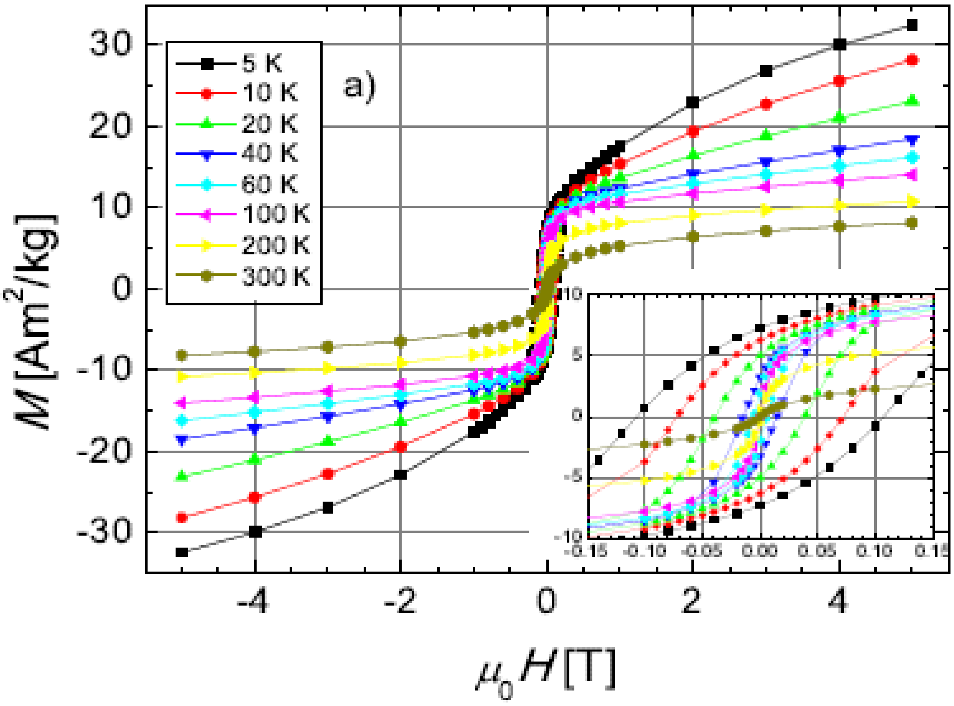

Figure 3.18: Hysteresis loops for NiCoB. Adopted from [15].

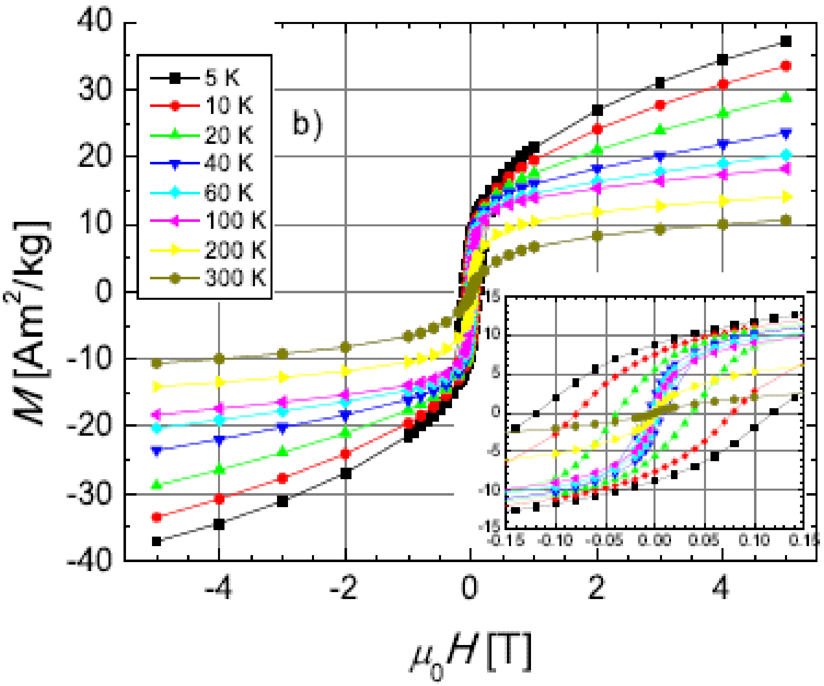

Figure 3.19: Hysteresis loops for NiCoB/SiO$_2$. Adopted from [15].

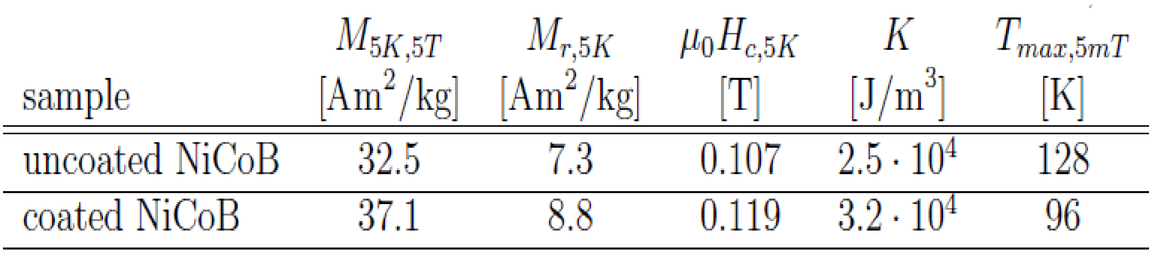

sample	$M_{5K,5T}$ [Am^2/kg]	$M_{r,5K}$ [Am^2/kg]	$\mu_0 H_{c,5K}$ [T]	K [J/m^3]	$T_{max,5mT}$ [K]
uncoated NiCoB	32.5	7.3	0.107	$2.5 \cdot 10^4$	128
coated NiCoB	37.1	8.8	0.119	$3.2 \cdot 10^4$	96

Table 3.3: Magnetic hysteresis parameters at 5 K (magnetization at 5 T, $M_{5K,5T}$, remanent magnetization $M_{r,5K}$, coercive field $\mu_0 H_{C,5K}$, anisotropy energy density K and temperature of maximum of ZFC magnetization curve in applied field of 5 mT, $T_{max,5mT}$. Adopted from [15].

The values of maximum magnetization (M_m) at 5 K are about one half of that for amorphous Co$_2$B alloy[17], which is reasonable, since the amorphous Ni-B alloys with B content above 18 at% are non-magnetic[18]. M_m of uncoated NiCoB particles is a little lower compared to the coated particles. The lower values of magnetization of uncoated NiCoB particles compared to the coated ones may be due to the dipolar interactions between NiCoB particles without SiO$_2$ coating (table 3.3).

The temperature dependence of the coercive field is shown in Figures 3.18 and 3.19. According to the Néel model of relaxation and a study by Bean and Livingston[14], the coercive field is expected to decrease with the square root of the temperature. The coercive fields of both uncoated and coated NiCoB particles do not decrease with $T^{1/2}$.

The reason for this discrepancy between theory and the observed behaviour of our particles is the distribution of particle sizes and the interaction between uncoated NiCoB particles. The temperature dependence of the coercive field is described by the exponential function, $H_c \propto e^{-bT}$, where b is a constant.

The values of K, calculated by applying this model, are presented in Table 3.3 (together with other data relevant to the samples). Similar values of K for uncoated and coated NiCoB particles justify the assumption that the magnetic cores of both types of particles have similar compositions and structures.[15]

3.5 NiCoB nanoparticles Prepared by Chemical Reduction of Metallic Salts

3.5.1 Introduction

NiCoB nanoparticles were also prepared by the method of chemical reduction of metallic salts. The advantage of this method in comparison with the older synthesis of NiCoB is in two main points.

As is described in the experimental part, ethylenediamine has been added in this synthesis as an additional chemical. Ethylenediamine kept the synthesis under alkaline pH condition, which is crucial for maintaining the reduction of metal salts and providing high yield of the reaction. The reducing agent $NaBH_4$ in neutral and acidic environments reduces hydrogen from water.

$NaBH_4(s) + 2H_2O(l) \rightarrow NaBO_2(a) + 4H_2(g)$ (3.4)

$NaBH_4$ in water can reduce the hydronium ion to elemental hydrogen:

$BH_4^-(aq) + 4H^+(aq) \rightarrow 2H_2(g) + B(OH)_3(aq)$ (3.5)

In an alkaline pH environment, the above reaction does not occur, due to the negligible concentration of existing H^+ ions. Ethylenediamine is freely soluble in water and reacts with water:

$H_2NCH_2CH_2NH_2(l) + H_2O(l) \rightarrow H_2NCH_2CH_2NH_3^+OH^-(aq)$ (3.6)

On the other hand, excessive OH^- in the environment can be counterproductive due to another reaction between the metal salt ($Co(NO_3)_2$) and OH^-.

$Co^{2+}(aq) + 2OH^-(aq) \rightarrow Co(OH)_2(s)$ (3.7)

To provide maximal chemical reduction of metal salts, the (Co, Ni) reaction should be maintained in a medium alkaline environment, between 8 and10 pH.

In that case, the reaction will be mostly the reduction of metallic salts into metal borides. Depending on the concentrations of reactants, one reaction will be faster and more favored. According to the equations of reaction speed (Eqs. 3.8 and 3.9), a major influence on whether certain products are obtained will be competition between the ions, in this particular case, OH^- and BH_4^-.

$V_1 = k_1 [OH^-]^2 * [Co^{2+}]$ (3.8)

$V_2 = k_2 [BH_4^-]^x * [Co^{2+}]$ (3.9) where V_1 and V_2 are the speeds of the particular reactions, while k_1 and k_2 are the kinetics constants of the observed reactions. In this experiment it is important to adjust the pH environment to medium alkaline and direct the reaction to reduce Ni^{2+} and Co^{2+} into Ni-Co-borides.

$$NiCl_2 + CoCl_2 + NaBH_4 + OH^- \rightarrow NiCoB + NaCl + H_2O \qquad (3.10)$$

Another great feature of the new synthesis is the addition of the surfactant sodium -dodecyl-sulphate (SDS), which prevents agglomeration of nanoparticles.

3.5.2 New NiCoB synthesis

Nickel-cobalt-boron amorphous nanoparticles were synthesised by the chemical reduction of metallic salts. $Ni(NO_3)_2$ and $Co(NO_3)_2$ were dissolved in DI water and reduced with the help of the reducing agent $NaBH_4$, which was previously dissolved in DI water. Before the chemical reaction, the dissolved chemicals were bubbled for 2 hours.

The chemical equipment was assembled from a funnel where Co and Ni compounds were dissolved and a three necked flask, where $NaBH_4$ was dissolved. Ethylenediamine was added into the three necked flask to maintain the reaction under alkaline pH conditions (pH ≈ 8-10) and also catalyse the reaction. Reaction with this catalyst can provide yields of up to 90%.

Finally SDS (sodium-dodecyl-sulphate) is added as a surfactant to prevent agglomeration of nanoparticles.

The synthesis was performed in a closed system under argon atmosphere, and all solutions were bubbled with argon for two hours prior to the reaction. The reaction was maintained at 273 K, and the duration of the reaction was less than 2 min. Black powder was formed instantly, and it was extracted from the solution by centrifuge. The black powder was washed with DI water and ethanol several times to remove residual ions. Finally, the powder was dried for two hours in desiccators.

3.5.3 Results and discussion

3.5.3.1 XRD analysis of NiCoB

According to the XRD patterns (Fig. 3.20), (uncoated and coated) NiCoB particles are mostly in the amorphous state. It can be observed that there is a very broad peak in XRD pattern extending from $2\theta \approx 35$ to ~ 50 degrees, as well as one relatively sharp peak at $2\theta \approx 62°$.

The explanation for the broad peak could be the presence of extremely small particles with strongly amorphous morphology. The relatively sharp peak at 62.5°, according to Zysler[16], could arise from metal-boride structure in the form of Ni_2B or Co_2B.

In an alloy structure, such as that of NiCoB nanoparticles with strong amorphous morphology and without crystalline order, it is difficult to distinguish the same particular phase. Considering the XRD pattern, it can be said that there is no emphasized phase, and the structure of the nanoparticles is highly amorphous.

In order to confirm results obtained from SEM analysis, crystallite size was also determined from X-ray diffraction line broadening. Diffractogram was typical for nanocrystalline sample with crystallite size smaller than 10 nm - it showed only two broad maxima, with large noise to signal ratio. For that reason the Rietveld analysis could not be performed. Therefore, the program XBroad was used for size-strain analysis. The basis for calculation is the Warren-Averbach-Bertaut method which is implemented in the program, and the details can be found in [17]. Analysis was done on the maximum located around 62 degrees, which was firstly smoothed in order to obtain best possible results. The results showed the area-weighted crystallite size (length of coherent diffraction columns) of 7 nm with negligible strain. Crystallite size obtained with XBroad is in full agreement with the SEM analysis.

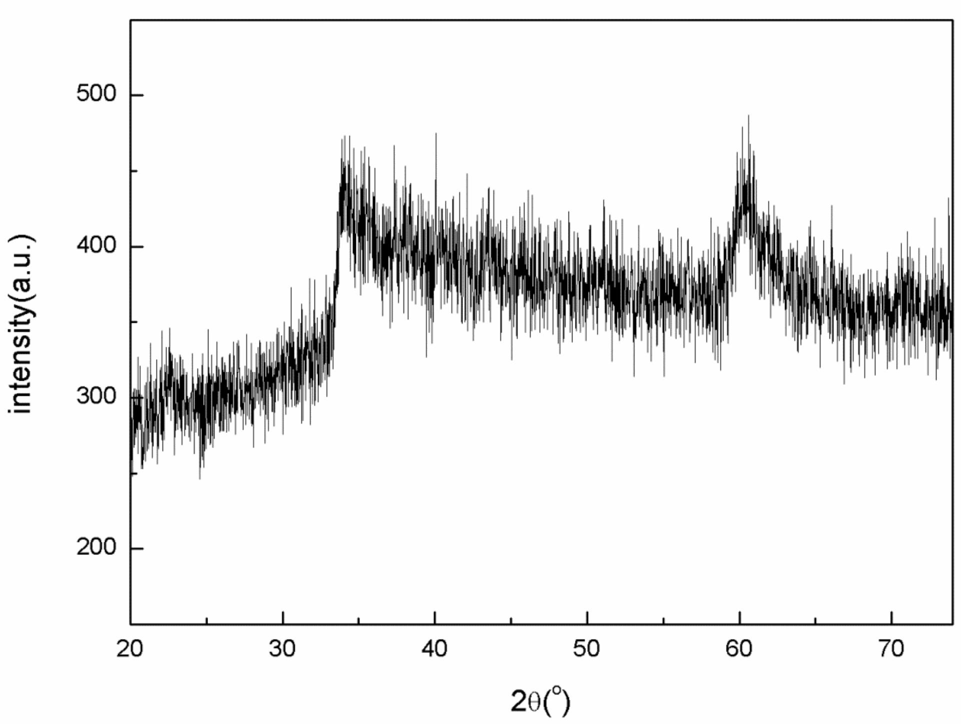

Figure 3.20: XRD pattern of NiCoB nanoparticles.

3.5.3.2 SEM images of NiCoB

The particle size distribution of NiCoB becomes very narrow with a mean diameter around 5 nm, as can be seen Figure 3.21 (a, b). All the observed nanoparticles lie in a narrowed distribution range within ±2 nm.

The SEM images do not show any agglomeration or cluster structure, which is a huge achievement for such small particles.

The size distribution was deduced from the SEM images and fitted by normal distribution functions. The size distribution in Figure 3.22 clearly shows that 90% of the particles are in the range of 5.0 to 5.8 nm.

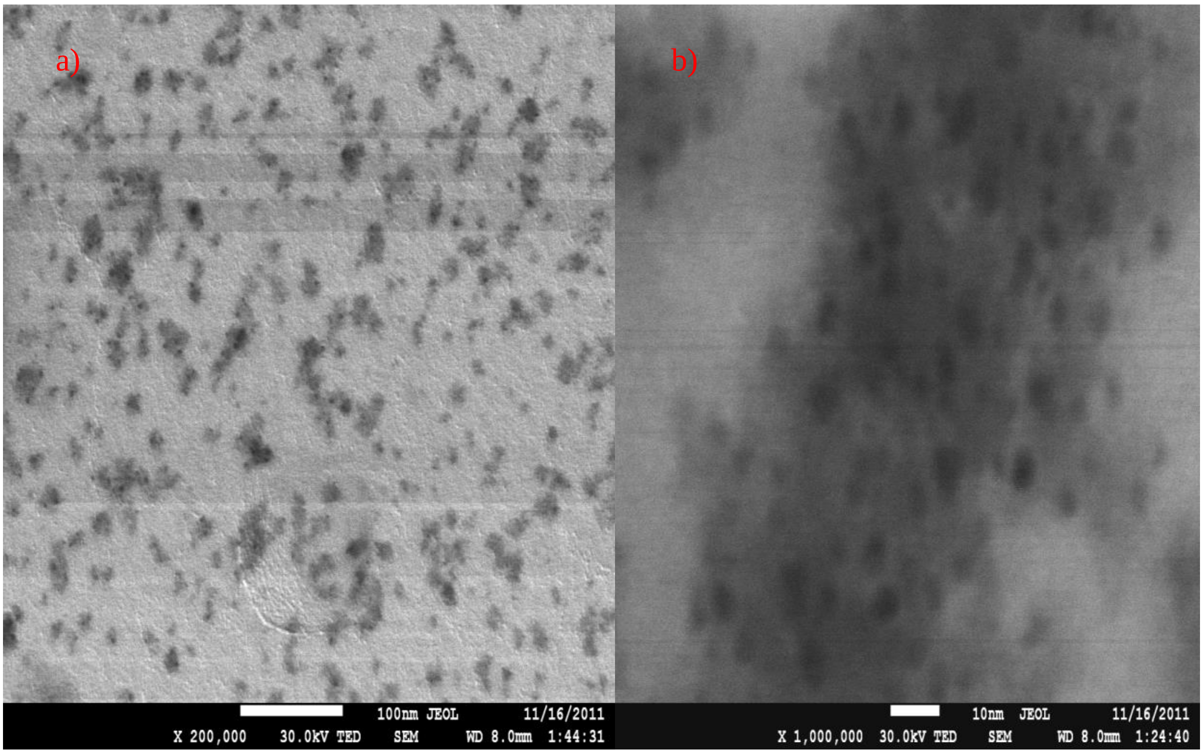

Figure 3.21 (a), (b): SEM images of NiCoB nanoparticles.

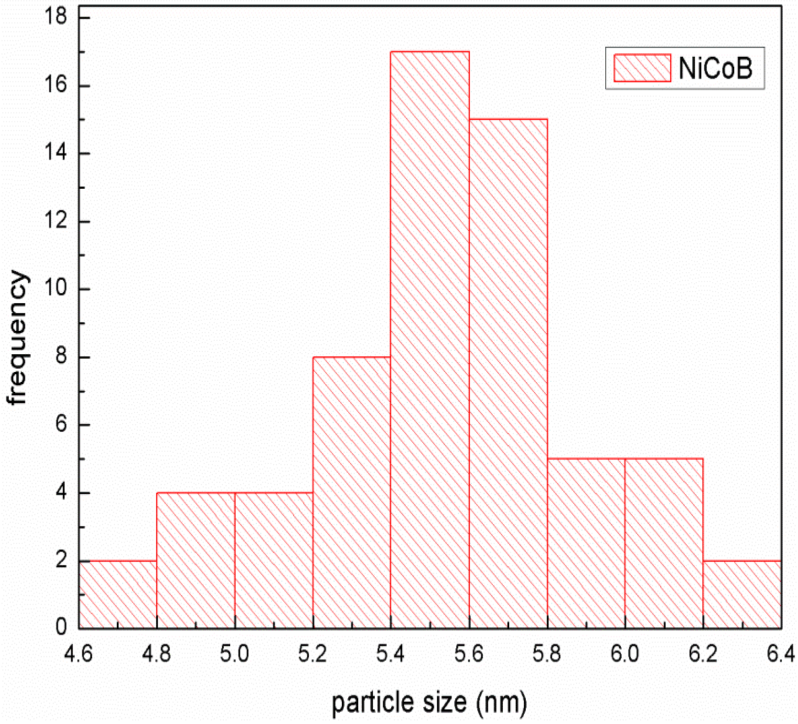

Figure 3.22: Distribution by size of NiCoB nanoparticles.

3.5.3.3 Magnetic measurements

Temperature dependences of the magnetization M(T) of NiCoB particles measured under different applied magnetic fields are presented in Figure 3.23. The results provided the blocking temperature (T_B) at the peak of the ZFC curve and the irreversibility temperature (T_{irr}) at the splitting of the ZFC and FC curves. A maximum magnetization can be observed in the ZFC curve (Fig. 3.23) at 90 K, indicating that 90 K is the blocking temperature (T_B) of NiCoB nanoparticles. Below 90 K (T_B), the particles are blocked and in the ferromagnetic state with an irreversible magnetization, whereas above T_B, the magnetization is still irreversible due to the interaction between some of the nanoparticles, and the particles are characterized by superparamagnetic behaviour.

The FC curve shows monotonic increment of the M_{FC} as the temperature drops. Splitting between the ZFC and FC curves is a consequence of magnetic moment blocking in the studied systems of nanoparticles, which causes slow relaxation of magnetization of the system. The difference between these two temperatures and the maximum on the ZFC curve are connected to the size distribution of the particles and possibly the magnetic interaction between aggregated particles. The difference between T_B and T_{irr} is quite big, which indicates the agglomeration of nanoparticles into clusters.

The curved shape of the hysteresis loops with an applied magnetic field of 2 T indicates the superparamagnetic behaviour of the nanoparticles (Fig. 3.24).

The irreversible M(H) curves were obtained at low temperatures (10 to 50 K). In this case the hysteresis loops are a consequence of the slow relaxation of the magnetization of the system of nanoparticles. At high temperatures (≥ 100 K), M(H) curves are reversible.

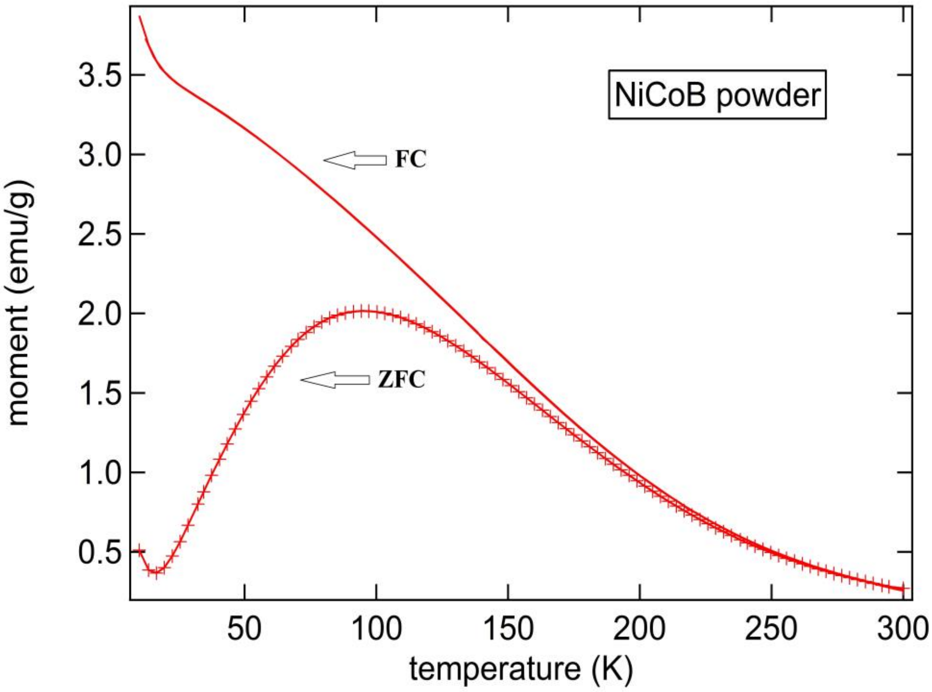

Figure 3.23: ZFC and FC curves of NiCoB nanoparticles.

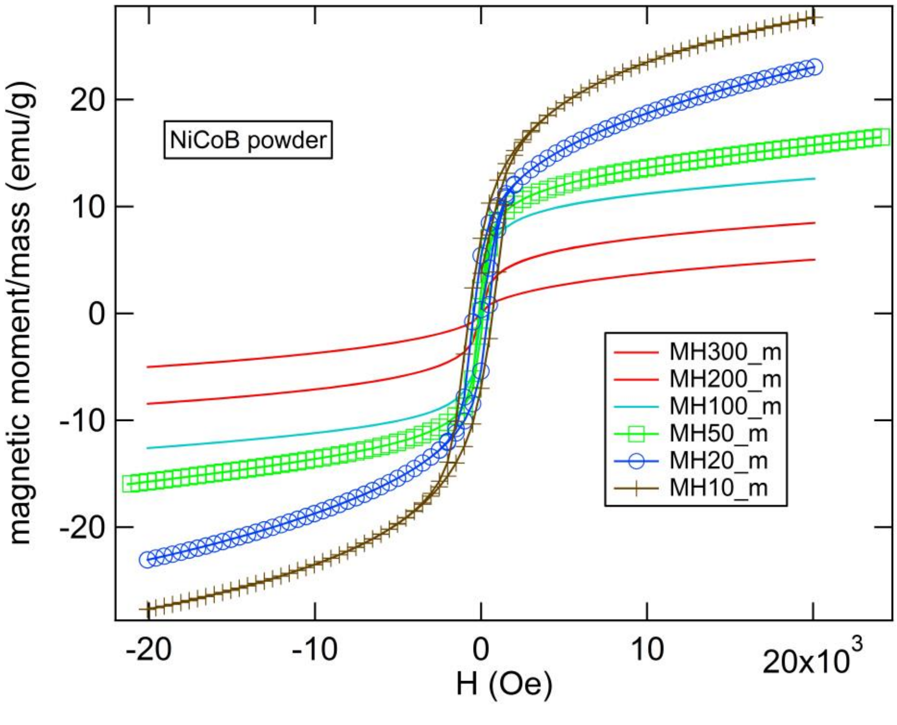

Figure 3.24: Hysteresis loops of magnetisation vs. field at different temperatures.

3.6 Silver Nanoparticles and Silver Coated with Graphene Oxide

3.6.1 Introduction

Synthesis of Ag nanoparticles is very common among many research teams. In general, obtaining nano-silver is very easily achieved by reduction of silver salts in aqueous solution by various reducing agents, such as hydrazine or $NaBH_4$. By using different surfactants, catalysts, and solvents it is possible to get different sizes, shapes, and compounds of silver. Also, the use of nano-silver is widespread in many branches of industry, technology, and medicine, particularly due to its strong antibacterial action.[18,19]

3.6.2 Ag and Ag/GO synthesis

Silver nanoparticles were synthesised by a wet technique with chemical reduction of silver salts, similar to the previous synthesis. Approximately 0.0035 mol of $Ag(NO_3)_2$ salt was dissolved in 30 ml DI water. In a separate three necked beaker, 1 ml (0.031 mol) of hydrazine was dissolved in 30 ml of DI water, with 3 droplets of ethylenediamine to provide an alkaline environment (≈10 pH).

Excess reducing agent (10 times more concentration than silver salt) and an alkaline environment provide the best conditions for rapid and strong reduction of silver salts. In alkaline solution the reaction proceeds according to the chemical reactions in Equations (3.11) and (3.12):

$$N_2H_4(l) + H_2O(l) \rightarrow N_2H_5^+OH^-(aq) \qquad (3.11)^{20}$$

$$N_2H_5^+OH^-(aq) + Ag^+(aq) \rightarrow Ag(s) + N_2(g) + H_2O(l) \qquad (3.12)$$

At all times during the experiment, reactants were maintained under argon protective atmosphere. Shiny gray precipitates were formed and collected in a cuvette. The powder was centrifuged and washed several times with DI water and acetone to remove residual ions. Finally, the powder was dried in vacuum desiccators.

Graphene oxide (GO) coated Ag nanoparticles were prepared in a few steps. First of all, graphene was oxidized into the graphene oxide with $KMnO_4$ in an acidic environment.

After the oxidation of graphene in aqueous solution, the prepared Ag nanoparticles were added and stirred for 2 hours. Finally, the powder was centrifuged, washed, and dried in vacuum desiccators.

3.6.3 Experimental results and discussion

3.6.3.1 SEM analysis

Morphologically, silver nanoparticles coated with graphene oxide have two different structural forms. Figure 3.25(a) indicates small particles with spherical structures and agglomerated clusters. The agglomerated clusters have irregular shape and size. The small particles have sizes around 100 nm and a spherical shape. Figure 3.25(b) presents a transparent network of graphene oxide with embedded spherical particles. It is interesting to observe that the embedded particles of silver have smaller size than the particles in Figure 3.25(a). That can be explained from the prevention of agglomeration, mostly by Ostwald ripening[21], due to stacking in the graphene oxide matrix.

The network actually prevents interaction between particles and thus the agglomerating process. On oxidation, there are large graphene sheets several microns in size, although and more are in smaller pieces in the nanosize range. At the same time, inert and monolithic graphene has been transformed by oxidation into graphene oxide with reactive functional groups such as -OH$^-$ and -COOH$^-$. Silver nanoparticles interact with those groups, mostly due to electrostatic interaction, and are pinned in the graphene oxide net.

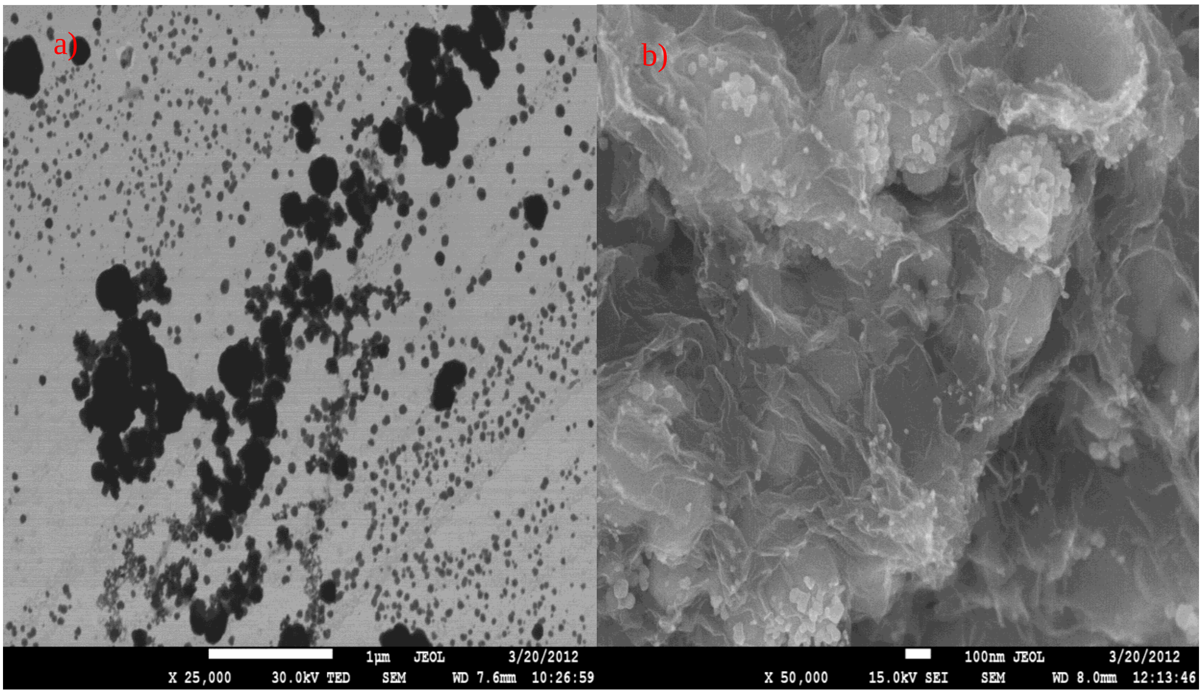

Figure 3.25 (a), (b): SEM images of Ag/GO at different magnifications.

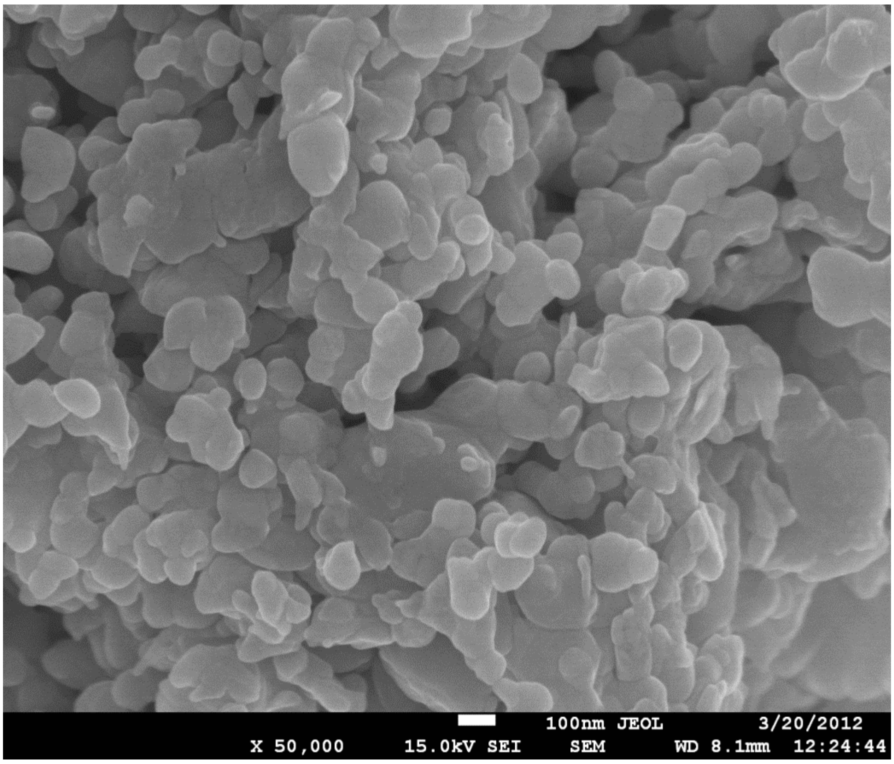

Figure 3.26: SEM image of Ag nanoparticles.

Figure 3.27 shows the size distribution of Ag particles. The observed grain sizes were put into categories and fitted by normal distribution functions. The majority of Ag particles have sizes between 100 and 120 nm.

The particles size is broadly distributed with the smallest particles size around 40 nm and the largest around 220 nm. Also, the shapes of the particles are mostly irregular, which can indicate a strong agglomeration process. Surfactant, which has a strong influence on the size distribution of particles, was not used during the synthesis.

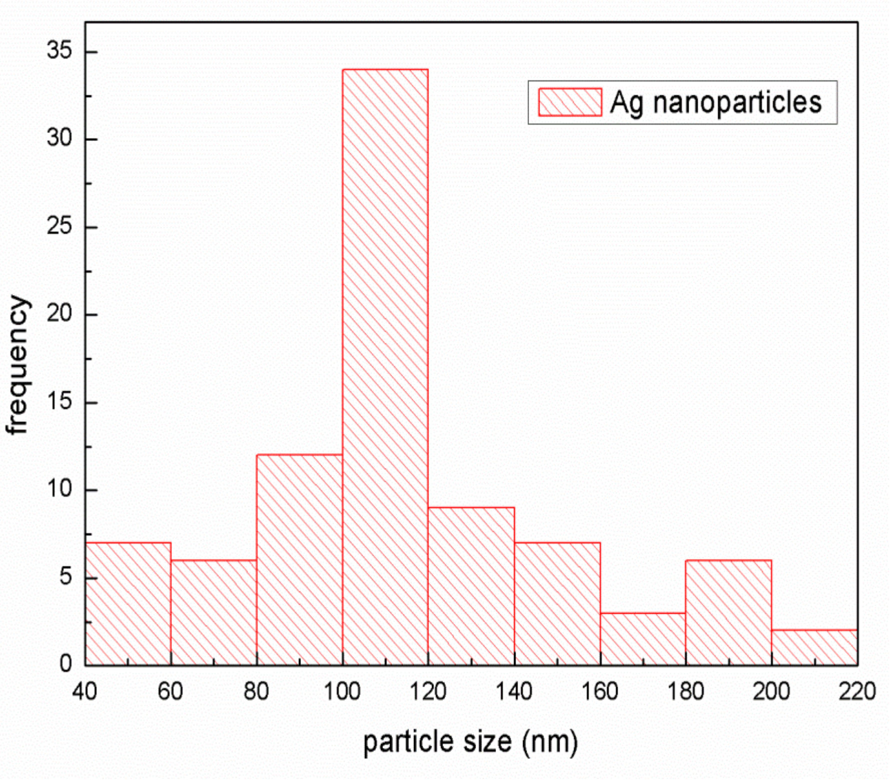

Figure 3.27: Size distribution of silver particles.

3.6.3.2 XRD analysis

Figure 3.28 shows XRD patterns of pure Ag and Ag coated with graphene oxide. Three sharp peaks at 38°, 45°, and 65° belong to pure Ag. The XRD pattern of Ag/GO contains graphen oxide peaks at 13°, 14.5°, and 17°.

The strong difference in intensity between the Ag and GO peaks indicates that there is only a very small amount of graphene oxide. As can be seen in Figure 3.25(b), the graphene oxide network is very thin (several nm) and transparent.

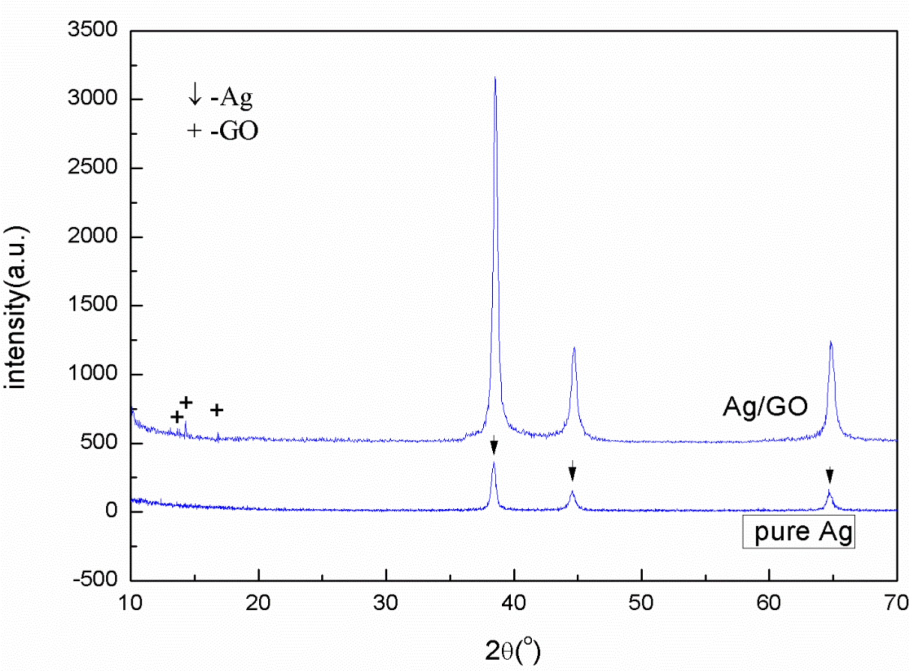

Figure 3.28: XRD pattern of Ag and Ag/GO powders.

3.6.4 Conclusion

The Fe_2B and Fe_2B/SiO_2 nanoparticles were sintered on very beginning of this study, and shows elementary problems of agglomeration, especially for core-shell structure. In synthesis of Fe_2B nanoparticles have been showed that the composition of magnetic particles with amorphous structure can be selected by choosing precursors and synthesis conditions in the reaction of reduction of metal ions by use of $NaBH_4$. Also has been produced core-shall structured nanoparticles, Fe_2B/SiO_2 in order to further change the properties and stability of magnetic particles. The complex magnetic behaviour is probably due to very broad size distribution of produced particles, with smaller particles contributing superparamagnetic behaviour and the bigger ones being ferromagnetic.

In the further work were synthesised amorphous particles of magnetic alloy NiCoB and $NiCoB/SiO_2$ through chemical method of co-precipitation in solution of metalic salts with average size smaller than 20 nm. Magnetic behaviour for both uncoated and coated NiCoB particles exhibit superparamagnetic behaviour, which can be well described within model of relaxation of magnetic moments of particles.

As a promising candidate for doping superconductors research with NiCoB nanoparticles have been continued. Further modification of chemical treatment had achieved nanoparticles with size of 5 nm, which have yielded the best results in the doping of MgB_2.

The obtained silver nanoparticles have shown very pure composition without any impurities and have an average particle size around 110 nm. The reason why the grain size is larger than 100 nm is because surfactant was not used during the reaction synthesis. A further major achievement is the creation of a complex structure of silver with graphene oxide. Here, two different morphological structures are obtained: Ag/GO clusters and the structure of the silver particles in the graphene oxide network.

3.7 References

1 F. Schüth, A.-H. Lu, and E. L. Salabas,, Magnetic Nanoparticles: Synthesis, Protection, Functionalization, and Application, Angew. Chem. Int. Ed., 46, 1222 – 1244, 2007

2 M. Knobel, W. C. Nunes, A. L. Brandl, J. M. Vargas, L. M. Socolovsky, and D. Zanchet, Physica 354, 80–87. 2004.

3 E. C. Stoner and E. P. Wohlfarth, Phil. Trans. Roy. Soc. London A240 (1948) 599–642, reprinted in IEEE Trans. on Magnetics 27 3475–3518., 1991.

4 J. Jiang, I. Dézsi, U. Gonser, X. Lin, J. Non-Crystalline Solid. 124**,** 139–144. 1990.

5 C. Saiyasombat, N. Petchsang, I. M. Tang, J. H. Hodak, Nanotechnology 19, 085705 (7pp). 2008.

6 M. Mustapić, D. Pajić, N. Novosel, E. Babić, K. Zadro, M. Cindrić, J. Horvat, Ž. Skoko, M. Bijelić, and A. Shcherbakovc, Synthesis, Structural Characterization and Magnetic Properties of Iron Boride Nanoparticles with or without Silicon Dioxide Coating, Chem. Acta 83,000. 2010.

7 A. T. Raghavender, D. Pajić, K. Zadro, T. Mileković, P. V. Rao, K. M. Jadhav, and D. Ravinder, J. Magn. Magn. Mater. 316 1–7. 2007.

8 D. Pajić, K. Zadro, R. E. Vanderberghe, and I. Nedkov, J. Magn. Magn. Mater. 281 353–363. 2004.

9 P. Allia, M. Coisson, P. Tiberto, F. Vinai, M. Knobel, M. A. Novak,and W.C. Nunes, Phys. Rev. B 64, 144420 (12pp). 2001.

10 M. Knobel, W. C. Nunes, A. L. Brandl, J. M. Vargas, L. M. Socolovsky, and D. Zanchet, Physica B 354, 80–87. 2004.

11 S. Blundell, Magnetism in Condensed Matter, Oxford University Press, New York, 2001

12 G. F. Korznikova, A. V. Korznikov, L. A. Syutina, and Kh.Ya. Mulyukov, J. Magn. Magn. Mater. 196–197, 207–208., 1999.

13 E. M. Chudnovsky and J. Tejada, Macroscopic Quantum Tunneling of the Magnetic Moment, Cambridge University Press, Cambridge, U.K., 1998.

14 C. P. Bean and J. D. Livingston, J. Appl. Phys. 30 S120−129. 1959.

15 N. Novosel, D. Pajić, Ž. Skoko, I. Lončarek, Stipe Galić, M. Mustapić, E. Babić, A. M. Tonejc, K. Zadro, Magnetic behaviour of amorphous NiCoB nanoparticles uncoated and coated in silicon dioxide, in preparation.

16 R. D. Zysler, H. Romero, C. A. Ramos, E. De Biasi, D. Fiorani, J. Magn. Matter. 266, 233–242. 2003.

17 Z. Skoko, J. Popovic, K. Dekanic, V. Kolbas and S. PopovicJ. Appl. Cryst. (2012). 45, 594-597

18 Lee, P. C., Meisel, D. J. Phys. Chem.**,** 86, 3391–3395, 1982.

19 Fang, Y. J. Chem. Phys.**,** 108, 4315, 1998.

20 Holleman, A. F.; Wiberg, E. "Inorganic Chemistry" Academic Press: San Diego, 2001.

21 W. Ostwald. Lehrbuch der Allgemeinen Chemie, vol. 2, part 1, 1896.

Chapter 4: Doping of MgB_2 with various metal-boride nanoparticles

4.1 Introduction

This study investigates the effects of various metal boride and metal oxide compounds on the electromagnetic properties of MgB_2 superconductors. Borides are compounds between transition metals or rare earths and boron. Metal borides are inert compounds with layered structures and high melting points. Magnetic properties are mostly paramagnetic and ferromagnetic. It was hoped that doping MgB_2 with magnetic borides would ensure better incorporation of magnetic nanoparticles into the MgB_2 matrix than some other compounds. There is also a possibility that chemical reactions would occur whereby magnetic ions would be doped into MgB_2. Grain connectivity was also expected to be better than for doping with other types of magnetic nanoparticles because of the expected tight incorporation of the nanoparticles into MgB_2.

This PhD program was a part of a bigger project between the University of Wollongong and the University of Zagreb, aimed at investigating the possibility of increasing the vortex pinning in MgB_2 by magnetic doping. Table 4.1 gives an overview of all nanoparticles doped into MgB_2 within this project, together with sintering temperatures for MgB_2 doped with the respective nanoparticles. All samples in series A-F were wires, whereas those in G-I were pellets. The combinations of nanoparticles and sintering procedures that resulted in improved critical current density (J_c) of MgB_2 are highlighted in green. The best results were obtained for next samples, followed by MgB_2 wires doped with 1.25wt% and 2.5wt% NiCoB (Series F), and 1.25 and 2.5wt% Ni/C, also in the form of wires. All samples in series A-F were prepared in Zagreb and sintered at 650°C or 750°C, whereas the samples in series G-I were prepared in Wollongong and sintered in temperature range from 650 to 950°C.

Samples prepared in Wollongong showed the best results for 2.5wt% NiCoB sintered at 850°C with J_c of 82000 A/cm^2 at 2 T and 20 K (Series G).

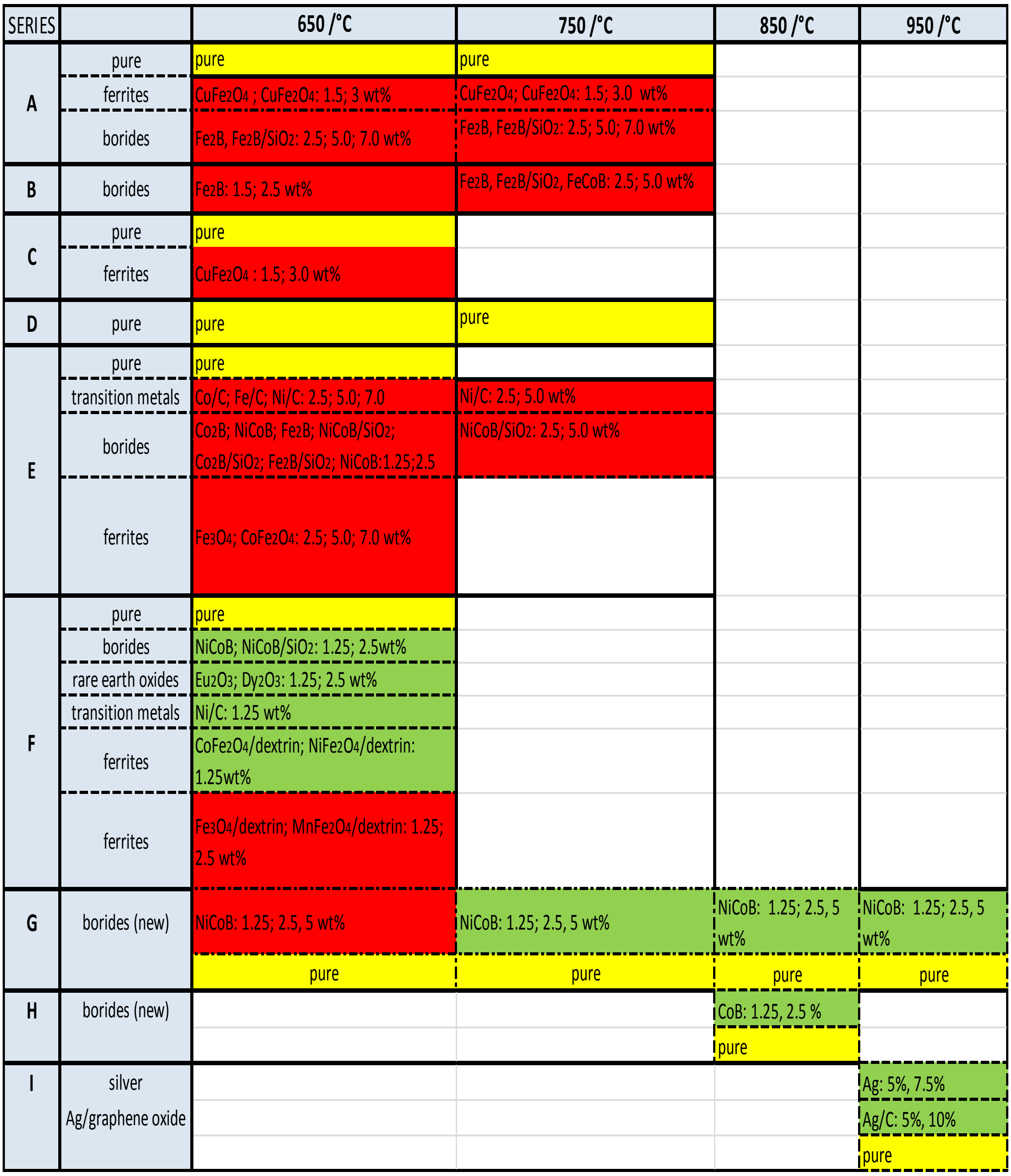

SERIES		650 /°C	750 /°C	850 /°C	950 /°C
A	pure	pure	pure		
	ferrites	$CuFe_2O_4$; $CuFe_2O_4$: 1.5; 3 wt%	$CuFe_2O_4$; $CuFe_2O_4$: 1.5; 3.0 wt%		
	borides	Fe_2B, Fe_2B/SiO_2: 2.5; 5.0; 7.0 wt%	Fe_2B, Fe_2B/SiO_2: 2.5; 5.0; 7.0 wt%		
B	borides	Fe_2B: 1.5; 2.5 wt%	Fe_2B, Fe_2B/SiO_2, FeCoB: 2.5; 5.0 wt%		
C	pure	pure			
	ferrites	$CuFe_2O_4$: 1.5; 3.0 wt%			
D	pure	pure	pure		
E	pure	pure			
	transition metals	Co/C; Fe/C; Ni/C: 2.5; 5.0; 7.0	Ni/C: 2.5; 5.0 wt%		
	borides	Co_2B; NiCoB; Fe_2B; $NiCoB/SiO_2$; Co_2B/SiO_2; Fe_2B/SiO_2; NiCoB:1.25;2.5	$NiCoB/SiO_2$: 2.5; 5.0 wt%		
	ferrites	Fe_3O_4; $CoFe_2O_4$: 2.5; 5.0; 7.0 wt%			
F	pure	pure			
	borides	NiCoB; $NiCoB/SiO_2$: 1.25; 2.5wt%			
	rare earth oxides	Eu_2O_3; Dy_2O_3: 1.25; 2.5 wt%			
	transition metals	Ni/C: 1.25 wt%			
	ferrites	$CoFe_2O_4$/dextrin; $NiFe_2O_4$/dextrin: 1.25wt%			
	ferrites	Fe_3O_4/dextrin; $MnFe_2O_4$/dextrin: 1.25; 2.5 wt%			
G	borides (new)	NiCoB: 1.25; 2.5, 5 wt%	NiCoB: 1.25; 2.5, 5 wt%	NiCoB: 1.25; 2.5, 5 wt%	NiCoB: 1.25; 2.5, 5 wt%
		pure	pure	pure	pure
H	borides (new)			CoB: 1.25, 2.5 %	
				pure	
I	silver				Ag: 5%, 7.5%
	Ag/graphene oxide				Ag/C: 5%, 10%
					pure

Table 4.1: All samples prepared during the PhD candidature.

As can be seen in the Table 4.1, different metal compounds were sintered at different temperatures with wide doping percentages. Over the course of the whole project, more than

10 different compounds have been investigated. Besides manipulating the sintering temperature and doping levels, various starting precursors and forms of samples (bulk, wires) were also investigated.

Only NiCoB nanoparticles showed consistent enhancement of critical current under different sintering conditions, with different types of boron as precursors, and different doping levels.

Because of this, the thesis is mostly focused on enhancement of the electromagnetic properties of MgB_2 doped with NiCoB nanoparticles (Chapters 5.1, 5.2, 5.3, 5.4).

For the sake of completeness, however, the results obtained with other nanoparticles doped into MgB_2 wires are briefly described, as a part of collaborative research at Zagreb University. The main responsibility of the candidate was the preparation of magnetic nanoparticles and doping them into MgB_2 at Zagreb University. This was extended into full sample characterization and preparation at Wollongong University.

The first part of PhD project (Series A-F) was done at the University of Zagreb. All samples from Zagreb were made in wire form. The boron used as precursor was Tangshan crystalline boron with purity of 96%. Iron-boride nanoparticles (Fe_2B) showed decreasing critical current density for all samples.

Different metal-oxide compounds (spinel) also did not give any success. Purchased elementary metal nanoparticles (Ni, Fe, and Co coated with thin film of carbon) produced an increase in critical current only in the case of nickel.

The second part of the PhD work was continued in Wollongong at the Institute for Superconducting and Electronic Materials (ISEM), and the research was expanded in several ways for the most promising nanoparticles: NiCoB.

A new way of preparing NiCoB nanoparticles of smaller size was developed, which gave better J_c. Different types of boron were tried for preparing MgB_2 pellets, and the boron most suitable for doping with NiCoB was identified. Best sintering procedure for NiCoB doped

MgB_2 was obtained, using the most suitable boron. Finally, the mechanism for improvement of J_c in nano-NiCoB doped MgB_2 pellets was obtained. All this work will be described in Chapters 5.3.

4.2 Fe_2B and Fe_2B/SiO_2 doped MgB_2

A brief overview of nano-Fe_2B and nano-Fe_2B coated with SiO_2 is presented in this section. The bare Fe_2B nanoparticles were expected to at least partly react with Mg, facilitating the incorporation of the nanoparticles into MgB_2. The SiO_2 coating, on the other hand, was expected to protect the Fe_2B nanoparticles from reactions, giving us a more insightful picture into the processes associated with this kind of doping.

4.2.1 Experimental part

Powders of magnesium (Mg, 99%) and amorphous boron (B, 99%) were well mixed in a mortar. For preparation of the doped MgB_2 wires 3, 7.5, and 12 wt% of Fe_2B and SiO_2-coated Fe_2B particles were added, respectively.

Coated Fe_2B nanoparticles have an average size of around 170 nm, while the uncoated Fe_2B particles were smaller, with an average size around 80 nm. The mixed powders were packed into pure Fe tubes of 10 mm and 6.5 mm outer and inner diameter, respectively. The tubes were drawn to wires 1.41 mm in diameter and with a core diameter of 0.8 mm. Finally, the reaction heat treatment was performed at 650°C and 750°C for 60 min, with a heating rate of 5 K/min in pure argon atmosphere.[1]

The X-ray diffraction (XRD) intensity was measured in the angular range of $20° \leq 2\theta \leq 70°$. Magnetization was measured at temperatures of 20 K and 5 K in magnetic fields up to 9 T using a physical properties measurement system (PPMS, Quantum Design). Magnetic critical current density values were determined from the magnetic hysteresis loops using the critical state model.[2,3] The resistance R(T,B) of the prepared samples was measured in the temperature range of 2–40 K in applied magnetic fields up to 16 T using AC current (I = 1 mA, f = 18.4 Hz)[4]. The transport J_c(B) curves were obtained from the V – I curves measured using the pulse method (rectangular pulses with a duration of 0.5 ms with maximum current of 320 A) at 20 K and 5 K.[1]

4.2.2 Experimental Results

4.2.2.1 XRD analysis

Samples doped with Fe_2B [5] (Figure 4.1) also showed the presence of FeB and Fe_2B crystalline phases in amounts which increased with increasing doping level. The XRD pattern of the sample doped with 7.5 wt% Fe_2B/SiO_2 particles[5] showed minor phase FeB. The amount of MgO increased with rising doping level. Both doped samples have the same phases and same intensity of corresponding peaks in XRD.

Figure 4.2(b) shows the XRD patterns of the Fe_2B/SiO_2 doped MgB_2 samples. In Fe_2B/SiO_2 doped wires, the amount of MgO phase increased with increasing doping level. The appearance of FeB phase and the increase in the amount of MgO phase with increasing doping with Fe_2B/SiO_2 particles indicate that to some extent a reaction between Mg, B, and the nanoparticles occurred during annealing of wires. This indicates that the SiO_2 coating around the Fe_2B particles was damaged during the preparation of wires, enabling the chemical reaction.[1]

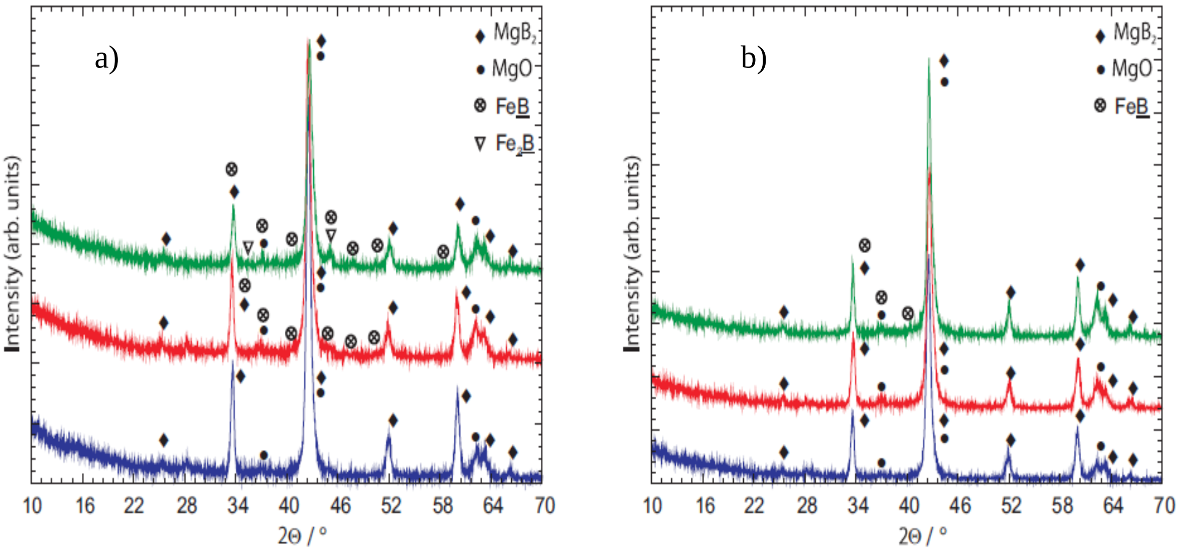

Figure 4.1: a) XRD patterns for Fe_2B doped MgB_2 samples (left): 0% (blue, bottom), 3 % (red, middle), 7.5 % (green, top). b) XRD patterns for Fe_2B/SiO_2doped MgB_2 samples (right): 0% (blue, bottom), 3 % (red, middle), 7.5 % (green, top). Adopted from [1].

4.2.2.2 Temperature dependence of resistance

In Figures 4.2(a) and (b) resistance R versus temperature T plots for un-doped and doped MgB_2 wires in applied magnetic fields are shown. A strong shift of the superconducting transition temperature, T_c, for undoped MgB_2 wire with magnetic field is observed, which is a consequence of the weak flux pinning in undoped bulk MgB_2 samples [6,7].

For doped wires (both Fe_2B and Fe_2B/SiO_2 particles)[5] T_c decreases as the doping level increases.

Shifting of T_c towards lower temperatures and broadening of the transition with increasing magnetic field is more pronounced for doped MgB_2 wires than for the undoped one, indicating that enhancement of the flux pinning in doped wires was not achieved.

T_{c0} decreases quite rapidly with the doping level, namely 0.72 K/wt% and 0.45 K/wt% for Fe_2B and Fe_2B/SiO_2 doped wires, respectively. For comparison, the rate of decrease of T_c in SiC doped MgB_2 is about 0.2 K/wt% [8,9]. The magnetic moment of the Fe_2B and Fe_2B/SiO_2 particles probably caused the breaking of Cooper pairs and additional reduction of T_c.

Larger resistance of samples doped with 3 wt.% of nanoparticles is due to the larger distance between the voltage leads in these wires (Fig 4.2(a)).

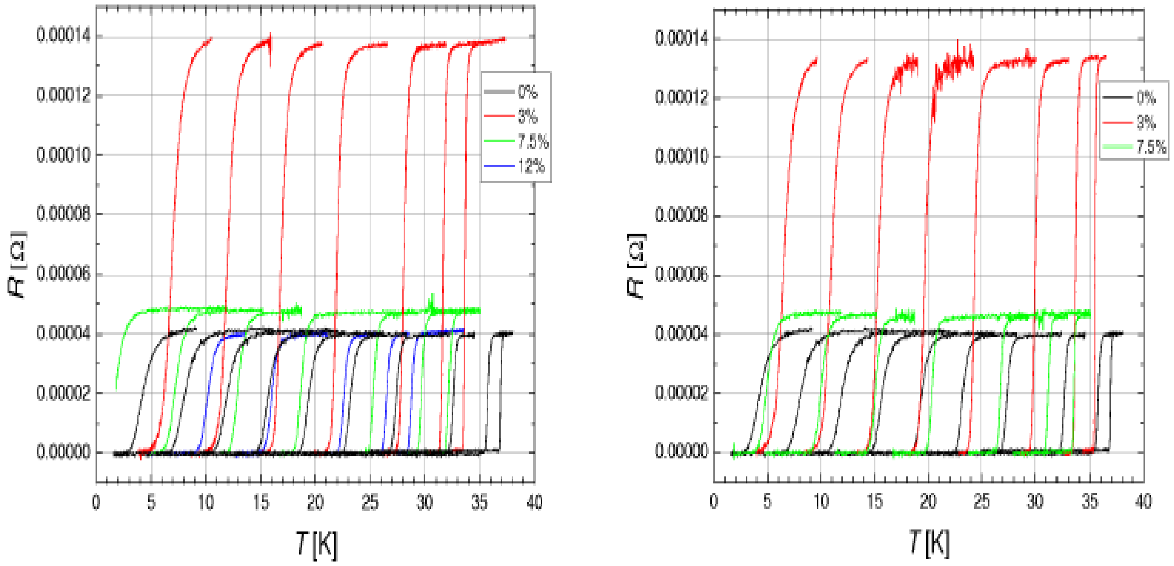

Figure 4.2:(a) Resistance versus temperature for undoped and Fe_2B doped MgB_2/Fe wires in magnetic fields: (right to left) B =0, 1, 2, 4, 6, 8, 10, 12, 14, 16 T. (b) Resistance versus temperature for undoped and Fe_2B/SiO_2 doped MgB_2/Fe wires in magnetic fields: (right to left) B =0, 1, 2, 4, 6, 8, 10, 12, 14, 16 T. Adopted from [1].

4.2.2.3 Transport and magnetic measurements of critical current density

The field dependence of the magnetic and transport critical current densities is shown in Figures 4.3 and 4.4. The transport J_c shows larger values than the magnetic J_c for all samples, which is in accordance with results given in[10]. As observed in Figures 4.4 and 4.5, J_c(B) curves for undoped and doped (both Fe_2B and Fe_2B/SiO_2) MgB_2 wires follow approximately the same trend both at high (20 K) and low (5 K) temperature, implying that the main pinning mechanism is the same.

Generally, all doped samples show decreasing J_c(B) with doping level. The reason for this is most likely worsening of the connectivity between the MgB_2 grains by doping. Furthermore, breaking of Cooper pairs caused from Fe and its compounds can also be responsible. [11]

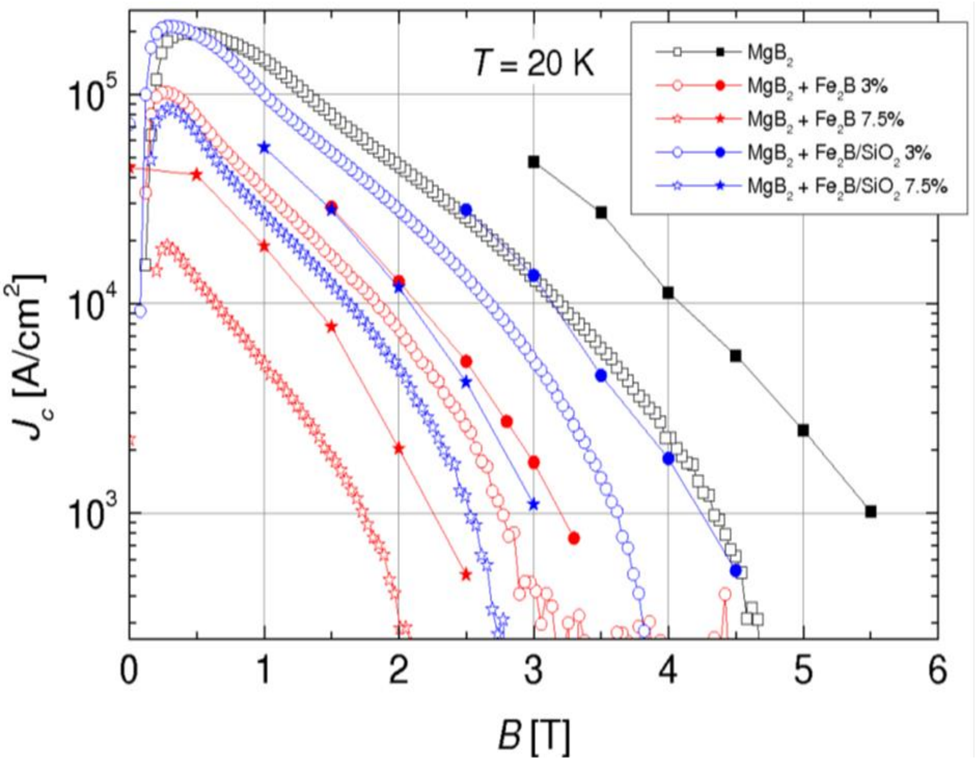

Figure 4.3: Magnetic (open symbols) and transport (solid symbols) critical current density versus applied magnetic field for undoped and doped (Fe_2B and Fe_2B/SiO_2) MgB_2 wires at 20 K. Adopted from [1].

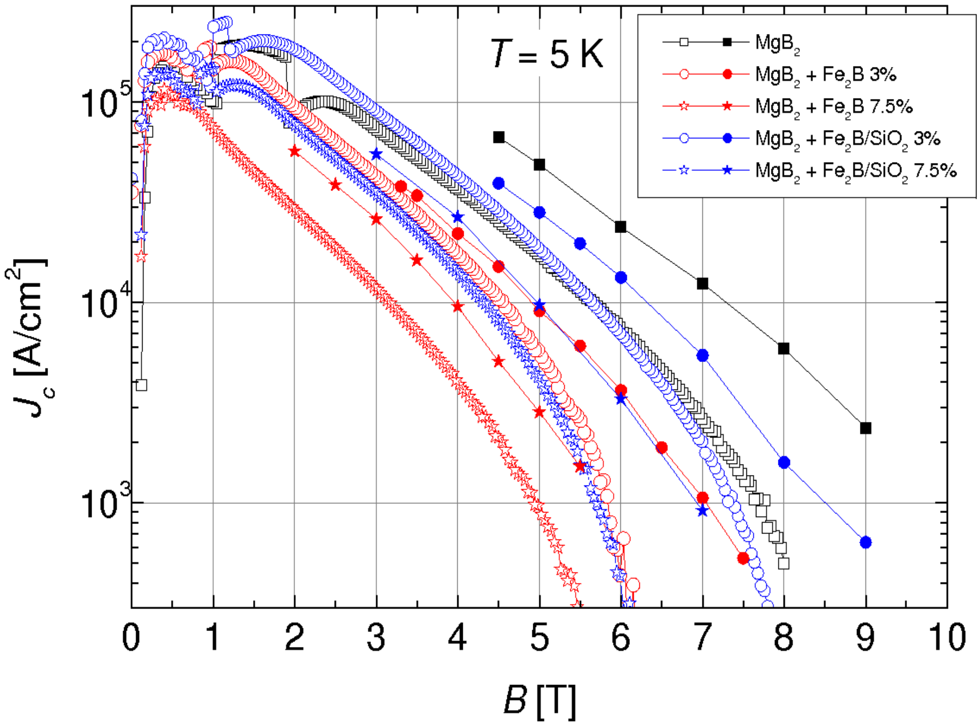

Figure 4.4: Magnetic (open symbols) and transport (solid symbols) critical current density versus applied magnetic field for undoped and doped (Fe_2B and Fe_2B/SiO_2) MgB_2 wires at 5 K. Adopted from [1].

Kramer plots of $J_c^{1/2} B^{1/4}$ versus B are shown in Figure 4.5. The rather curved Kramer plots for the doped wires indicate considerable inhomogeneity of the samples. During the preparation of the samples, agglomeration of the Fe_2B and Fe_2B/SiO_2 particles probably occurred because of their magnetic interaction. This probably enhanced the detrimental effects of the magnetic particles on the electromagnetic properties of MgB_2 wires.

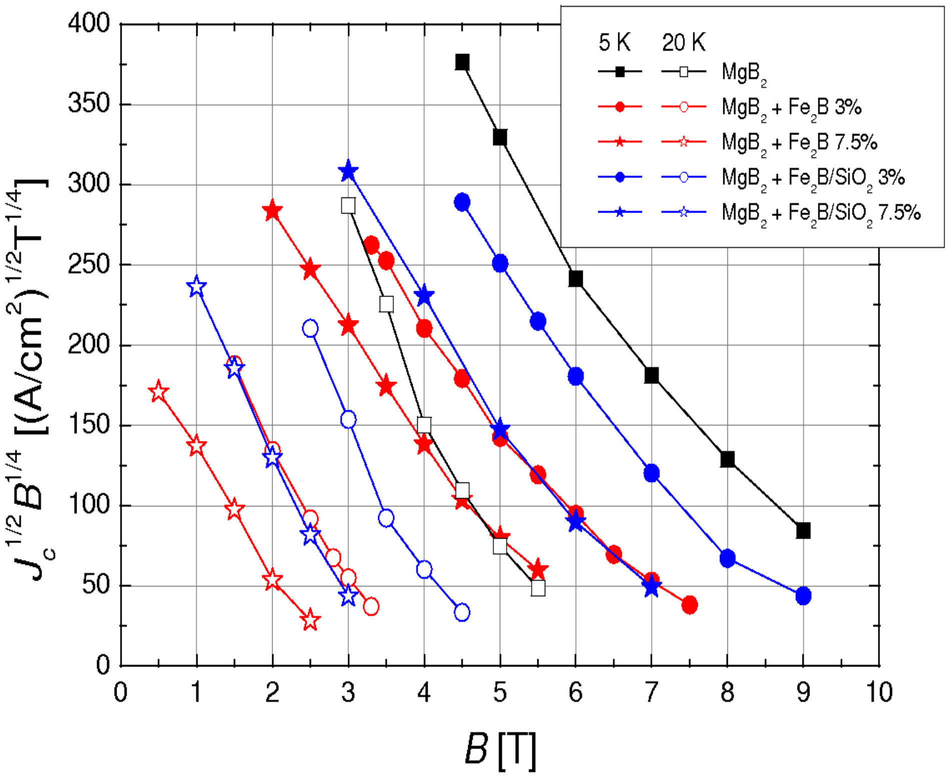

Figure 4.5: Kramer plots for undoped and doped (Fe_2B and Fe_2B/SiO_2) MgB_2 wires.[1]

4.2.3 Conclusion

This study indicates that MgB_2 wires doped with magnetic nanoparticles ≥ 50 nm in size are unlikely to show any enhancement of flux pinning. Rather strong suppression of the transition temperature T_c and $J_c(B)$ are observed with increasing content of the magnetic additive (Fe_2B), which probably indicates that magnetic pair breaking prevails in the doped samples. These detrimental effects are probably aided by inhomogeneities introduced into the samples by the dopants, as evidenced by the strongly curved Kramer plots of the doped samples. All this shows that the magnetic flux pinning situation in bulk MgB_2 samples is much more complex than that encountered in thin films.[12]

4.3 MgB_2 wires doped with Ni nanoparticles

4.3.1 Introduction

The main pinning mechanisms in MgB_2, as observed experimentally, are grain boundary pinning and pinning of vortices on non-magnetic nano-inclusions. Near grain boundaries, the coherence length becomes shorter due to the enhanced electron scattering, which results in attractive interaction between the grain boundary and vortices.

Normal impurities inside the superconductor also act as attractive pinning centres due to the recovery of part of the condensation energy of the vortex when it is situated at a non-superconducting impurity.

Enhancement of vortex pinning by a regular lattice of magnetic dots in superconducting thin films has been observed experimentally and theoretically predicted. [13,14,15,16]

Bulk superconducting materials with magnetic nano-inclusions have not been explored in great detail, neither experimentally nor theoretically[11,17,18].

The combination of magnetic pinning with carbon doping (more effective at high fields[19]) should enhance the electromagnetic properties of MgB_2 over the entire field range. Magnetic pinning depends on the magnitude and orientation of the magnetization vector of the particle, which makes this problem complex and challenging for both theoretical and experimental investigation. [20]

4.3.2 Experimental part

Iron sheathed MgB_2 wires doped with 0, 1.25, and 2.5 wt% carbon protected nickel super-paramagnetic nanoparticles (average diameter of particles 20 nm) and sintered at 650°C were prepared. The undoped and doped Fe-sheathed MgB_2 wires were prepared by the in-situ reaction method and the powder-in-tube technique. For preparation of doped wires were used commercial (NanoAmor Inc., USA) nickel nanoparticles (NP) protected with carbon, with average particle diameter of 20 nm. For the undoped MgB_2 sample, powders of magnesium (Tangshan Weihao Magnesium Powder Co. Ltd, China, 400 mesh) and nanocrystalline boron (Speciality Materials, Inc., USA, 0.02 − 0.1 μm) were mixed in the atomic ratio of 0.95 Mg : 2 B.

In experiment was used a smaller amount of magnesium because the sample prepared using the stoichiometric ratio of Mg and B powders resulted in a high amount (> 12 %) of unreacted magnesium, which had a detrimental influence on the electromagnetic properties of such a wire. (J_c decreased rapidly with the increasing magnetic field.) The measurement procedure was the same as in section 4.2.1.[21]

4.3.3 Results and Discussion

4.3.3.1 XRD results

XRD patterns of the undoped MgB_2 sample and the sample doped with 2.5 wt.% Ni/C nanoparticles are shown in Figure 4.6. Both the XRD patterns show well developed MgB_2 phase with approximately the same average crystallite size: 35 nm, as deduced from the Scherrer formula applied to the (100) and (002) maxima in the XRD patterns. Also, the presence of MgO phase (10 %) and a small amount (< 4%) of unreacted magnesium was detected.

The presence of nickel particles in the doped sample could not be detected due to the low doping level and the small amount of powder used for XRD analysis. XRD revealed that both the *a*-axis and the *c*-axis parameters of the MgB_2 lattice remained unchanged (within the experimental uncertainty) after doping with the carbon coated nickel particles, which may indicate that neither C substitution for B[22] nor Ni substitution for Mg [23] occurred.

This is not a surprising result because the reaction heat treatment was performed at relatively low temperature (650°C), at which C substitution for B in the MgB_2 lattice is very unlikely to take place, unless a highly reactive dopant is used (for example, when MgB_2 is doped with SiC nanoparticles and highly reactive C is produced).[24]

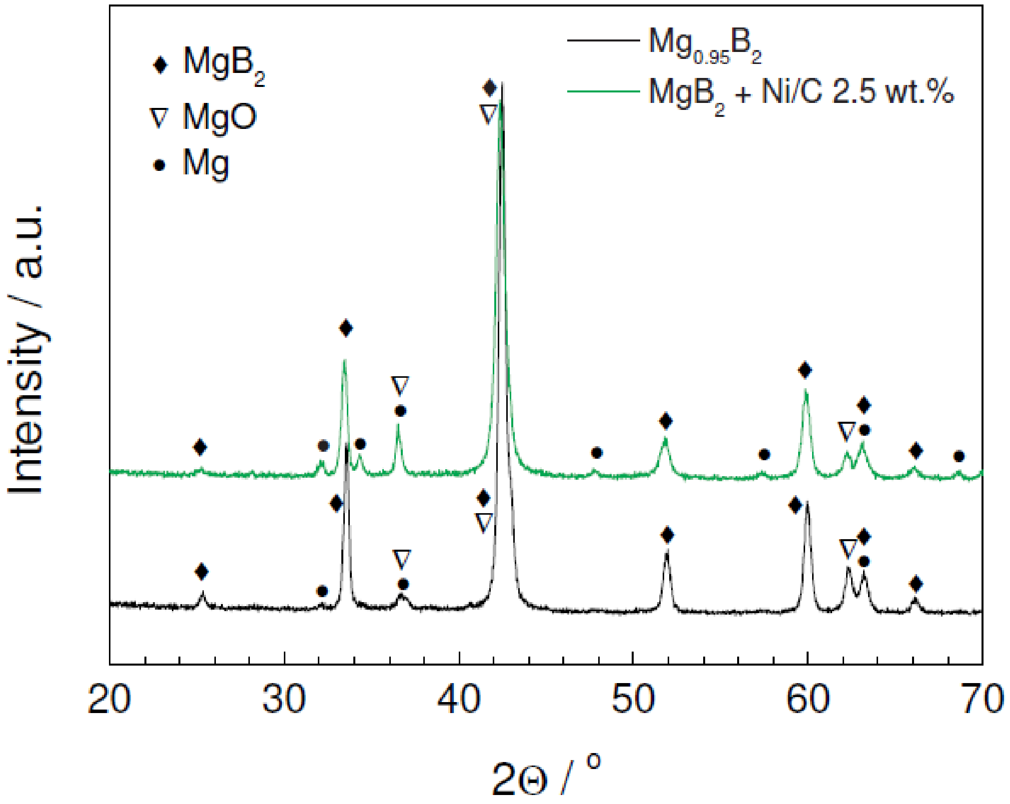

Figure 4.6: XRD patterns for undoped MgB_2 sample (black, lower curve) and MgB_2 doped with 2.5wt% Ni/C particles (green, upper curve). Adopted from [21].

4.3.3.2 SEM images

Figure 4.7(a) shows scanning electron microscope (SEM) images of the undoped MgB_2 sample and the sample doped with 2.5 wt% Ni/C nanoparticles. The size of the MgB_2 grains is approximately 230 ± 60 nm and 220 ± 60 nm for the undoped and the doped sample, respectively. Figure 4.7(b) presents energy dispersive X-ray spectroscopy (EDS) mapping of the MgB_2 sample doped with 2.5 wt% Ni/C nanoparticles.

MgB_2 grains and some MgO crystals (bright) can be clearly seen, as well as spherical particles located between the MgB_2 grains. EDS spectrum analysis revealed that these particles are composed of nickel or magnesium.

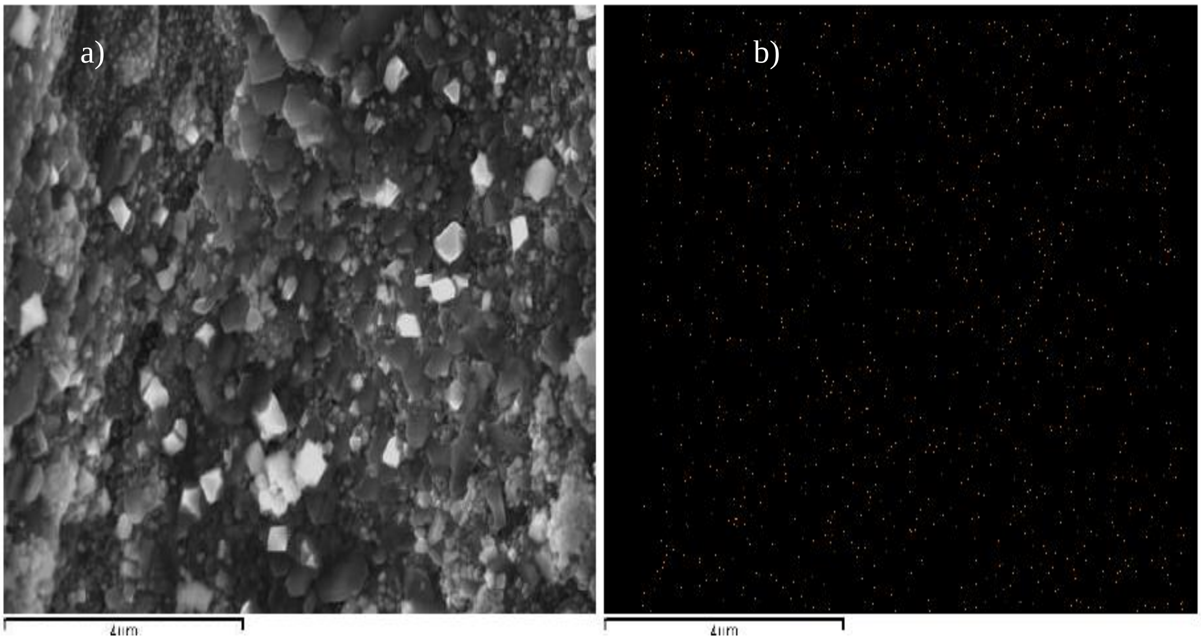

Figure 4.7: (a) SEM image of MgB_2 doped with 2.5 wt% Ni/C nanoparticles; (b) corresponding EDX mapping of Ni. Adopted from [21].

4.3.3.3 Electromagnetic properties

As expected, doping MgB_2 with Ni/C particles resulted in reduction of T_{c0}, where T_{c0} is the transition temperature at 0 T applied field. The rate of reduction of T_{c0} with tincreasing doping level is quite high, namely 1.4 K/wt%. The sharp diamagnetic transition indicates good homogeneity of the wires. Similar behaviour of T_{c0} with similar rates of suppression of T_{c0} was observed in MgB_2 samples doped with a variety of magnetic particles (Ni, Co, Fe, or Fe-based). [11, 1, 23, 25]

The active cross-sectional area, A_F, defined as $A_F = \Delta\rho_{ideal}/(\rho(300\ K)-\rho(40\ K))$, where $\Delta\rho_{ideal} = 7.3\ \mu\Omega cm$ is the change in resistivity between 300 K and 40 K for a fully connected MgB_2 sample[26], was also calculated, and the results are given in Table 4.2. Resistivity increases with increasing doping level, and A_F decreases accordingly. The presence of magnetic Ni particles, which causes additional electron scattering, probably explains both the higher resistivity and the lower A_F.

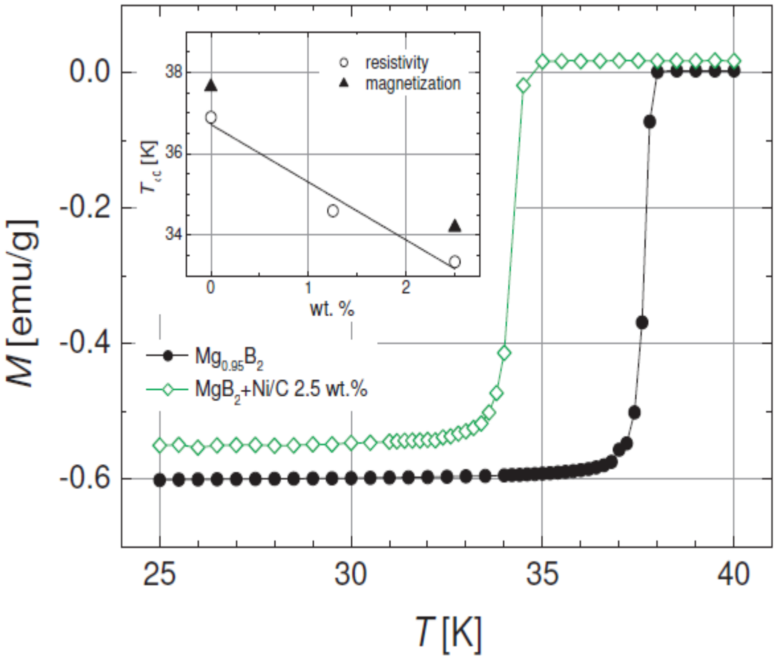

Figure 4.8: Temperature dependence of magnetization measured in applied field μ_0H = 1 mT of undoped MgB_2 (black, solid symbols) and MgB_2 doped with 2.5 wt.% Ni/C NPs (green, open symbols). The inset shows the dependence of T_{c0} on the doping level. Adopted from [21].

sample	T_{c0} [K]	ρ(40 K) [$\mu\Omega$cm]	A_F
$Mg_{0.95}B_2$	36.9	15.6	0.27
MgB_2+Ni/C 1.25 wt.%	34.6	27.7	0.225
MgB_2+Ni/C 2.5 wt.%	33.35	34.5	0.212

Table 4.2 Superconducting transition temperature in zero applied field T_{c0}, resistivity at 40 K, ρ(40 K), and active cross-sectional area A_F. Adopted from [21].

The field dependence of the transport critical current density J_c, measured at the temperatures of 5, 15, and 20 K, is shown in Figure 4.9. It should be noted that both at 20 K and at 5 K, J_c(B) for our pure wire ($Mg_{0.95}B_2$) is the same as that of high-quality MgB_2 wire made by using high purity amorphous boron[1].

This probably justifies the use of our non-stoichiometric $Mg_{0.95}B_2$ wire for the comparison with doped wires. Rather surprisingly, even at high temperature (20 K) the low field ($B \leq 4$ T) J_c(B) performance of both doped wires is practically the same as that of the undoped wire. Lowering the temperature, the in-field J_c performance of the doped wires is improved with the respect to the undoped MgB_2 wire, namely, at 15 K, the MgB_2 wire doped with 1.25 wt% Ni/C nanoparticles achieves higher values of J_c over the whole field range.

At low temperature (5 K), significant enhancement of J_c of both doped wires with the respect of undoped is observed. In particular, J_c (5 K, 10 T) = 3.3×10^4 A/cm^2 for both doped wires, which is about 2.5 times larger than that of the undoped wire. In order to investigate the types of pinning mechanisms achieved in the undoped and doped samples, the Kramer plots have been plotted for all samples (inset to Figure 4.9).

The similar shape of the Kramer plots for all samples and temperatures probably implies that the main pinning mechanism in all samples is the same. In particular, the linearity of these plots at intermediate fields is consistent with grain boundary pinning.[21]

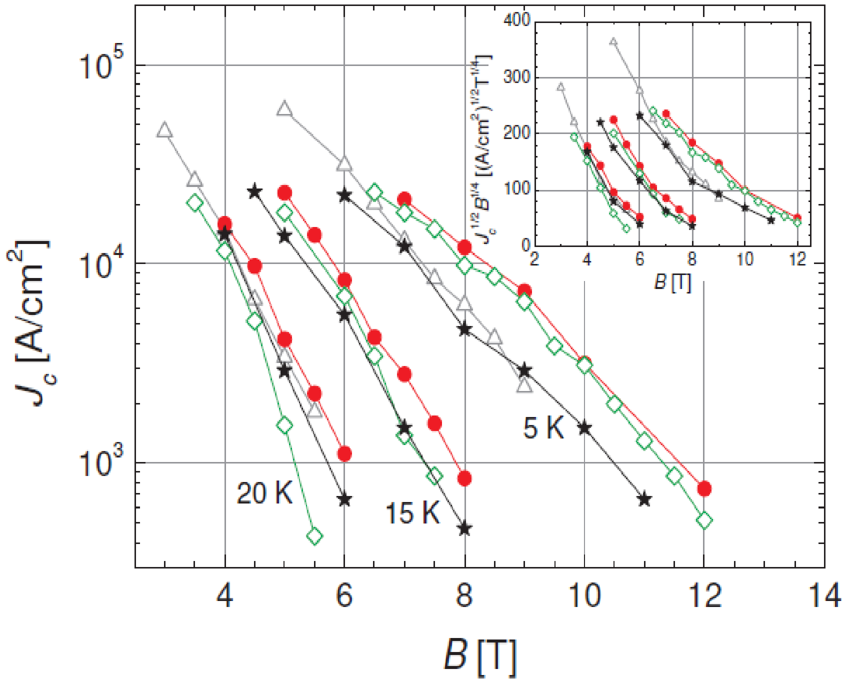

Figure 4.9: Field dependence of critical current density J_c(B) for undoped and dopedMgB$_2$ wires (black solid stars: $Mg_{0.95}B_2$, red solid circles: MgB_2 + Ni/C 1.25 wt.%, green open diamonds: MgB_2 + Ni/C 2.5 wt.%). The inset shows Kramer plots of the same samples. Adopted from [21].

The volume pinning force density $F_p = J_c*B$ versus B for the undoped and doped samples obtained from transport measurements is shown in Figure 4.10, where it exhibits the same trend as the J_c(B) variation at different temperatures.

At low temperature, F_p of the doped samples considerably exceeds F_p of the undoped wire, namely, F_p (5 K, 8 T) for the undoped sample is 4.5 × 10^8 N/m^3, while for the sample doped with 1.25 wt% Ni/C nanoparticles, it is 10^9 N/m^3. For comparison F_p (4.2 K, 8 T) = 7.5 × 10^9 N/m^3 in state-of-the-art Nb-Ti wires.[27] It drops to zero at 10 T, however, whereas in our wires it remains finite even above 10 T.

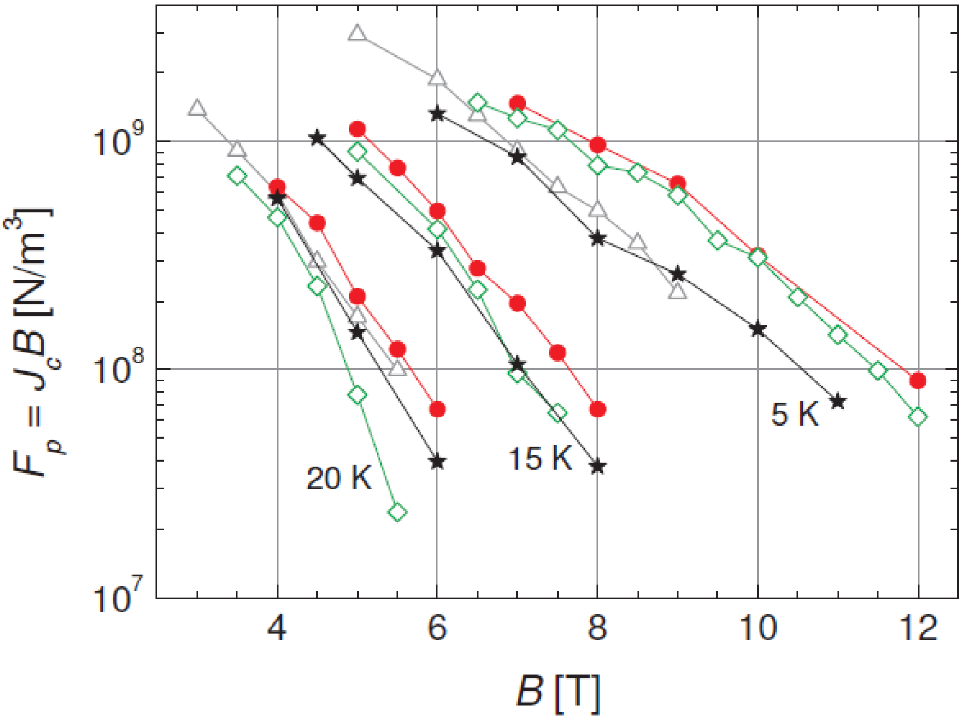

Figure 4.10: Field dependence of volume pinning force density F_p(B) for undoped and doped MgB_2 wires (black solid stars: $Mg_{0.95}B_2$, red solid circles: MgB_2 + Ni/C 1.25 wt%, green open diamonds: MgB_2 + Ni/C 2.5 wt%). Adopted from [21].

4.3.4 Conclusion

A comprehensive study of the structural, magnetic and transport properties of pure iron sheathed undoped MgB_2 wire and MgB_2 wires doped with approximately 1.25 and 2.5 wt.% superparamagnetic carbon protected nickel nanoparticles (average size ≈ 20 nm) was conducted.

Because the structural lattice parameters of undoped MgB_2 deduced from XRD measurements remained the same after doping, it can be concluded that substitution of neither C for B nor of Ni for Mg occurred. Measurements of critical current density J_c(B, T) showed positive effects of doping MgB_2 with selected nanoparticles. The observed enhancement of J_c of the doped samples at 5 K indicates an enhancement of vortex pinning in the doped samples, but its origin is not precisely clarified.

Kramer plots and the normalized volume pinning force density $F_p/F_{p,max}$ versus normalized field B/B_{max} curves at fields higher than 2 T indicate that the main pinning mechanism at all temperatures and in the high field range in the undoped and doped samples is the same, namely, grain boundary pinning.

4.4 MgB_2 wires doped with NiCoB and NiCoB/SiO_2 nanoparticles

4.4.1. Introduction

Doping with NiCoB magnetic nanoparticles has several advantages compared to other types of particle doping. First of all, the size and structure of the nanoparticles are closely suited to incorporation into the crystal structure of MgB_2, due to the amorphous structure and the particle size of approximately 15 nm. The magnetic properties of the transition metals Ni and Co in the structure of the nanoparticles could further enhance pinning based on magnetic interaction.[21,28,29,30]

The prepared samples are in the form of wires. The starting powders were well mixed in a ball mill with toluene, and ball milling additionally assisted in dispersion of nanoparticles in the starting powders.

One of the biggest problems in doping with magnetic nanoparticles is uniform dispersion of the magnetic particles due to their strong magnetic interactions. Creating a core-shell structure such as NiCoB/SiO_2 can change the size and magnetic properties of the nanoparticles and give them new abilities[31]. Such a complex structure of the nanoparticles provides additional opportunities in extending the applications of MgB_2, but also in other areas of science and medicine.

4.4.2 Experimental method

Powders of magnesium (Mg, 99%) and amorphous boron (B, 99%) were wet-mixed in a ball mill for 8 hours with toluene. In preparation of the doped MgB_2 wires, 1.37 and 2.5 wt% of NiCoB and SiO_2-coated NiCoB particles[31] were added, respectively. The mixed powders were packed into pure Fe tube 10 mm and 6.5 mm in outer and inner diameter, respectively. The tubes were drawn to wires 1.41 mm in diameter with a core diameter of 0.8 mm. Finally, the reaction heat treatment was performed at 650°C and 750°C for 60 min with a heating rate of 5 K/min in pure argon atmosphere. The measurement procedure was the same as in 4.2.1.

4.4.3 Experimental Results

4.4.3.1 XRD analysis

Figure 4.11 shows XRD patterns of the pure MgB_2 and the doped samples with 2.5 wt% NiCoB and NiCoB/SiO_2. From the Figure can be seen that there has been considerable change in the amount of MgO with doping. The intensity of the MgO phase apparently increases with doping.

Different trends can be observed for unreacted Mg. The pure sample has a significant amount of unreacted Mg compared to the doped samples, where intensity of Mg peaks almost disappeared. Samples sintered at a lower temperature such as 650°C usually have a significant amount of unreacted Mg. Doped samples have considerably less Mg, which indicates a reaction between the nanoparticles and the Mg. The high intensity peak of MgO phase in the MgB_2 doped with NiCoB/SiO_2 nanoparticles can be related to SiO_2.

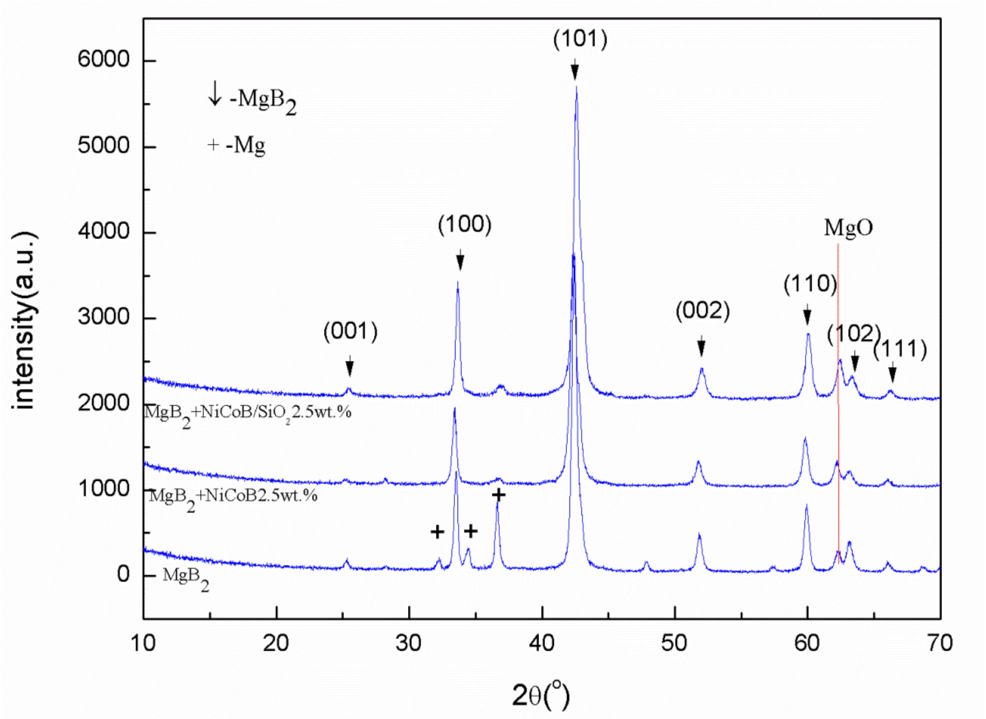

Fig. 4.11: XRD patterns of pure MgB_2 and MgB_2 doped with 2.5 wt% NiCoB and 2.5 wt% NiCoB/SiO_2. Adopted from [32].

4.4.3.2 Critical current density

The J_c results for the MgB_2 wires are presented in Figure 4.12. From the Figure 4.12, a slight enhancement of pinning can be observed for all doped samples at 5 K in the high fields region. At 20 K, there is no improvement of MgB_2 critical current density with doping. In comparison of the doped samples, better results were obtained with samples doped with 1.37 wt% than with 2.5 wt%, which indicates impediments to current flow with increasing doping.

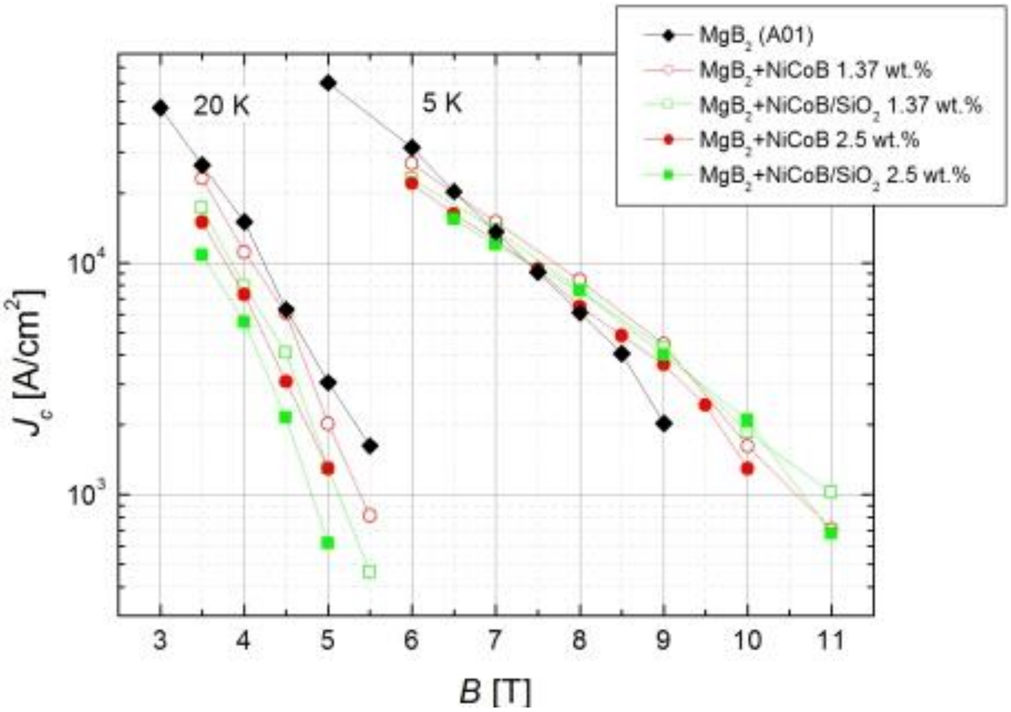

Fig. 4.12: Critical current density of MgB_2 wires for pure and doped samples sintered at 650°C. Adopted from [32].

4.4.3.3 SEM analysis

4.4.3.3.1 Pure MgB_2

Figure 4.13 shows an SEM image of the pure MgB_2 sample. The shape of the MgB_2 grains is mostly hexagonal, with an average size around 400 nm. Between the grains, small particles less than 100 nm in size can be observed, which are probably MgO. Table 4.3 shows the EDX data for pure MgB_2 with a considerable amount of oxygen. The relative atomic percentages of boron and magnesium are almost equal, which indicates more unreacted Mg. A small percentage of tungsten, the result of long-term ball milling, is also present.

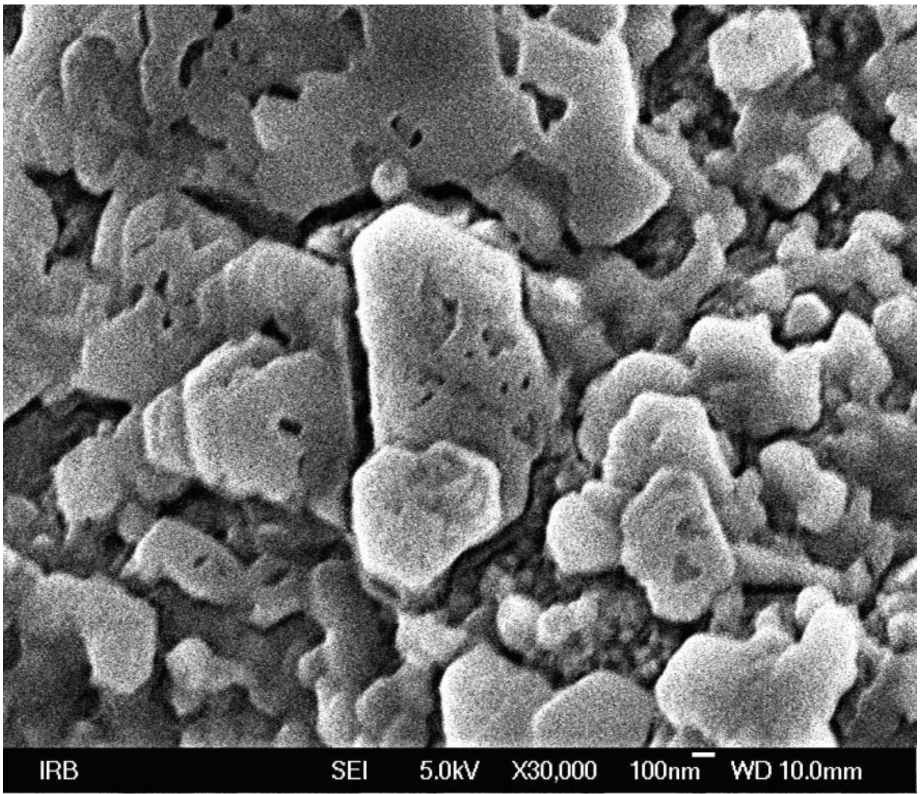

Fig. 4.13: SEM image of pure MgB_2 sample. Adopted from [32].

Element	Weight%	Atomic%
B	21.18	33.01
O	35.23	37.10
Mg	43.06	29.84
W	0.53	0.05
Total	100.00	

Table 4.3: EDX data on percentages of elements for pure MgB_2. Adopted from [32].

4.4.3.3.2 MgB_2 doped with 2.5 wt% NiCoB

Figure 4.14 shows an SEM image of MgB_2 doped with 2.5 wt% NiCoB. From the Figure, the sample contains hexagonal grains of MgB_2 size between 100 to 400 nm in size. A high concentration of small particles with brighter colour (MgO) approximately 50 nm in size can also be observed. Besides the small bright particles, larger bright grains 200 nm in size also appear, and these could also be MgO. The EDX data in Table 4.4 indicates a stoichiometric ratio of boron to Mg. The amount of oxygen is around 10 wt%. Dopant metals are below the detection level, around 0.2 wt%.

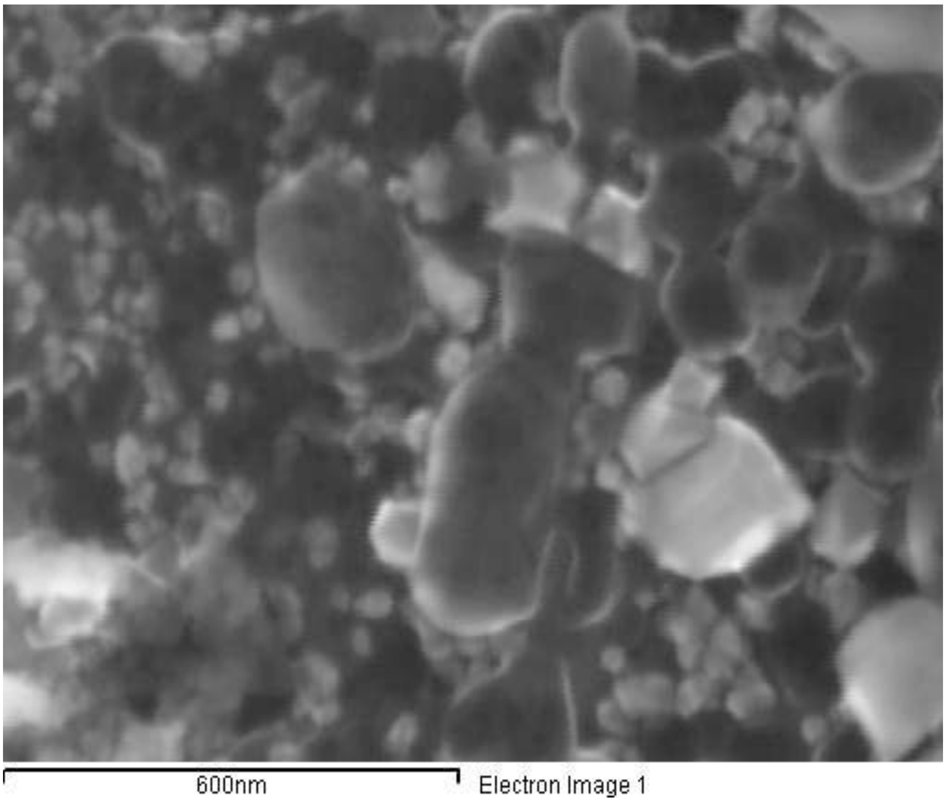

Fig. 4.14: SEM image of MgB_2 doped with 2.5 wt% NiCoB. Adopted from [32].

Element	Weight%	Atomic%
B	37.01	54.98
O	10.39	10.44
Mg	52.16	34.46
Co	0.20	0.05
Ni	0.23	0.06
Total	100.00	

Table 4.4: EDX data for MgB_2 doped with 2.5wt% NiCoB. Adopted from [32].

Mapping results are presented in Figures 4.15(b), 4.16(a, b), and 4.17(a, b). A detailed comparison of the above-mentioned figures reveals a strong connection between the white cubes and an excess amount of oxygen. At the same spots, the amount of boron drops considerably, while the amount of magnesium stays unchanged.

There seems to be a slightly inhomogeneous distribution of Ni and Co (Fig. 4.17(a, b)), which would indicate that the NiCoB nanoparticles are spread homogeneously throughout the MgB_2, but not, apparently, where there is obvious oxygen agglomeration. This oxygen agglomeration most likely represents MgO, which corresponds to the light grey crystallites in the SEM image (Fig. 4.15(a)).

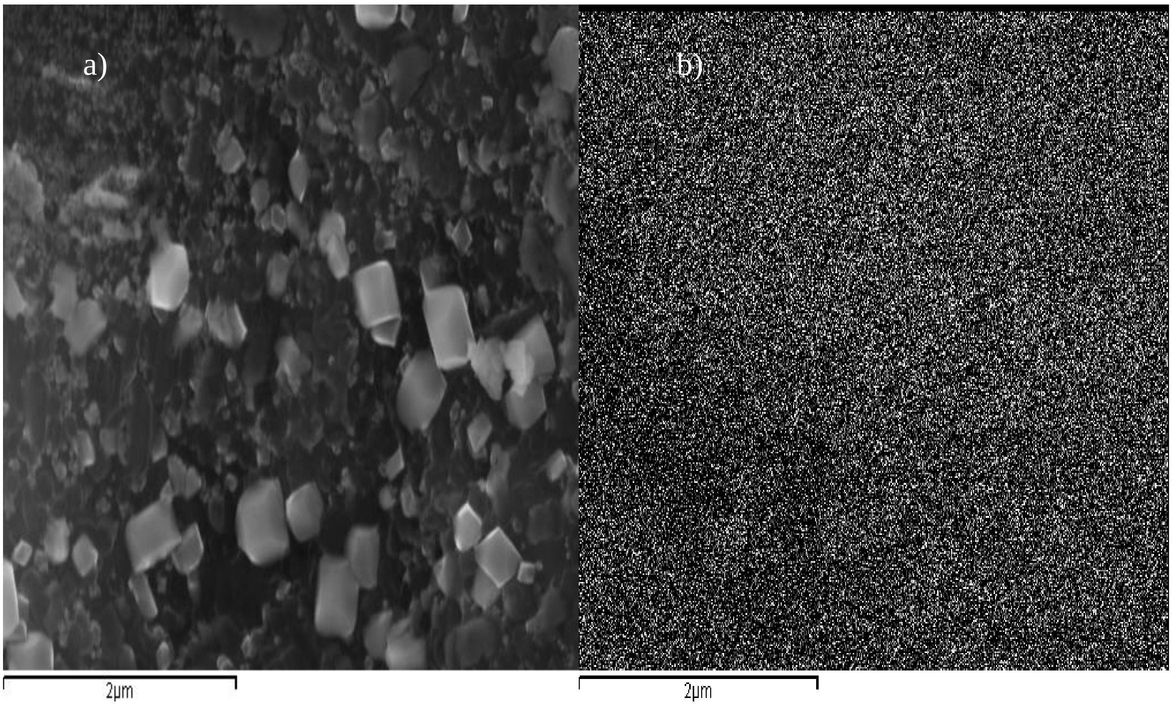

Fig. 4.15: (a) SEM image of MgB_2 doped with 2.5 wt% NiCoB; (b) EDS mapping results for magnesium. Adopted from [32].

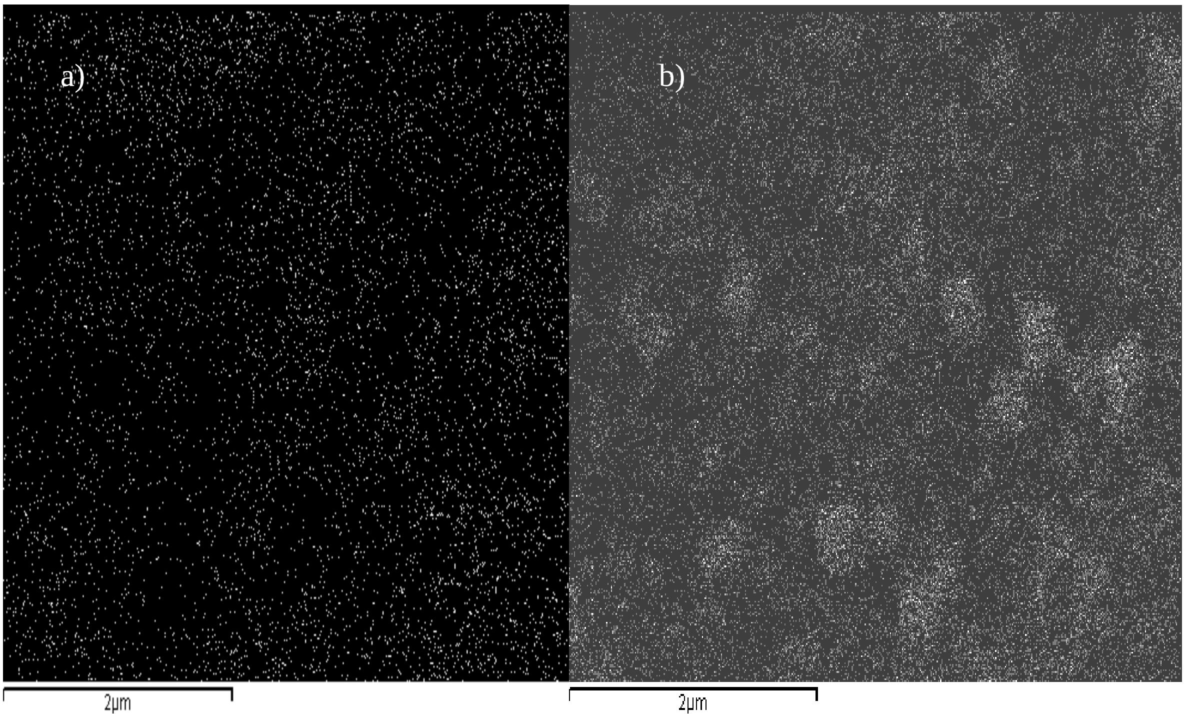

Fig. 4.16: (a) EDS mapping results for boron, (b) mapping results for oxygen. Adopted from [32].

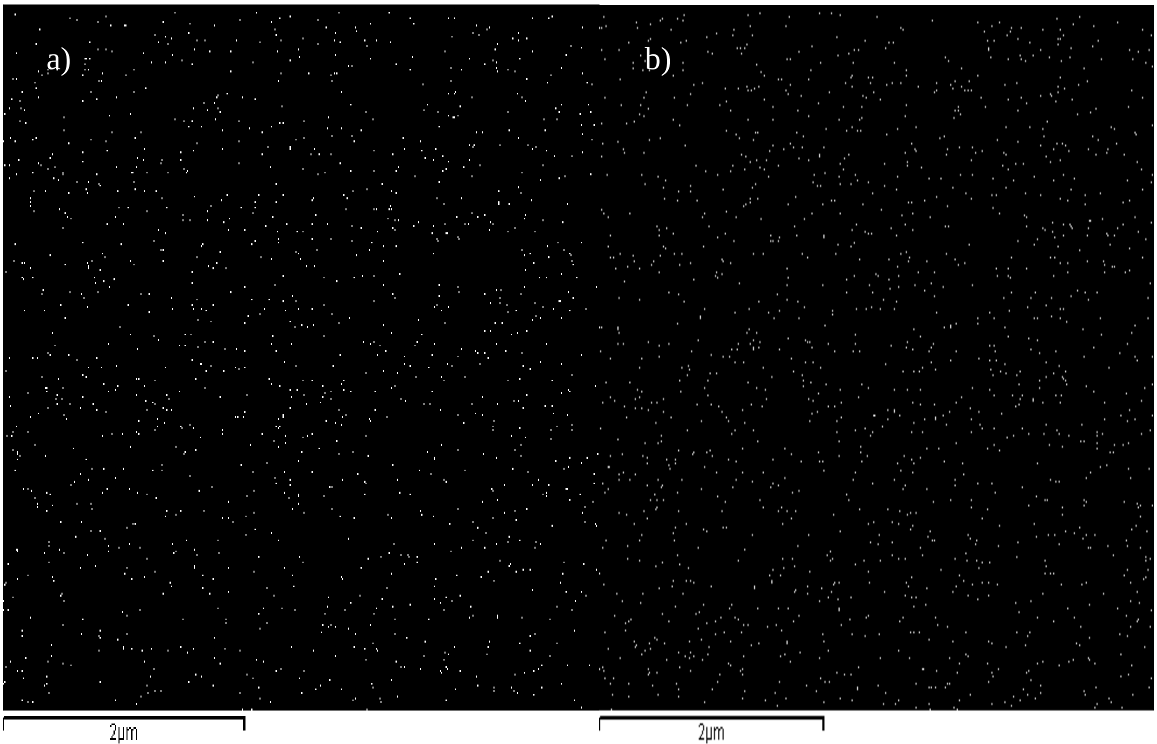

Fig. 4.17: (a) EDS mapping results for nickel, (b) mapping results for cobalt. Adopted from [32].

4.4.4 Conclusion

This study demonstrates that MgB_2 wires doped with magnetic nanoparticles, NiCoB and NiCoB coated with SiO_2, show a slight enhancement of J_c(H) at 5 K. The shape of curves at fields higher than 7 T indicate that the main pinning mechanism at 5 K and in the high field range is the same as for the Ni doped samples in the previous section, namely, grain boundary pinning. The SEM images and EDS data indicate a high concentration of MgO phase, which appears in small size grains (50 nm) and in large grains around 200 nm in size. The transition metals cobalt and nickel are observed in very small amounts but are widespread in the sample.

4.5 REFERENCES

1 N. Novosel, D. Pajić, M. Mustapić, E. Babić, A. Shcherbakov, J. Horvat, Ž. Skoko, K. Zadro, Journal of Physics: Conference Series 234**,** 022027, 2010.

2 C. P. Bean, Magnetization of hard superconductors, Phys. Rev. Lett. 8, 250-253, 1962.

3 C.P. Bean, Magnetization of High-Field Superconductors, Rev. Mod. Phys. 36, 31, 1962.

4 O. Husnjak, E. Babić, I. Kušević, X.L Wang, S. Soltanian and S.X Dou, Solid State Commun. 143 412–415. 2007.

5 M. Mustapić, D. Pajić, N. Novosel, E. Babić, K. Zadro, M. Cindrić, J. Horvat, Ž. Skoko, M. Bijelić, and A. Shcherbakovc, Synthesis Structural Characterization and Magnetic Properties of Iron Boride Nanoparticles with or without Silicon Dioxide Coating, Chem. Acta 83,000. 2010.

6 D.K Finnemore, J.E Ostenson, S. L. Bud’ko, G. Lapertot, and P.C. Canfield, Phys. Rev. Lett. 86 2420–2422, 2001.

7 W. K. Yeoh, J. Horvat, J. H. Kim, S. X. Dou, Improvement of Vortex Pinning in MgB_2 by Doping, (Hauppauge NY: Nova Science Pub. Inc.), 2008.

8 W. Häßler, M. Herrmann, C. Rodig, M. Schubert, K. Nenkov, and B. Holzapfel, Supercond. Sci. Technol. 21062001, 2008.

9 P. Kovač, B. Birajdar, I. Hušek, T. Holubek, and O. Eibl, Supercond. Sci. Technol. 21 045011, 2008.

10 Horvat J., Yeoh W. K., Kim J. H. and Dou S. X., Supercond. Sci. Technol. 21 065003 1–6, 2008.

11 S.X. Dou, S. Soltanian, Y. Zhao, E. Getin, Z. Chen, O. Shcherbakova, and J. Horvat, Supercond. Sci. Technol. 18**,** 710–715, 2005.

12 M. Vélez, J.I. Martın, J.E. Villegas, A. Hoffmann, E.M. González, J.L. Vicent, and I.K. Schuller, J. Magn. Magn. Mater. 320 2547–2562, 2008.

13 J. I. Martın, M. Velez, J. Nogues and I. K. Schuller, Phys. Rev. Lett. 79, 1929, 1997.

14 M. J. Van Bael, L. Van Look, K. Temst, M. Lange, J. Bekaert, U. May, G. Guntherodt, V. V. Moshchalkov and Y. Bruynseraede, Physica C 332, 12, 2000.

15 I. F. Lyuksyutov and V. Pokrovsky, Phys. Rev. Lett. 81, 2344, 1998.

16 M. V. Milošević, S. V. Yampolskii and F. M. Peeters, Phys. Rev. B 66, 174519, 2002.

17 C. Cheng and Y. Zhao, Physica C 463–465, 220, 2007.

18 V. P. S. Awana, M. Isobe, K. P. Singh, E. Takayama-Muromachi and H. Kishan, Supercond.Sci. Technol. 19, 551, 2006.

19 S. Zhou and S. X. Dou, Solid State Sci. 12, 105, 2010.

20 V. V. Moshchalkov and J. Fritzsche, Nanostructured superconductors (World Scientific Publishing Co., Singapore), Chap. 1. 2011.

21 N. Novosel, S. Galić, D. Pajić, Ž. Skoko, I. Lončarek, M. Mustapić, K. Zadro, and E. Babić, Enhancement of critical current density in MgB_2 wires doped with Ni nanoparticles, Supercond. Sci. Technol. **25,** 095018, 2012.

22 S. M. Kazakov, R. Puzniak, K. Rogacki, A. V. Mironov, N. D. Zhigadlo, J. Jun, Ch. Soltmann, B. Batlogg and J. Karpinski, Phys. Rev. B 71, 024533 and references therein.2005.

23 W. X. Li, R. Zeng, C. K. Poh, Y. Li and S. X. Dou, J. Phys.: Condens. Matter 22, 135701 and references therein. 2010.

24 S. X. Dou, O. Shcherbakova, W. K. Yeoh, J. H. Kim, S. Soltanian, X. L. Wang, C. Senatore, R. Flükiger, M. Dhalle, O. Husnjak and E. Babić, Phys. Rev. Lett. 98, 097002, 2007.

25 L. Gozzelino, A.Agostino, R. Gerbaldo, G. Ghigo, F. Laviano, J. Phys.: Conf. Ser. 234, 012014, 2010.

26 J. Jiang, B. J. Senkowicz, D. C. Larbalestier and E. E. Hellstrom, Supercond. Sci. Technol. 19, L33, 2006.

27 N. D. Rizzo, J. Q. Wang, D. E. Prober, L. R. Motowidlo and B. A. Zeitlin, Appl. Phys. Lett.89, 2285, 1996.

28 V. P. S. Awana, M. Isobe, K. P. Singh, E. Takayama-Muromachi and H. Kishan, Supercond. Sci. Technol. 19 551–555, 2006.

29 M. Kühberger and G. Gritzner, Physica C 370, 39–43, 2002.

30 Q. Zhao et al., IEEE Transactions on Nanotechnology, Vol. 10, No. 2, 2011.

31 N. Novosel, D. Pajić, Ž. Skoko, I. Lončarek, S. Galić, M. Mustapić, E. Babić, A. M. Tonejc, K. Zadro, Magnetic behaviour of amorphous NiCoB nanoparticles uncoated and coated in silicon dioxide, in preparation.

32 M. Mustapić at al., MgB_2 doped with NiCoB and $NiCoB/SiO_2$, in preparation

Chapter 5.1: Effects of type of boron on properties of MgB_2

5.1.1 Introduction

The effects of the properties of the boron source as a precursor on the superconducting properties of MgB_2 can be crucial for the performance of samples. In this study, the influence of crystalline and amorphous boron precursors from different producers was investigated. The borons used in this study have different morphology, particle sizes, and impurity percentages (B_2O_3). The properties of the B powders, such as purity, size distribution, particle size, and morphology need to be well studied and analysed, as they can play an important role in determining the fundamental properties of the MgB_2.

The boron samples investigated in this study include two different amorphous borons: amorphous nanosize 99% purity (AN99) and amorphous micron-size 99% purity (AM99) samples, as well as one crystalline boron sample, micron size 96% purity (CM96). More detailed descriptions of the boron powders are given in sections 5.1.3.6 and 5.1.3.7. The main topic of section 5.1 is the critical current density, J_c, dependence on the applied field for different boron precursor properties.

MgB_2 made from different types of boron characterized by $J_c(H)$, X-ray diffraction (XRD) and scanning electron microscopy (SEM). The results show that there are significant differences in the performance of amorphous and crystalline boron. The investigation of MgB_2 samples with various boron precursors has been widely discussed in the literature by other groups.[1,2,3,4]

A detailed understanding of the formation process of MgB_2 and the influence of precursors on formation processes can be crucial for obtaining samples with the best working performance. Control of intragrain scattering due to lack of reaction between precursors and nano-dopants, formation of grain boundary phases, and vacancies or excess of some of the reactants can all strongly affect the critical current of MgB_2.

5.1.2 Experimental procedure

All measured samples were prepared in pellet form. First of all, the powders were mixed (first NiCoB nanoparticles (Chapter 3.4), and then boron were added to magnesium), ground, and pressed with 10 tonnes pressure. The resulting pellets were cut into small bar-shaped pieces with dimensions of 1 × 2 × 3 mm^3.

All samples were enclosed in iron tubes and sintered at 850°C for 30 min under high-purity argon gas with a heating rate of 5° $Cmin^{-1}$.

All prepared pellets were examined by X-ray powder diffraction. XRD patterns were collected at room temperature using an automatic Philips powder diffractometer, model PW1820 (Cu Kα radiation) in Bragg-Brentano geometry. The structure of MgB_2 was refined with the aid of several program packages, first FullProf for plotting the curves and then Origin and Rietveld for drawing the XRD patterns and calculating lattice parameters.

Magnetization hysteresis loops were collected on a commercial Quantum Design Physical Properties Measurement System (PPMS), with the magnetic field applied parallel to the longest dimension of the sample.

Magnetic critical current density J_c was estimated based on the critical state model using the formula $J_c = 20\ \Delta M/[a(1-a/3b)]$,[5] where ΔM is the height of the M(T) hysteresis loop, and a and b are the sample dimensions perpendicular to the applied field, with $a < b$. The magnetization was measured at 5 K and 20 K in a time-varying magnetic field with sweep rate 50 Oes^{-1} and amplitude 9T. Due to the large sample size effect on the magnetic J_c for MgB_2, all the samples for measurement were made to the same dimensions (1 × 2 × 3 mm^3) for comparison.[6] The microstructure of MgB_2 samples, and the grain size and morphology were studied by scanning electron microscopy (SEM).

5.1.3. Experimental results

Analysis of different types of boron source as starting materials also shows the interesting result that nanoparticles only improve critical current for MgB_2 made from the amorphous borons, AN99 and AM99, while for the crystalline boron, CB96, no improvement of J_c was observed.

5.1.3.1 Critical current density of MgB_2 prepared from AN99 boron

Figure 5.1.1 shows significant gains in critical current for doped samples at both measured temperatures. MgB_2 samples were made using nano-boron (AN99) as precursor. J_c increased with increasing doping level, and the J_c(H) curves are parallel in semi-logarithmic plots. At 5 K, the results showed a regular interval in the improvement of J_c with doping. It is important to note the improvement at low applied field at 20 K, especially in comparison with carbon doped samples.

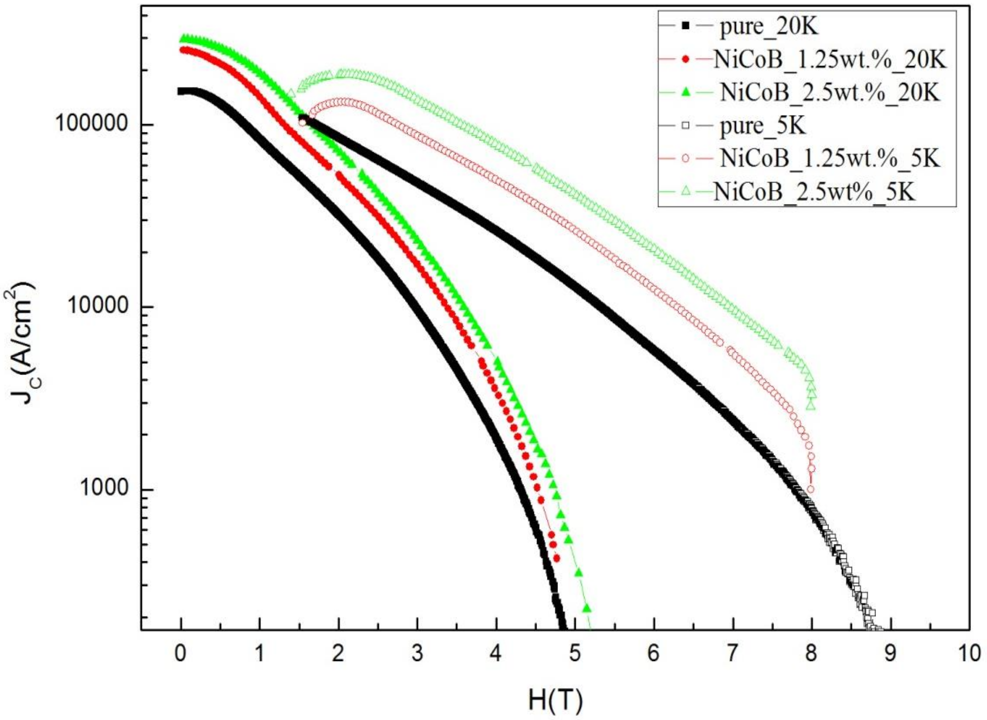

Fig.5.1.1: Critical current density of MgB_2 prepared from amorphous, nanosize boron (AN99) as a starting precursor, both pure and doped with NiCoB nanoparticles (size ≈ 5nm), with sintering at 850°C. J_c was measured at 20 K (solid symbols) and 5 K (open symbols).

Figure 5.1.2 shows substantial growth of critical current density with increasing doping at 5 K and a field of 5 T. The maximal obtained value of J_c at 5 K and 5 T applied field is 79500 A/cm^2.

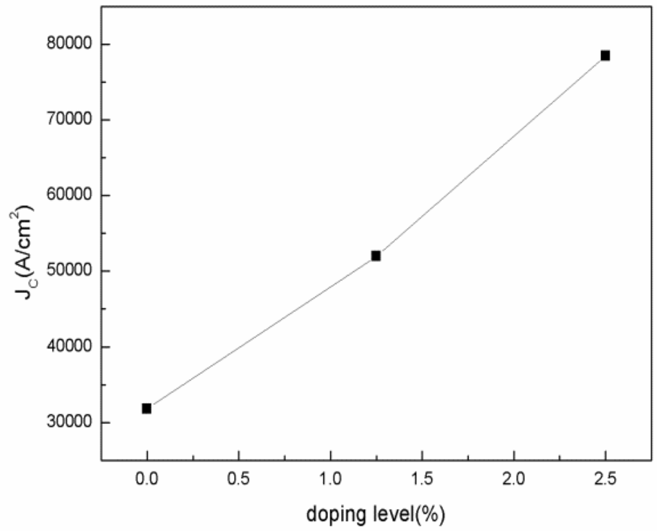

Fig. 5.1.2: J_c values of MgB_2 made from AN99, sintered at 850°C as a function of doping level, measured at 20 K and 2 T.

Figure 5.1.3 clearly presents a linear trend of increasing J_c values with doping level. These values have been measured at 5 K and 5 T applied field, and the maximal amount of current density obtained under those conditions is 40000 A/cm^2 for the sample doped with NiCoB 2.5wt%.

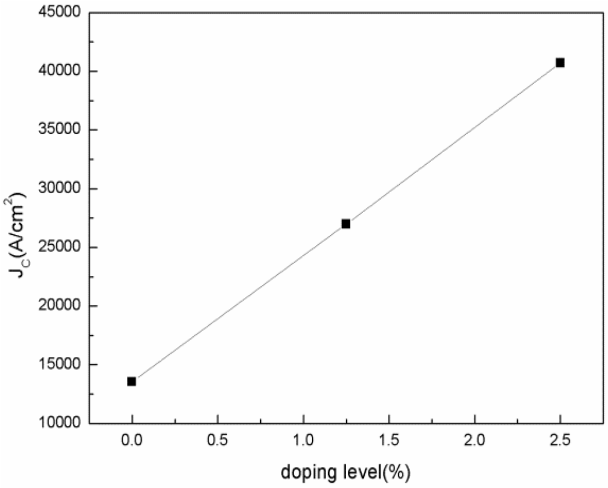

Fig. 5.1.3: Critical current density of pure and NiCoB doped MgB_2 made from AN99, sintered at 850°C as a function of doping level, measured at 5 K and 5 T.

5.1.3.2 Critical current density of MgB_2 prepared with AM99 boron

The J_c properties of MgB_2 samples prepared from AM99 boron are presented in Figure 5.1.4. From the Figure, it can be observed that there is considerable enhancement for the 2.5% and 5% doped samples at 5 K. At 20 K, a slight improvement is shown, but just for the 2.5% doped sample, while the curve for the 5% doped sample in a larger field range overlaps with that for pure MgB_2.

The 1.25% doped sample presents a small improvement at 5 K, but does not show any improvement at 20 K. It is important to note that the doped samples prepared with boron AM99 (micron-size) showed the best values of the critical current and the best improvement by doping in comparison to pure MgB_2. In comparison with nano-amorphous boron (AN99), microsize boron shows better results at higher sintering temperature. The main reason is likely to be the greater reactivity of nano-boron, which does not need higher temperature to complete the reaction to form MgB_2. Higher temperature provides worse connectivity and produces more weak-links for nano-size amorphous boron.

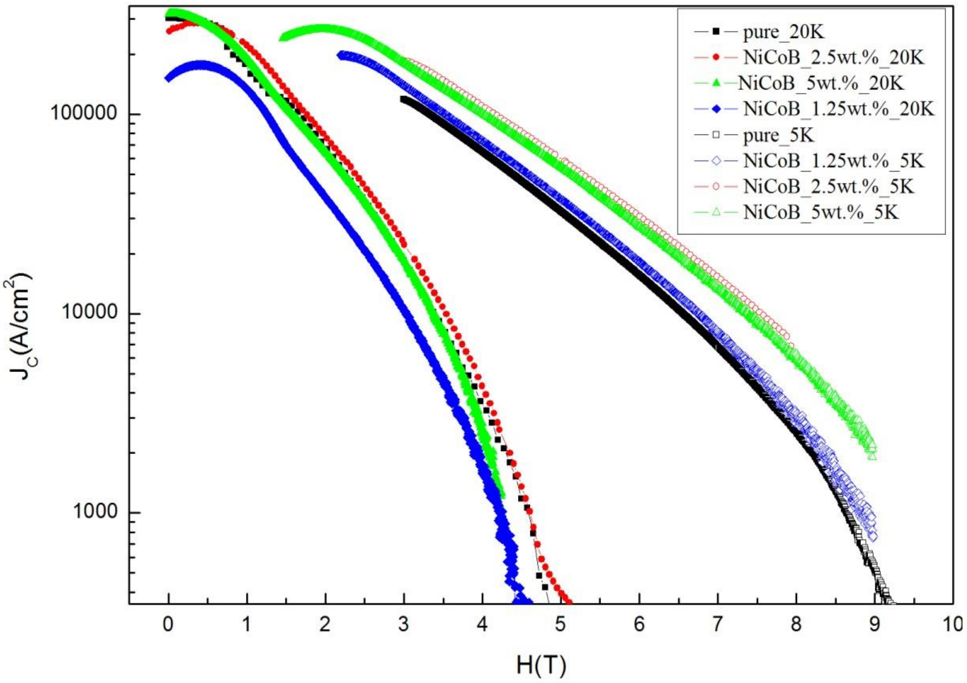

Fig. 5.1.4: Critical current density of MgB_2 prepared from amorphous, micron-size boron (AM99) as a starting precursor sintered at 850°C. J_c as measured at 20 K (solid symbols) and 5 K (open symbols).

Figure 5.1.5 shows J_c for MgB_2 samples made from AM99 boron with different NiCoB doping levels.

The trend in the obtained results is rapid growth of J_c with increasing doping level, reaching a saturation level at 2.5wt% NiCoB doping. The maximal measured value of J_c is 61000 A/cm^2.

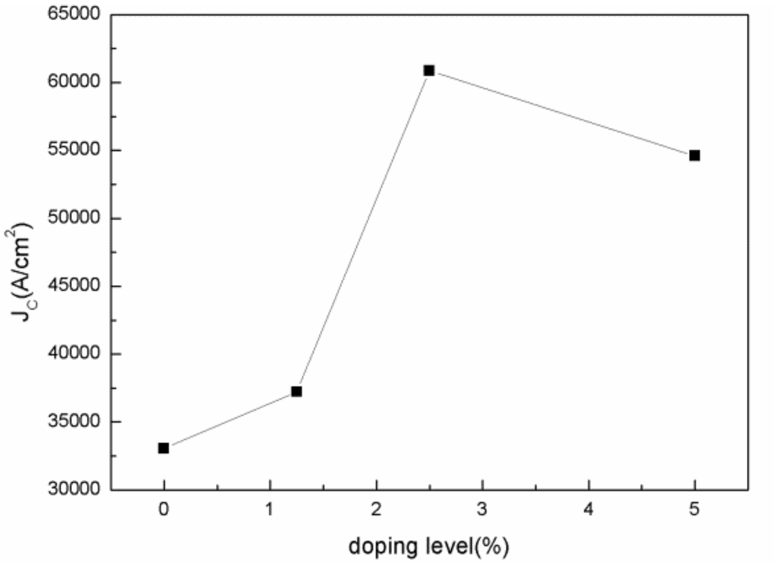

Fig. 5.1.5: J_c values for pure and NiCoB doped MgB_2 samples made from AM99 and sintered at 850°C, show a considerable increase with doping level, with the highest value for the 2.5wt% doping level. J_c are measured at 5 K and 5 T.

A different trend was obtained for measured J_c values at 20 K and 2 T, as can be seen in Figure 5.1.6. Calculated J_c results show decreasing J_c with small doping (1.25%), but a significant gain of J_c over the pure value for 2.5wt% doping, reaching the maximal value of 82000 A/cm^2, and finally, a slight drop in J_c for the highest doping level of 5wt% NiCoB.

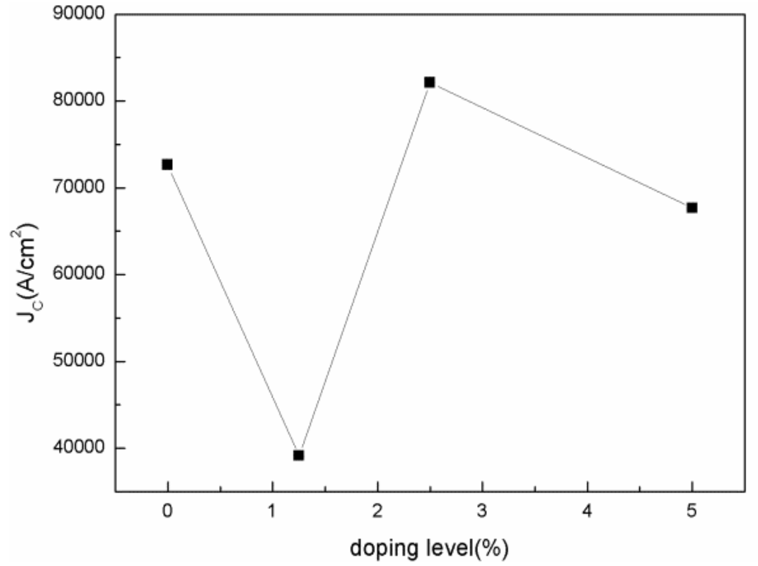

Fig. 5.1.6: 2 T and 20 K J_c results for pure and NiCoB doped samples made from AM99 show a zigzag trend with doping level.

5.1.3.3 Critical current density of MgB_2 prepared from crystalline boron (CB96)

Figure 5.1.7 shows J_c values of pure and doped crystalline boron CB96. The low doped samples with 1.25% and 2.5% NICoB showed no improvement in J_c at the measured temperatures, 5 K and 20 K. Also, these doped samples have very similar J_c curves in both observed cases.

Low reactivity of crystalline boron and slow formation of MgB_2 phase might be caused by the larger particle size of the starting boron precursor, which is proved by the SEM images and XRD analysis. Furthermore, the large amount of B_2O_3 in crystalline boron (XRD results) in combination with NiCoB nanoparticles ultimately had a negative impact on the formation of MgB_2 phase and the incorporation of nanoparticles into the MgB_2 matrix.

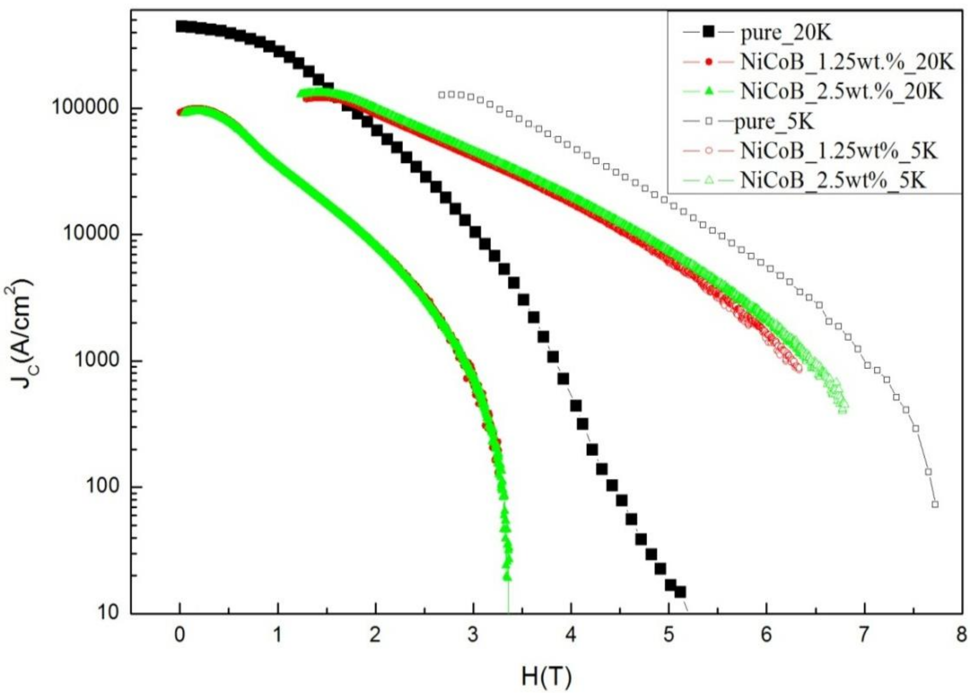

Fig.5.1.7: Critical current density of pure and NiCoB doped MgB_2 prepared from CB96 boron as a starting precursor and sintered at 850°C. J_c was measured at 20 K (solid symbols) and 5 K (open symbols).

Figure 5.1.8 shows a considerable decline of J_c with doping level. The maximum value obtained at 5 K and 5 T for the pure sample is 16000 A/cm^2, which is also considerably less in comparison with MgB_2 made from amorphous boron. The 2.5wt% doped samples have J_c values of approximately 7000 A/cm^2 in comparison to 61000 A/cm^2 for 2.5wt% doped sample made from AM99.

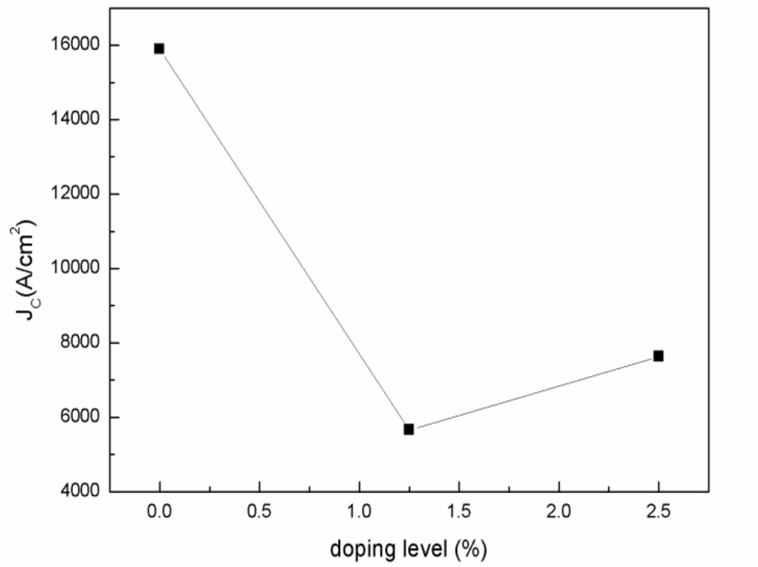

Fig. 5.1.8: J_c values (5 K and 5 T) shows a decrease with doping level for samples made from CB96. Sintering temperature of prepared samples is 850°C.

From Figure 5.1.9, it can be observed that there is a downward trend in the J_c values with doping at 20 K. The maximum J_c obtained at 20 K and 2 T for the pure sample is 65000 A/cm^2.

Both doped samples have the same value of J_c at 20 K and 2 T of around 9000 A/cm^2. In general, for both measured temperatures (5 and 20 K), J_c substantially decreased with doping with this boron powder. The only explanation for the ineffectiveness of the nanoparticles can be the weak reactivity of crystalline boron, which at this relatively high sintering temperature, does not show any improvement of J_c with doping.

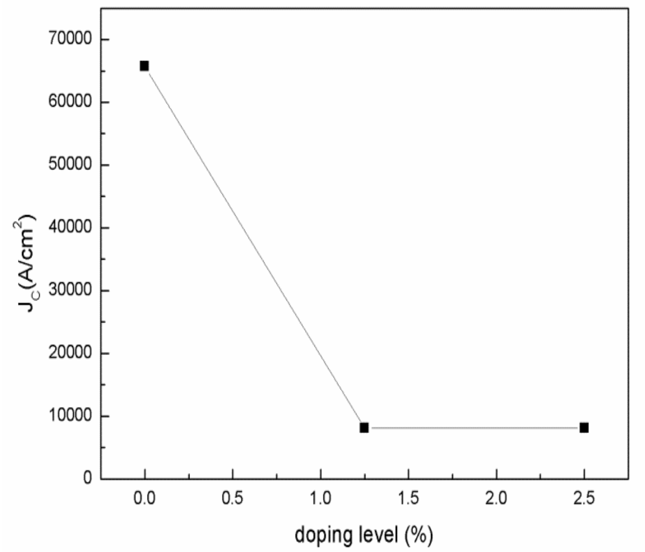

Fig.5.1.9: J_c values at 20 K and 2 T applied field are smaller for the NiCoB doped samples. The trend in J_c(H) is similar for both observed temperatures.

5.1.3.4 Comparison of critical current density of pure MgB$_2$ prepared with different types of boron

Figure 5.1.10 shows a comparison of J_c for the pure MgB$_2$ samples made from the three different boron powders. At 5 K, crystalline boron (CB96) gives better performance in the middle field range better results than amorphous nanosize boron (AN99), but at higher fields, J_c decreases much faster than for AM99 and AN99. On the other hand, AM99 presents the best values of J_c considering the whole field range for 5 K. The situation is more complicated at 20 K, with crystalline boron presenting the best values at low fields (1-2 T), while at higher fields, amorphous boron performed better. AM99 presented slightly better values of J_c than AN99.

The reason for the different effects of boron precursor in MgB_2 on values of J_c at different applied fields could be the grain size of MgB_2. As we can see from the SEM images (Figs. 5.1.18 and 5.1.17) the grain size of MgB_2 made from crystalline micron-size boron (CB96) is larger than for amorphous boron, and especially than for amorphous nanosize boron (AN99). In the high field region, the J_c of MgB_2 made from crystalline boron decreases faster than for that made from amorphous boron.

MgB_2 made from amorphous boron has smaller grain size and thus a larger amount of grain boundary surface. Following that conclusion, pinning on grain boundaries is also larger, which results in higher values of J_c at higher fields. According to the theoretical explanation of the two main pinning mechanisms, intergrain boundary pinning, point-defect pinning, can be dominant in the high fields region.[7,8]

At lower applied field, pinning is not so crucial, and more grain boundary makes for more defects, which has a negative impact on J_c values. This can explain our J_c(H) for pure MgB_2 prepared with different B powders..

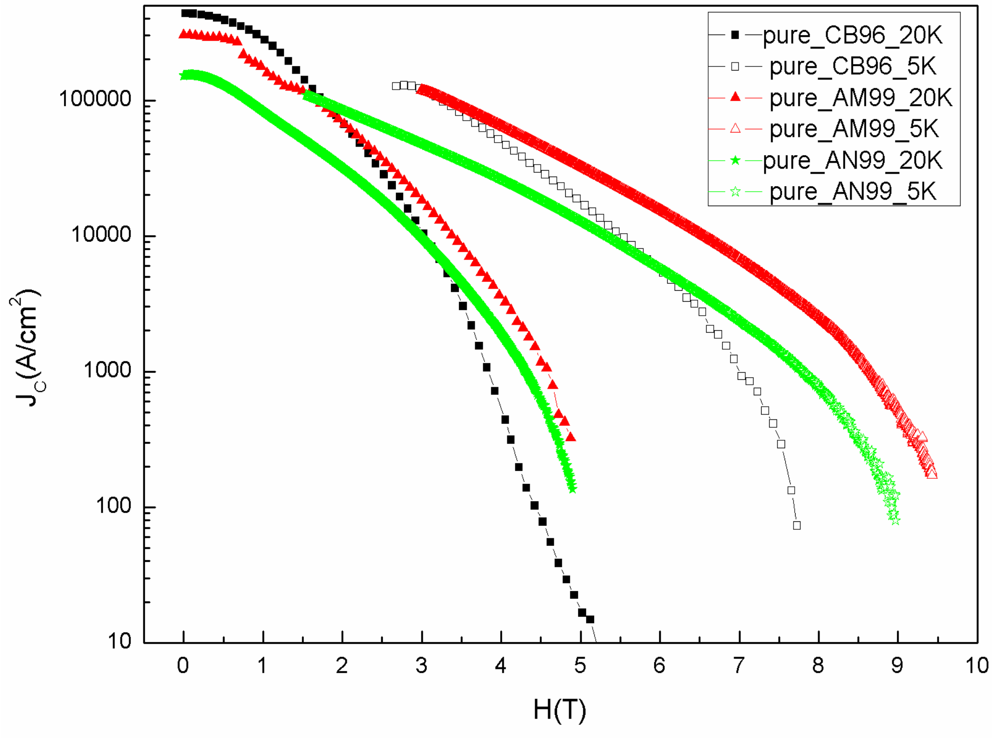

Fig.5.1.10: Pure MgB_2 samples made from different boron precursors and sintered at the same temperature, 850°C.

5.1.3.5 XRD patterns of NiCoB doped MgB_2 made from three different types of boron

Figure 5.1.11 shows the XRD patterns of pure and nano-NiCoB doped MgB_2 samples prepared from AN99 boron sintered at 850°C. Sharp MgB_2 peaks can be observed as strong and well distinguished lines marked with black arrows.

The MgO peak at 62.5° slightly increases with doping. Also, a very small peak of unreacted Mg at 36° is detectable, which is a feature present for all observed samples. The second phase and the impurities were not observed due to to the small percentage of doping with impurities.

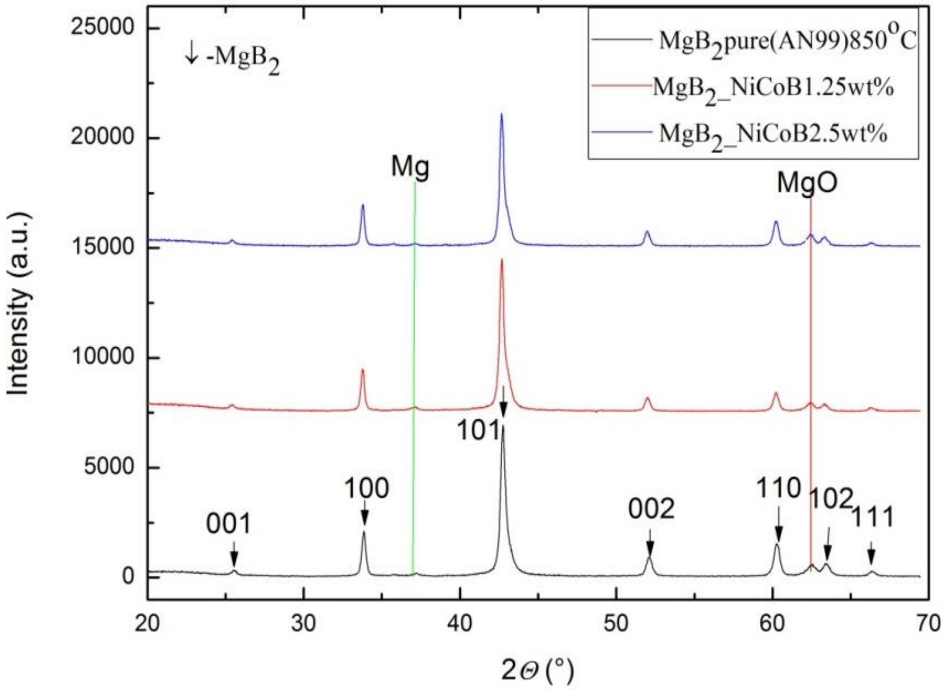

Fig. 5.1.11: XRD patterns of pure and NiCoB doped MgB_2, with AN99 boron used as a precursor and sintering at 850°C. Miller indices for MgB_2 are indicated in the figure.

Figure 5.1.12 presents the XRD patterns of pure and doped MgB_2 samples prepared from AM99 boron sintered at 850°C. These XRD patterns are very similar to those for the samples made from AN99.

Besides the dominant phase of MgB_2, these samples also contain MgO and a very small amount of un-reacted Mg. It is important to note that the intensity of the MgO and Mg phases does not grow with doping level, and it is generally the same for all doping levels, or it even slightly decreases.

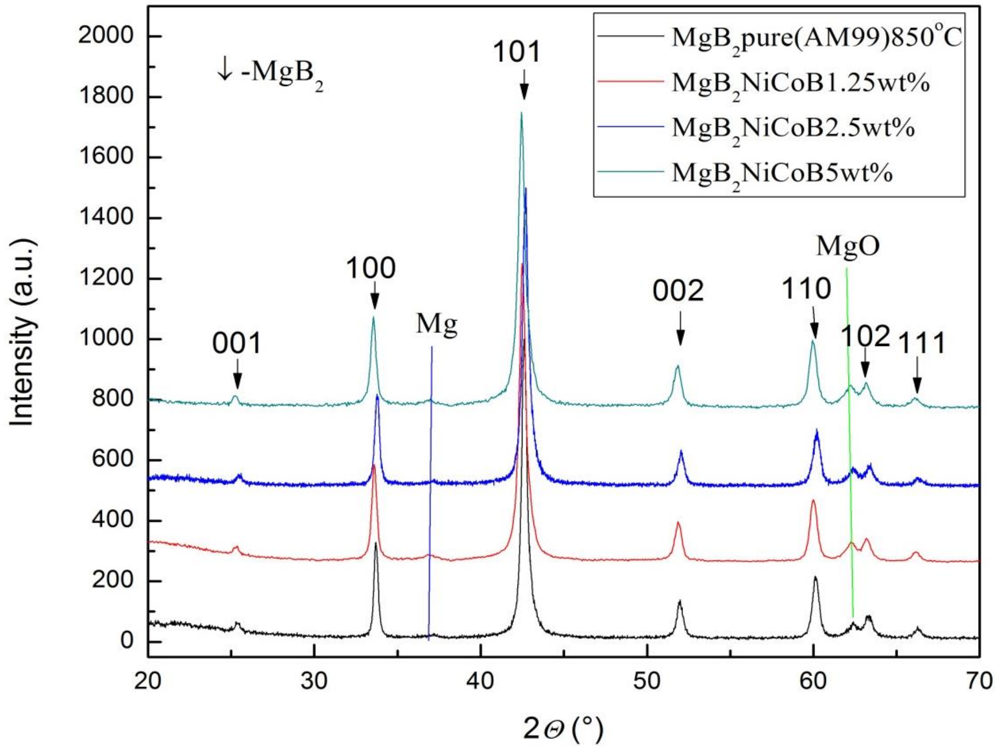

Fig. 5.1.12: XRD patterns of MgB_2, both pure and doped (1.25%, 2.5% and 5%) with NiCoB. Amorphous boron AM99 was used as a precursor, with sintering at 850°C. The XRD data for the AM99 MgB_2 samples showed great similarity with the AN99 samples. Miller indices for MgB_2 are indicated in the figure.

Figure 5.1.13 presents XRD patterns of pure and NiCoB doped MgB_2 samples prepared from CB99 crystalline boron and sintered at 850°C. From the Figure, there is a drastic increase in the amounts of MgO and Mg with doping.

On the other hand, the XRD pattern of pure sample does not show any excess intensity peaks of MgO and Mg. The XRD patterns further indicate the poor reactivity and even inhibitory effect of NiCoB nanoparticles on the reaction between boron and magnesium, which is directly manifested by poor connectivity between grains and finally, by very low values of J_c.

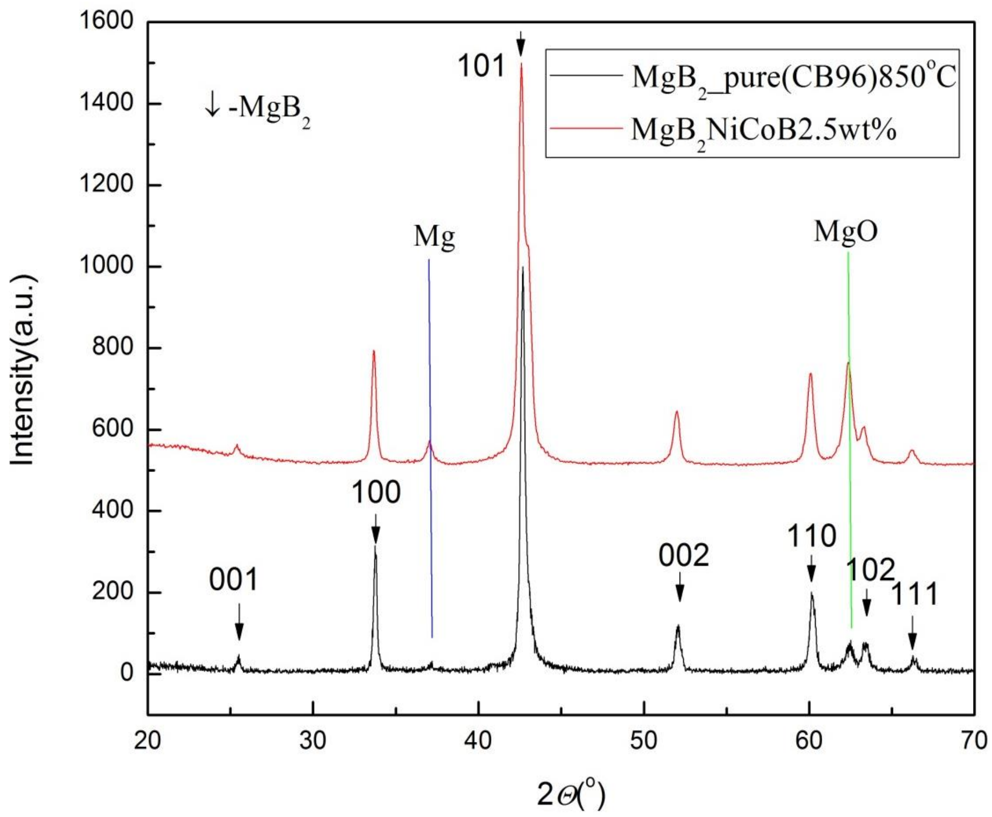

Fig. 5.1.13: XRD patterns of MgB_2 made from CB96, both pure and doped with NiCoB 2.5wt%, with sintering at 850°C. Apart from the strong MgB_2 peaks a sharp MgO peak at 62.5° for the doped sample and a residual Mg peak can be distinguished. Miller indices for MgB_2 are indicated in the figure.

.

Table 5.1.1 presents calculated values of the full width at half maximum (FWHM) of different peaks for pure samples prepared from different borons. It is obvious that there are considerable differences between MgB_2 samples made from the amorphous borons (AN99, AM99) and the crystalline boron, CB96. According to the Scherrer equation[9], increasing FWHM values indicates that the grain size has decreased as follows:

$$D_p = 0.94\,\lambda / \beta_{1/2} \cos\theta, \qquad (5.1.1)$$

where D_p is the crystal size, λ is the wavelength, $\beta_{1/2}$ is the FWHM, and θ is the peak position.

From this equation, crystal size is related to full width at half maximum (FWHM) of the peak in XRD, i.e. $\beta_{1/2}$. Generally FWHM width is inversely proportional to the grain size. This calculation is mostly only accepted as supporting information, because the FWHM results can be connected with size of impurities, defects, dislocations, and surface effects, as well as grain size. From the XRD measurements for pure samples made from different types of boron, we can conclude that MgB_2 samples prepared from the AM99 and AN99 borons have quite similar grain size: around 300 nm and 50-100 nm, respectively. On the other hand, MgB_2 prepared from CB96 boron has much larger grains, several microns in size. Grain sizes of MgB_2 are correlated to the size of boron precursors, as can be observed from Figures 5.1.16 and 5.1.17.

From Table 5.1.1 and Figure 5.1.14, it can be concluded that MgB_2 prepared from CB96 has much larger grain size in directions parallel to hexagonal plane (002) and perpendicular to the hexagonal plane (100), with grain size from 265 nm to 340 nm, respectively. MgB_2 samples prepared from the amorphous borons, AN99 and AM99, are very similar in grain size, with the size ≈ 260 nm (100) and ≈ 200 nm (002).

All samples have sharp and well-marked peaks of MgB_2. No other impurities have been detected in the doped samples except for MgO and un-reacted residual Mg.

The proportion of MgO is stable for the all pure samples and only grows considerably for the doped, CB96 boron sample. The increased MgO may have caused loss of the initial stoichiometry of Mg : 2B.

The MgO formed during the in situ reaction covers the MgB_2 grains or precipitates inside them. Residual Mg is also mostly detected in samples with higher doping levels. The correlation between MgO phase and un-reacted Mg, especially in the case of MgB_2 made from crystalline boron could be due to slow reaction between starting precursors, mostly boron and magnesium, and competition in the reaction between the dopant nanoparticles, and Mg and B.

Plane	(100)		(110)		(002)	
Samples	FWHM (°)	D_p (nm)	FWHM (°)	D_p (nm)	FWHM (°)	D_p (nm)
MgB_2(AN99) 850°C	0.322	260	0.458	201	0.426	207
MgB_2(AM99) 850°C	0.315	264	0.464	199	0.458	192
MgB_2(CB96) 850°C	0.243	340	0.451	204	0.334	265

Table 5.1.1: FWHM results and grain size for MgB_2 samples made from different types of boron and sintered at 850°C.

5.1.3.6 SEM images of boron precursors and MgB_2 prepared from different types of boron

Figure 5.1.14 presents an SEM image of crystalline boron CB96. It can be observed that the particle size of the reference 96% B is approximately 1 μm and can be bigger. The morphology of the boron powder is non-uniform and varies in size and shape. The magnified inset shows clearly defined crystals.

Figure 5.1.15 shows an SEM image of amorphous boron AM99. Mostly spherical (hexagonal) grain shapes are observed, with grain size around 100 nm. The grain size distribution seems to be quite narrow.

Minimization of the total surface energy of AM99 boron powder and of the MgB_2 made from AM99 leads to a spherical shape of grains (Fig. 5.1.16). In contrast, crystalline boron has much larger grain size, leading to MgB_2 grains with large differences in particle sizes and shape (Fig.5.1.17).[1] The tendency to minimize surface energy is the defining factor in the morphology. The above-mentioned characteristics of boron precursors strongly affect morphology and the phase transformation of MgB_2 during sintering.

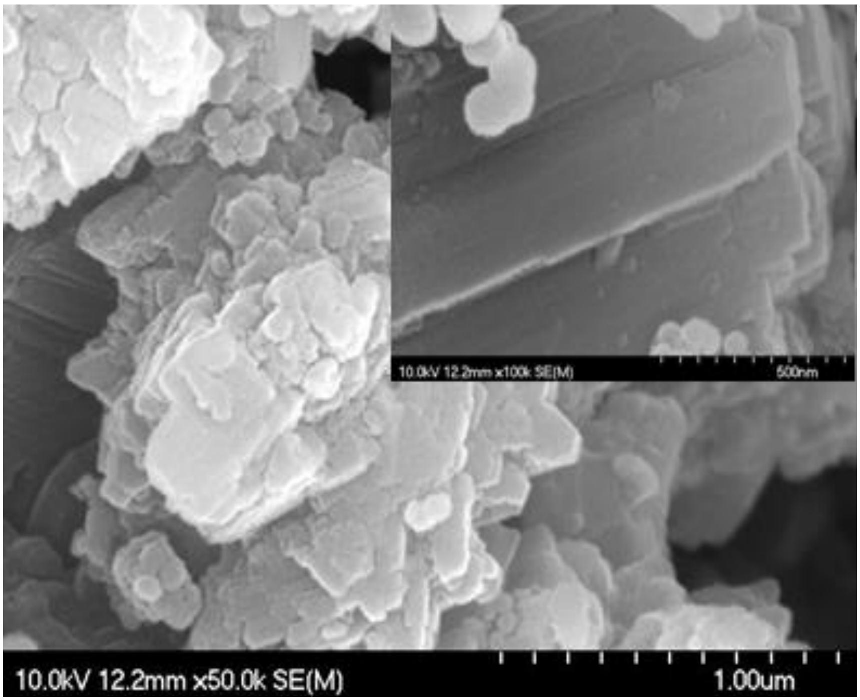

Fig. 5.1.14: SEM image of 96% purity crystalline boron (CB96). Inset shows a high magnification image. Adopted from[10].

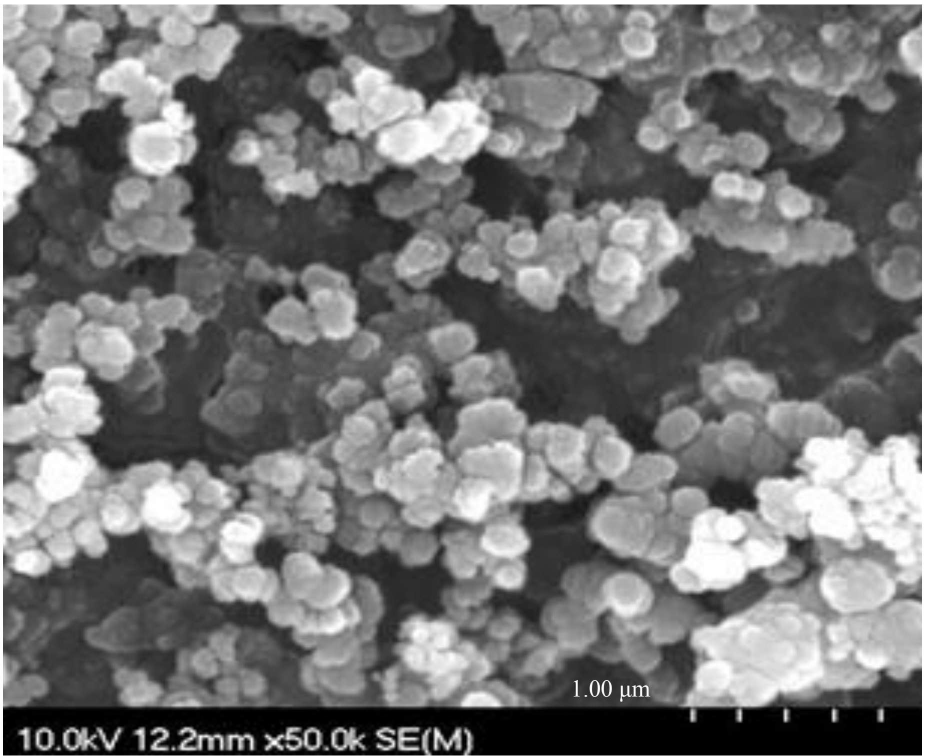

Fig. 5.1.15: SEM image of amorphous boron (AM99). Adopted from[10].

Figure 5.1.16 contains a SEM image of MgB_2 prepared from amorphous AM99 boron. It indicates the morphology, with the grain size between 150-300 nm and hexagonal shape of

MgB_2 crystals. High density and good connectivity between MgB_2 grains can also be observed. It can also be noted that grain size of MgB_2 (AM99, 850°C), calculated from XRD (Table 5.1.1) are in good agreement with grain size identified from SEM images. In the case of MgB_2 prepared from crystalline boron purity of 96% (CB96) (Fig. 5.1.17), can be observed considerably larger grain size in a ranges 200-600 nm. It should be noted that still substantial number of grains are in a range from 200 to 400 nm. Noticeable are grains with a size around 600nm but in a minor number. Compared with grain sizes obtained from XRD (Table 5.1.1) it can be concluded that the deviation between XRD calculated grain size and those observed from SEM images are larger than for MgB_2 prepared from amorphous boron AM99. A value obtained from XRD broadening (MgB_2, CB96) provides us with a volume-averaged size, of the crystallites from the larger volume, while the value obtained from SEM measurements provided us with the size averaged from the smaller volume. It is obvious from the SEM observations that the number of smaller grains is dominating (and this in good agreement with calculations from XRD measurements, Table 5.1.1) while there is a smaller amount of the larger grains which are taken into account in the size determination from SEM observations. It is well known from the literature that the grain sizes obtained from XRD and SEM measurements can differ for as much as 50%.

On the other hand MgB_2 made from the crystalline boron has a much larger grain size, up to 1 micron, but there are also grains around 300 nm, which indicates the broad distribution of grains and the unequal conditions of crystal formation. Grain connectivity is weaker, with a well distinguished border between grains (Fig 5.1.17). A substantial number of small bright-colored particles can also be seen between MgB_2 grains, which probably belong to MgO phase.

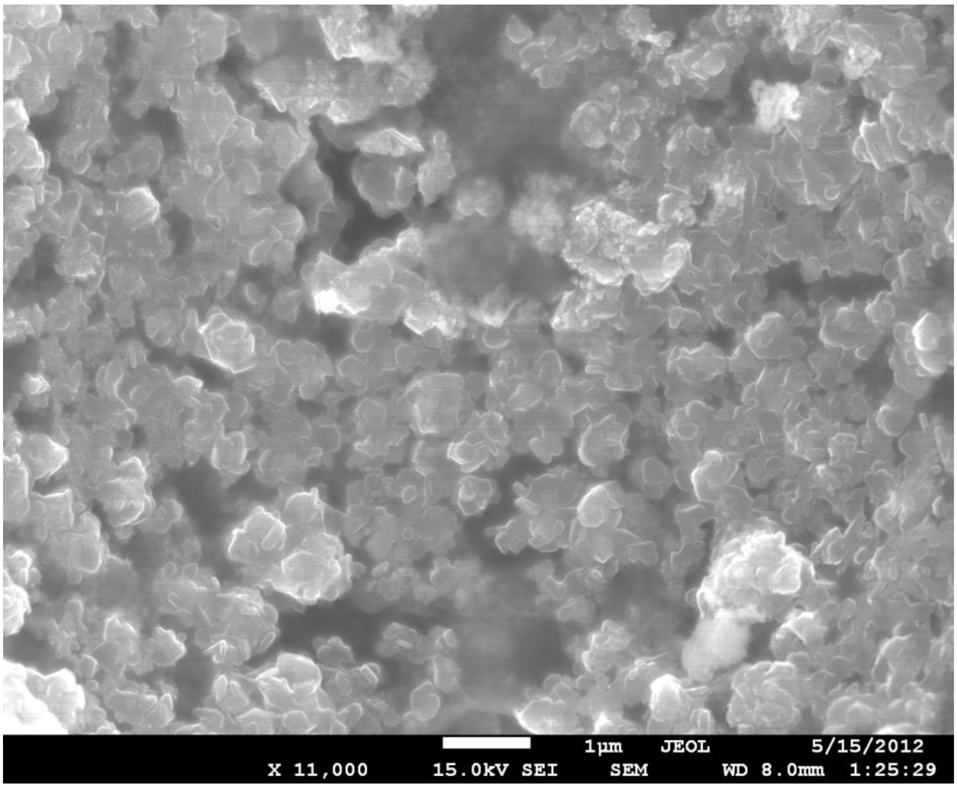

Fig. 5.1.16: SEM image of MgB_2 made from amorphous micron-size boron (AM99).

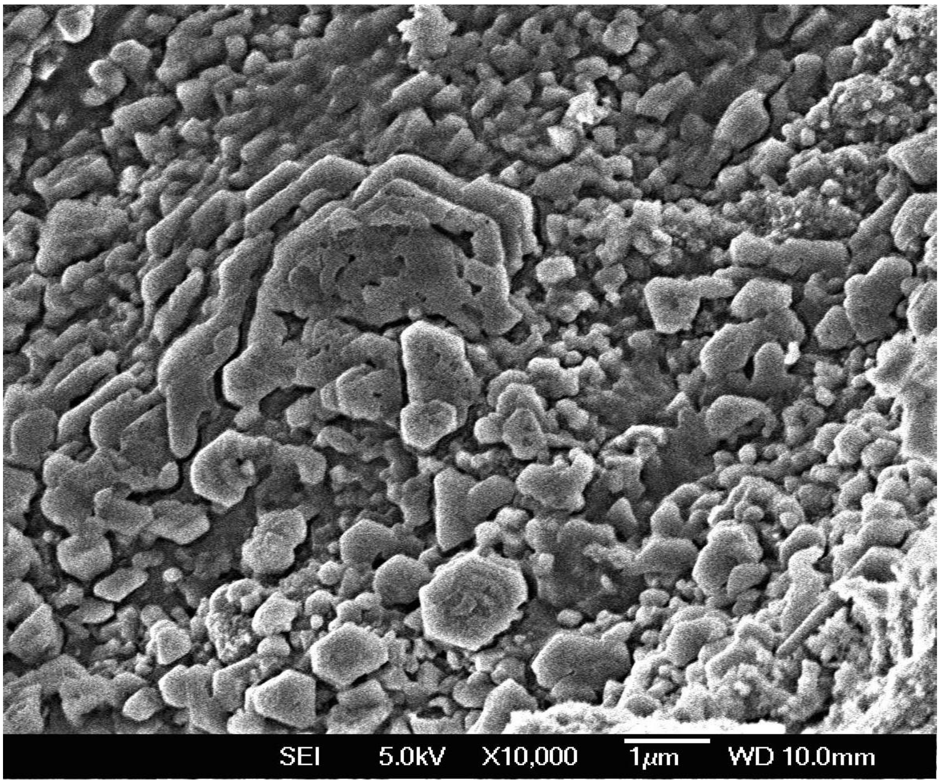

Fig. 5.1.17: SEM image of MgB_2 made from crystalline boron (CB96).

5.1.3.7 XRD characterization of different boron powders

A Comparison of XRD patterns for crystalline Tangshan boron CB96 and amorphous micron size boron AM99 is shown in Figure 5.1.18. The Figure implies a significant difference in the morphology of the two borons.

In addition, the crystalline boron has a substantial share of B_2O_3 phase. Crystalline boron CB96 has a β-rhombohedral (β-rhB) structure. The β-rhB phase is stable even at high reaction temperature, so it is not easy to achieve full reaction before the Mg melts.[12]

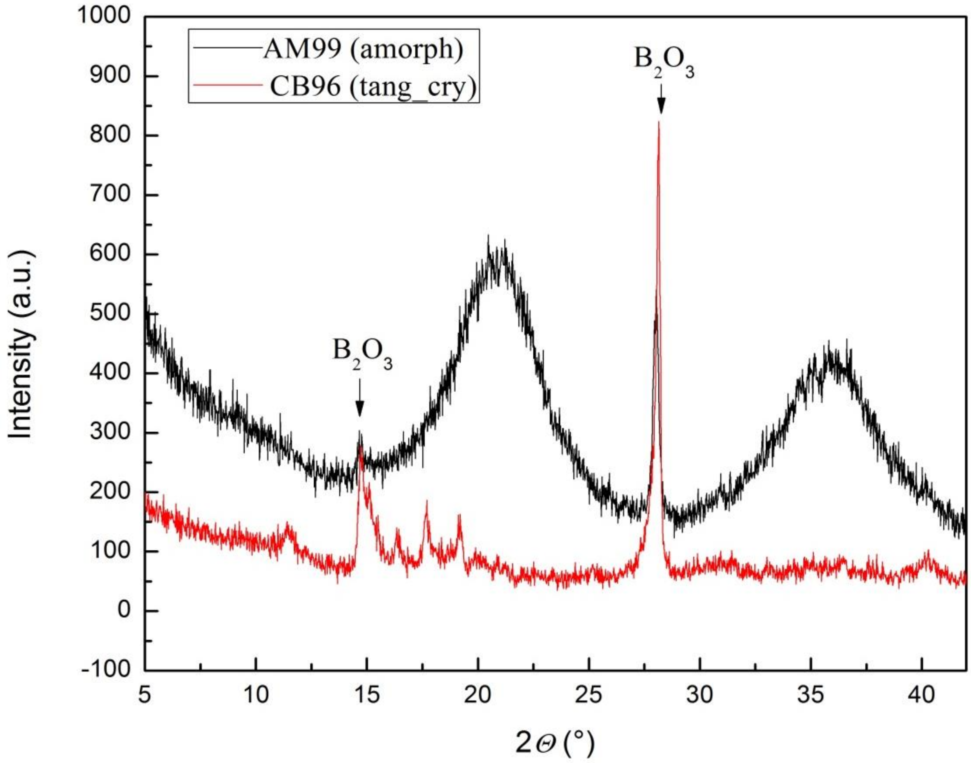

Fig. 5.1.18: XRD patterns of two different types of boron, crystalline CB96 (red) and amorphous AM99 (black).

The XRD pattern of nano-amorphous boron powder AN99 is presented in Figure 5.1.19. The XRD pattern shows the usual amorphous structure of B, with peaks centred at about 21° and 35 °, in addition to two sharp peaks of B_2O_3 at 15° and 27° [12]. The XRD pattern shows only a small amount of B_2O_3 impurities, as compared to the crystalline boron.

These characteristics directly promote a homogeneous reaction with Mg powder. In comparison, the XRD patterns of the two amorphous borons from Figs. 5.1.18 and 5.1.19 show a large similarity in morphology and in having only a small amount of MgO phase.

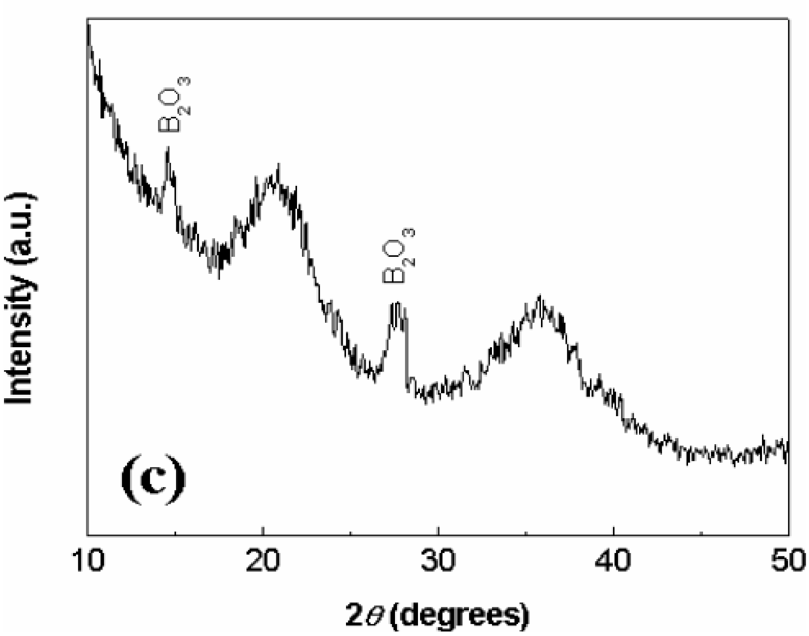

Fig.5.1.19: XRD pattern of nanosize AN99 amorphous boron. Adopted from [12].

5.1.3.8 Mg precursor characterisation

From Figure 5.1.20, it can be observed that the grain size of the 325 mesh Mg precursor is around 2.5 μm. XRD analysis indicates only pure Mg without any impurities. All peaks are sharp, with three main peaks at 33°, 35°, and 37°. From SEM images can be observed small bright grains attached on the surface of large Mg grains. Those particles can be MgO, but they are present in relatively small amount and attached to the surface of the Mg, leaving the purity of the bulk of the grain unaffected. MgO phase has not been detected in the XRD analysis, which can be seen in Figure 5.1.22.

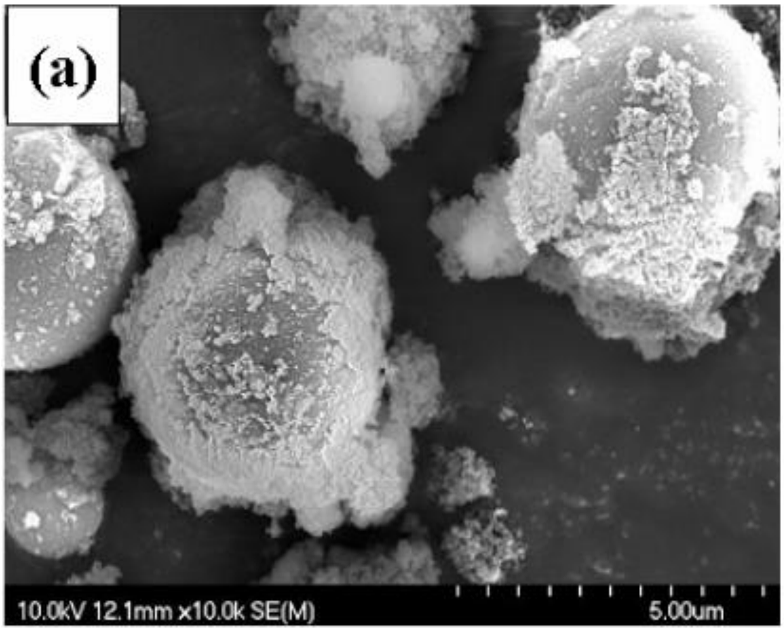

Fig. 5.1.20: SEM image of pure 325 mesh magnesium. Adopted from [12].

Figure 5.1.21 presents the XRD pattern of pure magnesium, and strong and sharp peaks of pure Mg can be seen. The first three peaks at 33.7°, 34.8°, and 37.3° are especially notable. Absence of any impurities in magnesium is very important for obtaining high quality samples of MgB_2, especially due to the very reactive nature of magnesium.

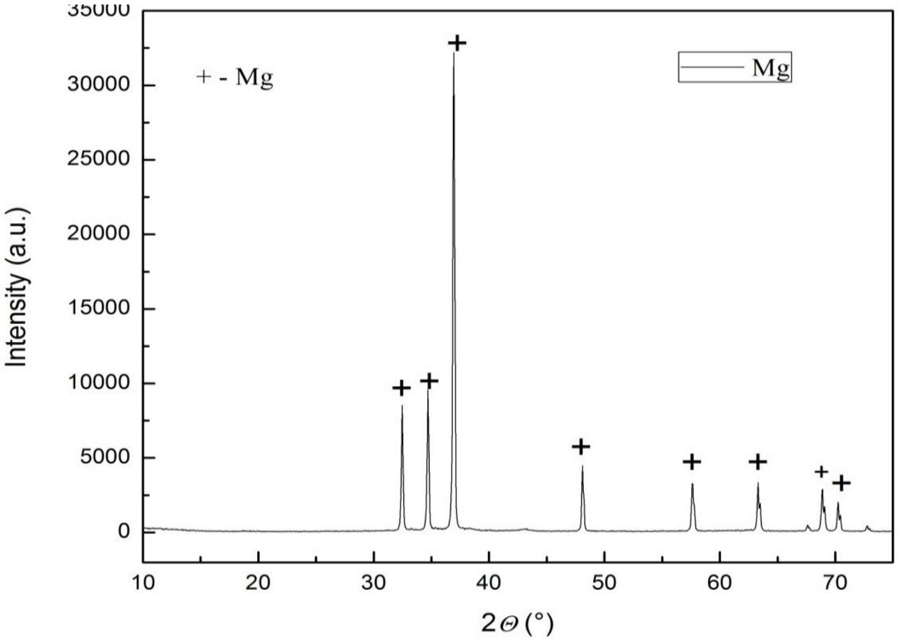

Fig.5.1.21: XRD pattern of pure magnesium mesh 325 size. All detected peaks belong to pure Mg, as marked by the + symbol, which indicates a very pure magnesium source without any impurities.

5.1.4 Discussion

5.1.4.1 Critical current

From the accompanying graphs of J_c(H) (Figs. 5.1.1, 5.1.4, and 5.1.7), it can be concluded that NiCoB nanoparticle doping only gives any improvement of critical current with amorphous boron as a precursor (AM99 and AN99), while in the case of crystalline boron, no improvement is obtained. This can be explained by the larger reacting area of amorphous boron and better reactivity in comparison to crystalline boron. Also, crystalline boron results in a large amount of other impurities, such as B_2O_3, which results in a larger amount of MgO in MgB_2 ($B_2O_3 + 3Mg \rightarrow 3MgO + 2B$), which will have negative effects on the grain connectivity and incorporation of NiCoB into the MgB_2 matrix. The size of the crystals in crystalline boron is several µm.[11]

MgB_2 prepared with from the micron-size amorphous boron (AM99) presents better results in terms of the critical current than nanosize amorphous boron (AN99), which is apparently surprising. The explanation could lie in the sintering temperature. Nanosize boron responds best to a lower temperature of sintering due to its very high reactivity. On the other hand, AM99 boron with larger particles needs a higher temperature for optimal results. This will have profound effects on the J_c of the final NiCoB-doped MgB_2. As shown in Chapter 5.3, nano-NiCoB doping only gives substantial improvement of J_c(H) when NiCoB reacts with the precursor powders at temperatures above 700°C. In comparing the J_c results for MgB_2 made from the two amorphous borons, the better J_c for the amorphous micron-size AM99 can be explained by the sintering at a relatively high temperature. Specifically, nanosize boron AN99 is more reactive and better suits sintering at lower temperature due to its high reactivity. At the same time, at lower temperature, dopant nanoparticles do not properly incorporate themselves into the matrix of MgB_2 and do not provide good pinning and connectivity between grains. At higher sintering temperature ≥ 770°C, synergy of two effects occurs, and the relatively less reactive amorphous boron, AM99, reacts completely with Mg, while the NiCoB nanoparticles are incorporated into the MgB_2 matrix and provide vortex pinning. In addition, good connectivity between MgB_2 grains is also obtained. Therefore, amorphous AM99 gives better J_c(H) for nano-NiCoB doped MgB_2. Too high a sintering temperature (950°C) leads to decomposition of MgB_2 into MgB_4 [13], which reduces the superconducting phase, increases impurities, and finally has a negative effect on J_c. Also, with increasing sintering temperature, the growth of MgB_2 grains increases, too, which can have a negative influence on grain connectivity.

5.1.4.2 XRD patterns

Comparing the three different MgB_2 samples made from the different boron precursors, the most obvious difference is the large amount of MgO phase in the MgB_2 made from crystalline boron.

All the samples show quite high purity of MgB_2, with relatively small amounts of MgO, except for the MgB_2 sample made from crystalline boron. According to Kim et al., the formation of MgO phase starts with $(Mg)B_xO_y$ impurity phases.[11]

From the XRD patterns, it can be seen that crystalline boron contains more B_2O_3 than the amorphous powders, AN99 and AM99. Beside the amount of B_2O_3 in the boron precursor, a strong influence on the formation of MgO phase is the size of the boron particles and the reactivity of the powders.

Crystalline boron has a particle size of several microns. On the other hand, the amorphous borons AM99 and AN99 are much smaller, below 500 nm and 50 nm, respectively. Small size of the boron particles means a larger surface area, and a larger surface are means better contact between the precursors and better reactions among them.[11]

Furthermore, the amorphous morphology is more isotropic and equally reactive from all sides, as compared to the crystalline boron. The reactivity of the amorphous boron powders is much higher than that of the crystalline powders. Hence, when the crystalline B powders come into contact with Mg powder, the reaction to form MgB_2 is relatively slow, and there is sufficient time for $(Mg)B_xO_y$ phases [11,1] to form. At the same time, the large amount of B_2O_3 provides more oxygen for this reaction.

On the other hand, for the amorphous powder, the Mg reacts rapidly with B to form MgB_2 and with B_2O_3 to form MgO + B.[1]

Unreacted Mg can be also detected in the XRD patterns for the MgB_2 samples prepared with crystalline boron, which supports the argument for a slow reaction between crystalline boron and Mg. Unreacted Mg is not been detected for MgB_2 made from amorphous boron with sintering at 850°C.

The unreacted Mg can be detected in large amounts in samples made with low sintering temperature (650°C) and where there is high content of other materials as nanoparticles.[14,15]

5.1.4.3 XRD of pure boron

The XRD patterns of the pure boron present significant differences between crystalline and amorphous boron. Amorphous boron has two characteristic amorphous humps, approximately at $2\theta \approx 21°$ and 35°, and two peaks belonging to B_2O_3 at $2\theta = 15°$ and 27°. Crystalline boron has B_2O_3 peaks and several other peaks which all belong to pure boron at $2\theta \approx 16.5°$, 17°, and 18.2°.

The origin of the boron powder and the way of obtaining boron precursors can have a measurable impact on the performance of MgB_2.

Usually, amorphous boron is obtained with the Moissan process[16], where boron-oxide is mixed in a crucible with magnesium turnings. The crucible is covered, placed in a furnace, and heated up to 1100°C. After a few minutes, a violent reaction starts and continues for another ten minutes at the same temperature. Finally, the reaction mixture is cooled and removed from the crucible. The full reaction equation can be displayed as a $B_2O_3 + 3Mg \rightarrow Mg_3(BO_3)_2 + B_2$.[16]

CB96 crystalline boron is first produced as an amorphous boron by the Moissan process, which is cheap and simple way for obtaining boron. The obtained boron contains a considerable amount of Mg impurity, which can be removed by crystallization.

The crystallization of amorphous boron powders can be conducted by pyrolytic or electrolytic processes at high temperature under inert atmosphere. Pyrolytic amorphous boron crystallizes as α-B_{12}, while electrolytic boron crystallizes directly as the thermodynamically stable β-rhombohedral modification, β-B_{106}.[17,18]

On the other hand, crystalline boron and amorphous boron can be obtained by reduction of boron halides, such as BCl_3, with H_2 gas. For this method, a high temperature is necessary for the production of boron, which usually is produced by the use of an electric arc.

The products of reaction are deposited directly on the tube, in larger crystalline plates and as a dark-brown powder (amorphous). Amorphous boron can also be obtained by this method and has higher purity than boron obtained with Moissan process. This reaction is reversible and can be written as a $2BCl_3 + 3H_2 \Leftrightarrow 2B + 6HCl$.[19]

The amorphous borons in this study were obtained by the described boron halide process.[19]

5.1.5 Conclusion

In conclusion, we can summarize that the morphology and particle size of the boron precursors are of critical importance to the $J_c(H)$ behaviour of MgB_2 samples.

The difference in $J_c(H)$ for the samples made from the crystalline and amorphous boron precursors can be explained in terms of a reduction in the reactive area between Mg, B, and the dopant nanoparticles as a result of the size effect and morphology of the precursor.

In addition, the presence of oxide impurities leads to more MgO impurity in the crystalline boron, and the different reactivity of crystalline and amorphous boron gives substantially different $J_c(H)$ results. The AM99 boron is less reactive than the AN99 boron. Therefore, MgB_2 has to be prepared at higher sintering temperatures when using the AM99 boron rather than the AN99 boron.

This fits well with the requirements of nano-NiCoB doping: as shown in Chapter 5.2: sintering temperatures higher than 700°C are required for improvement of J_c(H) by nano-NiCoB. The use of AN99 boron would result in worse J_c(H), because MgB_2 is formed at lower temperature and Mg loss from MgB_2 will occur when sintering at elevated temperatures with this boron powder. Therefore, AM99 boron was used for obtaining the best samples and for studying the effects of nano-NiCoB doping of MgB_2.

5.1.6 REFERENCES

1 S. K. Chen, K. A. Yates, M. G. Blamire and J. L. MacManus-Driscoll, Supercond. Sci. Technol. 18 1473, 2005.

2 M. A. A. Mahmud, M.A. Susner, D.M. Sumption, M. A. Rindfleisch, M. J. Tomsic, J. Yue, and W.E. Collings, IEEE Transactions on Applied Superconductivity, vol. 19, no. 3, 2009.

3 W. Häßler, B. Birajdar, W. Gruner, M. Herrmann, O. Perner, C. Rodig, M. Schubert, B. Holzapfel, O. Eibl, and L. Schultz, Supercond. Sci. Technol. 19 512–520, 2006.

4 W. Dongliang, Y. Ma, Z. Yu, Z. Gao, X. Zhang, K. Watanabe, E. Mossan, Superconductor Science and Technology, Volume 20, Issue 6, pp. 574-578, 2007.

5 C.P. Bean, Rev. Mod, Phys., 36, 31-36, 1964.

6 M. Avdeev, J. D. Jorgensen, R. A. Ribeiro, S. L. Bud'ko and P. C. Canfield Physica C 387 301–6, 2003.

7 S. Lee, H. Mori, T. Masui, Y. Eltsev, A. Yamamoto, and S. Tajima, J. Phys. Soc. Jpn. 70, 2255, 2001.

8 S. X. Dou, X. L. Wang, J. Horvat, D. Milliken, E. W. Collings, and M. D. Sumption, Physica C 361, 79, 2001.

9 P. Scherrer, Göttinger Nachrichten Gesell., Vol. 2, p 98, 1918.

10 X. Xu, J. H. Kim, W. K. Yeoh, M. Rindfleisch, M. Tomsic, Dayse I. dos Santos, and S. X. Dou, "Influence of Ball-Milled Low Purity Boron Powder on the Superconductivity of MgB_2", IEEE Trans. Appl. Supercond. 17 (2): 2782, 2007

11 J. H. Kim, S. X. Dou, D. Q. Shi, M. Rindfleisch, and M. Tomsic, *Supercond. Sci. Technol.* 20 1026-1031, 2007.

12 J. H. Kim, Yoon-Uk Heo, A. Matsumoto, H. Kumakura, M Rindfleisch, M. Tomsic and S X. Dou, Supercond. Sci. Technol. 23 075014, 2010.

13 Zi-Kui Liu, D.G. Schlom, Qi Li and X.X. Xi, Appl. Phys. Lett.78 3678, 2001.

14 W.X. Li, R. Zeng, J. L. Wang, Y. Li, S. X. Dou, J. Appl. Phys. 111, 07E135, 2012.

15 N. Novosel, D. Pajić, M. Mustapić, E. Babić, A. Shcherbakov, J. Horvat, Ž. Skoko, K. Zadro, Journal of Physics: Conference Series 234, 022027, 2010.

16 H. Moissan, Etude du Bore Amorphe, Ann. Chim. Phys., vol. 6, pp. 296–320, 1895.

17 O. O. Kurakevych, Y. Le Godec, T. Hammouda, C. Goujon, Comparison of solid state crystallization of boron polymorphs at ambient and high pressures, arXiv:1110.1731, 2011.

18 S. O. Shalamberidze, G. I. Kalandadze, D. E. Khulelidze and B. D. Tsurtsumia, Production of α-Rhombohedral Boron by Amorphous Boron Crystallization, J. Solid State Chem. 154, pp. 199-203. 2000.

19 A. K. Srivastava and P.C. Jain, Chemistry Vol. (1 & 2)

Chapter 5.2: Optimization of Sintering Procedure

5.2.1 Introduction

One of the most investigated topics associated with MgB_2 is finding the best sintering conditions (sintering temperature and time of sintering) and precursor combinations (doping level, starting precursor) which will provide the best performance of J_c. The main aim in this thesis is to improve J_c at elevated fields. The value of J_c at 5 T and 5 K was used as the criterion for assessing appropriateness of the procedure. The grain connectivity can become stronger as the sintering temperature increases. The sample sintered at 650°C consisted of MgB_2 with 50 – 150 nm grains, while the sample sintered at 1000°C consisted of 1–3 μm grains. The larger grains are also accompanied by improved density and grain connectivity.[1]

High sintering temperature can produce more MgO despite the protective Ar atmosphere. MgO can be a good pinning center, but also strongly degrades the connectivity if present between MgB_2 grains.

Optimizing the sintering conditions can considerably enhance J_c by improving the connectivity among grains and narrowing the grain size distribution.

The reasons for choosing 5 T were that all samples had measurably large J_c for this field at 5 K, and J_c(H) obtained in magnetic measurements was well defined at that field for all measured samples. For 20 K, the field of 2 T was used for the same reasons.

Improvement of critical currents and optimization of synthesis processes are one of the main topics of scientific and industrial research. MgB_2 preparation is a complex task, which is composed of several connected processes. Detailed study of these processes and the possibility of their improvement is the key to obtaining the best results.

5.2.2 Experimental procedure

MgB_2 pellets were prepared by mixing powders of magnesium (99% purity) and amorphous boron with micron size grains (99% purity), called BM99 for easier reference. Then, these powders were mixed and pressed with Mg (99%) powder and NiCoB nanoparticles. NiCoB nanoparticles were added to the Mg and B powders during the mixing in atomic ratio of Mg: 2B plus added NiCoB nanoparticles in weight percentages of 1.25 wt%, 2.5 wt%, and 5 wt%, respectively.

After mixing, the powder were pressed and sealed in iron tubes. Finally, the samples were sintered at four different temperatures, 650°C, 770°C, 850°C, and 950°C, for 30 min under high purity argon gas with heating rate of 5°Cmin^{-1}.

As in previous experiments, all samples were characterized by X-ray diffraction (XRD) and scanning electron microscopy (SEM). All XRD data were analysed with the FullProf and Origin programs.

The magnetic hysteresis loops were measured at 5 K and 20 K using a physical properties measurement system (PPMS, Quantum Design) in a time-varying magnetic field with sweep rate 50 Oe s^{-1} and amplitude 9 T. All the samples for measurement were made to the same dimensions (1 × 2 × 3 mm^3).

Sintering temperature/°C	Doping level of NiCoB
650	1.25wt%; 2.5wt%; 7.5wt%
770	2.5wt%; 5wt%
850	1.25wt%; 2.5wt%; 5wt%
950	2.5wt%; 5wt%

Table 5.2.1: All prepared MgB_2 samples with doping percentages and sintering temperatures.

5.2.3 Experimental results

5.2.3.1 MgB_2 samples sintered at 650°C

Figure 5.2.1 shows critical current density of MgB_2 samples prepared from micron-size amorphous boron (AM99) as precursor and sintered at 650°C. J_c values strongly decline with doping level for both measured temperatures. Samples doped with 2.5wt% and 5wt% NiCoB show similar J_c curves for the 5 K measurement.

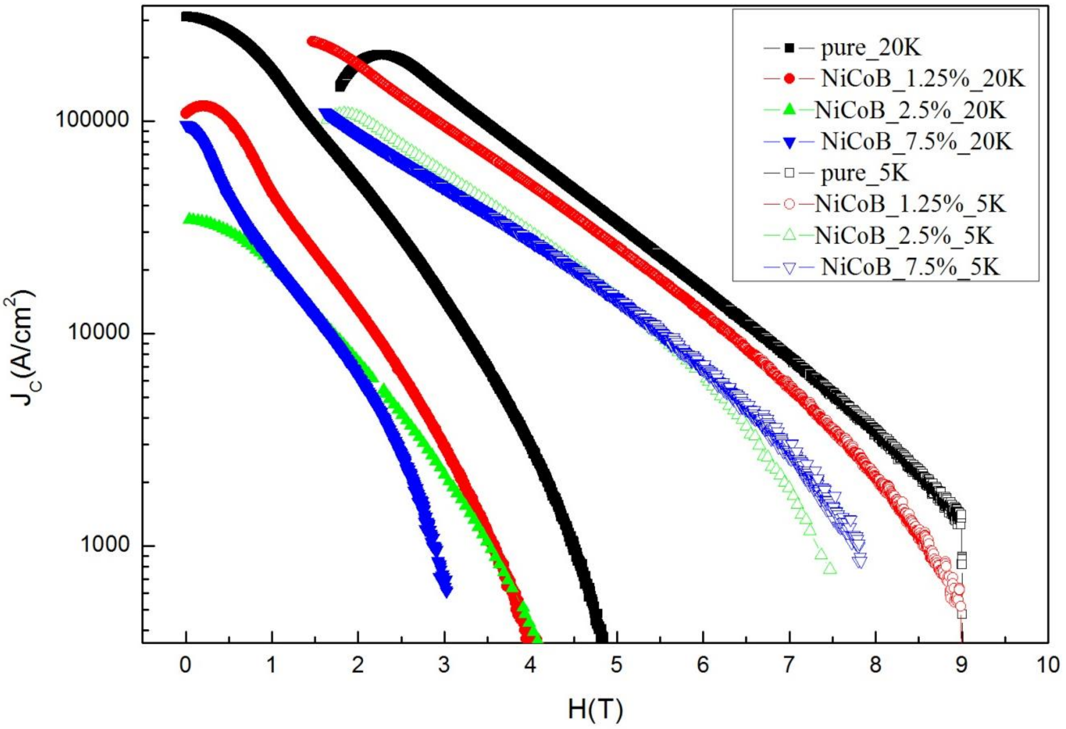

Fig.5.2.1: Field dependence of critical current density for pure MgB_2 and NiCoB doped MgB_2 (1.25wt%, 2.5wt% and 7.5wt%), sintered for 30 minutes at 650°C.

Figure 5.2.2 presents the decline of J_c with doping for samples sintered at 650°C and measured at 5 K and 5 T. The maximum value obtained is around 32000 A/cm^2 for the pure sample, while the best doped sample, the 1.25wt%, has J_c of 27000Acm^2.

The higher doped samples with 2.5 and 5wt% have substantially lower maximum values than for the pure one, only 15000 A/cm^2.

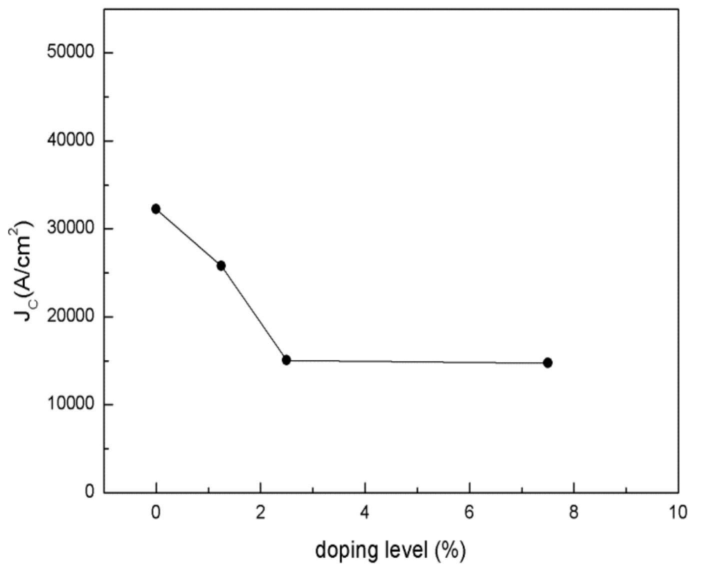

Fig. 5.2.2: Dependence of critical current density at field of 5 T and temperature of 5 K on the level of nano-NiCoB doping. All samples were sintered at 650°C.

The same trend has been observed for J_c values measured at 20 K, 2 T, as presented in Figure 5.2.3. At this temperature, of the decrease in J_c values with doping level is even sharper. The maximum obtained critical current density value is 47200 A/cm^2 for the pure sample, and for best doped sample (1.25 wt%), it is more than three times less, only 13500 A/cm^2. Only in the case of sintering at 650°C, did we fail to observe any improvement of critical current with doping.

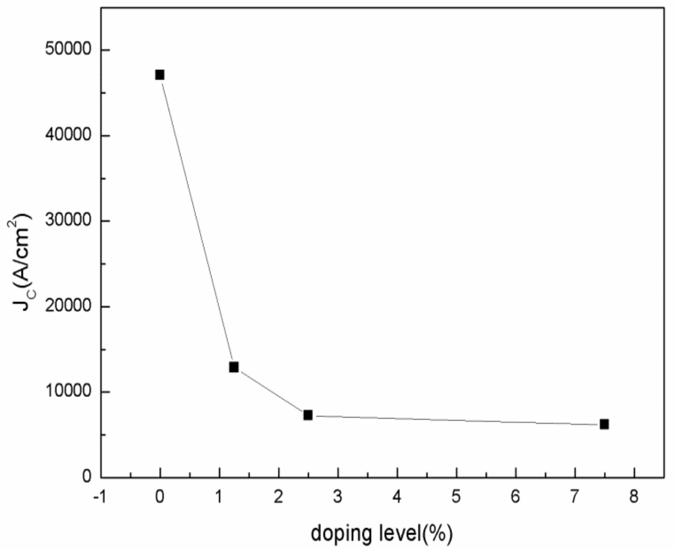

Fig. 5.2.3: Dependence of critical current density at field of 2 T and temperature of 20 K on the level of nano-NiCoB doping. All samples were sintered at 650°C.

Figure 5.2.4 shows that the amount of unreacted Mg increases with doping level, which negatively affects J_c. Mg phase is marked with the (*V*) symbol, and the MgB_2 phase with arrows (↓). From the XRD patterns, it can be observed that the proportion of unreacted Mg rises with doping level. MgO phase is stable for all samples, both pure and doped, and none show any excessive contribution.

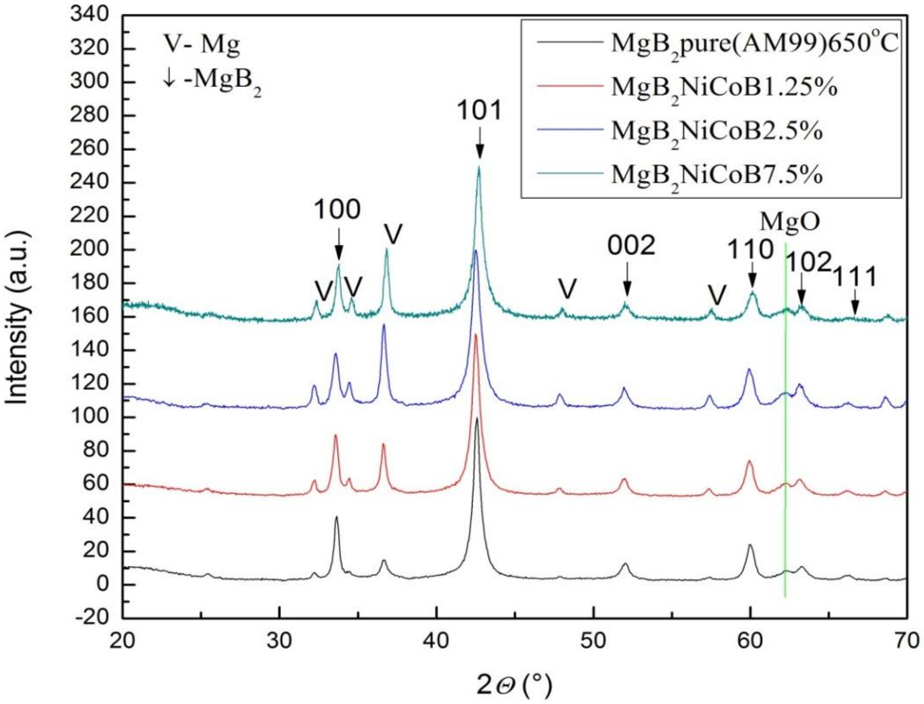

Fig. 5.2.4: XRD patterns of pure MgB_2 and MgB_2 doped with NiCoB at 1.25wt%, 2.5wt%, and 7.5wt%, with sintering at 650°C.

5.2.3.2 MgB_2 samples sintered at 770°C

Figure 5.2.5 shows slight improvement of J_c with doping for samples sintered at 770°C for both measured temperatures (5 K and 20 K). The J_c curves for pure and doped samples measured at 5 K are very close, with the best performance observed for the 2.5wt% doped sample. At 20 K, the pure sample and the 2.5wt% doped have almost the same values of J_c over the entire field range.

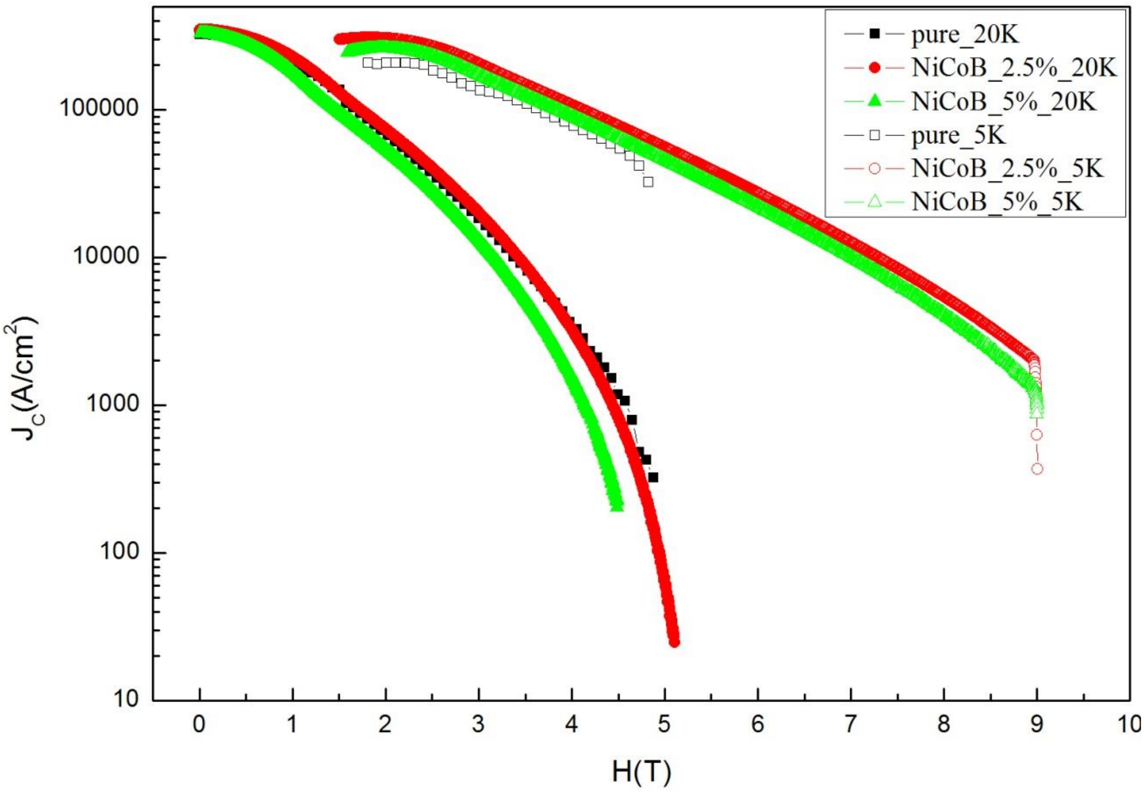

Fig. 5.2.5: Field dependence of critical current density for pure MgB_2 and NiCoB doped MgB_2, sintered at 770°C for 30 minutes.

Figure 5.2.6 shows the improvement of J_c with doping for samples sintered at 770°C and measured at 5 K, 5 T.

The maximum obtained value of 55800 A/cm^2 is for the 2.5wt% doped sample. It is interesting that the sample doped with 5 wt% NiCoB shows a considerably reduced maximum J_c value compared to the 2,5wt% sample of around 46000 A/cm^2, but even with this reduced performance, all the doped samples measured at 5 K are better than the pure MgB_2.

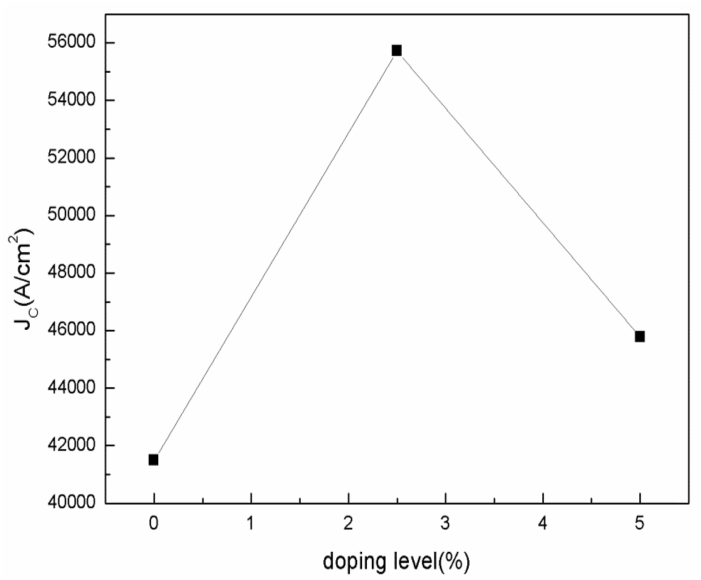

Fig. 5.2.6: Dependence of critical current density at field of 5 T and temperature of 5 K on the level of nano-NiCoB doping. All samples were sintered at 770°C.

The results measured at 20 K and 2 T present a slightly different situation, as can be observed from Figure 5.2.7. The 2.5wt% doped sample still has the best value of J_c, but in this case, the pure sample has significantly better J_c results than the 5wt% doped. For 770°C sintering temperature, the maximum value of critical current is 72500 A/cm^2 for the 2.5% doped sample.

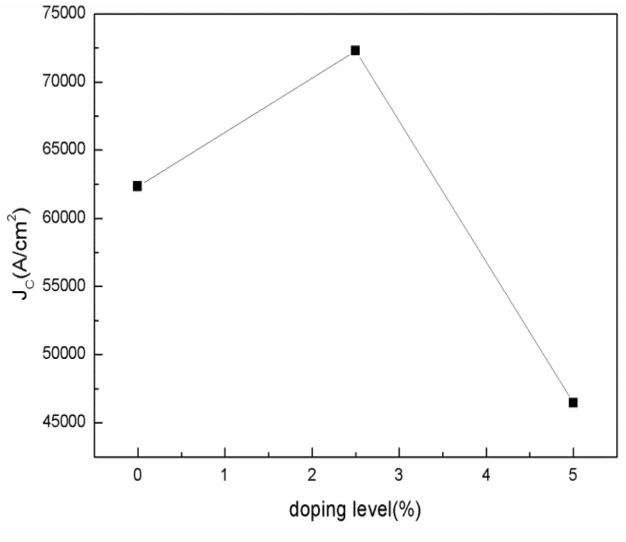

Fig. 5.2.7: Dependence of critical current density at field of 2 T and temperature of 20 K on the level of nano-NiCoB doping. All samples were sintered at 770°C.

According to the XRD patterns in Figure 5.2.8, can be stated that there are no big differences in peak position and intensity between the pure and doped samples. This conclusion can be linked to the results on critical current densities, which are quite close for all samples for both measured temperatures. Intensity of the MgO peak slightly decreases with doping, which is somewhat unexpected.

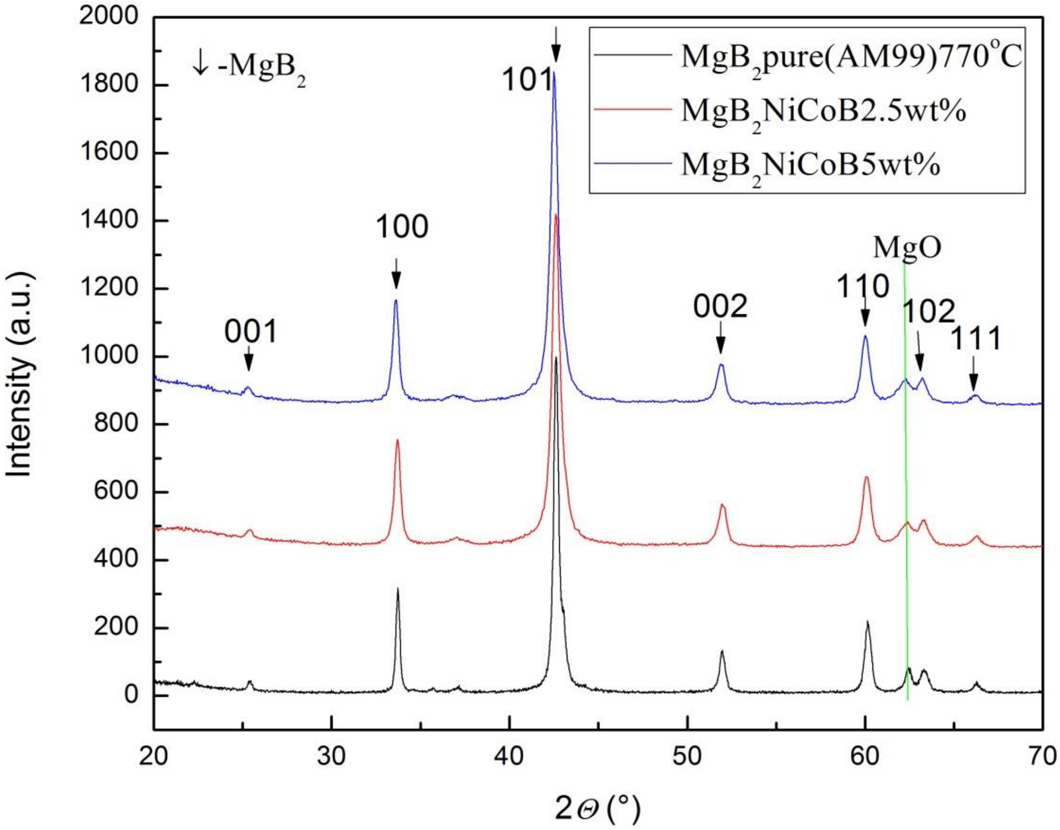

Fig. 5.2.8: XRD patterns of pure MgB_2 and MgB_2 doped with 2.5wt% and 5wt% NiCoB with sintering at 770°C.

5.2.3.3 MgB$_2$ samples sintered at 850°C

Figure 5.2.9 shows the improvement of J_c with doping for MgB$_2$ samples sintered at 850°C. From the Figure, considerable enhancement can be observed for the 2.5wt% and 5wt% doped samples at 5 K. At 20 K, only the 2.5wt% doped sample shows a slight improvement, while the 5wt% doped sample overlaps with pure MgB$_2$ over most of the field range.

The 1.25wt% doped sample presents a small improvement at 5 K, but doesn't show any improvement at 20 K.

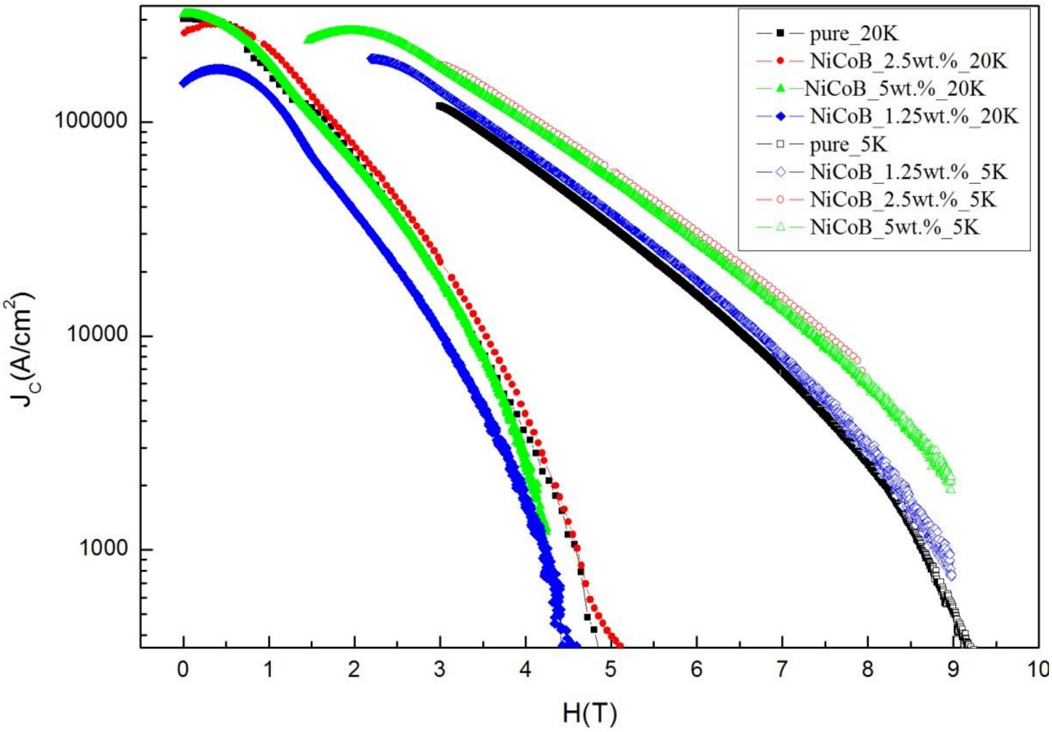

Fig. 5.2.9: Field dependence of critical current density for pure MgB$_2$ and nano-NiCoB doped MgB$_2$, sintered at 850°C for 30 minutes.

Figure 5.2.10 presents the J_c results for MgB$_2$ samples sintered at 850°C. The trend in the obtained results is rapid growth of J_c values with increasing doping level at 5 K and 5 T, with the doping level reaching saturation at 5wt% NiCoB doping. The maximum measured value of J_c is 61000 A/cm^2.

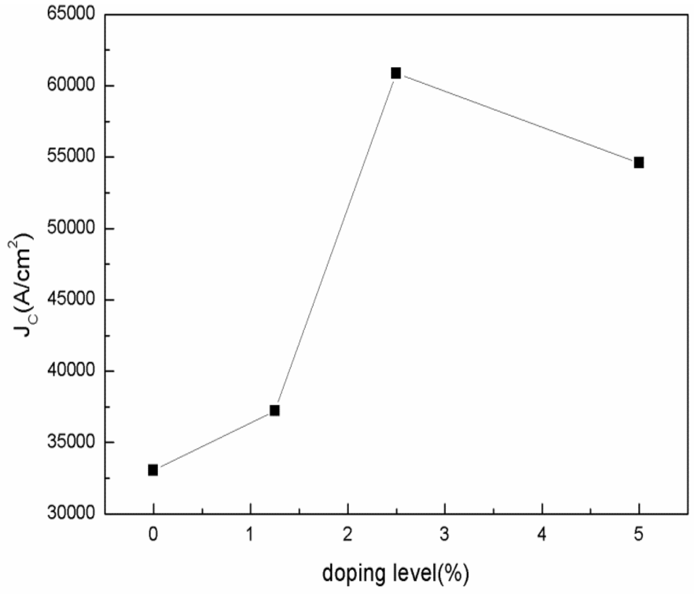

Fig. 5.2.10: Dependence of critical current density at field of 5 T and temperature of 5 K on the level of nano-NiCoB doping. All samples were sintered at 850°C.

The trend in obtained results is rapid growth of J_c values with increasing doping level at 20 K and 2 T. Saturation of doping is reached at 2.5wt% NiCoB doping. The maximum measured value of J_c is 82000 A/cm^2 for the 2.5wt% doped sample. There is a noticeable trend of increasing critical currents with doping and achievement of saturation at approximately the 2.5wt% doping level.

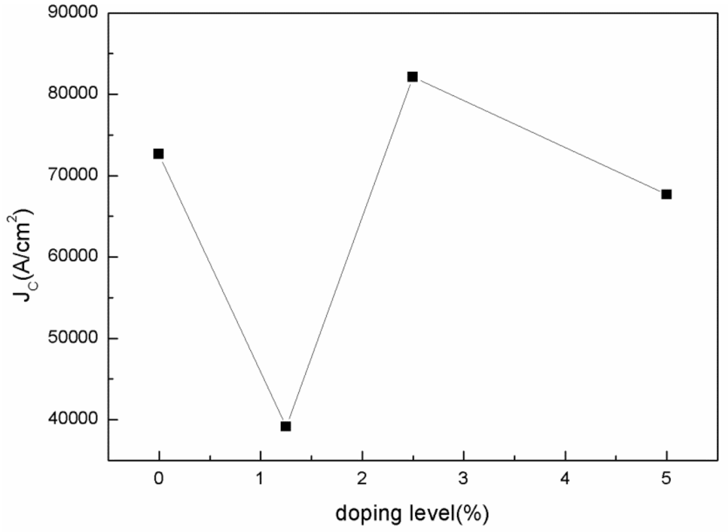

Fig.5.2.11: Dependence of critical current density at field of 2 T and temperature of 20 K on the level of nano-NiCoB doping. All samples were sintered at 850°C.

Figure 5.2.12 shows the XRD patterns of pure and doped MgB_2 samples sintered at 850°C. From the analysis of the results, we can reach the same conclusions as for samples sintered at 770°C. Unreacted Mg phase has almost disappeared, while the intensity of MgO phase is the same as for pure sample or very slightly increased with doping level.

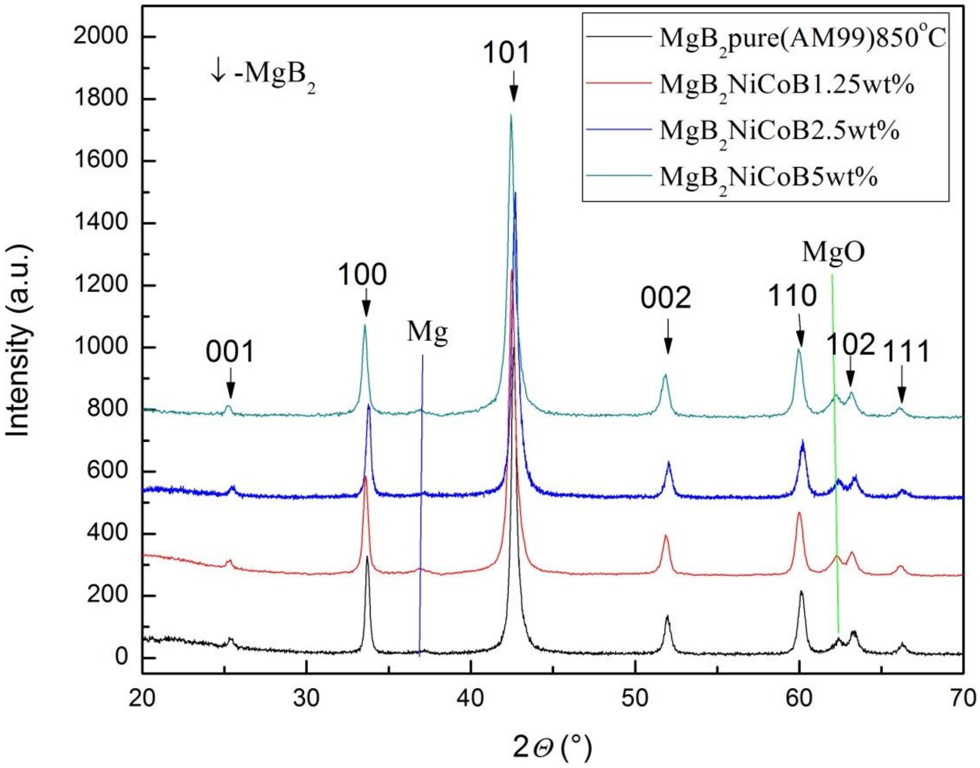

Fig. 5.2.12: XRD patterns of pure and doped MgB_2 samples sintered at 850°C.

5.2.3.4 MgB$_2$ samples sintered at 950°C

Figure 5.2.13 shows the J_c results for MgB$_2$ samples sintered at 950°C. At both measured temperatures, there is significant improvement of J_c, especially at 5 K. For 5 K, a slight change can be observed in the gradient of the $J_c(H)$ curve at high fields with the doping, which indicates increased pinning due to the doping. One of the reasons for such a large enhancement of J_c could be the strongly decreasing J_c with field for the pure sample, which will be seen in comparison with other pure samples sintered at lower temperatures.

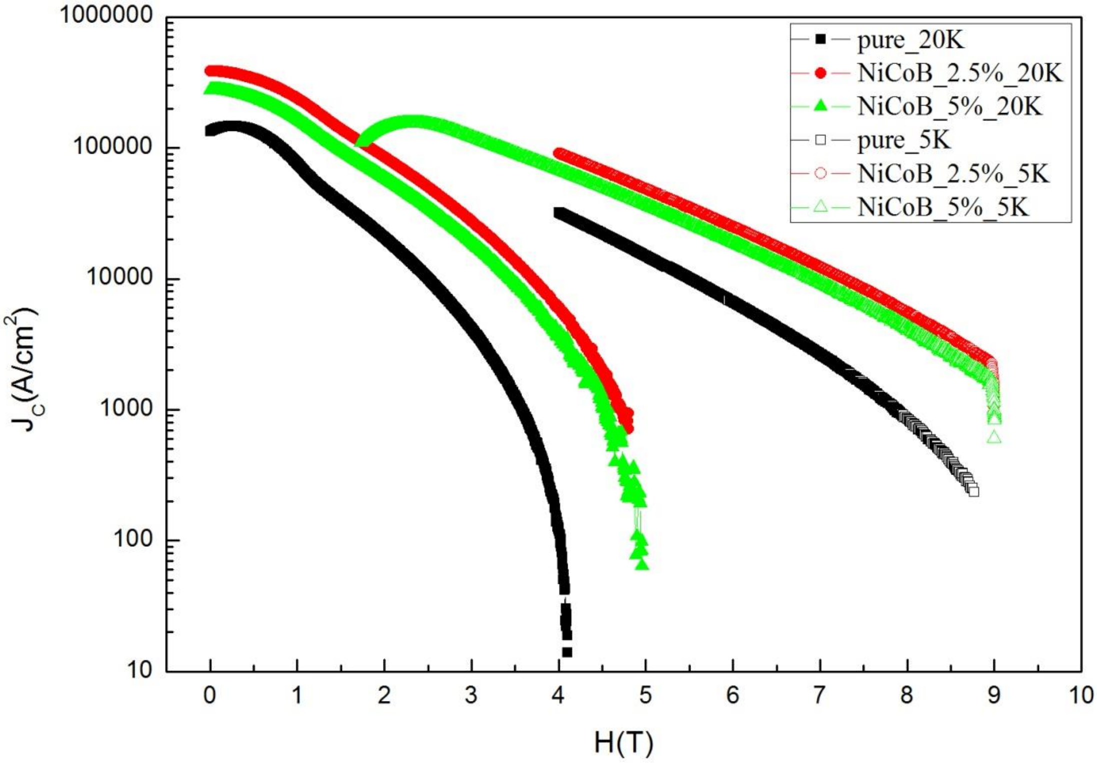

Fig. 5.2.13: Field dependence of critical current density for pure MgB$_2$ and nano-NiCoB doped MgB$_2$, sintered at 950°C for 30 minutes.

Figure 5.2.14 presents the J_c results for MgB$_2$ samples sintered at 950°C. The trend in the obtained results is excellent growth of J_c values with increasing doping level, with a slightly decline from the maximum for 5wt% NiCoB doping. The maximum measured value of J_c is 50000 A/cm^2 for the 2.5wt% sample.

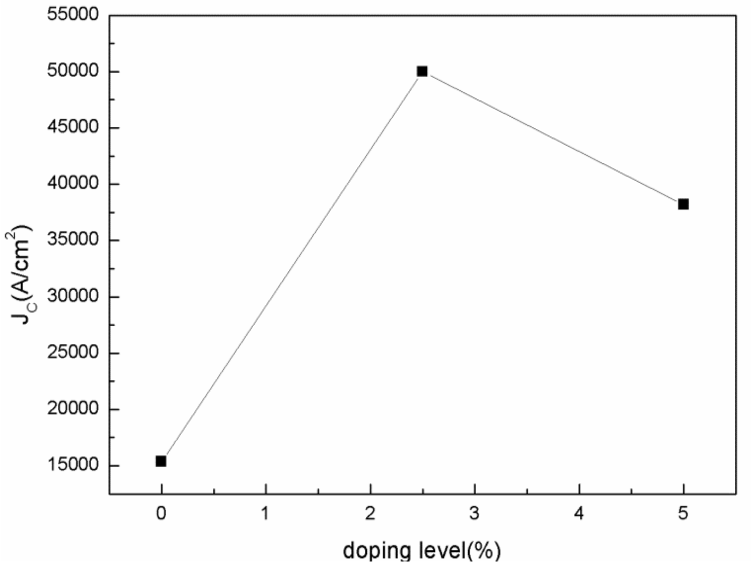

Fig.5.2.14: Dependence of critical current density at field of 5 T and temperature of 5 K on the level of NiCoB doping. All samples were sintered at 950°C.

The obtained results for the pure and doped samples sintered at 950°C and measured at 20 K and 2 T are presented in Figure 5.2.15. The results indicate rapid growth of J_c values with 2.5wt% doping, with the saturation level reached at 5wt% NiCoB doping. The maximum measured value of J_c is 80000 A/cm^2 for the 2.5wt% doped sample, which is very close to the best obtained value of 82000 for the 2.5wt% doped sample sintered at 850°C.

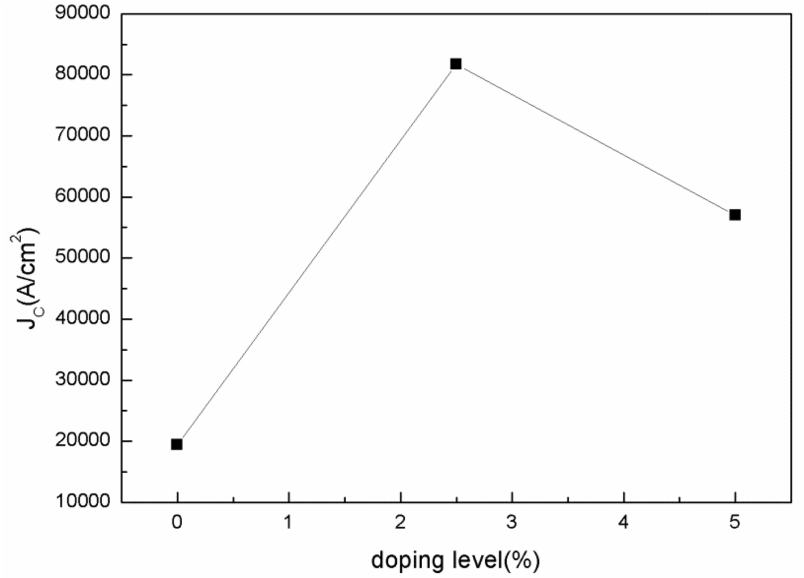

Fig.5.2.15: Dependence of critical current density at field of 2 T and temperature of 20 K on the level of NiCoB doping. All samples were sintered at 950°C.

The XRD patterns for the samples sintered at 950°C the appearance of a new phase, MgB_4, as can be seen in Figure 5.2.16. According to the literature[3], MgB_4 forms at higher sintering temperature and is generated by decomposition of MgB_2, according to the equation,

$2MgB_2 \rightarrow MgB_4 + Mg$. MgB_4 is a non-superconductive phase, so a high amount can negatively affect the electromagnetic properties.

Due to the volatile nature of Mg, the samples prepared above 850°C have started to decompose into MgB_4, as is shown by the XRD results. A small amount of MgB_4 phase can form good pinning centres, according to many research groups.[3]

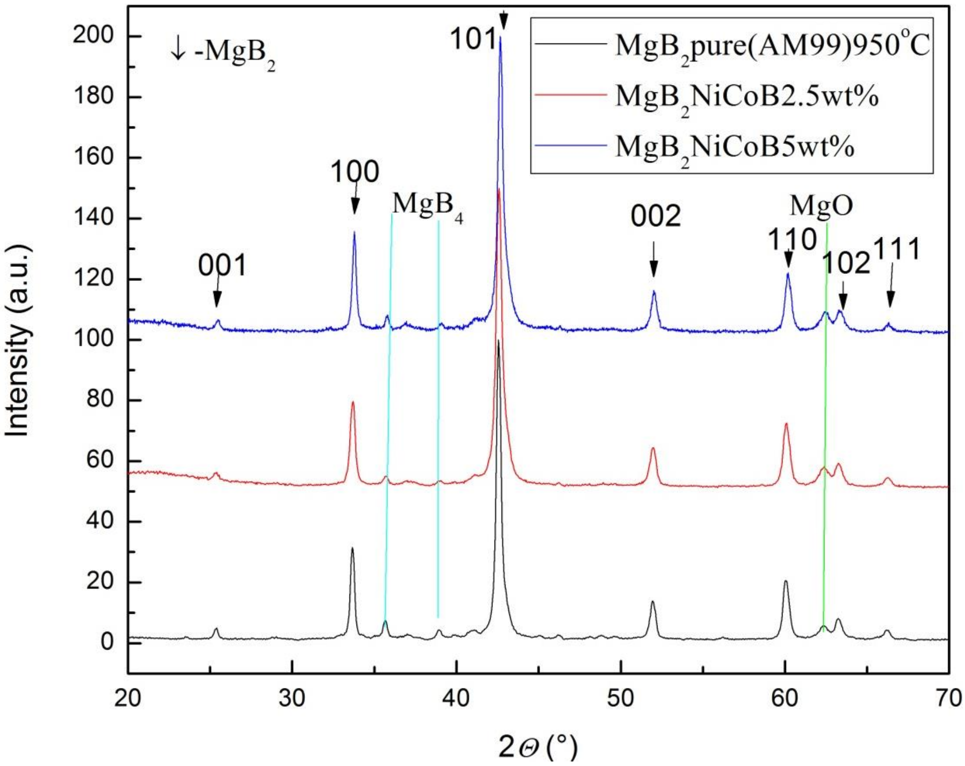

Fig. 5.2.16: XRD patterns of pure and NiCoB doped MgB_2 samples sintered at 950°C.

5.2.3.5 Comparison of the best values of J_c for the doped samples sintered at different temperatures

Figures 5.2.17 and 5.2.18 show comparisons of the best doped samples for different sintering temperatures. For all four sintering temperatures, the best doped samples are the 2.5wt%, forepart from 650°C, where enhancement is not obtained with doping. From both Figures, the same trend of J_c dependence on doping level can be seen.

The highest value is for the sample sintered at 850°C for both measured temperatures. The only difference is in the second best sample: at 5 K the second best sample was sintered at 770°C, and for 20 K, it was sintered at 950°C.

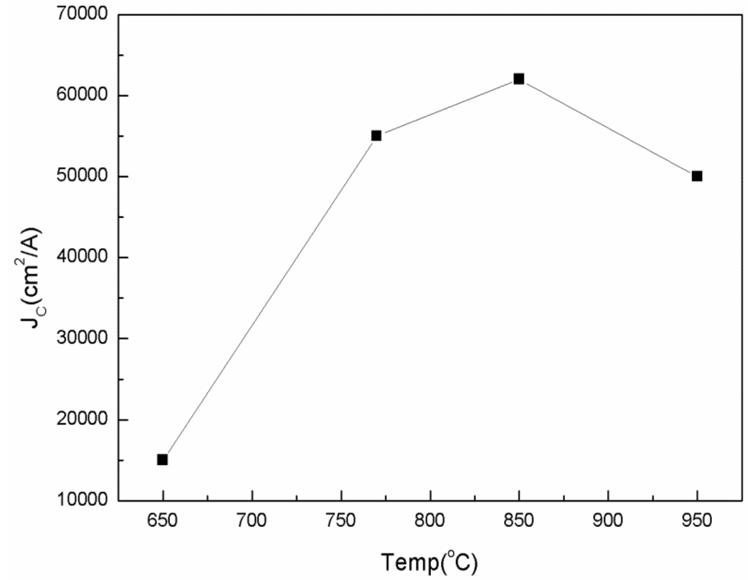

Fig. 5.2.17: J_c values (5 T, 5 K) of MgB_2 doped with the optimised best doping level (2.5%wt) for different sintering temperatures.

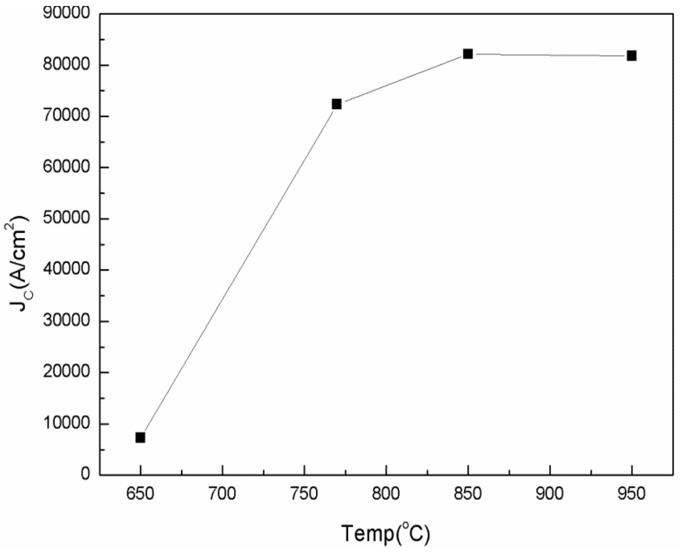

Fig. 5.2.18: J_c values (2 T, 20 K) of MgB_2 doped with the optimised best doping level (2.5%wt) for different sintering temperatures.

5.2.3.6 Comparing J_c values of pure samples sintered at different temperatures

A comparison of J_c for the pure samples sintered at different temperatures using the same boron source as for the best doped samples, AM99, can be observed in Figure 5.2.19. It is quite apparent that the pure samples sintered at 650°C, 770°C, and 850°C have almost the same shape of $J_c(H)$ at 20 K and for a wide range of fields at 5 K.

The only difference that can be observed for highest fields is at 5 K, where the 650°C sample has better performance. The pure sample sintered at 950°C has a significantly smaller value of J_c for both measured temperatures, which can be explained by lack in connectivity between the grains.

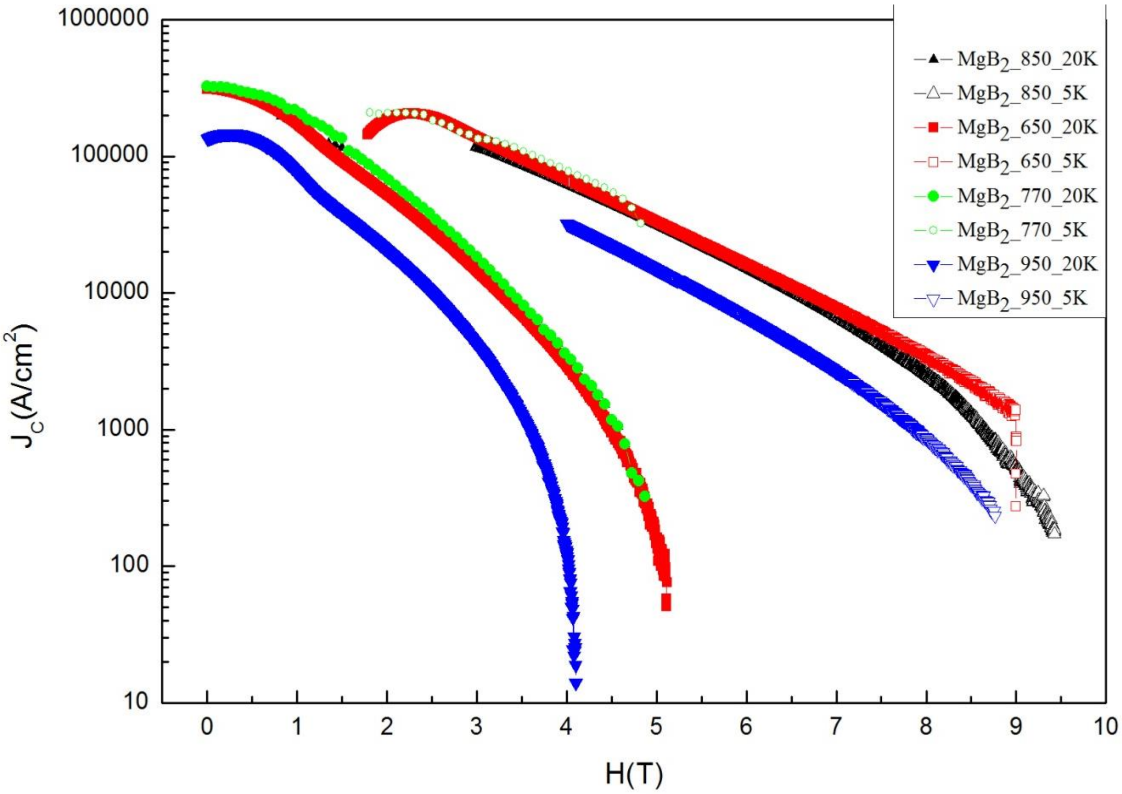

Fig. 5.2.19: Pure MgB_2 samples sintered at different temperature. AM99 was used as the boron precursor.

From Figure 5.2.20, we can draw several conclusions. Only att the lowest sintering temperature (650°C), did we detect unreacted Mg phase (V) in significant amounts. Samples sintered at 770°C and 850°C show almost the same results, which indicates that in that temperature range the formation of phases is very similar.

The J_c values are also very similar. Finally, at the highest sintering temperature 950°C, a new phase appeared, MgB_4 (B). This new phase has a negative influence on J_c values for pure MgB_2. The proportion of MgO phase is very similar for all temperatures and does not show any growth with rising temperature.

On comparing critical current density for samples sintered at different temperatures, it is obvious that there are large differences between them. The doped samples showed improvement of critical current density for all sintering temperatures in comparison to pure MgB_2, except for the doped samples sintered at 650°C. The opposite trend for the effect doping on critical current density is obtained for the sintering temperature of 650°C in comparison with other temperatures.

From the accompanying graphs of $J_c(H)$, it is clear that the best results for the critical current density were obtained at 850°C, and for the 2.5wt% doping level. That doping level presents the best values of J_c for every sintering temperature where enhancement of J_c was achieved. The sintering temperature range between 750°C and 850°C gives the best results for J_c overall.

This can be explained by the formation of a new phase between the MgB_2 precursor powders and the NiCoB nanoparticles (section 5.4), as well as by the optimum grain size and connectivity. The new phase promotes good vortex pinning and provides good connectivity among the grains as well. This conclusion will be explained in the next chapters based on SEM, differential thermal analysis (DTA), and XRD results.

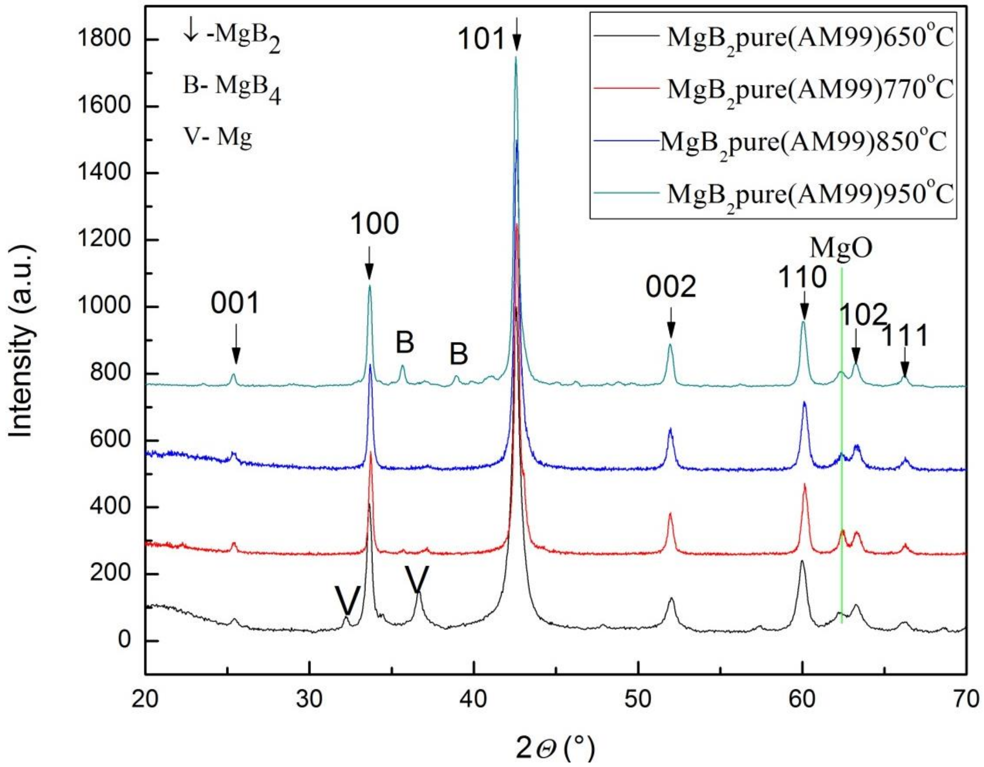

Fig.5.2.20: XRD for pure MgB_2 samples prepared at different sintering temperatures, made with AM99 boron.

Changes in the morphology of the MgB_2 samples with sintering temperature can be explained by the improvement in crystallinity with temperature, which is usually connected with increasing grain size.

Table 5.2.2 shows that the smallest grain size is for the sample sintered at 650°C, in agreement with the literature.[4,5,6,7]

Increasing the sintering temperature from 770 to 950°C decreases the grain size, according to the full width at half maximum (FWHM) results for the main peaks in XRD. This can be explained by the presence of more impurities and surface dislocations at higher temperature. Samples sintered at the highest temperature 950°C of have begun to show decomposition of MgB_2 grains into MgB_4 and Mg, which produces more impurities and small size crystals. Improvement of crystallinity is also associated with better grain connectivity of MgB_2 grains, resulting in increased density of the MgB_2, as shown in the SEM pictures of MgB_2 in chapter 5.3.3.

Table 5.2.3 shows the calculated densities and lattice parameters for the pure and 2.5wt% doped samples sintered at the three different temperatures: 650°C, 850°C, and 950°C. The pure samples showed considerable homogeneity in terms of density. The doped samples, on the other hand, presented significant deviation. The 650°C doped sample has a lower value than for the pure samples, while 850°C doped sample has a higher value.

The 950°C has a value very close to that of the pure samples. Higher density and better connectivity with fewer voids can be one of the main reasons for the good J_c results observed for the 850°C doped sample. It was also observed that the lattice parameters did not change within the sintering temperature range of 650°C to 950°C or the doping within the accuracy of error. The lattice parameter results suggest that Co or Ni could not substitute into Mg sites. The lattice parameters were calculated by the Rietveld refinement method using the Jade 5.0 program (XRD pattern processing).

XRD patterns of all the sample shows sharp peaks of MgB_2 phase with a small fraction of MgO. The amount of MgO is steady for all sintering temperatures except for the 650°C sample, where large amounts of residual Mg have been observed, especially for the doped samples. MgB_2 peaks become sharper and stronger with increasing temperature, indicating better phase purity and/or crystallinity.

FWHM of all the peaks decreases significantly with increasing sintering temperature, indicating that the grain size of MgB_2 increases with sintering temperature.

Plane	(100)		(110)		(002)	
Samples	FWHM (°)	D_p (nm)	FWHM (°)	D_p (nm)	FWHM (°)	D_p (nm)
MgB_2(AM99) 650^{o}C	0.444	186	1.370	70	0.754	118
MgB_2(AM99) 770^{o}C	0.270	307	0.371	247	0.372	238
MgB_2(AM99) 850^{o}C	0.315	264	0.464	199	0.458	192
MgB_2(AM99) 950^{o}C	0.358	232	0.517	177	0.438	203

Table 5.2.2: Calculations of FWHM and grain size for pure MgB_2 samples sintered at different temperatures.

Samples	ρ (g/cm^3)	a (Å)	c (Å)
Pure 650°C	2.615	3.090	3.526
Pure 850°C	2.624	3.084	3.527
Pure 950°C	2.618	3.086	3.529
NiCoB_2.5wt%_650	2.281	3.073	3.508
NiCoB_2.5wt%_850	2.633	3.085	3.528
NiCoB_2.5wt%_950	2.612	3.086	3.529

Table 5.2.3: Calculated densities and lattice parameters for pure MgB_2 and 2.5wt% NiCoB doped samples sintered at different temperatures.

5.2.3.7 Calculation of maximum pinning force (F_{pmax})

Pinning force (F_p) dependence on temperature is usually obtained by plotting the normalized pinning force $F_p = F_p/F_{pmax}$ versus the magnetic field normalized by the irreversibility field, B/B_{irr}. According to the Dew-Hughes theory of pinning and general relations, the pinning mechanisms can be determined in superconductors[8]:

$$F_p(h) = F_p/F_{pmax} \propto h^p(1-h)^q \quad (5.2.1)$$

where p and q are dimensionless parameters depending on the specific characteristics of flux pinning in superconductors, and h is the reduced magnetic field B/B_{irr}. Different types of pinning mechanisms are described by different values of p and q.

According to Kramer, in this model, p=1/2 and q=2 describe normal core correlated pinning, while p=1 and q=2 describe normal core point pinning.[9]

The pinning curves of the NiCoB doped samples are shifted to higher values of B/B_{irr}. The observed results can be fitted with the expression $h^{0.9}(1-h)^{2.6}$.

Fit to the data presented in Fig. 5.2.21 using the equation 5.2.1 cannot give a satisfactory agreement with the experimental points. Therefore, this procedure cannot be used for determining the type of pinning in our samples. One possible reason for this is the artefacts obtained in magnetic measurements due to sample porosity[12]. Nevertheless, grain boundary pinning is expected to have a significant role for these samples, due to large surface area of grain boundaries.

The explanation could be that doping with NiCoB nanoparticles has effectively changed the properties of MgB_2.

These changes are most likely due to the reduced grain size and better connectivity between the grains, as also seen in SEM images (Chapter 5.3.), both of which will be responsible for the enhanced upper critical field and flux pinning force. Also, there will be the effects of secondary phases, Mg_2Co/Co_2Mg and Mg_2Ni, as described in section 5.4.[10]

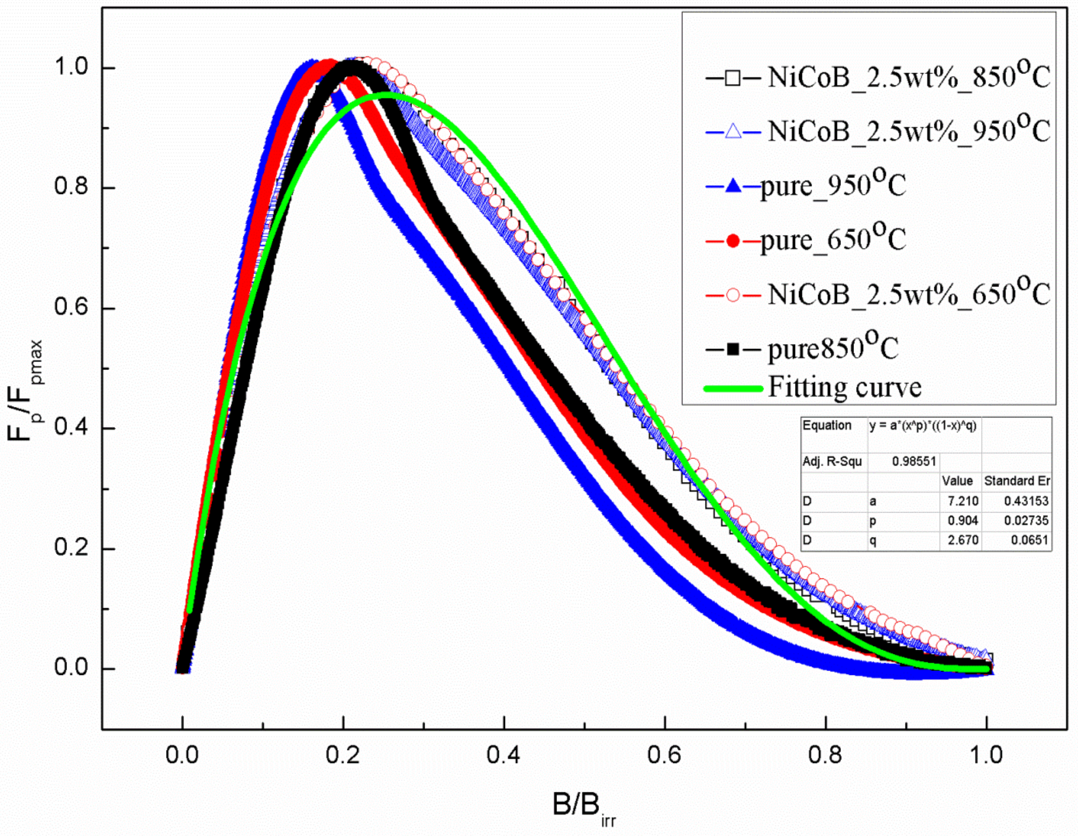

Fig. 5.2.21: Normalized volume pinning force ($F_p/F_{p,max}$) as a function of field at 5 K for the MgB_2 samples. The volume pinning force is $F_P=J_c \times B$. The F_p is normalized by the maximum volume pinning force $F_{p,max}$.

According to the pinning force calculated by the formula $F_P=J_c \times B$, there is substantial enhancement of the pinning force for the doped samples (2.5wt %) sintered at 850°C and 950°C, as can be seen in Figure 5.2.22. The observed curves for the doped samples also have the peak maximum shifted slightly to higher field.

This indicates that the maximum pinning force occurs at higher magnetic fields for the doped samples. The sample sintered at 950°C has the biggest value of the pinning force measured at 5 K. A significantly reduced pinning force was identified for the samples sintered at 650°C. For the pure MgB_2 samples, the highest value of the pinning force at 5 K was obtained for sintering at 650°C, while the minimum pinning force was for the sample sintered at 950°C. The improvement of pinning could also be due to the occurrence of new phases (Mg_2Co/Co_2Mg and Mg_2Ni), which can provide a large number of impurities with good pininng abilities.

Figures 5.2.21 shows the normalized flux pinning force density f_p (F_P/F_{Pmax}, where $F_P = J_c \times B$) as a function of applied magnetic field.

The improved pinning in the optimized (2.5wt% NiCoB doped, 850°C) sample seems to be caused by enhanced pinning from the new phase discussed above, provided by the large number of impurities with good pinning abilities.

From the figure, it is clear that all doped samples show a shift in their maximum pinning force to higher field. From the second figure, the highest value of the pinning force was for the doped sample sintered at 850°C. The sample sintered at 950°C shows the second best value of the pinning force, and the maximum is most shifted to higher field compared with the other samples.

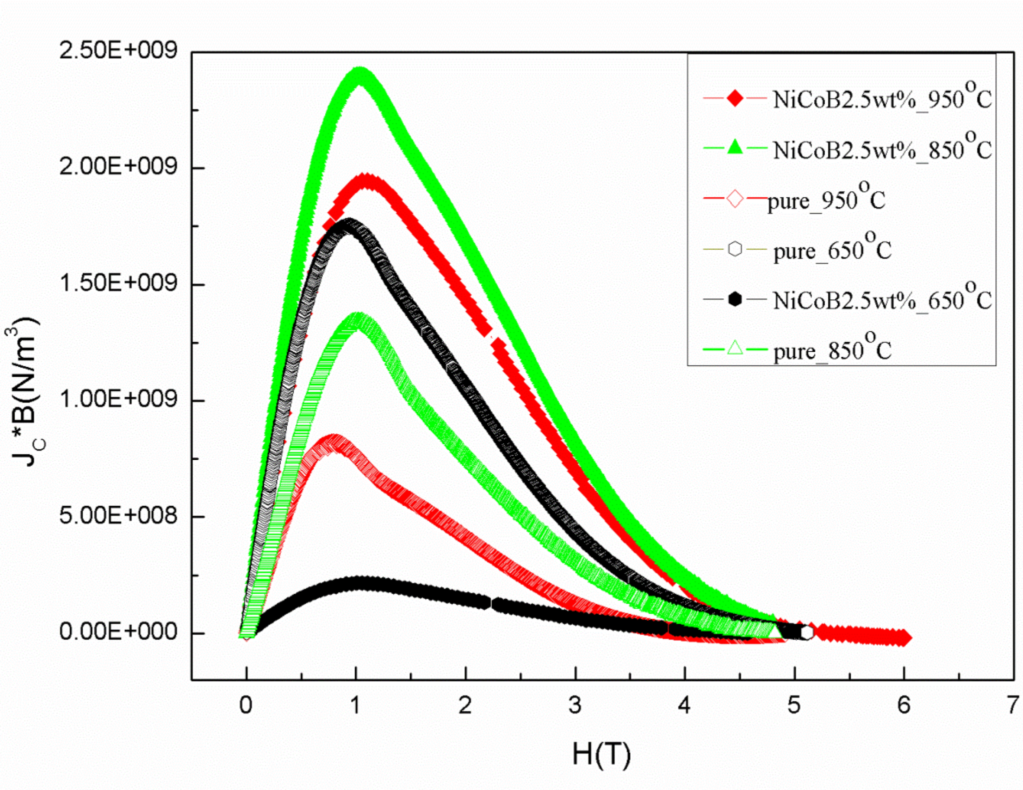

Fig.5.2.22: Values of pinning force $Fp = J_c \times B$, for doped (2.5wt%) and pure samples sintered at different temperatures.

5.2.3.8 Kramer plots for different temperatures

The pinning force strength, $F_K = J_c^{1/2}B^{1/4}$, is expected to be a linear function of magnetic field *(B)*.[11,9] F_K is not really linear, however, in particular at low J_c, where it is observed to have a curvature.

It was observed that the pinning force strengths of all NiCoB doped samples sintered at 850 and 950°C were considerably larger than that of the reference sample (Figs. 5.2.24 and 5.2.25). Only the doped samples sintered at 650°C show reduced F_K (Fig. 5.2.23). Also, $\boldsymbol{F}_K$ is not really linear at low field and is gradually curving at higher fields. In comparison, curves of the doped and pure reference sample in Figures 5.2.24 and 5.2.25 can be observed to gradually merge as they approach higher fields. It can be concluded that the pinning of doped samples is much stronger in the low and middle field range and gradually decreases in the higher field range.

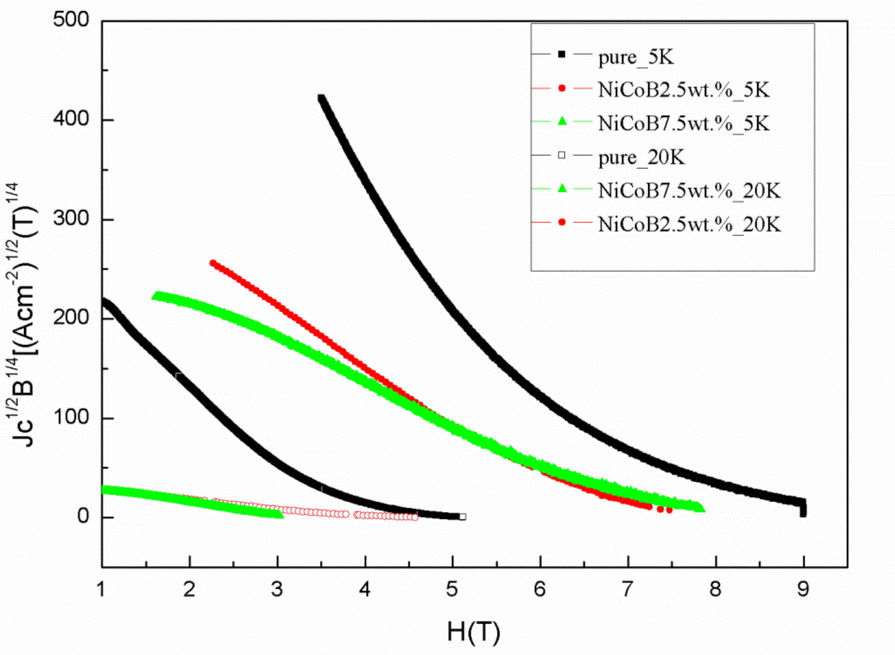

Fig. 5.2.23: Kramer plots for pure and doped samples sintered at 650°C, calculated for 5 K and 20 K.

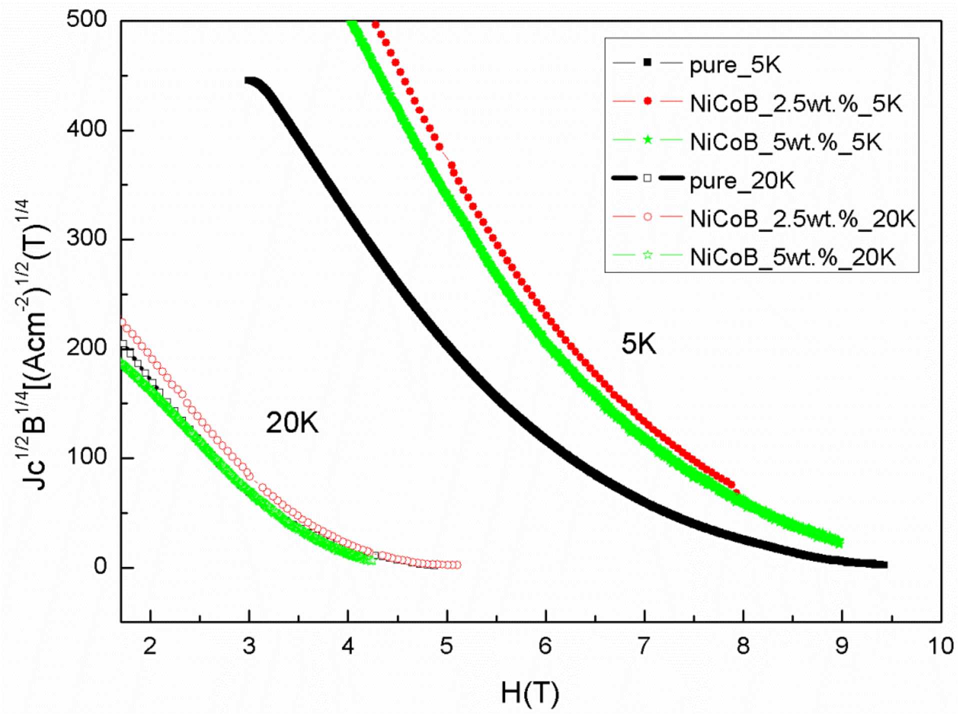

Fig. 5.2.24: Kramer plots for pure and doped samples sintered at 850°C, calculated for 5 K and 20 K.

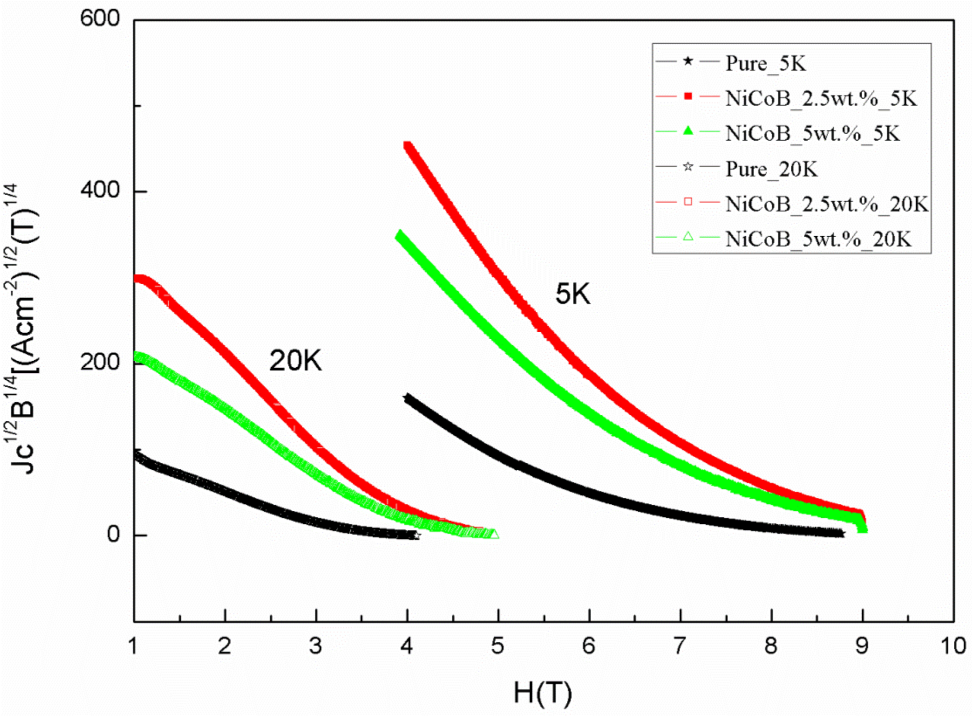

Fig.5.2.25: Kramer plots for pure and doped samples sintered at 850°C, calculated for 5 K and 20 K.

5.2.4 Conclusions

Optimal preparation procedures for obtaining the best J_c at elevated fields were established in this chapter for nano-NiCoB doped MgB_2 pellets. In this study, samples were sintered for 30 minutes at four different temperatures from 650°C to 950°C. The best results were obtained for the 2.5 wt.% NiCoB doped MgB_2 sintered at 850°C, using amorphous boron powder with around 0.5 μm grain size and Mg of several microns.

It is important to emphasize that the improvement in critical current density is observed for all samples sintered above 750°C, which is connected with the completion of the reaction between boron and magnesium, and incorporation of dopant nanoparticles in the MgB_2 matrix. It is interesting that despite the increase in grain size with increasing temperature, the obviously improved connectivity and pinning from the newly formed phase was instrumental in this improvement of critical current.

XRD analysis also indicates that optimal performance is associated with the formation of a new phase in the sample. A detailed investigation of the mechanisms for this improvement of J_c with nano-NiCoB doping is presented in the following chapters. The doping did not result in improvement of J_c at 20 K, which can be explained by the higher thermal excitation of super-electrons, especially in the π-gap.

5.2.5 REFERENCES

1 X. Xu, J. H. Kim, S. X. Dou, S. Choi, J. H. Lee, H. W. Park, M. Rindfleish, and M. Tomsic, Journal of Applied Physics, 105 (10), 1-5., 2009.

2 Zi-Kui Liu, D.G. Schlom, Qi Li and X.X. Xi, Appl. Phys. Lett.78 3678, 2001.

3 K. Singh, R. Mohan, N. Kaur, N.K. Gaur, M. Dixit, V. Shelke, R.K. Singh, Physica C 450 124–128, 2006.

4 Y.U. Jung, M.-S. Park, W. N. Kang, M.-S. Kim, K. H. P. Kim, S. Y. Lee, and S.-Ik Lee, Appl. Phys. Lett. 78, 4157, 2001.

5 S. X. Dou, A. V. Pan, S. Zhou, M. Ionescu, X. L. Wang, J. Horvat, H. K. Liu, and P. R. Munroe, J. Appl. Phys. 94, 1850, 2003.

6 S. X. Dou, A. V. Pan, S. Zhou, M. Ionescu, H. K. Liu, and P. R. Munroe, Supercond. Sci. Technol. 15, 1587, 2002.

7 W. X. Li, R. Zeng, L. Lu, Y. Li, and S. X. Dou, J. Appl. Phys. 106, 093906, 2009.

8 D. Dew-Hughes, Philos. Mag. 55, 459, 1987.

9 E. J. Kramer, J. Appl. Phys. 44, 1360, 1973.

10 S.R. Ghorbani, X.Wang, S.X. Dou, S. Lee, and M. Hossain, Flux-pinning mechanism in silicone-oil doped MgB_2, Physical Review B, 78(18), pp. 184502-1-184502-5., 2008.

11 V. Braccini, L. D. Cooley, S. Patnaik, D. C. Larbalestier, P. Manfrinetti, A. Palenzona, and A. S. Siri, Appl. Phys. Lett. 81 4577-4579, 2002.

12 J. Horvat, S. Soltanian, X.L. Wang, and S.X. Dou, Effect of sample size on magnetic J_c for MgB_2 superconductor, Applied Physics Letters, 84, 3109, 2004.

Chapter 5.3: Improvement of J_c by NiCoB Nanodoping

5.3.1 Introduction

Improvement of critical current density of MgB_2 superconductor usually can be done in two main ways improving the flux pinning by adding different flux pinning centres as defects, dislocations, and precipitates,[1,2,3,4] and by improving the connectivity between grains by optimizing the sintering and material parameters.[5,6]

The superconducting properties of superconductors can be considerably improved by doping with various elements and compounds. Many groups have reported successful enhancement of the critical current density, J_c, the irreversibility field, H_{irr}, and the upper critical field, H_{c2}, by doping MgB_2 with elements such as as carbon, Zr,[7] Al,[8] Si,[9] and Sn[10] and with various compounds such as SiC,[11] ZrB_2,[12] Co_2O_3,[13] and Fe_2O_3 [14].

Adjusting the preparation conditions for the best performance of MgB_2 is the most important priority in doping with new substances, as will be presented in this chapter. NiCoB nanoparticles with less than 10 nm in size have great potential in various scientific fields. The size of NiCoB nanoparticles roughly matches the size of the coherence length of MgB_2, which make them ideal pinning centers. The complex structure of nanoparticles and their high reactivity justify their selection for doping MgB_2, but also represent substantial obstacles to the discovery of their influence on the properties of superconductors.

On the other hand, doping with nanoparticles can result in undesirable effects, such as agglomeration of nanoparticles, poor reactivity with boron, increase of oxygen in the sample, etc, which will have negative effects on the properties of MgB_2.

Chemical doping, especially with nanoparticles, is one of the commercially most efficient ways of obtaining significant improvement of the critical parameters of MgB_2. As well, this technique can provide a great many combinations in terms of the shape, size, and type of dopants, which can give big and diverse opportunities for further improving MgB_2 and other superconductors. In this section, the doping of MgB_2 with NiCoB was investigated.

5.3.2 Experimental procedure

The samples were prepared by mixing Mg and amorphous AM99 boron in the stoichiometric ratio and adding NiCoB nanoparticles at 1.25, 2.5 and 5.0 wt%. The samples were pressed into pellets at 1000 bar. The pellets were enclosed in iron tubes and heat-treated at 850°C for 30 min in protective argon atmosphere. The microstructure was studied by scanning electron microscope (SEM, JSM-6400 (JEOL, Japan)) and by X-ray diffractometer (XRD), while the electromagnetic properties were studied by a physical properties measurement system (PPMS) magnetometer, with the critical current density calculated by the critical state model.[15]

Magnetic hysteresis loops were collected at 5 K and 20 K using PPMS (Quantum Design) in a time-varying magnetic field with sweep rate 50 Oe s^{-1} and amplitude 9 T. Due to the large sample size effect on the magnetic J_c for MgB_2, all the samples for measurement were made to the same dimensions ($1 \times 2 \times 3$ mm^3) for comparison. For these dimensions, the samples are big enough so that the magnetic J_c exhibits a very weak dependence on the sample size[16,17].

Furthermore, by keeping the sample size the same for all measurements, any variations in obtained J_c due to the artefact of the sample size are further minimized. Magnetic relaxation was measured on the PPMS. In this measurement, the decay of magnetisation was measured as a function of time at constant temperature (5 K and 20 K) and stable applied field (4 T and 2 T, respectively). The procedure suggested by Yeshurun was used in these measurements.[18]

The sample was first cooled in zero field from room temperature to the measurement temperature. A large magnetic field was then applied, making sure that the sample was fully penetrated by the field. The field was then reduced by at least 3 times the field of full penetration, to 4 T or 2 T. The temperature dependence of the resistivity was studied by using the standard four-probe method from 30 K to 300 K.

5.3.3 Experimental results

5.3.3.1 SEM images: Pure MgB_2 sintered at 850°C and 650°C

Figure 5.3.1 (a, b) shows scanning electron microscope (SEM) images of pure MgB_2 sintered at 850°C while Figure 5.3.2 (a, b) shows SEM images of pure MgB_2 sintered at 650°C. By analysing the SEM images of the two MgB_2 samples sintered at 650°C and 850°C, differences in the morphology and size of grains can be observed. In agreement with other research, the grain size increases with increasing temperature, which is explained by sufficient energy for greater crystalline growth at higher temperature. The average MgB_2 grain size for 850°C is from 500 nm to 750 nm (Figure 5.3.1 (a, b)), whereas for 650°C, it is below 500 nm (Figure 5.3.2 (a, b)).

Likewise, the morphology shows considerable differences: the 650°C samples show fine hexagonal and mostly randomly oriented MgB_2 grains. The 850°C samples have grains shaped like towels in a pile, which indicates better connectivity between grains. For the pure sample sintered at 650°C, a significant number of bright particles with 50 nm in size can be distinguished, which probably belong to unreacted Mg.

Higher brightness can be related to the SEM electron beam, where conductive materials conduct more electrons from electron gun. Some clusters with smaller grain size than unreacted Mg can also be observed, which can be associated with MgO. Equally, for the pure sample sintered at 850°C, only MgO clusters with size less than 20 nm can be detected.

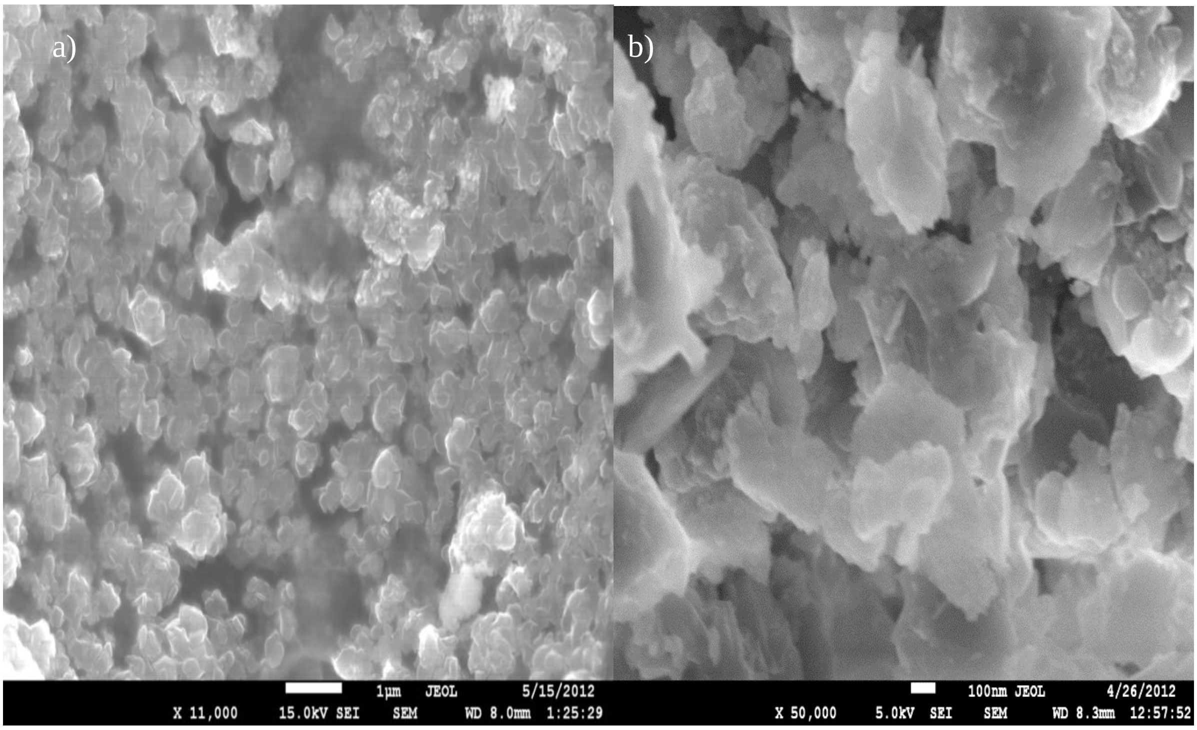

Fig.5.3.1 (a), (b): SEM images of pure MgB_2 sintered at 850°C at different magnifications.

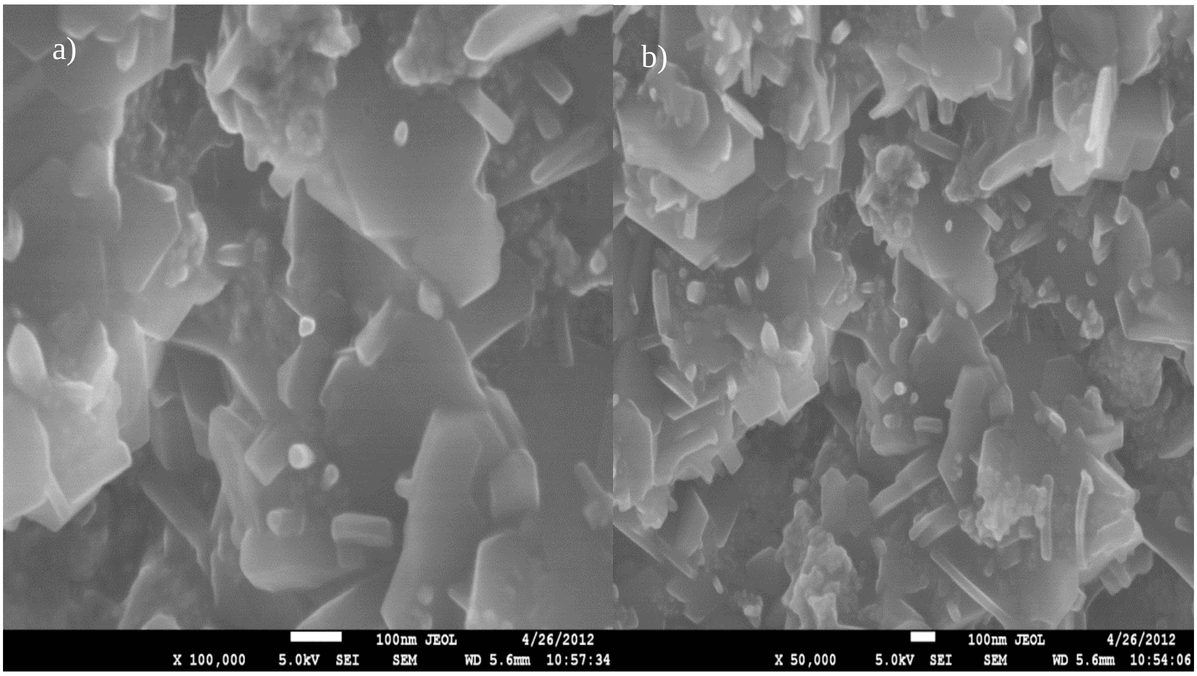

Fig.5.3.2 (a), (b): SEM images of pure MgB_2 sintered at 650°C.

5.3.3.2 EDS of pure MgB_2 sintered at 850°C

Figure 5.3.3 presents energy dispersive spectroscopy (EDS) analysis for the pure sample sintered at 850°C based on the areas indicated by the rectangles, with associated tables of the EDS data for the areas marked as 001 to 005.

From the EDS data a balance can be observed in the mass ratio of magnesium to boron for all observed areas. The lack of any excess magnesium points to well-prepared samples and good sintering conditions. The contribution of oxygen (MgO) is a quite high in all observed sections, except for area 001 (Table 5.3.1). The morphology of area 001 is different from that of the other areas, displaying a smoother surface without too many grain boundaries.

On the other hand, areas 002, 003 and 004 (Table 5.3.1) have similar structure with more excess oxygen, which is associated with more grain boundaries, and small bright particles approximately 50-100 nm in size. Area 005 (Table 5.3.1) has a smaller amount of oxygen, which can be explained by the lack of small particles in that area. From the EDS data, it can be concluded that there is a correlation between the appearance of small particles and excess of oxygen.

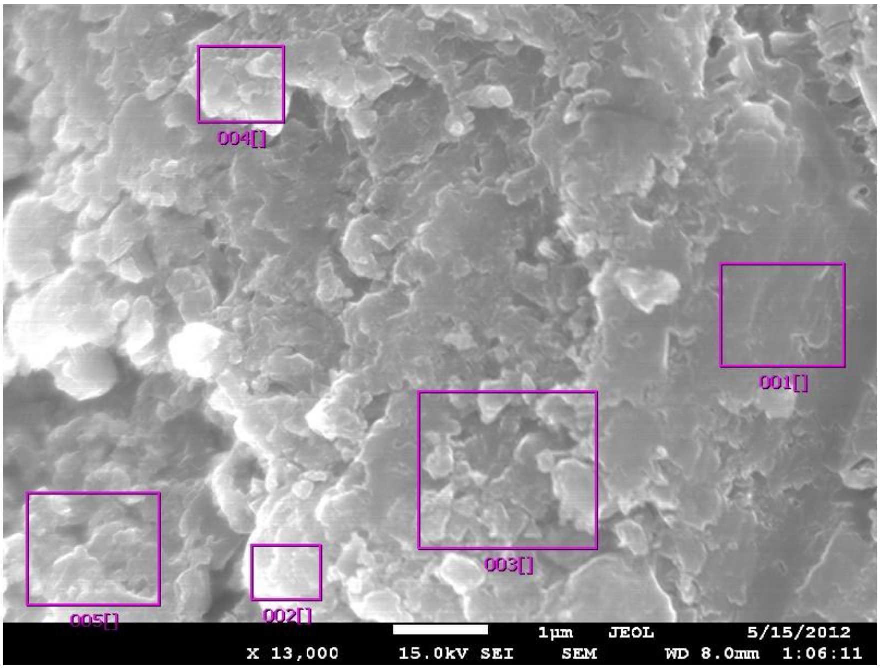

Fig.5.3.3: SEM image of pure MgB_2 sample sintered at 850°C with rectangles indicating areas analysed by EDS.

Area 1. Elements	mass%	mol%	sigma	**Area 2. Elements**	mass%	mol%	sigma
B*	52.17	70.39	0.13	B*	66.54	80.35	0.05
O*	2.92	2.66	0.18	O*	6.02	4.91	0.11
Mg	44.91	26.94	0.07	Mg	27.44	14.74	0.04
Total	100.00	100.00		Total	100.00	100.00	
Area 3. Elements	mass%	mol%	sigma	**Area 4. Elements**	mass%	mol%	sigma
B*	61.57	77.02	0.07	B*	63.98	78.20	0.05
O*	5.54	4.68	0.13	O*	7.87	6.50	0.12
Mg	32.89	18.29	0.05	Mg	28.15	15.30	0.05
Total	100.00	100.00		Total	100.00	100.00	
Area 5. Elements	mass%	mol%	sigma				
B*	64.39	79.26	0.07				
O*	4.39	3.65	0.14				
Mg	31.22	17.09	0.05				
Total	100.00	100.00					

Table 5.3.1: EDS data for pure MgB_2 sample sintered at 850°C, Fig.5.3.3 (area 001-005)

5.3.3.3 EDS of pure MgB_2 650°C

Figure 5.3.4 shows of the areas selected for EDS analysis in the SEM image of the pure sample sintered at 650°C, with EDS data in tables (Tables 5.3.2,) for areas 001 to 004, respectively.

Just like the pure sample sintered at 850°C, the mass ratio of magnesium to boron is in the stoichiometric range.

The percentage of oxygen is slightly higher here than for the 850°C sintered sample. Also, areas 650°C sample has more oxygen in smooth dark areas (areas 001 and 004, Tables 5.3.2) and without detectable bright particles, unlike the 850°C sample.

The explanation for this observation can be different occurrence of oxygen in this case, as a thin layer around the MgB_2 grains.

Generally speaking, the observation of more oxygen for the pure samples sintered at 650°C is in contradiction with the expectation that higher sintering temperature favours increasing oxidation. The higher sintering temperature (850°C) probably promoted recrystallization of oxygen from the layers into MgO particle form.

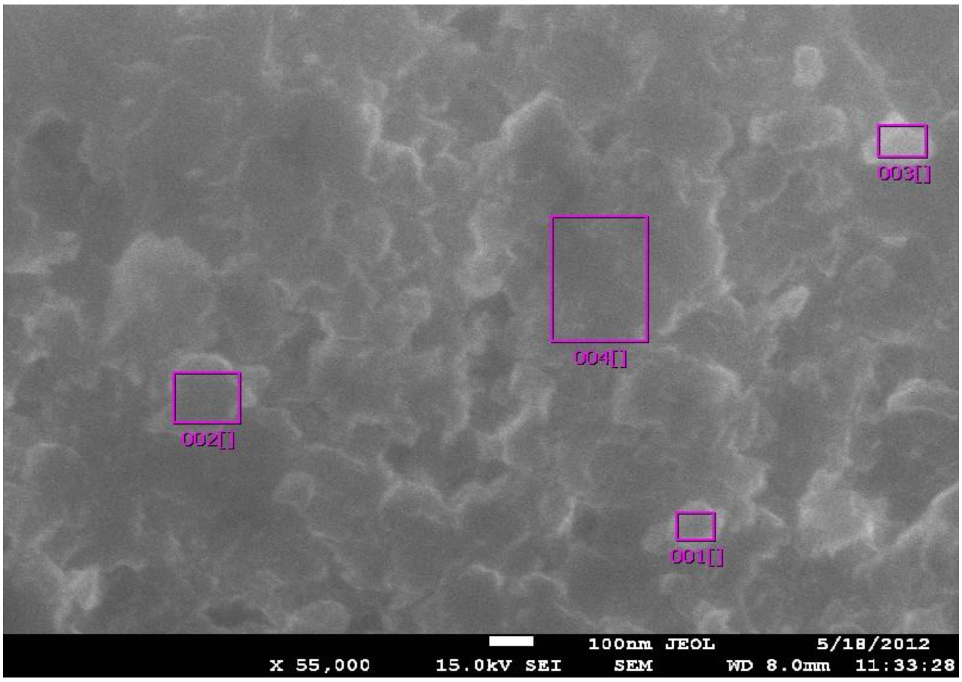

Fig. 5.3.4: SEM image of pure MgB_2 sintered at 650°C with rectangles marking the areas for EDS analysis.

Area 1. Elements	mass%	mol%	sigma	**Area 2. Elements**	mass%	mol%	sigma
B*	53.70	70.41	0.08	B*	61.67	76.79	0.06
O*	8.57	7.59	0.13	O*	6.89	5.80	0.13
Mg	37.73	22.00	0.05	Mg	31.44	17.41	0.05
Total	100.00	100.00		Total	100.00	100.00	
Area 3. Elements	mass%	mol%	sigma	**Area 4. Elements**	mass%	mol%	sigma
B*	62.80	77.59	0.06	B*	58.50	74.37	0.08
O*	6.90	5.76	0.11	O*	7.39	6.35	0.14
Mg	30.30	16.65	0.04	Mg	34.11	19.28	0.06
Total	100.00	100.00		Total	100.00	100.00	

Table 5.3.2: EDS data for pure MgB_2 sample sintered at 650°C, Fig.5.3.4 (area 001-004)

5.3.3.4 SEM images of doped MgB_2 samples with NiCoB 2.5 wt%, sintered at 850°C and 650°C

Figures 5.3.5 and 5.3.6 present SEM images of the doped samples with NiCoB 2.5wt%, sintered at 850 and 650°C, respectively. The doped samples show the presence of small nanoparticles for both sintering temperatures. As well doped samples, these have kept the morphology of the pure samples for both temperatures.

An intriguing difference between the samples are the small particles on the SEM image for 650°C doped sample (Fig. 5.3.6 (a, b)). That observation can be explained by poor incorporation of NiCoB nanoparticles into the MgB_2 matrix and stacking of particles between the grain boundaries, which can affect the weak-links among grains.

The 850°C doped sample shows similar particles but they are in lower concentration and more incorporated into the matrix of MgB_2 (Fig. 5.3.5(a, b)). Also, these particles are not as distinguishable as for the 650°C doped sample.

Nevertheless, the 850°C doped sample shows better connectivity between grains with more structures that are irregular shape, which can indicate more defects and dislocations. From the SEM images, it can be concluded that Mg could form a eutetic phase with Ni and Co, and easily diffuse and react with boron.[19]

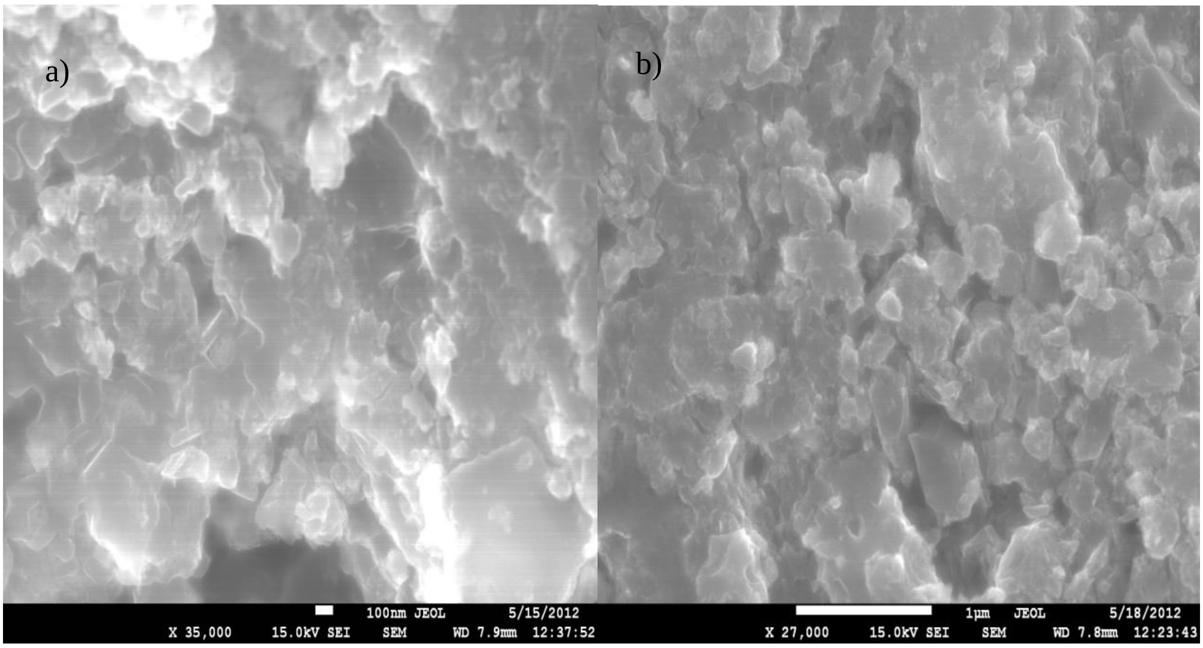

Fig. 5.3.5(a), (b): SEM images of MgB_2 doped with NiCoB 2.5wt%, sintered at 850°C.

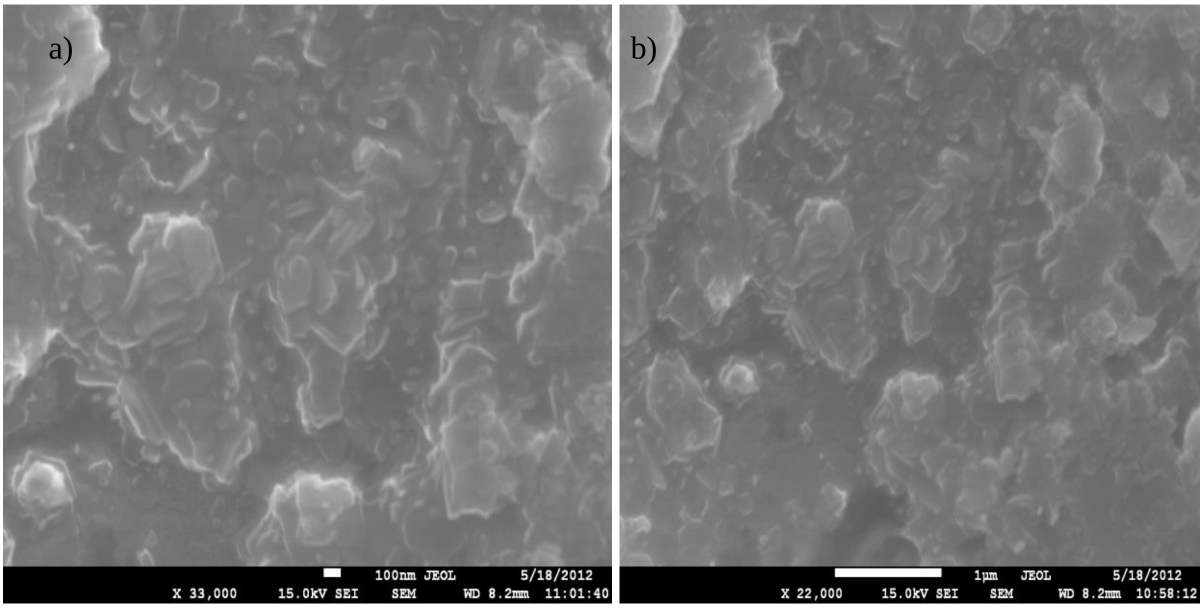

Fig. 5.3.6 (a), (b): SEM images of MgB_2 doped with NiCoB 2.5wt%, sintered at 650°C.

5.3.3.5 EDS analysis of MgB_2 samples doped with NiCoB 2.5wt%, sintered at 850°C

Figure 5.3.7 presents the EDS analysis of the NiCoB 2.5wt% doped sample sintered at 850°C with associated tables, from Table 5.3.10 to Table 5.3.19. The EDS data for the doped sample indicates a more complex system than for pure MgB_2. First of all, the stoichiometric proportions are distorted for both doped samples in comparison with the pure samples.

The doped samples sintered at 850°C have a small excess of magnesium in areas 006, 008, 009, and 010, as can be seen in Tables 5.3.15, 5.3.17, 5.3.18, and 5.3.19, respectively.

Those EDX data are not directly supported by the XRD pattern for the same doped sample, so excess of magnesium can be claimed for the small observation areas only.

With detailed examination of the SEM images and EDS data, a strong correlation can be seen between excess magnesium and the appearance of the dopant elements nickel and cobalt (areas 008, 009, 0010, Tables 5.3.17, 5.3.18, 5.3.19).

This can be clearly seen in Figure 5.3.8, which shows the number of mols of Ni and Co plotted against the excess of Mg: beyond (mol of Mg)/(2*mols of B), for all the examined areas shown in Fig. 5.3.7.

If the excess of Mg factor in a particular area is 1, then the amounts of Mg and B correspond to MgB_2 stoichiometry in that area. If the excess of Mg factor is larger than 1, an excess of Mg is present in that area.

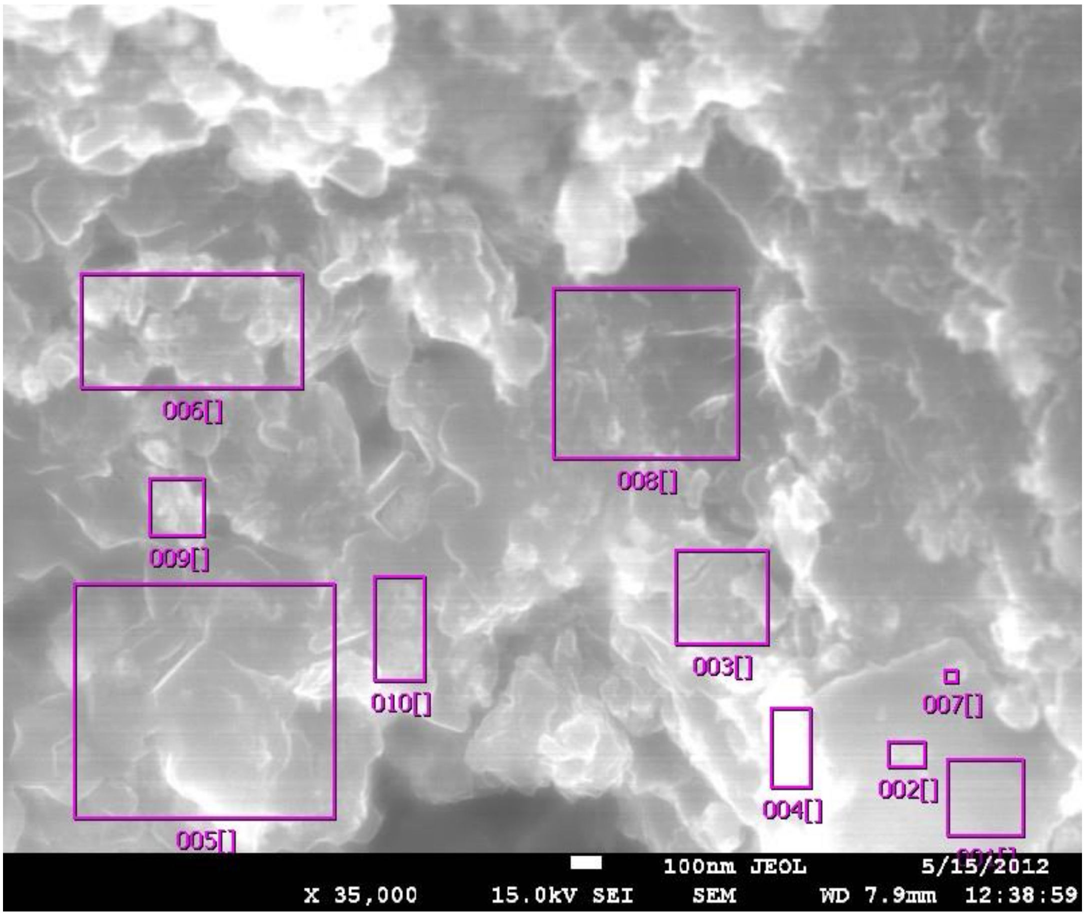

Fig. 5.3.7: EDS analysis of MgB_2 doped with NiCoB 2.5wt%, sintered at 850°C, with the rectangles indicating the areas selected for EDS analysis.

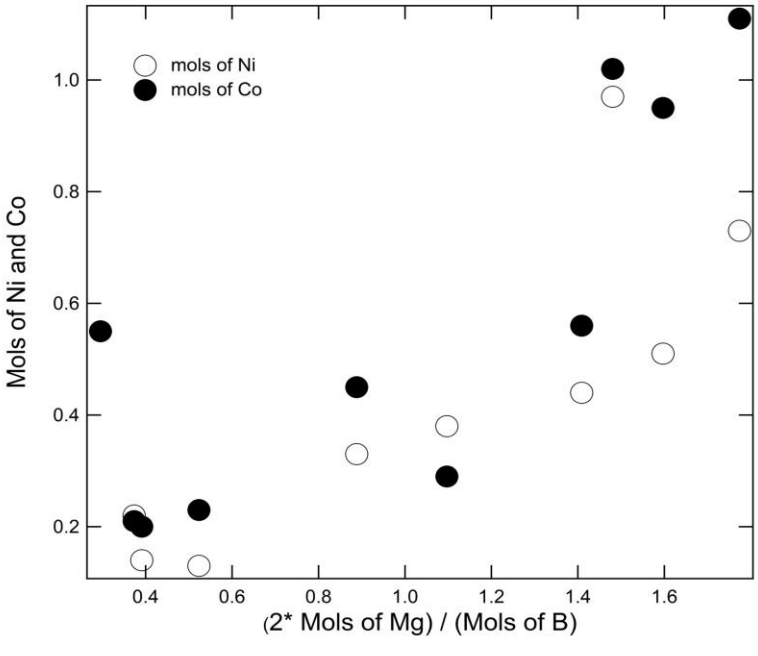

Figure 5.3.8: Correlation between the amount of Ni and Co and excess of Mg in the selected EDS areas (Fig. 5.3.7) for 2.5% NiCoB doped MgB_2 sintered at 850°C, as obtained from the EDS measurements.

The appearance of Mg in selected areas indicates the presencce of a new phase consisting of transition metal and magnesium. This is in agreement with other results on the existence of new phases: Mg_2Ni and Mg_2Co (section 5.4).

Also, it is important to note that despite an increase in the magnesium, the content of oxygen was significantly lower than for pure samples. From this it can be concluded that the doped metals have inhibitory effects on the creation of MgO.

The reason is their competition for Mg in the reaction with magnesium. Prevention of the growth of MgO, especially of thin MgO layers around the MgB_2 grains has a positive impact on the connectivity between grains.

A certain percentage of oxygen has been detected in form of small particles, however, which can have a positive effect on the pinning (areas 002 and 007, Tables 5.3.3 and 5.3.4).[26]

Area 1. Elements	mass(%)	mol(%)	sigma	**Area 2. Elements**	mass(%)	mol(%)	sigma
B*	72.29	85.38	0.03	B*	66.90	81.76	0.05
O*	1.08	1.16	0.08	O*	3.07	2.54	0.10
Mg	25.02	12.62	0.03	Mg	28.11	15.27	0.04
Co*	1.06	0.55	0.21	Co*	0.95	0.21	0.47
Ni*	0.55	0.29	0.28	Ni*	0.96	0.22	0.61
Total	100.00	100.00		Total	100.00	100.00	
Area 3. Elements	mass(%)	mol(%)	sigma	**Area 4. Elements**	mass(%)	mol(%)	sigma
B*	48.82	67.59	0.11	B*	62.08	78.31	0.07
O*	1.71	1.61	0.13	O*	1.63	1.83	0.13
Mg	47.46	30.02	0.05	Mg	34.75	20.50	0.05
Co	1.74	0.45	0.66	Co*	0.99	0.23	0.41
Ni*	1.26	0.33	0.85	Ni*	0.54	0.13	0.49
Total	100.00	100.00		Total	100.00	100.00	
Area 5. Elements	mass(%)	mol(%)	sigma	**Area 6. Elements**	mass(%)	mol(%)	sigma
B*	43.61	63.49	0.18	B*	36.93	57.40	0.23
O*	1.05	1.02	0.19	O*	1.10	1.16	0.20
Mg	52.86	34.82	0.08	Mg	58.45	40.43	0.09
Co*	1.07	0.29	0.73	Co*	1.97	0.56	0.73
Ni*	1.40	0.38	0.82	Ni*	1.55	0.44	0.86
Total	100.00	100.00		Total	100.00	100.00	

Table 5.3.3: EDS data of MgB_2doped with NiCoB 2.5wt.%, sintered at 850°C, Fig.5.3.7 (area 001-006)

Area 7. Elements	mass(%)	mol(%)	sigma	**Area 8. Elements**	mass(%)	mol(%)	Sigma
B*	65.24	80.20	0.05	B*	31.13	51.32	0.17
O*	4.53	3.77	0.11	O*	1.12	1.31	0.14
Mg	28.70	15.69	0.04	Mg	61.71	45.52	0.07
Co*	0.91	0.20	0.54	Co*	3.66	1.11	0.80
Ni*	0.62	0.14	0.69	Ni*	2.38	0.73	1.02
Total	100.00	100.00		Total	100.00	100.00	
Area 9. Elements	mass(%)	mol(%)	sigma	**Area 10. Elements**	mass(%)	mol(%)	sigma
B*	33.46	53.88	0.27	B*	35.00	55.46	0.19
O*	1.51	1.64	0.22	O*	1.37	1.51	0.17
Mg	60.09	43.02	0.10	Mg	58.27	41.05	0.08
Co*	3.21	0.95	0.85	Co*	2.37	1.02	0.95
Ni*	1.73	0.51	0.91	Ni*	2.59	0.97	1.03
Total	100.00	100.00		Total	100.00	100.00	

Table 5.3.4: EDS data of MgB_2 doped with NiCoB 2.5wt.%, sintered at 850°C, Fig.5.3.7 (area 007-010)

5.3.3.6 EDS analysis of MgB_2 samples doped with NiCoB 2.5wt% and sintered at 650°C

Figure 5.3.9 shows the EDS analysis for the NiCoB 2.5wt% doped sample sintered at 650°C with connected Tables 5.3.5. Comparing two doped samples sintered at different temperatures, the amount of oxygen is slightly higher for the 850°C doped sample in correlation with expectation.

On the other hand, the percentage of unreacted Mg is much higher in the 650°C doped sample (Fig. 5.3.9), which is two times or more higher than boron in the same area (areas 1 and 5, Tables 5.3.5). Another significant difference is the inability to detect nickel in the same area for the 650°C doped sample.

NiCoB nanoparticles are very small and of amorphous morphology, so detection of them is very difficult, especially for a very small percentage of dopant. From the SEM image and EDS data, it can be concluded that NiCoB nanoparticles were not activated at this temperature or incorporated into the MgB_2 matrix.

At 650°C, Mg starts to melt, and the NiCoB nanoparticles probably did not react completely at this temperature. Also, at higher temperature, Mg_2Ni and Mg_2Co/Co_2Mg can recrystallise into a new phases and be incorporated into the MgB_2 matrix.

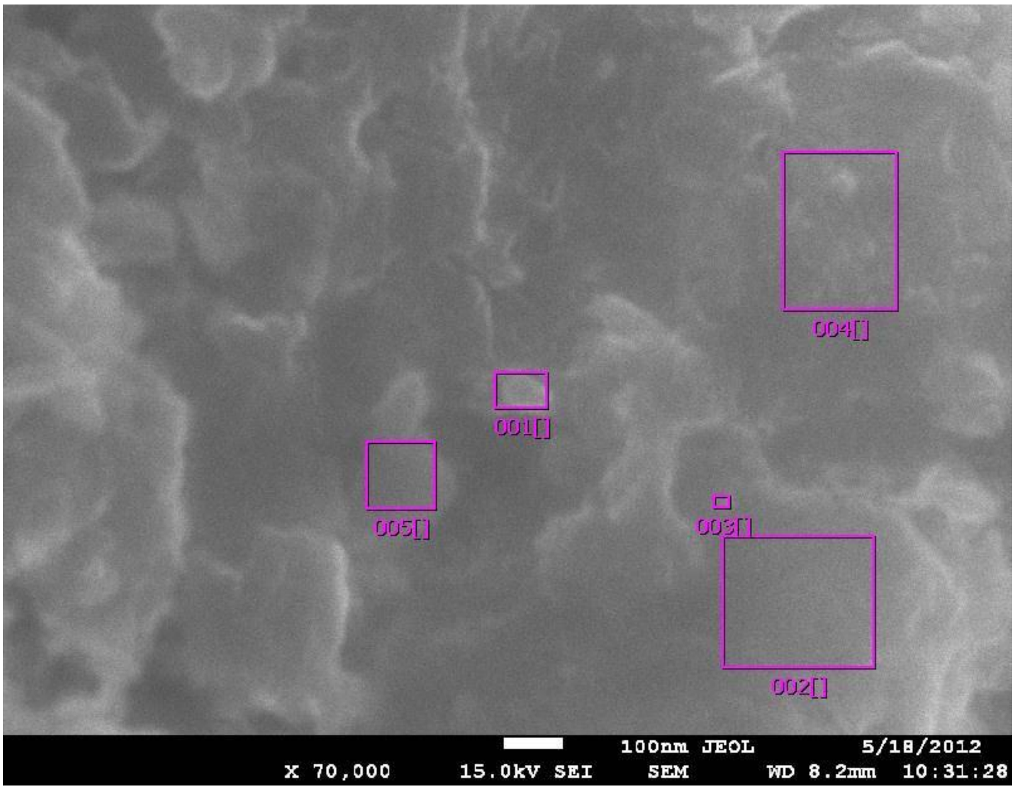

Fig. 5.3.9: SEM image of MgB_2 doped with NiCoB 2.5wt% and sintered at 650°C. The rectangles mark the areas selected for EDS analysis.

Area 1. Elements	mass(%)	mol(%)	sigma	**Area 2. Elements**	mass(%)	mol(%)	sigma
B*	19.05	34.62	1.14	B*	53.68	71.22	0.26
O*	1.86	2.28	0.65	O*	1.14	1.46	0.38
Mg*	77.31	62.50	0.32	Mg	42.59	26.18	0.16
Co*	1.78	0.59	0.67	Co*	1.59	0.64	0.98
Ni	nd	nd		Ni	1.00	0.5	0.8
Total	100.00	100.00		Total	100.00	100.00	
Area 3. Elements	mass(%)	mol(%)	sigma	**Area 4. Elements**	mass(%)	mol(%)	sigma
B*	35.33	55.05	0.54	B*	40.17	60.33	0.53
O*	3.87	4.08	0.47	O*	1.63	1.66	0.51
Mg	57.70	39.98	0.22	Mg	55.64	37.16	0.22
Co*	2.17	0.62	0.69	Co*	1.32	0.36	0.79
Ni*	0.93	0.27	0.87	Ni*	1.24	0.49	0.90
Total	100.00	100.00		Total	100.00	100.00	
Area 5. Elements	mass(%)	mol(%)	sigma				
B*	25.19	42.98	0.97				
O*	0.95	1.24	0.63				
Mg	71.71	54.41	0.29				
Co*	1.94	1.29	0.85				
Ni*	0.22	0.07	0.95				
Total	100.00	100.00					

Table 5.3.5: EDS data of MgB_2 doped with NiCoB 2.5wt.%, sintered at 650°C, Fig.5.3.9 (area 001-005)

5.3.3.7 XRD results

Figure 5.3.10 presents the XRD patterns of pure and doped samples sintered at 850°C. More explanation is in the previous chapter, section 5.1.3.5. On the MgB_2 doped XRD pattern, it is very difficult to detect any other phase except MgB_2 and MgO. The doped amount of nanoparticles is very small, and on the other hand, the nanoparticles are amorphous, which makes detection even more difficult.

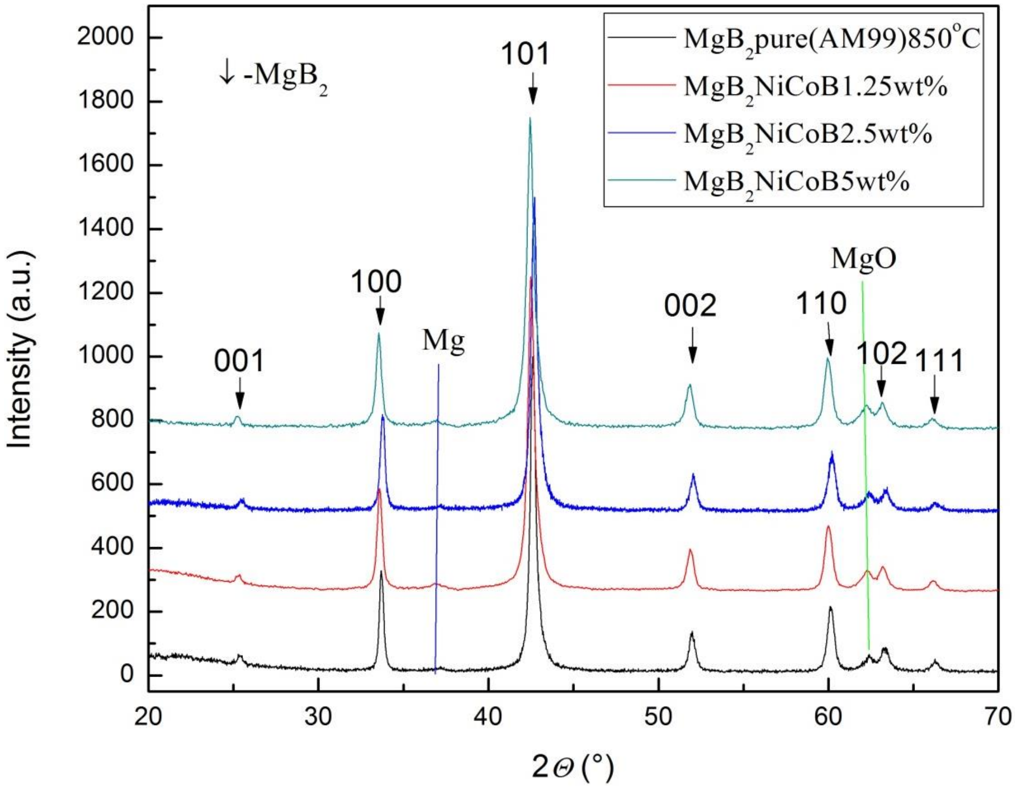

Fig.5.3.10: XRD patterns of pure MgB_2 and NiCoB doped samples (1.25wt%, 2.5wt% and 5wt%) sintered at 850°C.

Calculations of the full width at half maximum (FWHM) of selected peaks for the pure and doped samples sintered at 850°C are presented in Figure 5.3.25. The obtained results show an increasing trend of FWHM values with doping, which indicates that grains become smaller with doping.

The pure MgB_2 sample (AM99) has a grain size considerable larger than those of the doped samples, with average size 264 nm (100) and 192 nm (002). Also, the grain size slowly decreases with doping, as can be seen in Table 5.3.25. Smaller grain size is associated with more grain boundaries and defects. This result can be explained by the formation of a eutectic system between the nanoparticles and the Mg, and by local diffusion of melted Mg so as to form small grains of MgB_2

Table 5.3.26 presents the calculated relative amounts of MgO and MgB_2 from the intensity ratio of the MgO peak (220) to the MgB_2 peak (120).

Ratio of the relative intensities of MgO (220) and MgB_2 (102) shows a slight decrease in MgO with doping, especially for the MgB_2 sintered at 770°C. These results are related to the EDS data, which show a strong inverse correlation between the appearance of MgO and NiCoB doping (Table 5.3.26).

Plane	(100)		(110)		(002)	
Samples	FWHM (°)	D_p (nm)	FWHM (°)	D_p (nm)	FWHM (°)	D_p (nm)
MgB_2(AM99) 850°C	0.315	264	0.464	199	0.458	192
MgB_2(AM99) 1.25 wt%	0.464	179	0.650	141	0.587	150
MgB_2(AM99) 2.5 wt%	0.467	178	0.656	140	0.605	146
MgB_2(AM99) 5 wt%	0.466	178.5	0.764	120	0.701	126

Table 5.3.6: Calculations of FWHM for pure and doped samples sintered at 850°C.

	650°C			**770°C**			**850°C**		
	pure	2.5w%	5wt%	pure	2.5w %	5wt%	pure	2.5wt%	5wt%
$I(MgO)_{220}/I(MgB_2)_{102}$	0.80	0.75	0.77	1.07	0.89	0.90	0.82	0.79	0.88

Table 5.3.7: Relative intensity of MgO (62.5°) and MgB_2 (63.5°) peaks.

5.3.3.8 Critical current density of pure and doped MgB_2 samples sintered at 850°C

Figure 5.3.11 shows J_c field dependence for pure and NiCoB doped MgB_2 samples sintered at 850°C, more explanation is presented in chapter 5.1.3.2. From the $J_c(H)$ curve, it is clear that the best result of critical current is for sintering at 850°C. All the samples were sintered at 850°C. There is a noticeable trend towards increasing critical currents with increasing doping level, with best measured samples doped with 2.5 wt%.

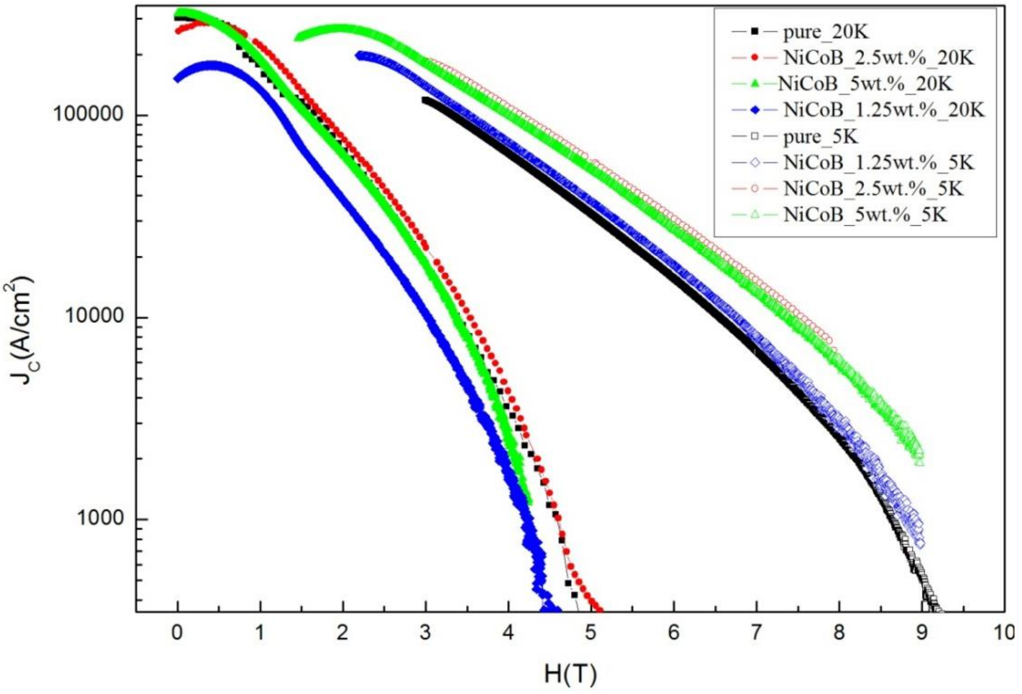

Fig. 5.3.11: Field dependence of critical current density for pure MgB_2 and nano-NiCoB doped MgB_2, sintered at 850°C for 30 minutes.

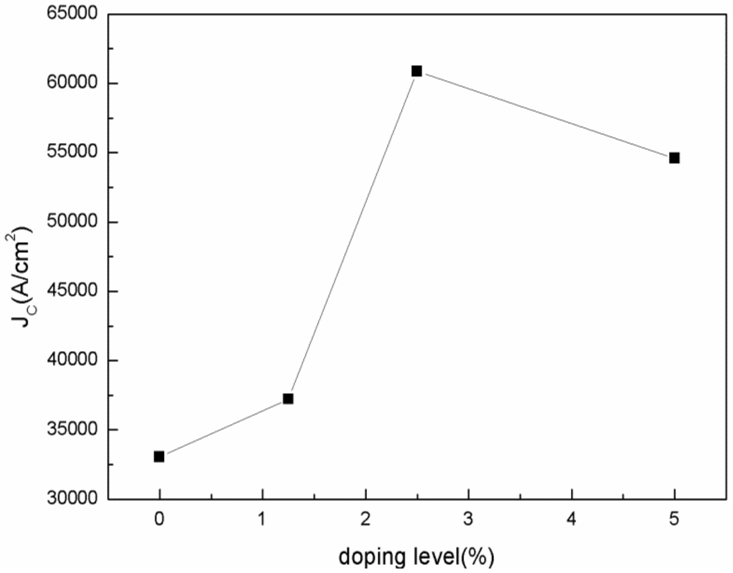

Fig.5.3.12: Dependence of critical current density at field of 5 T and temperature of 5 K on the level of nano-NiCoB doping.

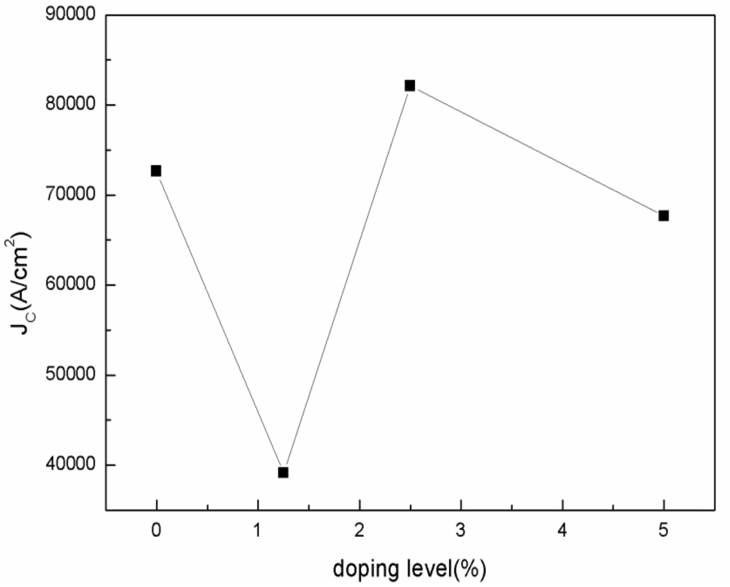

Fig.5.3.13: Dependence of critical current density at field of 2 T and temperature of 20 K on the level of NiCoB doping.

The theoretical explanation for enhancement of J_c only for the 5 K measurement temperature could be based on the nature of the two superconductive gaps. MgB_2 has two superconducting energy gaps: the σ gap (which corresponds to the p_x and p_y orbitals), with superconductive energy gap, $\Delta(0) \approx 5.9$ meV, and the π gap (which corresponds to p_z-

orbitals), with $\Delta(0)$ = 2 meV. According to the Bardeen Cooper Schrieffer) (BCS theory, the energy gap, E_g, in the superconductor is expressed as: $E_g = 2*\Delta(0) = 2* 1.76\ k_BT_c$.

Here, T_c is the critical temperature. High energy optical phonons (about 570 meV) are E_{2g} labelled and connected to the motion of B atoms in the *ab*-plane. Large coupling of the E_{2g} phonon mode is connected with σ bonds. On the other hand the π plane has a lower energy gap, and the pinning is only effective for the π –gap.

At higher measurement temperatures more super-electrons are affected by thermal excitation and absorb energy enough to cross the energy gap and transfer from the superconductive state into the normal state. Interactions between electrons increase the energy dissipation, and more electrons make the transition from the superconductive to the normal state. Therefore, the high-energy optical phonons are responsible for the thermoelectric power behaviour at high temperatures.[20, 21,]

Figures 5.3.13, 5.3.14, and 5.3.15 present plotted graphs of $d(lnJ_c)/dH$ against H. Assuming that J_c decreases with field as:

$$J_c = J_{c0} e^{-\frac{H}{H_0}}, \tag{5.3.1}$$

the derivative gives us the inverse of H_0, the characteristic field, which is associated with vortex pinning. Experiment shows that the field dependence of J_c for MgB_2 can be well approximated by this equation.[22]

Therefore, a larger value of $-d(lnJ_c)/dH$ means that the sample has weaker pinning and shows a stronger decrease of J_c with H.

The present figures show a slower decrease of J_c with field for the 2.5 wt%) doped sample sintered at 850°C and 950°C, while the trend is the reverse for the samples sintered at 650°C. Differences in the rate of decline of critical current with magnetic field can be associated with increased pinning in the doped samples. New phases are formed above 770°C (Mg_2Ni and Mg_2Co/Co_2Mg) that can make good pinning centres in the MgB_2 matrix.

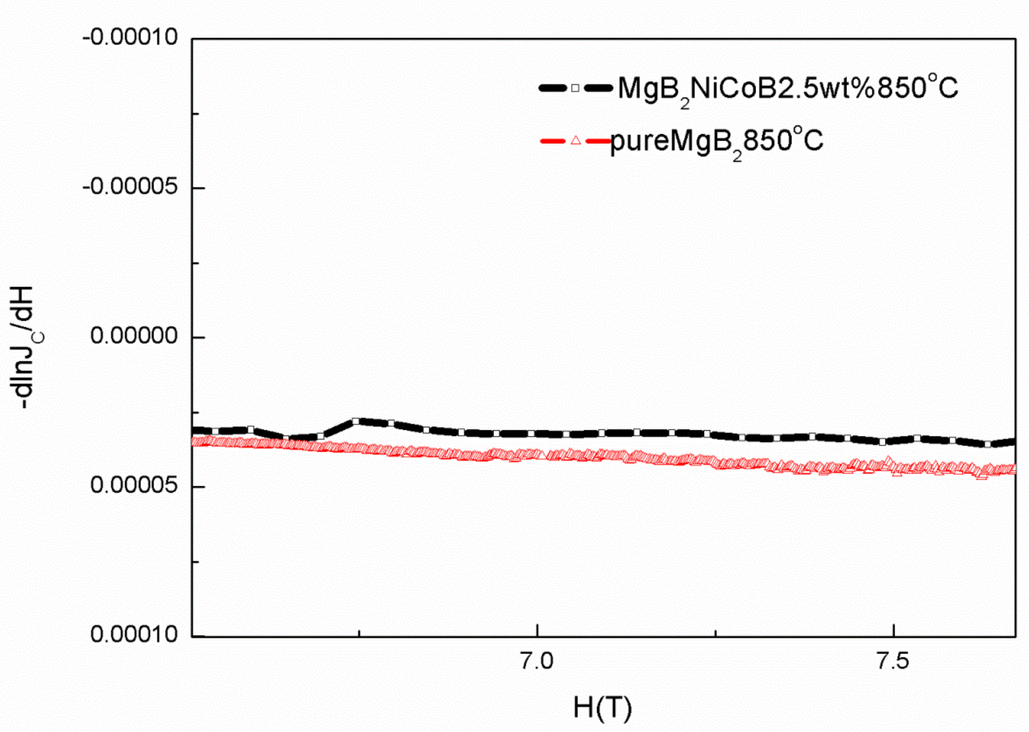

Fig.5.3.14: Derivative of J_c as a function of field for doped and pure samples that were sintered at 850°C.

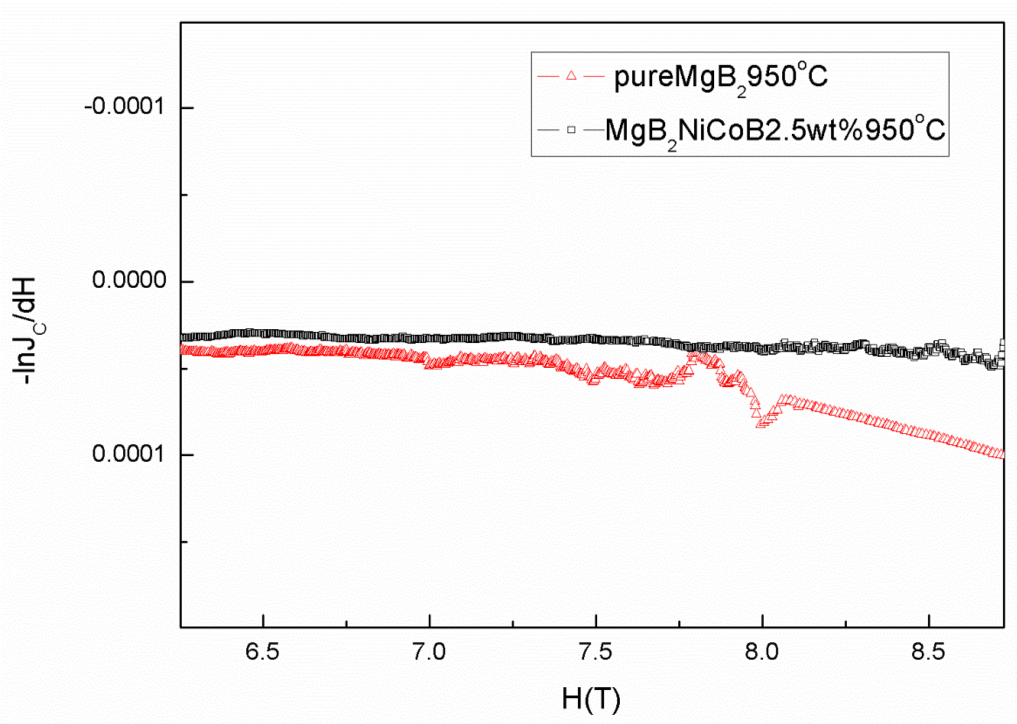

Fig.5.3.15: Derivative of J_c as a function of field for doped and pure samples sintered at 950°C.

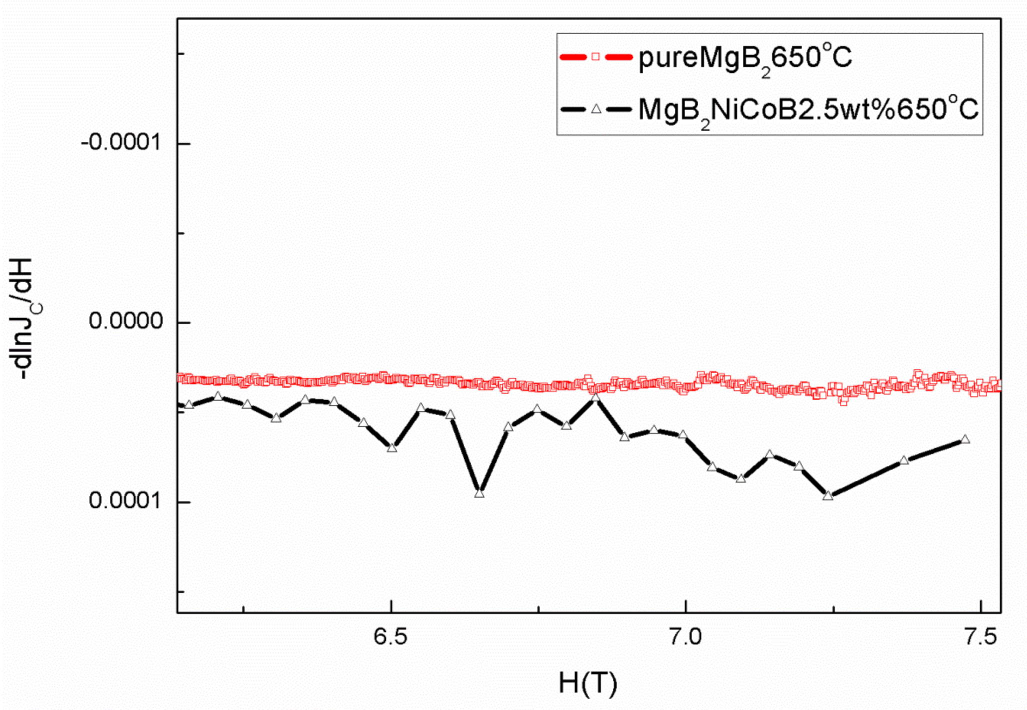

Fig.5.3.16: Derivative of J_c as a function of field for doped and pure samples sintered at 650°C.

5.3.3.9 Resistivity results

The temperature dependence of the resistivity was studied for pure MgB_2 and for the combination of NiCoB doping level and sintering temperature that was shown in section 5.2 to provide the best values of J_c: the 2.5wt% NiCoB doped sample with sintering at 850°C.

According to connectivity analysis[23], the active cross-sectional area fraction (A_F) represents the connectivity, which is estimated by comparing the measured values of resistivity at 300 and 40 K for a bulk porous sample with that of a single crystal:

$$A_F = \Delta\rho /(\rho_{300\ K} - \rho_{40\ K}) \qquad (5.3.2)$$

where is $\Delta\rho$ = 7.3 μΩcm, ideal resistivity for single crystal, and ρ_{300}, ρ_{40} are resistivity at 300K and 40K, respectively.

The values of A_F obtained in this way increase from 0.22 for the pure to 0.32 for doped samples, directly indicating the increase in connectivity.

The residual resistance ratio (RRR) is defined as the ratio of the resistance measured at 300 K to that 40 K. RRR gives information on the contribution of the crystal defects to the resistance of the sample, and the effective cross-sectional area of the sample is cancelled out. Therefore, a large RRR value indicates that the phonon mediated resistance dominates the defect mediated resistance, and pinning in such a sample is expected to be weaker than for a sample with small RRR.

The values of RRR for the pure and the 2.5wt% doped MgB_2 are 2.5 and 1.67, respectively, as can be seen from Table 5.3.27. The increased value of ρ_{40K} observed for the doped sample, resulting in a decrease in RRR, is due to increased impurity scattering in the lattice for several different reasons, such as doping, ball milling, sintering at different temperature, etc. Microscopically, there is an increase in the lattice strain, dislocations, and other defects in the MgB_2 matrix. With increased NiCoB nanoparticle doping, the effect is to introduce an even larger number of defects and dislocations into the MgB_2 crystal lattice. In our case, the formation of new phases causes more disorder in the crystal lattice.

Precipitates in MgB_2 matrix shrink the mean free path of superconductive electrons, l.

According to the Pippard relation, the coherence length decreases as: $1/\xi = 1/\xi_0+1/l$, where ξ_0 is the intrinsic coherence length. Decreasing coherence length will directly increase H_{c2} and H_{irr}.

This result shows that the vortex pinning in the doped sample is likely to be increased with doping, because of increased defect density due to the pinning. Not all defects will be effective pinning centres, however, and therefore this result does not necessarily prove by itself that the vortex pinning was improved by the doping.

That is why we also performed other types of measurements to test if the pinning indeed was improved. In addition to the field dependence of resistivity presented above, magnetic relaxation is a good method to compare vortex pinning in the two samples because it directly probes the vortex dynamics.

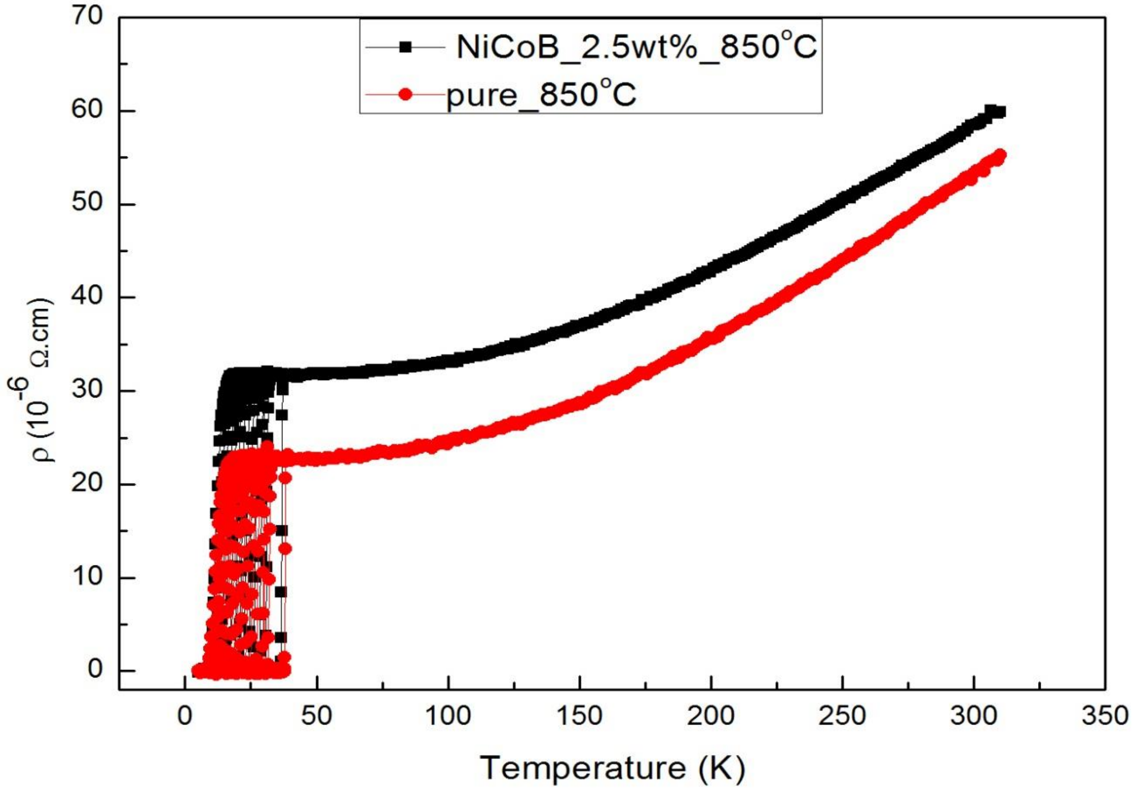

Fig.5.3.17: Temperature dependence of resistivity for pure MgB_2 and MgB_2 doped with NiCoB 2.5wt% (AM99 boron), sintering temperature 850°C.

Sample	ρ_{40K} (μΩ·cm)	ρ_{300K} (μΩ·cm)	(ρ_{300K}-ρ_{40K}) (μΩ·cm)	RRR	A_F	T_c
pure	22	55	33	2.5	0.22	37.9
NiCoB 2.5wt%	34	57	23	1.67	0.32	36.6

Table 5.3.8: The measured resistivity values, residual resistivity ratios (RRR), and active cross-sectional area fraction (A_F) for pure and NiCoB 2.5wt% doped.

Resistivity (ρ) versus temperature (T) data are plotted for pure sample and the one doped with 2.5 wt% NiCoB nanoparticles. It is shown that all the samples present metallic resistivity down to the transition temperature of about 40 K, where samples make a transition to the superconducting state with $\rho = 0$.

The normal state resistivity increases with increasing amounts of NiCoB in the samples, indicating increased disorder in the crystal structure of MgB_2. The decrease in T_c in NiCoB-doped samples can be due to several reasons, such as the presence of secondary phases such as Mg_2Ni and Mg_2Co/Co_2Mg, and the temperature dependence.

The value of resistivity near the critical temperature is affected by the vortex dynamics. The thermal energy at these temperatures is comparable to the pinning energy, and vortices can be unpinned from pinning sites, resulting in vortex creep and the development of electrical resistance. The temperature dependence of resistance for very small values of resistance near the superconducting transition can be described by the Arrhenius relation:

$$R = R_0 \exp(-\frac{U}{k_B T}) \qquad (5.3.3)$$

where R_0 is the temperature independent part of the resistance, and U is the pinning potential, which is assumed to be temperature independent at all measured temperatures. U can be obtained from linear plots of lnR vs. 1/T. Thus obtained values of the pinning potential are shown in Fig. 5.3.18 for pure and 2.5% NiCoB doped MgB_2.

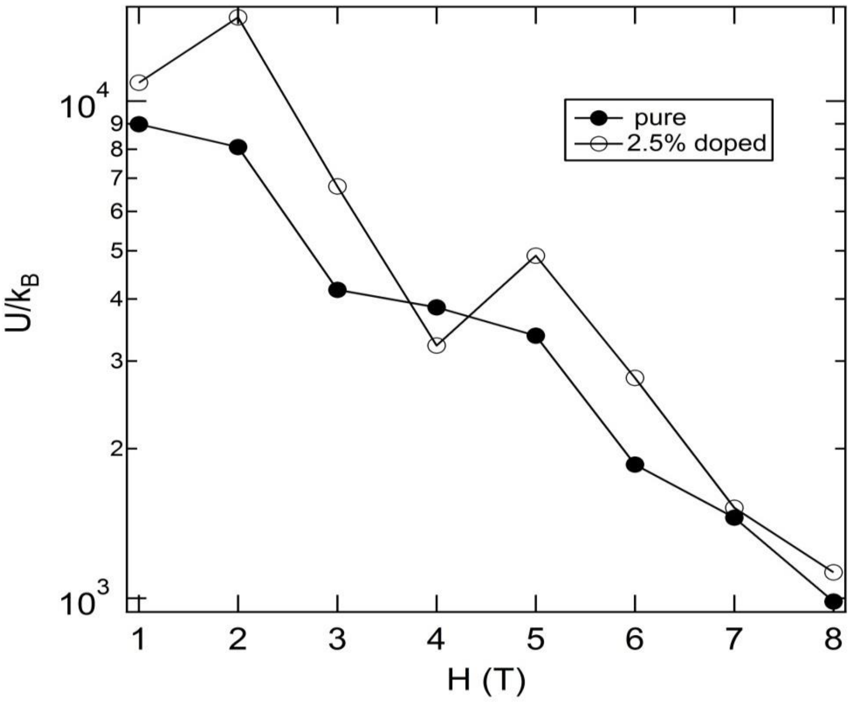

Fig.5.3.18: Pinning potential energy of 2.5wt% NiCoB doped and pure MgB_2 sintered at 850°C.

The values of pinning potential calculated from resistivity measurements (Fig. 5.3.18) are higher for doped samples at almost all fields.

5.3.3.10 Magnetic relaxation results and discussion

Figure 5.3.19 shows decay of magnetization as a function of time for pure MgB_2 and 2.5 wt% NiCoB doped MgB_2 at 5 K and 4 T. Both samples were sintered at 850 °C. The magnetization for the doped sample decayed more slowly with time than the pure sample. This result indicates stronger pinning for the doped sample.

Figure 5.3.20 presents the decay of magnetization with time at 20 K and 2 T. The magnetization decays at 20 K and 2 T at the same rate for pure and doped MgB_2. This indicates that the vortex pinning did not improve with doping at 20 K, which is consistent with the transport measurements.

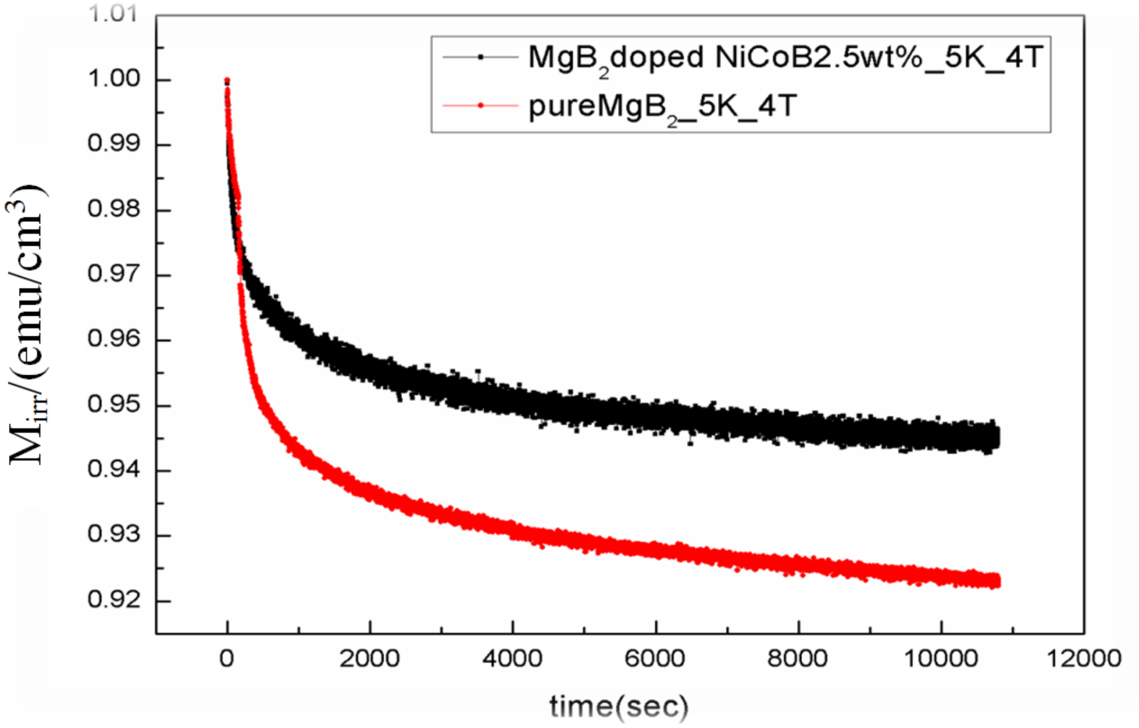

Fig.5.3.19: Decay of the normalized magnetization as a function of time: magnetic relaxation of pure and doped samples (NiCoB 2.5wt%) at 5 K, 4 T applied field.

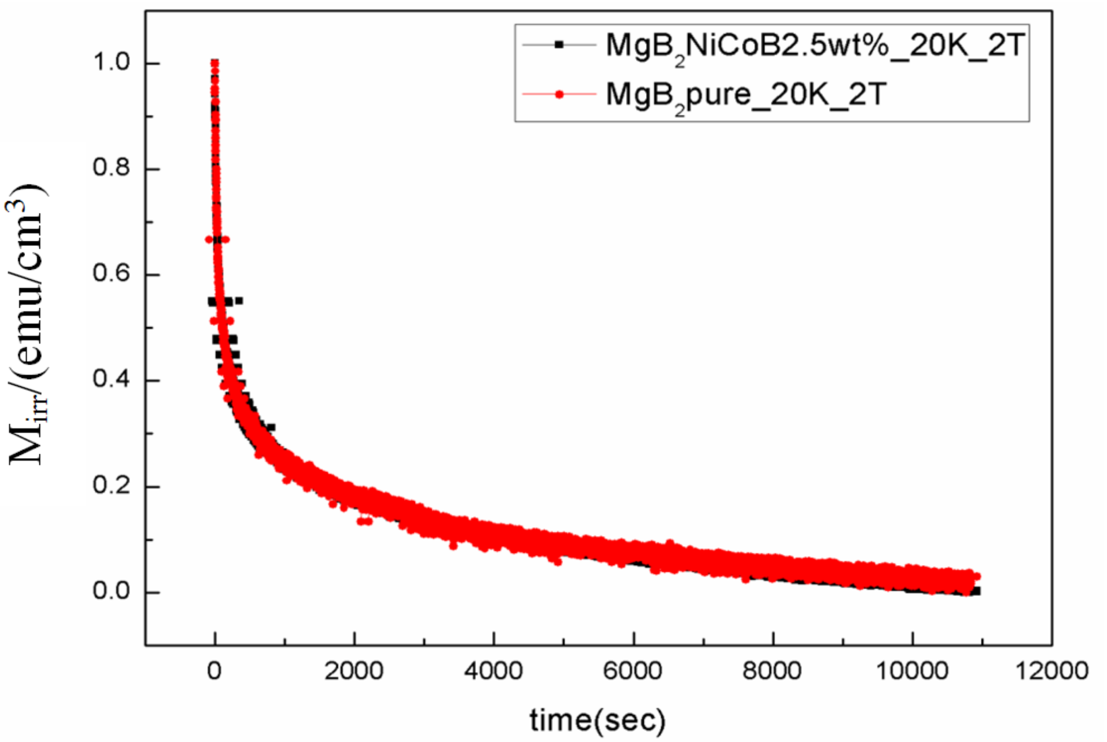

Fig.5.3.20: Magnetic relaxation of pure and doped samples (NiCoB 2.5wt%) at 20 K, 2 T applied field.

At any temperature above 0 K, thermal activation cause hopping of magnetic vortices or vortex bundles out of their pinning potential wells. The magnetic vortices and bundles overcome the pinning barrier and start moving, which is commonly named flux creep. Therefore, at non-zero temperatures, flux motion is possible due to thermal activation or thermal assistance of flux motion.

This flux motion leads to dissipation, which manifests itself in form of a decay of superconducting currents with time or flow resistance if an electric current is passed through a superconductor in a magnetic field.

The pinning potential is characterized by the well depth U. The pinning potential depends on the thermodynamic temperature and magnetic field because it originates from the difference in free energy inside the well and in the neighbourhood of the pinning centre.[18]

Flux creep by thermal excitation was first described by Anderson and Kim (1962, 1964) using the simple Arrhenius relation. The hopping time t is given in terms of the potential-energy barrier height U, the Boltzmann constant k_B, and the temperature T:

$$t = t_0 \exp (U/k_BT). \tag{5.3.4}$$

Anderson and Kim introduced the basic concept of thermal activation of magnetic flux lines out of pinning sites, which proceeds at a rate proportional to $\exp(-U/k_Bt)$. U should be a decreasing function of J. To connect these two values, the dependence of U on J_c can be written as a,

$$U=U_0\,[1-J/Jc_0]. \tag{5.3.5}$$

Thermal activation of pinned vortices or bundles of vortices contributes to the dissipation. For this pin-breaking mechanism, standard expressions for the activation energy of flux jumps could be used, e.g., $U(B,T) = U_0(1-t)^{3/2}B^{-1}$, where U_0 is the field and temperature independent part of the pinning barrier.

Combining Eqs. (5.3.4) and (5.3.5), and solving for J, we obtain the classic equation of flux creep:

$$J = J_{c0}\,[1 - \frac{k_BT}{Uo}\ln\left(\frac{t}{to}\right)] \tag{5.3.6}$$

The normalized relaxation rate can be derived directly from Eq. (5.3.6.):

$$S = \frac{d\mathrm{lnMirr}}{d\mathrm{lnt}} = \frac{-k_BT}{Uo} \tag{5.3.7}$$

where the irreversible magnetization M_{irr} is proportional to J, according to the critical state model[15]. Thus, in the Anderson-Kim theory[24,25], measurement of the normalized relaxation rate determines the pinning barrier U_0.

In experiment, I measured the decay of magnetization with time at constant temperature of 5 and 20 K, and applied field of 4 and 2 T, respectively. It can be clearly seen that magnetization for the doped sample at 4 T decays more slowly than for the pure MgB_2, which indicates that higher thermal energy is needed to depin vortices from the potential well for the doped sample. The pinning potential calculated for our samples by Equation (5.3.3) is shown in Figs. 5.3.21 and 5.3.22.

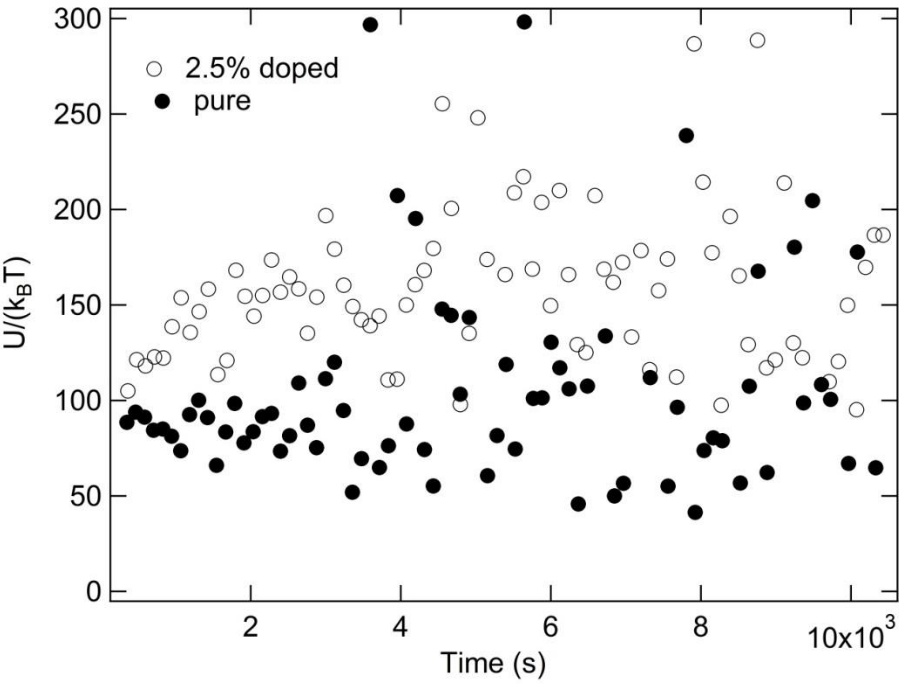

Figure 5.3.21: Pinning potential obtained for pure and 2.5% NiCoB doped MgB_2, obtained from magnetic relaxation measurements (Fig. 5.3.17) using Eq. (5.3.2). The measurements were performed at 5 K and 4 T.

Despite the substantial noise in the data, due mainly to the differentiation of the measured points (Eq. 5.3.3), it can be seen that the pinning energy for the doped sample is higher than for the pure sample at 5 K.

The pinning energy for the 2.5wt% NiCoB doped MgB_2 sample, measured at 5 K and 4 T can be roughly estimated as (150 +/-50) k_BT. On the other hand, pure sample measured in same conditions, has shown pinning energy of around (80 +/-40) k_BT. From these results can be observed significant difference in pinning energy between doped and pure samples.

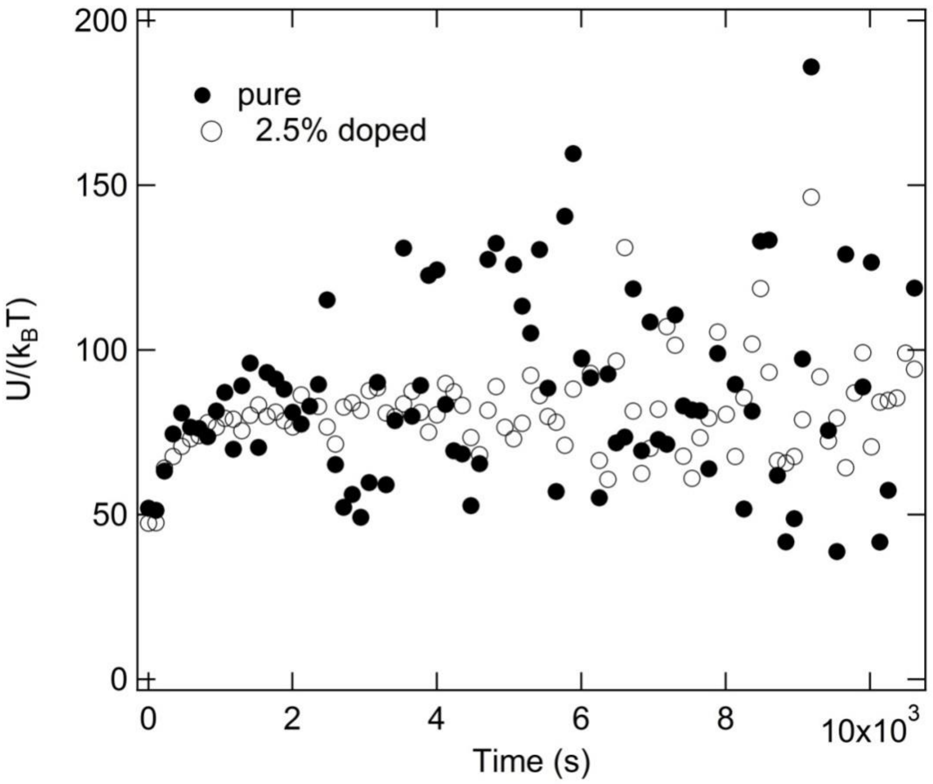

Figure 5.3.22: Pinning potential for pure and 2.5% NiCoB doped MgB_2, obtained from magnetic relaxation measurements (Fig. 5.3.18) using Eq (.5.3.2). The measurements were performed at 20 K and 2 T.

Figure 5.3.22 does not show any detectable difference in pinning energy between the pure and doped MgB_2 at 20 K and 2 T. For both samples, the pinning energy can be estimated as (75 +/-40) k_BT.

Therefore, our measurements of magnetic relaxation confirm that the vortex pinning at 5 K did increase with the NiCoB doping, whereas pinning at 20 K did not improve. These findings are in agreement with the measurements of $J_c(H)$. The average values of pinning potential measured at 20 K for both samples is around (75 +/-30) k_BT.

5.3.4 Conclusion

This chapter presents the best achieved J_c(H) in MgB_2 samples with optimized temperatures of sintering, optimized starting precursors, and optimal NiCoB doping level. To achieve a high critical current in magnetic fields, the doping level of 2.5wt% NiCoB and sintering temperature of 850°C give the best results.

The increase of J_c with NiCoB doping is associated with improvements of both grain connectivity and of vortex pinning. Improvement of grain connectivity seems to be the dominant factor in improving J_c[26]. The effective cross sectional area obtained by Rowel's method increased from 0.22 to 0.32 with the doping. This is associated with observed decrease of oxygen content in the sample after NiCoB doping and high temperature sintering. NiCoB most likely competes for Mg with MgO to create Mg_2Ni and Mg_2Co/Co_2Mg, preventing creation of MgO in large amount. This results in substantially improved grain connectivity, since MgO tends to coat superconducting crystals with insulating layer[26]. The remaining MgO is in the form of small particles that may contribute to vortex pinning. Apparent refinement of MgB_2 grain by NiCoB doping at high sintering temperatures may also play a role in grain connectivity, since clean crystal surfaces will have larger connecting area.

The analysis of the field dependence of J_c, resistive transition and magnetization decay all show that vortex pinning at 5 K is improved with NiCoB doping and high sintering temperature. Pinning at 20 K, however, is not improved with the doping. This can be explained by assuming that the doping increases vortex pinning only in π-band, which is closed at temperatures above about 16 K. The pinning seems to be associated with the presence of Mg_2Ni and Mg_2Co/Co_2Mg phases and increased surface area of MgB_2 crystals due to refinement of the grains with doping. Small MgO crystals may also play a role.

5.3.5 REFERENCES

1 S. X. Dou, S. Soltanian, J. Horvat, X. L. Wang, S. H. Zhou, M. Ionescu, H. K. Liu, P. Munroe, and M. Tomsic, Appl. Phys. Lett. 81, 3419, 2002.

2 S. X. Dou, W. K. Yeoh, J. Horvat, and M. Ionescu, Appl. Phys. Lett. 83, 4996, 2003.

3 Y. W. Ma, X. P. Zhang, G. Nishijima, K. Watanabe, S. Awaji, and X. D. Bai, Appl. Phys. Lett. 88, 072502, 2006.

4 H. Yamada, M. Hirakawa, H. Kumakura, and H. Kitaguchi, Supercond. Sci. Technol. 19, 175, 2006.

5 A. V. Pogrebnyakov, J. M. Redwing, J. E. Jones, X. X. Xi, S. Y. Xu, Q. Li, V. Vaithyanathan, and D. G. Schlom, Appl. Phys. Lett. 82 4319-4321, 2003.

6 J. H. Kim, S. X. Dou, J. L. Wang, D. Shi, X. Xu, M. S. A. Hossain, W. K. Yeoh, S. Choi, and T. Kiyoshi, Supercond. Sci. Tech. 20 448-451, 2007.

7 P. Kováč, I. Husek, T. Melisek, C. R. M. Grovenor, S. Haigh, and H. Jones, Supercond. Sci. Technol. 17 1225, 2004.

8 J. Y. Xiang, D. N. Zheng , J.Q. Li, S. L. Li, H. H. Wen, and Z. X. Zhao, Physica C, 386, 611, 2003.

9 X. L. Wang, S. H. Zhou, M. J. Qin, P. R. Munroe, S. Soltanian, H. K. Liu, and S. X. Dou, Physica C 385 461-465, 2003.

10 M. Kühberger, G. Gritzner, Effects of Sn, Co and Fe on MgB_2, Physica C 370, 39–43, 2002.

11 S. X. Dou, O. Shcherbakova, W.K. Yeoh, J.H. Kim, S.Soltanian, X.L. Wang, C. Senatore, R. Flukiger, M. Dhalle, O. Husnjak, and E. Babic, 2007 *cond-mat*/0701391

12 Y. Ma, H. Kumakura, A. Matsumoto and K. Togano, Appl. Phys. Lett. 83 1181, 2003.

13 V. P. S. Awana, M. Isobe, K. P. Singh, E. Takayama-Muromachi and H. Kishan, Supercond.Sci. Technol. 19, 551, 2006.

14 A. Snezhko, T. Prozorov and R. Prozorov, Phys. Rev. 71, 024527, 2005.

15 C. P. Bean, Rev. Mod, Phys., 36, 31-36, 1964.

16 M. Avdeev, J. D. Jorgensen, R. A. Ribeiro, S. L. Bud’ko and P. C. Canfield Physica C 387 301–6, 2003.

17 J. Horvat, S. Soltanian, X.L. Wang, and S.X. Dou, Effect of sample size on magnetic J_c for MgB_2 superconductor, Applied Physics Letters, 84, 3109, 2004.

18 Y. Yeshurun, A. P. Malozemoff, A. Shaulov, Magnetic relaxation in high-temperature superconductors, Reviews of Modern Physics, Vol. 68, No. 3, 1996.

19 Z. Ma and Y. Liu, Sintering Process and Its Mechanism of MgB_2 Superconductors, Sintering of Ceramics - New Emerging Techniques, 2012.

20 Y. Kong, O.V. Dolgov, O. Jepsen, and O.K. Andersen, Phys. Rev. B64, 020501(R), 2001.

21 K.-P. Bohnen, R. Heid, and B. Renker, Phys. Rev. Lett., 86, 25, 2001.

22 Y.B. Kim, C.F. Hempstead, A.R. Strand, *Phys. Rev. Lett.* 9, 306, 1962.

23 J. M. Rowell, Supercond. Sci.Technol. 16 R17, 2003.

24 P. W. Anderson, ‘‘Theory of flux creep in hard superconductors,’’Phys. Rev. Lett. 9, 309. 1962.

25 P. W. Anderson, and Y. B. Kim, ‘‘Hard Superconductivity: Theory of the motion of Abrikosov flux lines,’’ Rev. Mod. Phys. **36**, 39. 1964.

26 M. Egilmez, L. Ozyuzer, M. Tanoglu, S. Okur, O. Kamer and Y. Oner, Supercond. Sci. Technol. 19 359–364, 2006.

Chapter 5.4: Reaction of NiCoB Nanopowders with MgB_2 Precursors

5.4.1 Introduction

The emphasis of this thesis project is on the materials preparation and chemistry of magnetic nanoparticles, and their incorporation into MgB_2, starting from the chemical synthesis of various nanoparticles, solving problems of reaction and formation between precursors and nanoparticles, and finally measuring the change in properties due to those reactions.

5.4.2 Experimental procedures

To study the reaction of NiCoB nanopowder with the precursor powders for MgB_2, NiCoB nanoparticles were mixed with: boron only, magnesium only, and magnesium and boron.

The powders were mixed in small quantities (200 mg) and measured by differential thermal analysis/thermogravimetric analysis (DTA/TGA) up to 1100°C. X-ray diffraction (XRD) patterns for all samples were measured for different stages of DTA/TGA analysis.

To test if magnetic NiCoB nanoparticles were reacted into non-magnetic phases during the heat treatment, samples were prepared for magnetic measurement by mixing Mg and 10wt% NiCoB nanoparticles. In mixing 10 wt% NiCoB, it was important to be sure that in the reaction with Mg, new phases would be visible on X-ray analysis. The prepared powder was first separated in two parts. One part was sintered at 850°C, while the other one was measured without sintering. Both samples were measured on a magnetic properties measurement system (MPMS), and full magnetic hysteresis loops were observed in field region of ±4 T. DTA/TGA analysis did not show any reaction between boron and NiCoB.

5.4.3 Experimental results and discussion

5.4.3.1 DTA analysis

5.4.3.2 Reactions of B + NiCoB, and pure NiCoB powders

Figures 5.4.1 and 5.4.2 show the DTA results for NiCoB nanoparticles and a mixture of boron and NiCoB nanoparticle powders in the temperature range from 50 to 1000°C, respectively. The same amorphous micron-sized boron was used as for making the best NiCoB doped MgB_2 samples (AM99). DTA results for the NiCoB and boron mixture did not show any reaction between the boron and the NiCoB (Fig. 5.4.2).

This result is in accordance with theoretical knowledge about elemental boron, which is inert in terms of chemical reactivity and has a high melting point, 2300°C. NiCoB nanoparticles by themselves are stable up to 1000°C and do not decompose at the measured temperatures (Fig. 5.4.1). Figure 5.4.1 does not reveal any endothermic peak that would indicate the melting point of the nanoparticles. The nanoparticles did not react with the protective argon gas, as expected, and no oxidation of nanoparticles was detected.

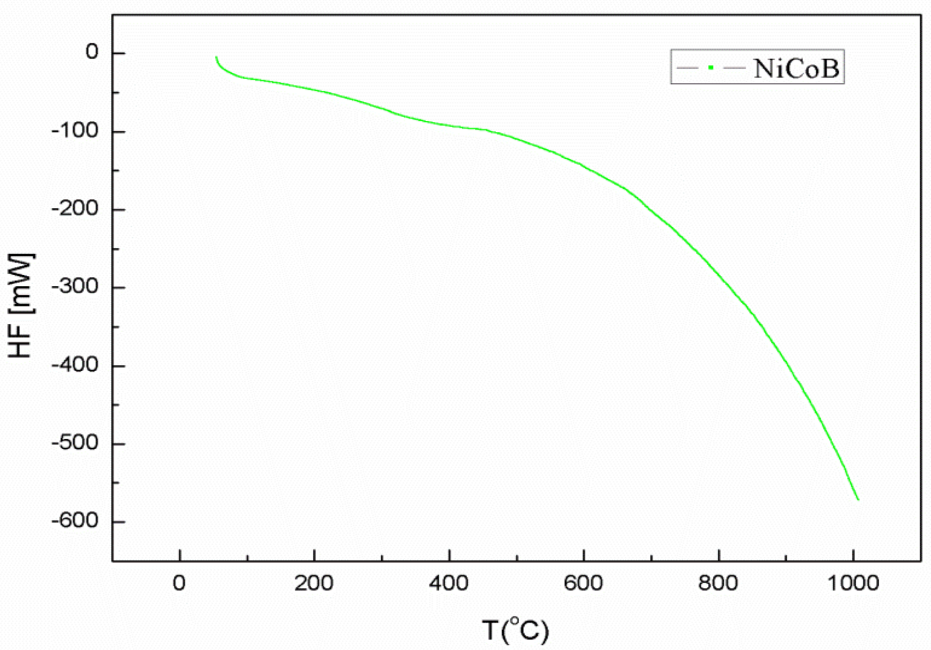

Fig.5.4.1: DTA curve for pure NiCoB nanoparticles in the temperature range of 50-1000°C.

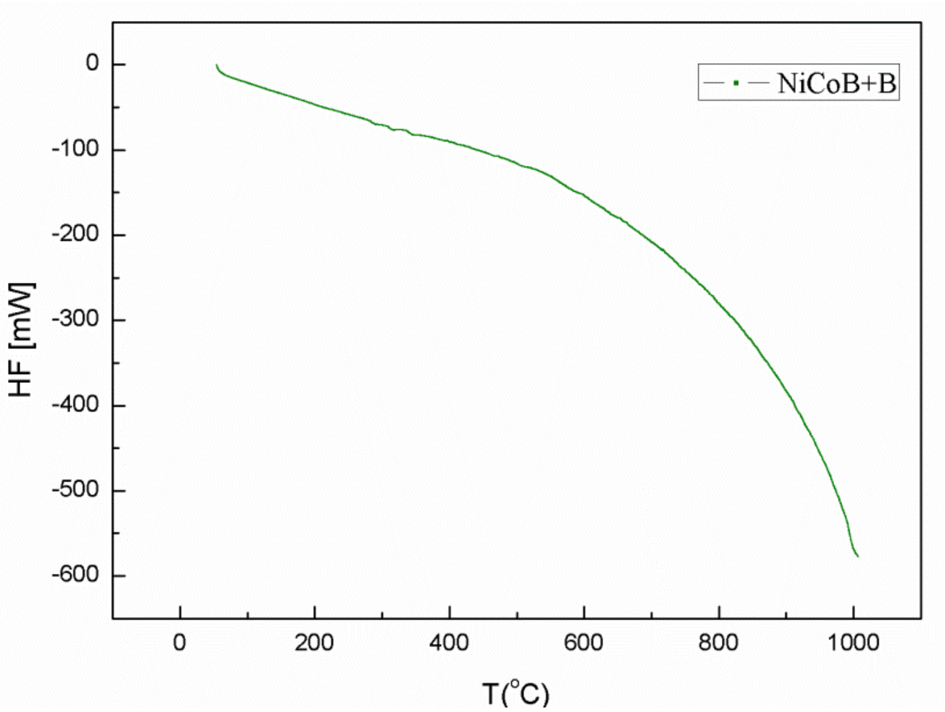

Fig. 5.4.2: DTA curve for mixed powders of AM99 boron and NiCoB nanoparticles (10 wt%).

5.4.3.3 Reactions for Mg + NiCoB powders

Figure 5.4.3 shows DTA curve for the reaction between Mg and NiCoB nanoparticles without boron. Important information was observed on the DTA curve relating to the reaction of the nanoparticles and magnesium. The small exothermal peak close to 500°C (peak A) suggests the reaction of the nanoparticles with magnesium.

This small peak, which is accompanied by a broad plateau, can be described as a slow local solid-solid reaction between NiCoB and Mg. The nanoparticles react with Mg and form a eutectic system[1,2] before Mg melts at 650°C. Melted Mg can easily diffuse and reacts with B [3]. Furthermore, with particle size of less than 10 nm, the nanoparticles are extremely reactive, even at lower temperature than bulk NiCoB, due to their large surface area.

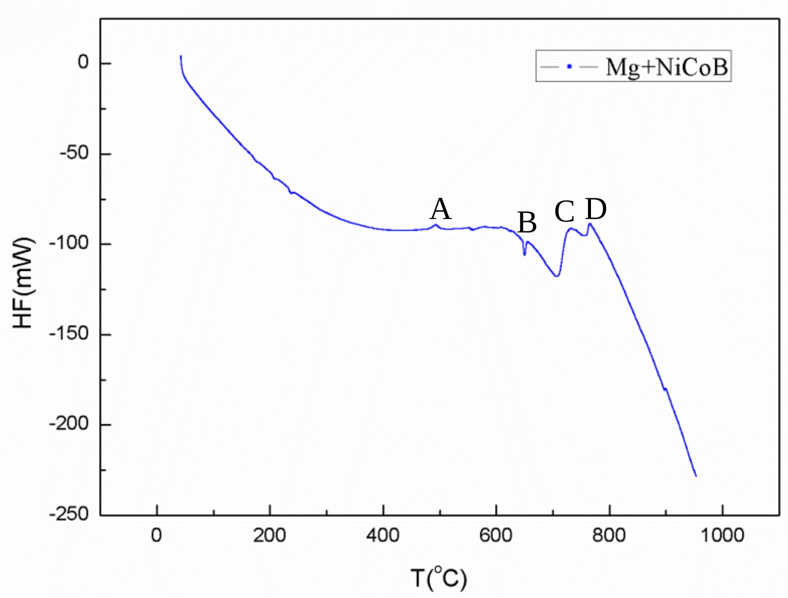

Fig. 5.4.3: DTA curve of NiCoB + Mg system.

Melting of magnesium can be clearly observed at 650°C as endothermic peak B in the DTA curve. With increasing temperature, two further distinct peaks appear, peak C at about 700°C and peak D at 770°C (Fig. 5.4.3).

Peak C represents the formation of Mg_xB_y phase, since approximately 30 at% of the atoms in NiCoB are boron. The exothermal peak D at 770°C most likely represents the formation of the stable phases Mg_2Ni and Co_2Mg (Mg_2Co).[4] Further supporting evidence for the formation of these phases will be given later in this section. Phase transformation into a stable phase is associated with the lowest value of the Gibbs free energy.

It is worth noting that in the DTA curve for NiCoB + B + Mg, just one broad peak from 700 to 800°C can be observed (Fig. 5.4.6). Measurements of critical current density, J_c, for NiCoB doped MgB_2 show that improvement is obtained only for sintering at temperatures above the temperatures of the peaks C and D. Therefore, reactions at these temperatures will be responsible for the improvement of J_c.

Figure 5.4.4 shows the phase diagram for the Mg-Ni and Mg-Co systems. Study of the Mg-Co binary phases shows that there are no equilibrium phases, except the original elements for Mg content smaller than 50%. One line compound exists for this system in the Laves phase, $MgCo_2$. Mg_2Co was reported to be formed by dehydrogenation of Mg_2CoH_5, prepared from Mg and Co nanoparticles[5]. In systems such as NiCoB+ Mg, phase transformation is more complicated and includes boron too. The presented phase diagram can be used as a rough indication of what may happen when NiCoB nanoparticles react with a mixture of Mg and B powders. From these phase diagrams, Mg_2Ni and $MgCo_2$ phases can be expected in NiCoB doped MgB_2. Nanostructural effects and the presence of boron should also be considered in relation to the formation of the phases.

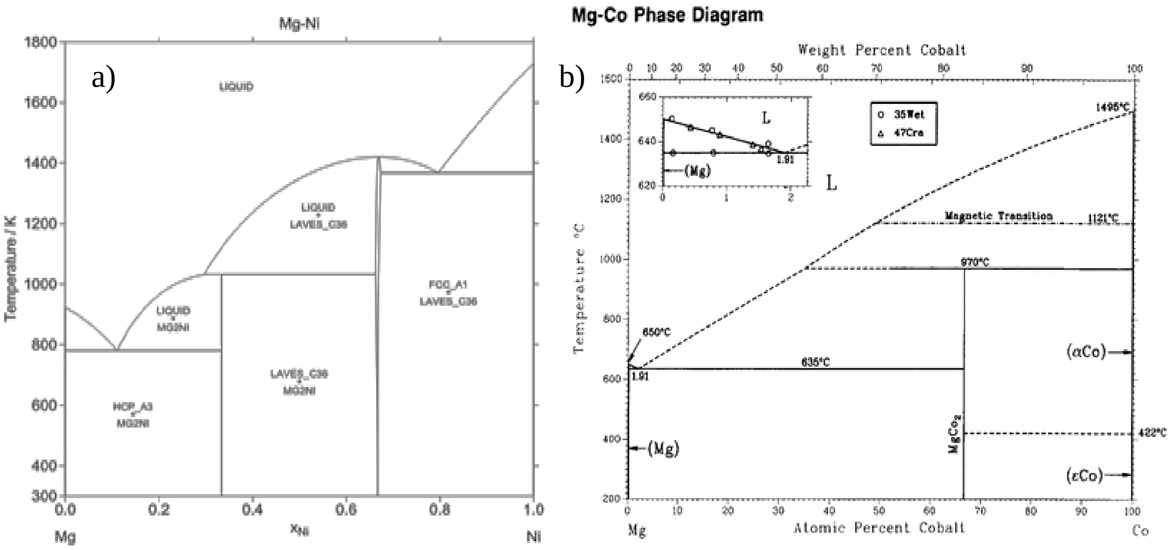

Fig. 5.4.4 a), b): Characteristic features of binary phase diagram for (a) Mg–Ni and (b) Mg–Co. Adopted from[4].

Figure 5.4.5(a-d) shows a schematic explanation of the reaction between Mg and Ni nanoparticles, which form a local eutectic system, and thus the reaction of melted Mg at lower temperature with boron. The presented figure gives an indication for the mechanisms of the slow solid-solid reaction and the formation of MgB_2 below melting point of Mg, as represented by the broad plateau in Fig. 5.4.3. The NiCoB nanoparticle system is more complex than for Ni nanoparticles, however, this mechanism can provide an indication on what happens with the NiCoB system.

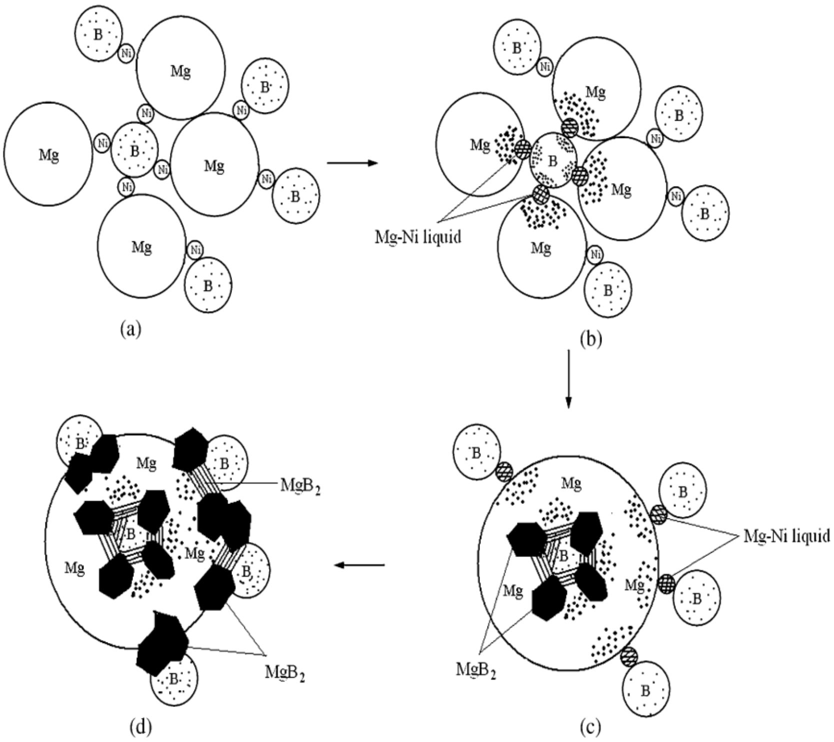

Fig. 5.4.5: Schematic illustration of the reaction between Mg and B with the assistance of Ni nanoparticles. Adopted from [2].

5.4.3.4 Reactions of Mg + B + NiCoB powders to form new phases

Figure 5.4.6 shows the reactions between Mg, boron, and NiCoB nanoparticles in the temperature range from 50°C to 1000°C. The DTA image clearly shows a wide exothermal peak which starts around 750°C. That exothermal peak indicates the chemical reaction to form new phases between magnesium and the transition metals: cobalt and nickel. The DTA results show that NiCoB reacts with magnesium, and there is no reaction between boron and the nanoparticles (Fig. 5.4.2). According to the XRD data and reports in the literature [6,7,8,9,10], the new phases forming at low temperatures (< 500°C) could be Mg_2Ni and Mg_2Co. The reaction between Mg and NiCoB before the melting of Mg can only be a solid–solid reaction, which is very slow. The Mg_2Ni and Mg_2Co/Co_2Mg phases will be formed much faster in a solid-liquid reaction at higher temperatures, where Mg is melted.

Two important processes happened above 750°C, the first is the formation of the new phases Mg_2Ni and Mg_2Co/Co_2Mg, and the second is the completion of the reaction between Mg and B, completely forming MgB_2 as the dominant phase. It is important that the two processes occur together, incorporating new phases into the MgB_2 matrix and completing the formation of MgB_2. This all happens between 750-800°C, providing good pinning centres and improving J_c.

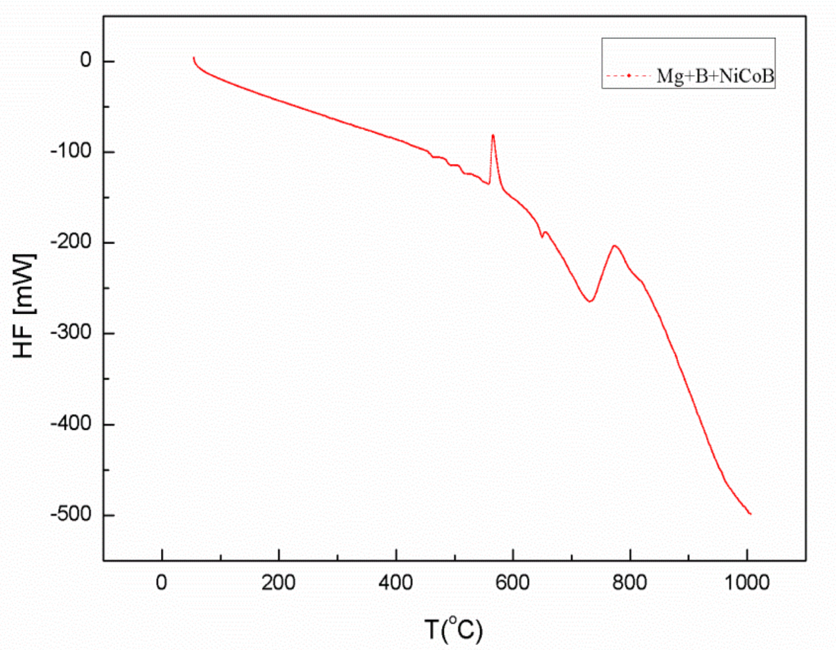

Fig. 5.4.6: DTA curve of mixture of powders: Mg + B + NiCoB.

5.4.3.5 Formation of MgB_2

Figure 5.4.7 presents the DTA curve for the formation MgB_2. The DTA curvew shows a broad exothermic peak just below 600°C, corresponding to formation of pure MgB_2 phase (Fig. 5.4.8 black curve, Fig. 5.4.7), before the melting of Mg. That peak indicates the solid-solid reaction between Mg and boron, which has already been reported several times in the literature[1,2,3,11]. The characteristics of a solid–solid reaction include very limited reacting area and slow reacting time, due to solid diffusion at low temperature. Small MgB_2 grains in a local area exist in the bulk material after the solid-solid reaction, together with residual Mg and B particles.[1]

Crystallinity of the resulting MgB_2 will be poor, giving relatively strong vortex pinning. Nanoparticles can improve the reaction as a catalyst or by forming a eutectic solution with Mg, which can then easily react with boron, as described schematically in Fig. 5.4.5. This can be observed on the DTA curves, with a strong sharp peak at ~550°C when NiCoB nanoparticles are included in the precursor powder (Figs. 5.4.7 and 5.4.8).

At 650°C, the residual Mg melts (endothermic peak) and rapidly reacts with B in a liquid-solid reaction. This process is faster than the first step because of the contribution of the Mg liquid, so a large amount of the MgB_2 phase will be formed at this stage.

After melting of the residual Mg at 650°C, the reaction between Mg and boron accelerates and is completed at around 750°C. Molten Mg will also interact with the existing MgB_2 formed in the solid-solid reaction, improving its crystallinity and the connection between the crystals.[1,2]

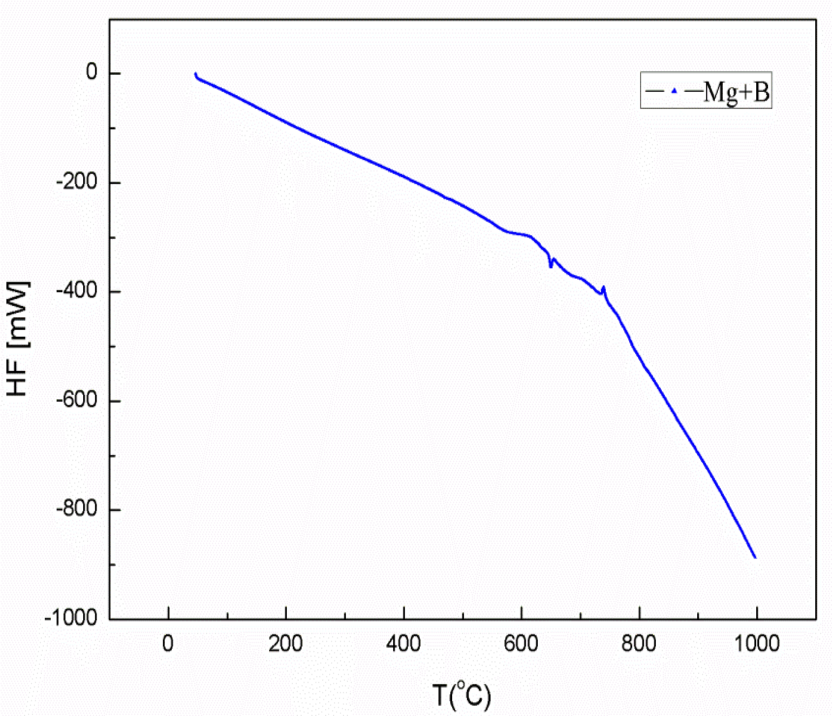

Fig. 5.4.7: DTA curve for formation of pure MgB_2 (Mg+B).

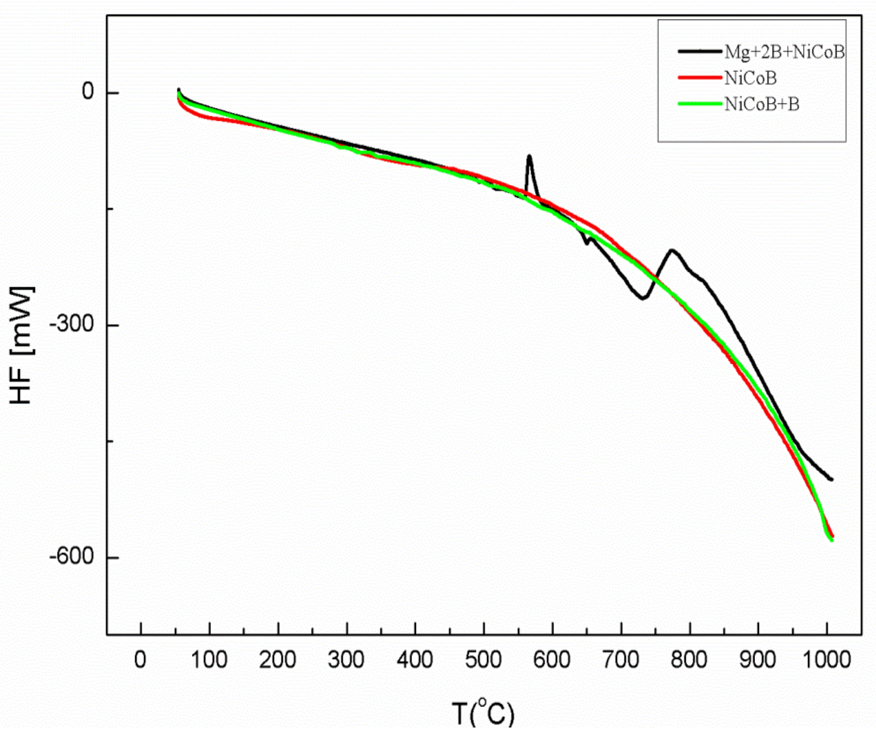

Fig. 5.4.8: DTA curves for pure NiCoB (red), NiCoB nanoparticles with boron (green) and NiCoB with Mg and boron (black).

5.4.3.6 Magnetic moment of nanoparticles

Magnetic hysteresis loops of Mg + NiCoB powders were collected at room temperature before and after a heat treatment at 850°C, to test if the magnetic properties changed in the heat treatment. This could provide useful information on the reaction of nanoparticles with Mg. Figure 5.4.9 shows magnetic hysteresis loops of Mg + NiCoB powder before and after the heat treatment. Before the heat treatment, a hysteresis loop typical for superparamagnetic nanoparticles was obtained, as expected for such small nanoparticles. A magnetic moment of 2.9 Am^2/kg was obtained at 4 T.

After the heat treatment, the magnetic moment at 4 T fell to 0.045 Am^2/kg. This shows that in the reaction at high temperatures, NiCoB nanoparticles are converted into another phase that has much smaller, or no, net magnetic moment.

The shape of the magnetic hysteresis loop after the heat treatment suggests paramagnetic behaviour. There could still be residual NiCoB nanoparticles in the sample after the heat treatment that could contribute to the measured small moment. Alternatively, the newly formed phases could have a small magnetic moment and behave as a superparamagnetic system. Comparing the values of magnetic moment before and after the heat treatment, a decrease of ~60 times is obtained.

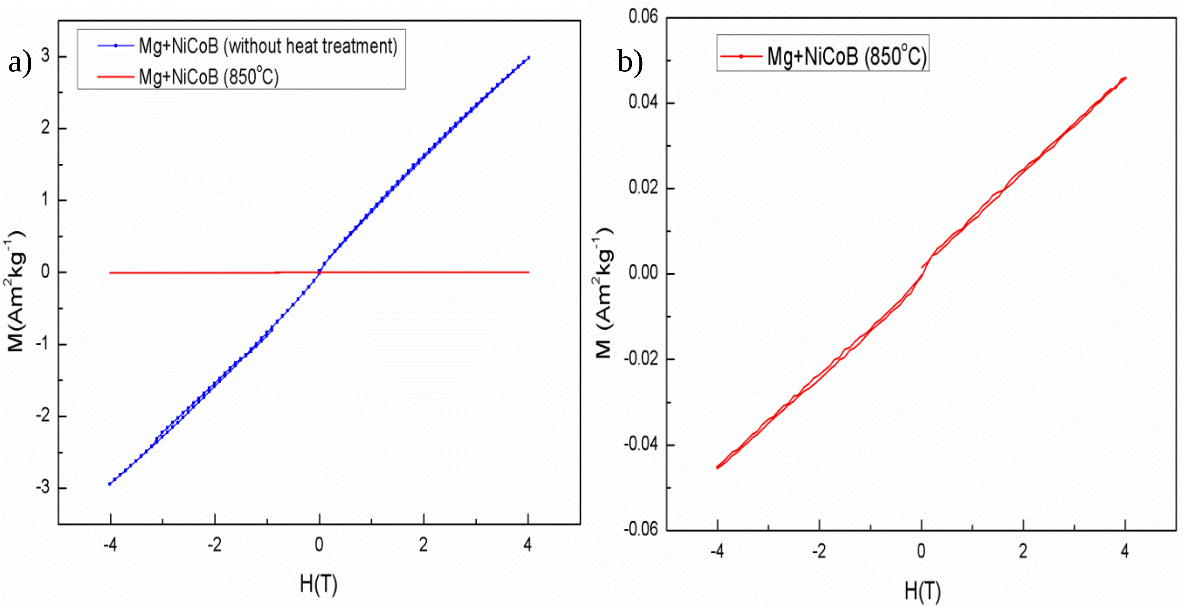

Fig. 5.4.9: Magnetic hysteresis loops of Mg+NiCoB with (a) heat treatment (850°C), and (b) without heating (left). Enlargement of hysteresis loop after heat treatment (right).

Reports in the literature show that the Mg_2Ni and Mg_2Co that are expected to occur in this reaction would be paramagnetic.[7,8,4] The loss of the magnetically ordered phase upon sintering is consistent with results of Masafumi Chiba et al., where the magnetic moment was decreasing steadily as Mg content increased in the Mg-Co system.[7]

Their results are shown in Figure 5.4.10. The closed and open circles show the saturation magnetizations for the Mg–Co system and the Mg–Fe system, respectively.

The magnetization decreases steadily as the amount of Mg increases. This indicates that the new Mg-Co phase, which is formed in increasing amounts as the amount of Mg increases, is not magnetically ordered. Saturation magnetization per unit mass decreases by the increase of the ratio of added non-magnetic Mg.[7]

According to the research of Aizawa et al., the product of the solid state reaction from a refined elemental mixture of Mg–Co to Mg_2Co is mostly non-magnetic.[4]

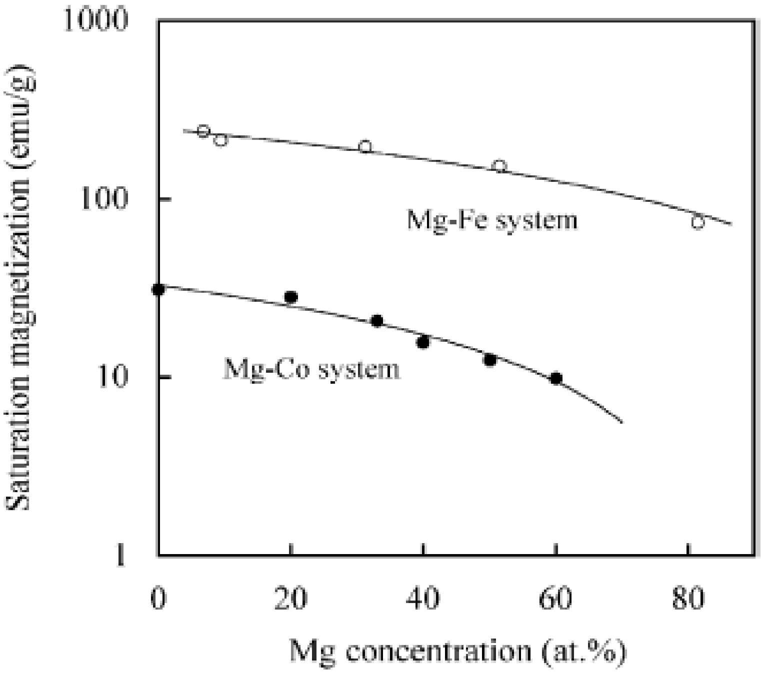

Fig. 5.4.10: Dependence of the saturation magnetization for mechanically alloyed Mg-Fe and Mg-Co powders on the Mg concentration. Adopted from [7].

5.4.3.7 XRD results and discussion

5.4.3.7.1 XRD pattern of magnesium precursor

Figure 5.4.11 presents a comparison of the XRD patterns of pure Mg and Mg after heat treatment at 850°C in protective argon. All peaks marked with (+) belong to pure magnesium. This pattern can be used for detecting unreacted magnesium in MgB_2 for different sintering temperatures.

The three dominant peaks are at 32.2°, 34.4°, and 36.7°, and the rest are at 47.8°, 57.4°, 63.2°, 69°, and 70.1°. It is difficult to find the MgO peaks in the Mg powder samples, however, because they are small and some peaks overlap with the Mg peaks. Small MgO peaks at 43° and 62.5° can be distinguished.

The XRD patterns revealed some changes after the heat treatment at 850°C for 30 min under protective argon gas. MgO peaks appeared at 37°, 43°, 62.2°, and 78.6°, while the remaining peaks belonged to already mentioned unreacted Mg. From this analysis we can conclude that oxidation of magnesium occurred in the heat treatment under argon atmosphere.

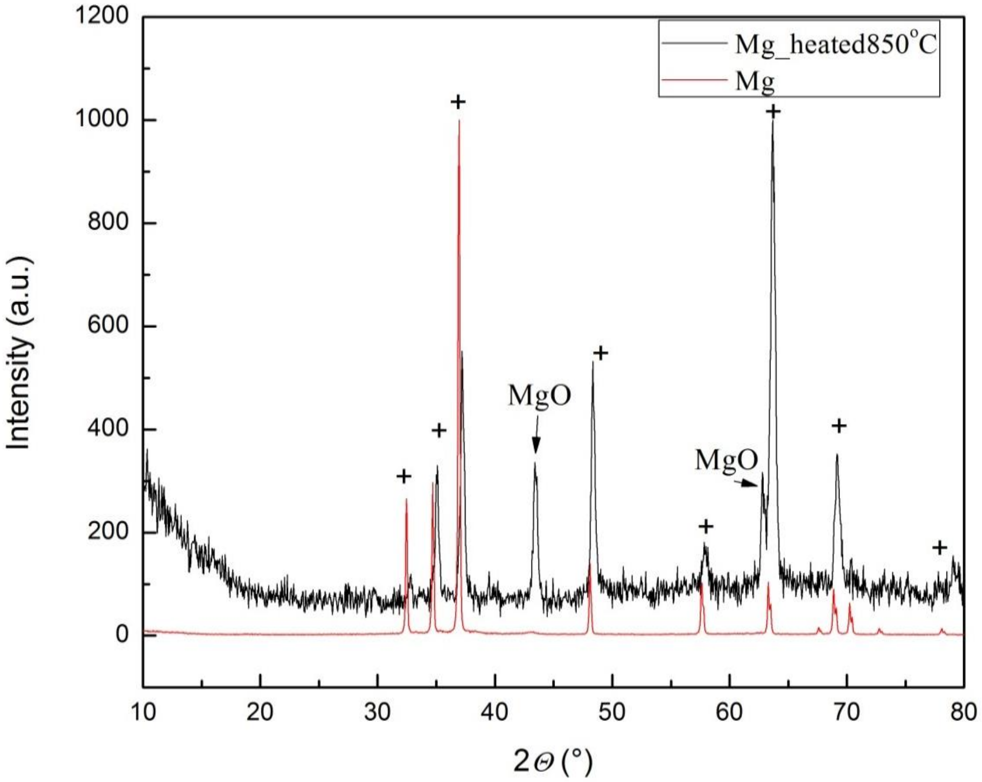

Fig. 5.4.11: XRD pattern of pure Mg and Mg after heat treatment in Ar.

5.4.3.7.2 XRD pattern of Mg + NiCoB

Figure 5.4.12 shows XRD patterns of the Mg + NiCoB sample after sintering at three different temperatures. The reaction between magnesium and the NiCoB nanoparticles of NiCoB is revealed and can be compared in these XRD patterns.

In Figure 5.4.12 three main peaks of residual Mg can be clearly observed at 32.5°, 34.8° and 36.9°, respectively. The sintering temperature for these powders were 650°C, 750°C, and finally, 850°C, the same as for NiCoB doped MgB_2 . The most interesting phases, Mg_2Co/Co_2Mg and Mg_2Ni, have appeared even at the lowest temperature of 650 °C. This observation is in agreement with a report in which the formation of Mg_2Ni occurred at 400°C during ball milling of Mg and Ni.[4,7,10]

At that temperature and under those conditions, only a solid-solid reaction can be obtained because magnesium has a melting point of 650°C. From that point of view, we can conclude that the small peaks in the DTA curve (Fig 5.4.3) in the temperature range between 400 to 500°C can be the same reaction in our case.

Small nanoparticles can react very easily with magnesium in localized areas. The solid –solid reaction is slow and probably not so intensive with amount of released energy in reaction, which can be a problem for detection.

The peaks of $MgCo_2$ are at 41.1°, 44°, 47.9°, and 69.1°, and most of them can be clearly detected. On the other hand, Mg_2Ni is much more difficult to observe, but several peaks appeared on the XRD patterns for all sintering temperatures, at 57.5° and at 37°, where they overlap with those for pure Mg.

Boron from NiCoB nanoparticles probably also reacts with magnesium and forms compounds such as MgB_2 and MgB_4. It is huge problem to prove that conclusion directly from peaks in the XRD pattern due to the overlapping of many phases, especially with Mg and $MgCo_2$.

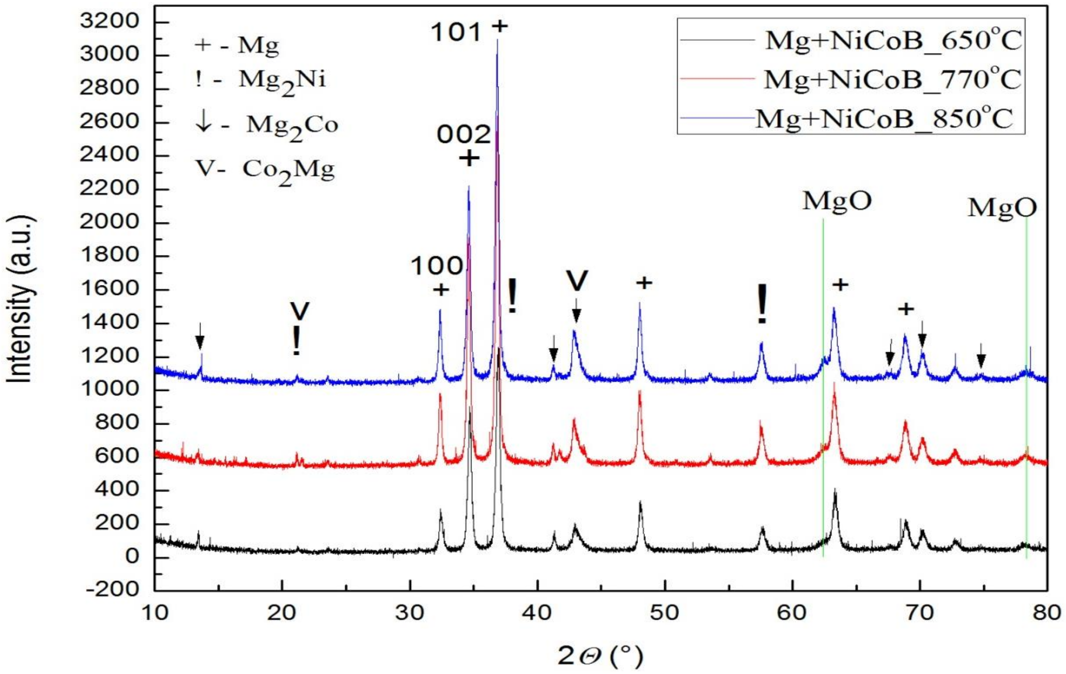

Fig. 5.4.12: XRD patterns: Mg+ NiCoB nanoparticles sintered at different temperatures (650°C (black), 770°C (red), and 850°C (blue)).

Table 5.4.1 shows XRD data for pure Mg, Mg_2Ni, and Mg_2Co_2, with characteristic angles and intensities.[7]

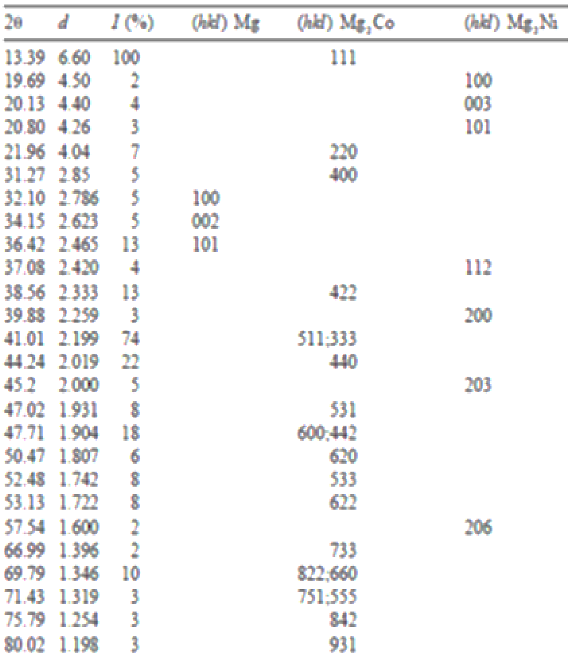

2θ	*d*	*I* (%)	(*hkl*) Mg	(*hkl*) Mg_2Co	(*hkl*) Mg_2Ni
13.39	6.60	100		111	
19.69	4.50	2			100
20.13	4.40	4			003
20.80	4.26	3			101
21.96	4.04	7		220	
31.27	2.85	5		400	
32.10	2.786	5	100		
34.15	2.623	5	002		
36.42	2.465	13	101		
37.08	2.420	4			112
38.56	2.333	13		422	
39.88	2.259	3			200
41.01	2.199	74		511;333	
44.24	2.019	22		440	
45.2	2.000	5			203
47.02	1.931	8		531	
47.71	1.904	18		600;442	
50.47	1.807	6		620	
52.48	1.742	8		533	
53.13	1.722	8		622	
57.54	1.600	2			206
66.99	1.396	2		733	
69.79	1.346	10		822;660	
71.43	1.319	3		751;555	
75.79	1.254	3		842	
80.02	1.198	3		931	

Table 5.4.1: XRD pattern data for pure Mg, Mg_2Ni, and Mg_2Co. Adopted from [7].

Figure 5.4.13 presents the XRD pattern of Co_2Mg phase. According to the phase diagram in Figure Fig. 5.4.4(b), Co_2Mg is the only stable phase with Co and Mg and is more likely to occur that Mg_2Co[4].

Detailed observation of the XRD pattern can reveal the same peaks in Fig. 5.4.12, which can belong to Co_2Mg phase. The small size of nanoparticles and spatial agglomeration of nanoparticles can change the ratio with Mg and produce different phases. According to Figure 5.4.12, the observed peaks mostly belongs to Mg_2Co phase, but same peaks overlap as at 21.5° and 43°, so in the same area, there is the possibility of peaks for Co_2Mg phase. Observing the XRD patterns of Mg + NiCoB sintered at different temperatures, different intensities and shapes of peaks, and even the appearance new phases can be detected.

The formation of new phases in a reaction with nanoparticles often can have local differences, depending on the spatial ratio of reactants, temperature fluctuation.

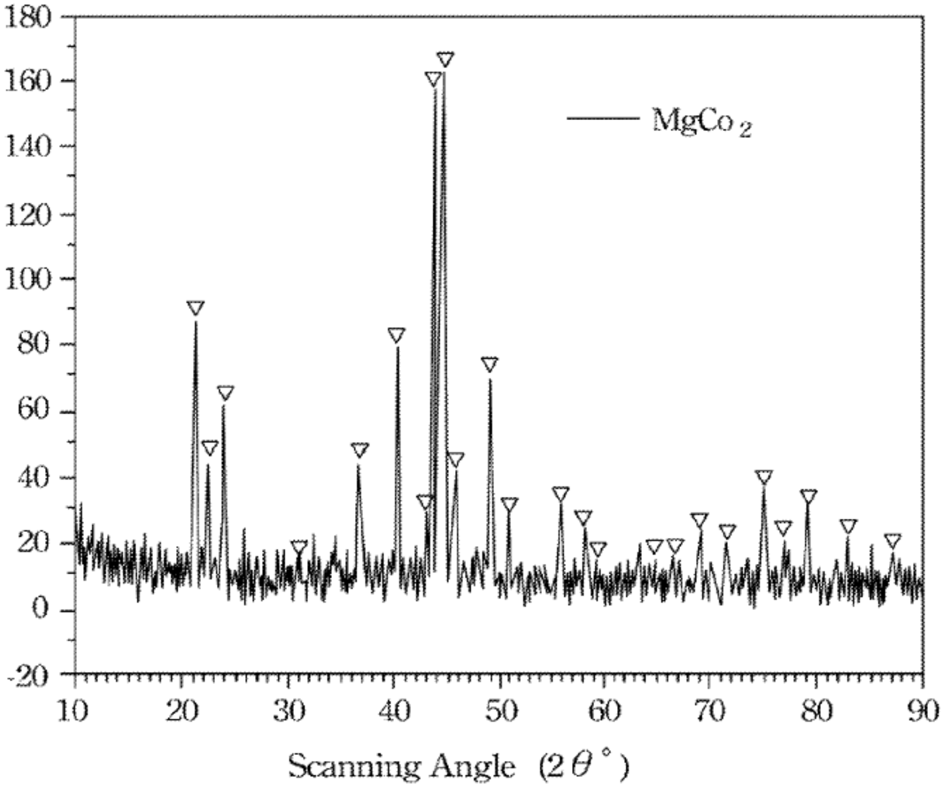

Fig. 5.4.13: XRD pattern of Co_2Mg. Adopted from [9].

Figure 5.4.14 shown XRD pattern of Mg+ NiCoB nanoparticles sintered at 850°C with all possible phases wich can be formed between Mg, NiCoB and oxygen.

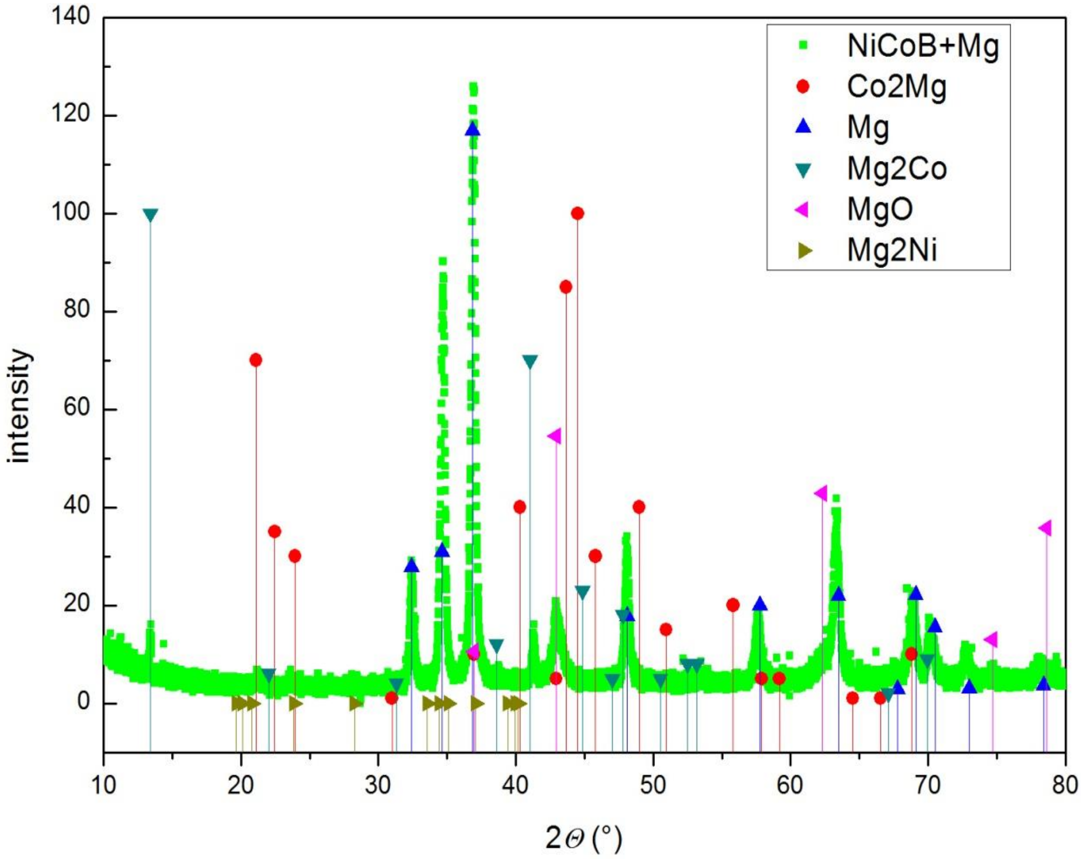

Fig.5.4.14: XRD patterns: Mg + NiCoB with observed phases.

5.4.4 Conclusion

Magnetic NiCoB nanoparticles that are added to Mg and B powders to dope MgB_2 react only with Mg, forming paramagnetic Mg_2Ni and $MgCo_2$ phases. Formation of these phases starts occurring well below 600°C in a slow solid-solid reaction. This process also promotes slow creation of MgB_2 at low temperatures. After melting of Mg at 650 °C, these reactions speed up, and they are fastest between 750 and 800 °C. Improvement of J_c by doping is associated with these fast reactions at high temperatures. Since MgB_2 and the new particles are formed simultaneously, the particles are incorporated into MgB_2. At the same time, the grain boundaries are not coated with MgO due to competition of Mg_2Ni and $MgCo_2$ (Mg_2Co) with MgO for Mg. This results in better grain connectivity and improved vortex pinning, as observed in the $J_c(H)$ measurements. It should be stressed that the new nanoparticles are not magnetic, and they do not contribute to magnetic vortex pinning, as anticipated at the beginning of this project.

Finally, above 750°C boron and Mg complete the formation of MgB_2 and the incorporation of new stable phases into the matrix of MgB_2.

5.4.5 REFERENCES

1 Z.Q. Ma, Y.C. Liu, Q.Z. Shi, Q. Zhao and Z.M. Gao: Supercond. Sci. Technol., 2008 21 065004.

2 Q. Zhao, Y. Liu, N. Zhao, S. Penner, and Z. Ma**,** IEEE Transactions on Nanotechnology, vol. 10, no. 2, 2011.

3 M. Kühberger, and G. Gritzner, Physica C 370, 39–43, 2002.

4 A. Tatsuhiko, K.-I. Hasehira, C. Nishimura, Materials Transactions, Vol. 44, No. 4 pp. 601 to 610, 2003.

5 H. Shao, T. Liu, Y. Wang, H. Xu and X. Li, J. Alloys Comp. 465, 527, 2008.

6 Y. Chen et al., Journal of Materials Research, Vol. 24, No.4, 2009.

7 M. Chiba, H. Hotta, T. Nobuki, A.Sotoma, T. Kuji, Journal of Magnetism and Magnetic Materials 316, e454–e457, 2007.

8 E. M. Kirkpatrick, D. Leslie-Pelecky, S.-H. Kim, R.D. Rieke, J. of Appl. Phys. Vol. 85, p. 8-15, 1999.

9 S.-L. Lee, R.-R. Jeng, C.-W. Hsu, Y.-C. Tsai, Method of synthesizing magnesium-cobalt pentahydride, US patent, no.: US 8,163, 267 B1

10 J.-L. Bobet, E. Akiba, B. Darriet, Journal of Alloys and Compounds 297 192–198, 2000.

11 J. H. Kim, X. Xu, M. S. A. Hossain, D. Q. Shi, Y. Zhao, X. L. Wang, S. X. Dou, S. Choi, T. Kiyoshi, Applied Physics Letters, Vol. 92 Issue 4, p.042506-042509, 2008.

Chapter 6: Conclusion

In this research work parallel has been parallel studied synthesis of nanoparticles, and the influence of prepared nanoparticles on electromagnetic properties of MgB_2. In early beginning of research of MgB_2 most of the effort was focused on improving with chemical doping. Despite of many research in this area, very few are focused on doping with magnetic nanoparticles and explanation of magnetic pinning mechanism.

As mentioned earlier more than 10 different compounds have been investigated and mostly characterized. Many of them did not show any improvement, as iron borides. The investigation was focused on compound with best results, NiCoB. That complex compound with amorphous structure during the research was reduced to size of quantum dots, 5 nm. Throughout the study can be constantly monitored progress and improvements in the synthesis of nanoparticles which gradually gave positive results for MgB_2.

This work was particular in many ways, firstly was separate in two parts, work in Zagreb and work on ISEM institute. Work in Zagreb was characterized with improving of chemical synthesis technique and producing MgB_2 wires. On the other hand, work in ISEM institute was based on detailed investigation of best obtained doping with NiCoB nanoparticles and producing bulk samples of MgB_2.

All this work can be separate on chemical part (nanoparticles synthesis) and physical part which include doping to MgB_2. The main differences between two works, except reducing size of nanoparticles were in sintering condition and starting precursors.

In chapter 5.1 has been shown that influence of starting precursor has a strong impact on properties of MgB_2. Amorphous borons (AM99 and AN99) presented much higher value of J_c than crystalline boron CB96. Both amorphous borons have much smaller particles size below 1 μm in comparison with crystalline boron with particles size of several microns. Reducing the size of starting material enhances the reaction between boron, magnesium, and NiCoB nanoparticles due to larger contact area. Due to slower reaction and more impurities as a MgO, MgB_2 made from crystalline boron gave substantially decreasing of J_c with doping.

Sintering condition has been studied in chapter 5.2, and presents remarkably influence of sintering temperature on properties of MgB_2 samples. The main point of this study is that all improvement in critical current density is observed for all samples sintered above 750°C. It is two main factors which are occurred above 750°C, completing the reaction between boron and magnesium, and incorporation of dopant nanoparticles in the MgB_2 matrix, and forming stable phase between Mg and nanoparticles. Incorporating the nanoparticles into the matrix of MgB_2 according to expanded investigation is mostly due to improving connectivity between grains. Small impact on improving pinning can come from new phase Mg_2Ni and Mg_2Co/Co_2Mg. The doping did not result in improvement of J_c at 20 K, which can be explained by the higher thermal excitation of super-electrons, especially in the π-gap.

Further investigation concentrated on best obtained samples (MgB_2 doped with 2.5 wt% NiCoB sintered at 850°C) showed that improving of J_c is associated with both improvements of grain connectivity and of vortex pinning, with more impact on improving connectivity. As a evidence of this conclusion is the effective cross sectional area obtained by Rowel’s method increased from 0.22 to 0.32 with the doping. This is associated with observed decrease of oxygen content in the sample after NiCoB doping and high temperature sintering. NiCoB most likely competes for Mg with MgO to create Mg_2Ni and Mg_2Co/Co_2Mg, what significantly improved grain connectivity, since MgO tends to coat superconducting crystals with insulating layer.

Magnetization decay measurement present that vortex pinning at 5 K is improved with NiCoB doping and high sintering temperature while pinning at 20 K, however, is not improved with the doping. The explanation can be that the doping increases vortex pinning only in π-band, which is closed at temperatures above about 16 K.

Finally in last chapter 5.4 has been studied reaction between starting materials, what proved reaction between Mg and nanoparticles and forming new phases Mg_2Ni and Mg_2Co/Co_2Mg.

Important information is provided by measuring magnetization after and before reaction Mg and nanoparticles what present considerably decreasing of magnetization after sintering. The whole project was based on idea of magnetic doping and possibility of pinning with magnetic interaction between vortex and magnetic particles. Decreasing of magnetization and after sintering strong minimize possible influence of magnetic pinning. This study indicates that magnetic pinning is possible but technique of preparing samples must be modified.

Future work will be focused on synthesis of new nanoparticles not necessary with magnetic respond. Parts of that work has been presented in last section of chapter 3, where is presented silver nanoparticles coated with grapheme oxide.

Unifying different fields of science offers great advantages and new opportunities for further improvements of existing materials and creates new superconductors with higher critical temperatures.

List of publication:

1) M. Mustapić, D. Pajić, N. Novosel, E. Babić, K. Zadro, M. Cindrić, J. Horvat, Ž. Skoko, M. Bijelić, and A. Shcherbakovc, ”Synthesis, Structural Characterization and Magnetic Properties of Iron Boride Nanoparticles with or without Silicon Dioxide Coating”, Croatica Chem. Acta 83, 3; 275-282, 2010.

2) N. Novosel, D. Pajić, M. Mustapić, E. Babić, A. Shcherbakov, J. Horvat, Ž. Skoko, K. Zadro, ”Flux pinning and inhomogeneity in magnetic nanoparticle doped MgB_2/Fe wire”, Journal of Physics: Conference Series 234**,** 022027, 2010.

3) N. Novosel, S. Galić, D. Pajić, Ž. Skoko, I. Lončarek, M. Mustapić, K. Zadro and E. Babić, ”Enhancement of the critical current density in MgB_2 wires doped with Ni nanoparticles”**,** Supercond. Sci. Technol. 25, 095018, 2012.

4) N. Novosel, D. Pajić, Ž. Skoko, M. Mustapić, E. Babić, K. Zadro, J. Horvat, ”The influence of $CuFe_2O_4$ nanoparticles on superconductivity of MgB_2”, Physics Procedia, 36 1498-1503, 2012.

5) N. Novosel, S. Galić, D. Pajić, Ž. Skoko, I. Lončarek, M. Mustapić, K. Zadro, and E. Babić, ”Effect of magnetic NiCoB nanoparticles on superconductivity inMgB_2 wires”**,** Supercond. Sci. Technol.26, 065004, 2013.

6) M. Mustapić, J. Horvat, M. S. Hossain, Ž. Skoko and S. X. Dou., “Enhancing superconducting properties of MgB_2 pellets by addition of amorphous magnetic Ni-Co-B nanoparticles” Supercond. Sci. Technol. 26 075013, 2013

7) M. Mustapić, J. Horvat, M. S. Hossain, Ž. Skoko and S. X. Dou, “Effects of type of boron on properties of MgB_2” in preparation.

8) M. Mustapić, J. Horvat, M. S. Hossain, Ž. Skoko and S. X. Dou, “New preparation of Ni-Co-B nanoparticles and study of reaction with magnesium and boron precursors in forming MgB_2“ in preparation.